Fluid drift and spheroid rotation in viscous density stratified fluids

JNCASR

Arun Kumar Varanasi

Engineering Mechanics Unit
Jawaharlal Nehru Centre for Advanced Scientific Research, Bangalore

This dissertation is submitted for the degree of
Doctor of Philosophy

August 2022

Dedicated to my mother Asha Jyothi and my brother Kiran …

Declaration

I hereby declare that the matter embodied in the thesis entitled **"Fluid drift and spheroid rotation in viscous density stratified fluids"**, is the result of research work carried out by me at the Engineering Mechanics Unit, Jawaharlal Nehru Centre for Advanced Scientific Research, bangalore, India, under the supervision of Prof. Ganesh Subramanian, and that it has not been submitted elsewhere for the award of any degree or diploma.

In accordance with the general practice in reporting scientific observations, due acknowledgement has been rendered appropriately, whereever the work described is based on the findings of other investigators.

V. Arunkumar

Arun Kumar Varanasi
August 2022

Certificate

I hereby certify that the matter embodied in this thesis entitled **"Fluid drift and spheroid rotation in viscous density stratified fluids"** has been carried out by Mr. Arun Kumar Varanasi at the Engineering Mechanics Unit, Jawaharlal Nehru Centre for Advanced Scientific Research, Bangalore, India, under my supervision, and that it has not been submitted elsewhere for the award of any degree or diploma.

Dr. Ganesh Subramanian
Professor
Engineering Mechanics Unit
JNCASR, Bangalore August 2022

Acknowledgements

I would like to thank my research supervisor Prof. Ganesh Subramanian for introducing these set of non-trivial problems associated with particles moving in density stratified fluids. I am thankful to him for his patience (especially during the pandemic time), and guidance throughout this thesis work. Experience of working with him will certainly aid in my future research work. I also like to thank him for his course on fluid mechanics and giving me a chance to work as a teaching assistant for this course for two of the semesters during my Ph.D. time.

I am thankful to Prof. K.R. Sreenivas, Prof. Santosh Ansumali and Prof. Diwakar Venkateshan for their financial support at various stages of my time at JNCASR. I thank faculty members of EMU mentioned above along with Prof. Meheboob Alam and Prof. Meher Prakash for their insightful courses in the early stages of my Ph.D. I am also thankful to JNCASR and DST for financial support during this Ph.D. I would like to thank the administration and support staff of JNCASR. I thank all the past and present students of EMU for making life in JNCASR enjoyable. I would like to thank my collaborator Dr. Navaneeth Marath, IIT Ropar, for the discussions related to the Chapter 4 of this thesis. I am thankful to Dr. Indumati Rao and Prof. N.S. Vidhyadhiraja for giving me a chance to teach parts of mathematics and physics to 10 + 2 students as part of the student mentoring program of JNCASR. I am thankful to the fellow senior mentors of the program for various discussions.

My first steps/initiation in research is during my Masters at Department of Chemical Engineering, IISc. I am forever grateful to the professors of the department, especially my Masters advisor Prof. K Ganapathy Ayappa, for teaching many important and necessary qualities. I am indebted to all my close friends, especially Gopal, Anji, Krishna babu, Aarthi, Mari, Upendra and Balu for their encouragement. I am also indebted to my family members, especially my mother, brother, sister and my in-laws who have supported me throughout the course of Ph.D. I would not have been able to make this far without my mother and brother. This thesis is dedicated to both of them. Special thanks to my brother-in-law Dr. Rana Howlader for his guidance.

Finally, I thank Jeshmine and Rachith for staying close to me all throughout.

Abstract

This thesis broadly deals with the motion of passive particles in density stratified fluids in the viscous limit and can be divided into two parts. The first part is concerned with the evaluation of the drift volume, as defined by Darwin [1953], due to slow settling of a sphere in a weakly stratified fluid in the convection dominant limit. This problem is motivated by the intent to examine the validity of the rather provocative proposal of a biogenic contribution to ocean mixing [Katija and Dabiri, 2009; Leshansky and Pismen, 2010; Subramanian, 2010]. The main intention is therefore to evaluate the drift volume due to a passive sphere settling, in the regime mentioned above, which in turn requires the velocity field generated by sphere translation. Thus, the problem considered in the first part is concerned with the evaluation of the velocity and density fields due to translation of a sphere in a stably stratified ambient in the limit of small Reynolds ($Re \ll 1$) and viscous Richardson ($Ri_v \ll 1$) numbers; here, $Re = \frac{\rho U a}{\mu}$ and $Ri_v = \frac{\gamma a^3 g}{\mu U}$ with a being the sphere radius, U the translation speed, ρ and μ the density and viscosity of the stratified ambient, g the acceleration due to gravity, and $\gamma (> 0)$ the density gradient (assumed constant) characterizing the stable ambient stratification. In contrast to most earlier efforts, our study primarily considers the convection dominant limit corresponding to $Pe = \frac{Ua}{D} \gg 1$, D being the diffusivity of the stratifying agent. However, the diffusion dominant ($Pe \to 0$) regime [Ardekani and Stocker, 2010; List, 1971] is also considered for purposes of completeness, with a few new results, with regard to the structure of the velocity and density fields being presented. Using a combination of numerical computations and far-field asymptotics, we have characterized in detail the velocity and density fields in what we term the Stokes stratification regime, defined by $Re \ll Ri_v^{1/3} \ll 1$, and corresponding to the dominance of buoyancy over inertial forces. We have used a Fourier transform approach to write down the velocity and density fields as Fourier integrals, and a far-field analysis of these integrals leads us to distinguish between different regions of the flow field. On the whole, buoyancy forces associated with the perturbed stratification fundamentally alter the viscously dominated fluid motion at large distances. At distances of order the stratification screening length, that scales as $aRi_v^{-1/3}$ in the large-Pe limit, the fluid motion transforms from the familiar fore-aft symmetric Stokesian form to a fore-aft asymmetric pattern of recirculating cells with primarily horizontal motion

within; except in the vicinity of the rear stagnation streamline. At larger distances, the motion is vanishingly small except within (a) an axisymmetric horizontal wake whose vertical extent grows as $O(Ri_v^{-1/5} r_t^{2/5})$, r_t being the distance in the plane perpendicular to translation and (b) a buoyant reverse jet behind the particle that narrows as the inverse square root of distance downstream. For $Pe = \infty$, the motion close to the rear stagnation streamline starts off pointing in the direction of translation, in the inner Stokesian region, and decaying as the inverse of the downstream distance; the motion reverses beyond a distance of $1.15aRi_v^{-1/3}$, with the eventual reverse flow in the far-field buoyant jet again decaying as the inverse of the distance downstream. For large but finite *Pe*, the narrowing jet is smeared out beyond a distance of $O(aRi_v^{-1/2}Pe^{1/2})$, leading to an exponential decay in the aforementioned reverse flow.

The velocity field obtained above in the convection dominant limit, is used to calculate the associated fluid pathlines, drift displacements, drift surfaces, and finally, the drift volume for different viscous Richardson (Ri_v) and Peclet (Pe) numbers. In order to account for the finite size of the sphere, a uniformly valid expression for the velocity field is found by means of an additive composite approximation involving the summation of the inner and outer region expressions and subtraction of the overlapping contribution. Numerical integration of the ODE's governing the positions of the fluid elements is carried out using the composite velocity field above (both axial and transverse components), at each time instant, with the outer-region contribution being given as Fourier integrals. At the initial time $t = 0$, fluid elements are assumed to occupy a horizontal plane $z = 0$. The calculations of the upstream and downstream drift components are then carried out by integrating to suitably large negative and positive times, respectively. Our results clearly show that the pathlines and the drift displacements thus obtained do not show the characteristics associated with a homogeneous Stokes flow. In particular, the drift displacements do not exhibit a logarithmic-in-time divergence characteristic of a homogeneous Stokesian regime. Further, the downstream calculations show a reversal of fluid pathlines due to the effects of the aforementioned existence rearward jet for times $t > O(Ri_v^{-1/3})$. The drift surfaces, corresponding to times approaching negative and positive infinity, are shown to asymptote to finite limiting forms, implying that the drift volume converges to a finite value in a density stratified fluid for any finite Pe. For sufficiently large Pe, the upstream and downstream components of the total drift volumes are shown to scale as $Ri_v^{-2/3}$, although the convergence to this limiting large-*Pe* plateau is much faster for the upstream component. The final drift volume has the character of a reflux owing to the aforementioned reversal of fluid pathlines, and the cancellation between the upstream and downstream components appears to result in a net drift volume that is smaller than that expected from naive scaling arguments, with the scaling obtained from the numerics being closer to $Ri_v^{-1/3}$. Further, the fact that the total drift volume has the character of a reflux clearly indicates the singular role of stratification, for sufficiently long times, on the drift induced by particles in density stratified fluids.

The second part of the thesis is concerned with the rotation of a sedimenting spheroid, of an arbitrary aspect ratio, in a weakly stratified fluid again in the convection dominant limit. This work is primarily motivated by the recent experiments of Mercier et al. [2020]; Mrokowska [2018, 2020a,b]. These recent efforts demonstrated the non-trivial effects of stratification on settling anisotropic particles such as the emergence of a longside-on settling regime, and evidence of long-lived orientations with an inclination intermediate between the limiting broadside-on and longside-on configurations. In order to explain this behavior, we consider the rotation of a spheroid in a viscous density stratified fluid in the convection-dominant limit. We derive analytically the angular velocity of a spheroid of aspect ratio κ, sedimenting in a linearly stratified ambient. A generalized reciprocal theorem is used to write down the different contributions to the angular velocity. The analysis demarcates regions in parameter space corresponding to broadside-on and edgewise (longside-on) settling in the limit $Re, Ri_v \ll 1$, where $Re = \rho_0 UL/\mu$ and $Ri_v = \gamma L^3 g/\mu U$, the Reynolds and viscous Richardson numbers, respectively, are dimensionless measures of the importance of inertial and buoyancy forces relative to viscous ones. Here, L is the spheroid semi-major axis, U an appropriate settling velocity scale, μ the fluid viscosity, and $\gamma (> 0)$ the (constant) density gradient characterizing the stably stratified ambient, with ρ_0 being the fluid density taken to be a constant within the Boussinesq framework. We use the generalized reciprocal theorem formulation to identify three different contributions to the torque: (1) an $O(Re)$ inertial contribution that already exists in a homogeneous ambient, and orients the spheroid broadside-on; (2) an $O(Riv)$ hydrostatic contribution due to the ambient linear stratification that also orients the spheroid broadside-on; and (3) a hydrodynamic contribution arising from the perturbation of the ambient stratification by the spheroid whose nature depends on Pe; $Pe = UL/D$ being the Peclet number with D the diffusivity of the stratifying agent. Our work shows that, for $Pe \gg 1$, the hydrodynamic contribution is $O(Ri_v^{2/3})$, and therefore dominant over the $O(Ri_v)$ hydrostatic one, in the Stokes stratification regime characterized by $Re \ll Ri_v^{1/3}$, and orients the spheroid edgewise regardless of κ. Further, the hydrodynamic stratification torque exhibits a non-trivial orientation dependence on account of its singular character, in contrast to the regular $\sin\psi \cos\psi$ dependence exhibited by the inertial torque; ψ here being the angle between the spheroid orientation and gravity. The differing orientation dependencies of the inertial and large-Pe hydrodynamic stratification torques imply that the broadside-on and edgewise settling regimes are separated by two distinct κ-dependent critical curves in the $Ri_v/Re^{3/2} - \kappa$ plane, with the region between these curves correponding to stable intermediate equilibrium orientations. The predictions for large Pe are shown to be broadly consistent with the aforementioned experimental observations [Mercier et al., 2020; Mrokowska, 2018, 2020a,b].

Table of contents

List of figures

List of tables

Chapter 1

Introduction

Motion of particles in continuous and sharply stratified fluid environments occurs in a wide variety of problems, transcending an immense range of length scales from those relevant to microfluidic applications to those pertaining to astrophysical scenarios [Magnaudet and Mercier, 2020]. This clearly points to the importance of studying particle motion through a density-stratified fluid medium. The case of naturally occurring settings is particularly important since both the atmosphere and oceans, on average, are stably stratified fluids, and thus motion of particles moving through them is a ubiquitous phenomenon [Magnaudet and Mercier, 2020]. In the case of oceans, there exist examples of both active and passive particles moving through the pycnocline, the layer of the ocean corresponding to the largest (stable) density gradients. Examples of passive particles (the so-called marine snow) moving in the oceanic ambient consist primarily of a variety of organic and inorganic matter such as dead or dying animals, phytoplankton, sand and fecal matter, and these are known to play an important role in oceanic carbon cycle [Dutkiewicz et al., 2019]. With regard to active particles, the relevant examples are the smallest swimming organisms (zooplankton) since they contribute to the major portion of the oceanic bioamass (note further that the majority of the aquatic biomass is located within the oceans). The diurnal migration pattern of these small swimming organisms through the oceans has, in fact, been termed the largest migration on earth [Martin et al., 2020]. Thus, investigation of the fluid mechanical processes arising from perturbation of the ambient density stratification, by both swimmers and passive particles, will potentially help us better understand the various issues concerning environmental pollution and climate variability.

Most earlier studies, that have focused on the particles moving through stratified fluids, have examined the increase in the drag on, and the associated slowing down of, the particles when they move through discontinuous/continuous stratified environments Candelier et al. [2014]; Srdić-Mitrović et al. [1999]; Yick et al. [2009]; Zvirin and Chadwick [1975]. Previous studies have also reported the accumulation of particles/marine snow at density interfaces [Alldredge et al., 2002; MacIntyre et al., 1995]. An ambient stratification has also been known to alter the dispersion characteristics of both the passive and active particles [see Magnaudet and Mercier [2020] and references therein; Clercx et al. [2018]]. Apart from the translation of particles that is directly affect by the drag, it is also important to examine the role of density stratification on the orientation degrees of freedom when the particles are anisotropic, and the nature of the induced fluid motion for both spherical and anisotropic particles.

Since the first part of this thesis is concerned with the role of density stratification on the fluid motion, we briefly motivate this problem to begin with. Meridional overturning circulation of oceans [Summerhayes and Thorpe, 1996; Vallis, 2011] [see Figure 1.1 for an artist's representation] has been known to be driven by winds, tides, and contributions from Coriolis effects, cabeling, etc. Estimates indicate that there exists a shortfall in the energy budget (of the order of Terawatts) required for large-scale ocean mixing after accounting for the energy supply from the above mentioned well known sources Munk and Wunsch [1998]; Munk [1966]. Katija and Dabiri [2009] in their article have argued that it is possible for small swimming microorganisms (which constitute most of the oceanic biomass, as mentioned above) to mix the oceans by an amount comparable to winds and tides. In contrast to the winds and tides, the energy input in this so-called biogenic contribution occurs at the smallest scales. The aforementioned authors' arguments for the biogenic mixing mechanism are based on the concept of the drift of fluid elements induced by small moving (or swimming) bodies. This 'drift' correlates to the net fluid displacement induced by the zooplankton or copepods, involved in the aforementioned migration across the pycnocline, and that range in sizes from tens of microns to a few millimeters. The idea of a drift was first analyzed theoretically by Maxwell [1869] and Darwin [1953] in the inviscid limit, for a translating cylinder (Darwin [1953] considered the drift due to a translating sphere as well). The authors postulate that lower Reynolds numbers (*Re*), as is the case for the smallest swimmers above that constitute the dominant aquatic biomass, would tend to enhance the drift of fluid elements via the slowly decaying velocity field in the organism's wake. However, Katija and Dabiri [2009]'s arguments are in error as clarified by Subramanian [2010] and Leshansky and Pismen [2010], since they have not differentiated between the velocity fields generated by a translating passive particle and an active swimmer. Regardless of this error, however, the calculation of the drift volume associated with a single translating passive or active particle, in a viscous ambient, remains an interesting and non-trivial question. The drift volume, for any finite Reynolds number (*Re*), associated with a translating passive particle is essentially infinite [Chisholm and Khair, 2017; Eames et al., 2003]; this in turn arises owing to the divergent drift displacements undergone by fluid elements entrained by the viscous wake. As indicated by Subramanian [2010], to obtain a sensible finite estimate for the drift volume, one would have to also account for the stratification of the ocean, since stable stratification would act to inhibit the vertical motion of fluid elements, thereby truncating the divergence in the drift volume that would otherwise occur in a homogeneous fluid. This can be understood from the fact that any fluid element displaced from its equilibrium position in a stably stratified ambient (like the ocean) would undergo an oscillation (given by the Brunt-Vaisala frequency [Turner, 1979] in the case of an inviscid oscillation) due to a restoring buoyant force. Thus, the objective of the first part of the thesis is to consider the motion of a passive particle in a stratified medium, along the ambient density gradient, in an attempt to estimate the drift volume as a function of the underlying dimensionless parameters. For a homogeneous fluid, the only parameter that influences the drift volume is the Reynolds number; for the stratified medium under consideration, the drift volume will be both a function of the Reynolds (Re) and the viscous Richardson numbers (Ri_v). For small Re, Ri_v is a measure of the strength of the buoyancy forces in relation to viscous forces (note that this is in contrast to the usual Richardson number which is a measure of buoyancy forces in comparison to inertial forces). There is an additional dependence on the Peclet number based on the diffusivity of the stratifying agent; excluding very small particles, the Peclet number (Pe) may be regarded as large when assuming salt to be the agent responsible for the stratification. Finally, the medium stratification considered is continuous and a linear function of the vertical coordinate, keeping in mind that the particles of relevance are marine snow and small aquatic swimmers (copepods of a size much smaller than the typical scale of the stratification associated with ocean's pycnocline).

The second part of the thesis is mainly motivated by recent experiments on the anisotropic particles settling in density stratified fluids [Mercier et al., 2020; Mrokowska, 2018, 2020a,b] and we give a brief motivation below. A large fraction of the research on the vertical motion of particles through stratified fluids, including cases of both sharp (Srdić-Mitrović et al. [1999],Camassa et al. [2009]) and continuous (Hanazaki [1988],Hanazaki et al. [2009a],Yick et al. [2009],Doostmohammadi et al. [2012],Doostmohammadi et al. [2014], Mehaddi et al. [2018]) stratification profiles has focused on spherical particles (including the first part of the present thesis). Although this research has shed light on the non-trivial effects of stratification on the structure of the disturbance flow field induced by a sedimenting sphere, for instance, its sensitive dependence on the diffusivity of the stratifying agent via the Peclet number (Pe) (see List [1971], Ardekani and Stocker [2010], Doostmohammadi et al. [2012], Shaik and Ardekani [2020b] and the first part of the present thesis), the vast majority of particles and living (micro)organisms in natural scenarios depart from the idealized spherical

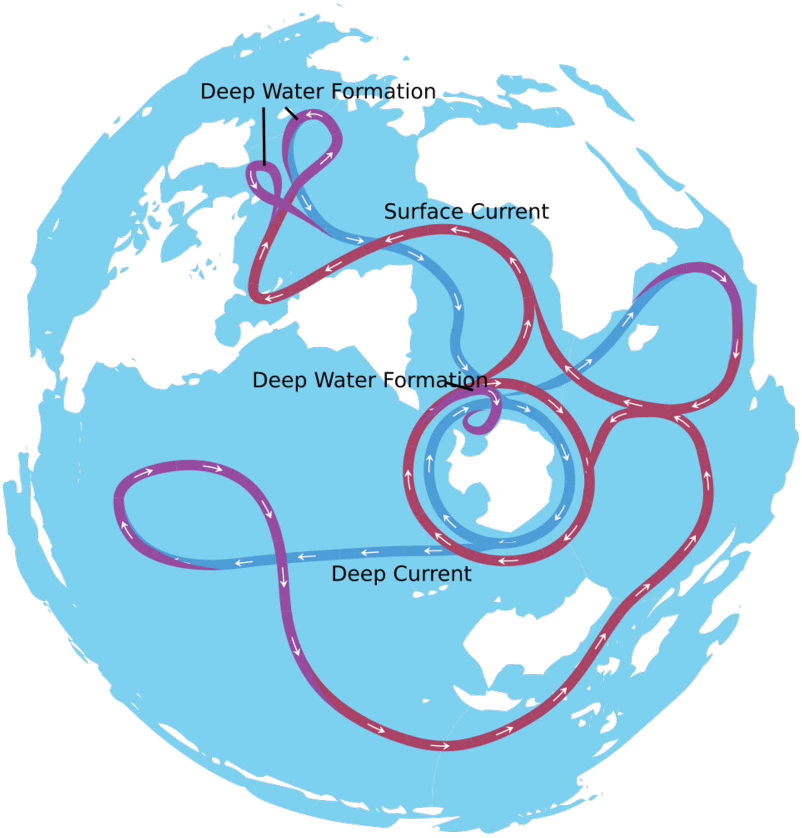

Fig. 1.1 Schematic of meridional overturning oceanic circulation (Adapted from wikipedia [Wikipedia contributors, 2022] under Creative-Commons BY-SA 4.0 license)

shape. Indeed, both marine phytoplankton and zooplankton come in an astonishing variety of shapes (Lab [2018], Kiorboe [2011]), and it is, in fact, known that the shape distribution of marine phytoplankton is peaked at an aspect ratio considerably greater than unity (about five; see Clavano et al. [2007]) . Other classes of organic particles including marine snow aggregates (Prairie et al. [2015]), phytodetritus and faecal pellets, which make up the so-called biological pump (Turner [2015]), and undesired microplastics (Turner and Holmes [2011],Matthew et al. [2011]), also depart significantly from the canonical spherical geometry. Extensive research over a long time has now led to a fairly mature understanding of the dynamics of anisotropic particles sedimenting in a homogeneous ambient (Guillaume and Magnaudet [2002],Auguste et al. [2013]). While the non-trivial effects of unsteady wake dynamics come into play at higher Reynolds numbers (*Re* greater than about 100), as manifest by the onset of path instabilities of sedimenting spheroids (Patricia et al. [2012]), the simplest scenario which prevails for low to moderate Reynolds numbers, when the wake has a quasi-steady character, involves inertial forces acting to turn sedimenting anisotropic particles broadside-on. For small *Re*, and in the case where the anisotropic particle is a prolate or an oblate spheroid, the inertial torque acting to turn the spheroid broadside-on has been determined analytically as a function of the spheroid aspect ratio (Dabade et al. [2015a],Jiang et al. [2020]). Recent DNS simulations have shown this inertial torque to strongly influence the orientation distribution of such particles in an ambient turbulent flow (Gustavsson et al. [2019],Anand et al. [2020]), with these distributions exhibiting a pronouncedly non-Gaussian character (Anand et al. [2020]).

It is natural to ask if there are other reorientation mechanisms, competing with inertia-induced rotation, that arise in a stratified ambient. Indeed, non-trivial effects have been observed in very recent experiments involving cylindrical and disk-shaped particles [Mercier et al., 2020; Mrokowska, 2018, 2020a,b]. that are among the first to systematically explore the role of shape anisotropy for sedimenting particles in a heterogeneous stably stratified fluid ambient. The experiments and computations reported by Mercier et al. [2020] pertain to a linearly stratified ambient, while the experiments reported in Mrokowska [2018, 2020a,b] pertain to a non-linearly stratified fluid layer sandwiched between homogeneous upper and lower layers (see Figure 1.2). While the detailed results obtained for the two sets of experiments differ on account of the differing nature of the ambient stratification, one of the most important findings, common to both sets of experiments, pertains to the ability of the torque due to buoyancy forces to oppose, and even overwhelm the aforementioned inertial torque that acts in a homogeneous setting, thereby turning the particle longside-on. The existence of long-lived intermediate orientations (between the longside-on and broadside-on limits) is also observed in the experiments of Mrokowska [2020a]. Thus, the second part of

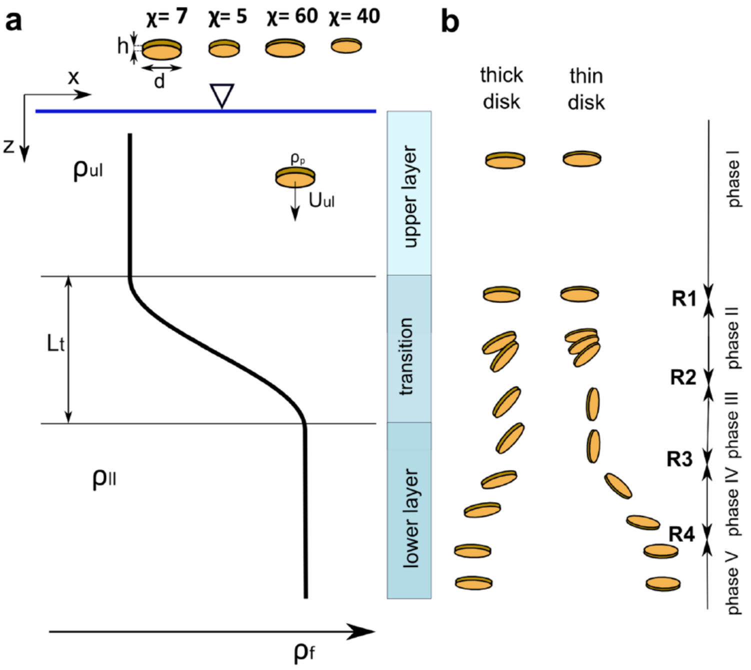

Fig. 1.2 Schematic of thin and thicks disks falling through a three layered fluid system where the intermediate layer is stratified and is sandwitched between two homogeneous layers (Reproduced with permission from Mrokowska [2020a])

the thesis is devoted completely to explaining the behaviour of the anisotropic particles in density stratified fluids, with the intent of characterizing the different settling regimes in an appropriate parameter space.

Outline of the Thesis

This thesis is organized into three main chapters (Chapter 2, 3 & 4). The first two of these chapters are concerned with the settling of a sphere in a density stratified fluid in the viscous limit, whereas Chapter 4 considers the orientation dynamics of a sedimenting spheroid, of an arbitrary aspect ratio, in the same limit. A brief outline of each of these chapters is given below.

In Chapter 2, we give a detailed introduction to the literature of the motion of passive particles in stratified fluids, before the equations governing fluid motion are analyzed in the limit of $Re \ll 1$, $Riv \ll 1$ for the diffusion ($Pe \ll 1$) and convection dominant ($Pe \gg 1$) limits. For both these limits, the length scales at which the stratification becomes important are obtained by using scaling arguments in the limit of negligibly small Re, corresponding to the Stokes stratification regime. The diffusion dominant limit, although analysed in the earlier literature, has nevertheless been considered here first, and a few additional results, determined using both numerical and analytical approaches, are given with regard to features associated with the structure of the far-field velocity disturbance. Next, a similar approach towards the convection dominant limit is taken. The convection dominant limit is the main focus of this thesis considering its applicability to oceanic processes. The detailed characterization of the velocity and density fields, around the translating particle, is again obtained via numerical evaluation, and asymptotic calculation, of the associated Fourier integrals. Effects of weak inertia (small but finite Re), on the far-field structure of the disturbance fields, are finally analyzed via scaling arguments, towards the end of this chapter.

In Chapter 3, we give a detailed introduction to the literature on the drift volume and its importance in the problems concerning particles moving through the 'density-stratified' fluids. With the intention of obtaining insights into the fluid drift displacements and drift volume, in the convection dominant limit, we use the results obtained in Chapter 2 to evaluate both the drift displacements and volume for varying Ri_v and Pe. The numerical results are used to infer the drift volume scaling with Ri_v, in the limit $Pe \gg 1$, in the Stokes stratification regime. Further estimates for the drift volume are obtained, via scaling arguments, outside this regime. We end this chapter by examining the different directions along which the present work may be usefully extended.

In Chapter 4, the problem of rotation of an arbitrary aspect ratio spheroid (both prolate and oblate), in a density-stratified fluid, is considered in the Stokes stratification regime. We use the reciprocal theorem formulation that helps us identify the different contributions to the spheroid angular velocity arising both from inertial forces in a homogeneous ambient, and from the effects of density stratification. The latter contributions may be further separated into two distinct components, namely the hydrostatic and hydrodynamic contributions. For large Pe, the hydrodynamic contribution is shown to arise from the outer region, characterized by the lengthscales of $O(Ri_v^{-1/3})$, and is accordingly formulated as a Fourier integral by using the convolution theorem. The major portion of this chapter is devoted to an analysis of the hydrodynamic contribution, and using these results to organize the spheroid orientation dynamics in an $Ri_v/Re^{3/2} - \kappa$ parameter plane, κ here being the spheroid aspect ratio (κ is greater and less than unity for prolate and oblate spheroids, respectively). In Chapter 5, we summarize our results from the chapters 2, 3 & 4 and mention possible future directions of the present effort.

Chapter 2

Motion of a sphere in a viscous density stratified fluid: velocity and density fields

2.1 Introduction

As mentioned in the first chapter of this thesis, the phenomena of particles moving in a density stratified environment is a common occurrence in nature especially since both the atmosphere and the oceans are, on average, stably stratified. In this chapter, we consider a passive particle moving along the density gradient direction although the motion of particles in stratified fluids moving vertical to the density gradient is also of interest in literature previously [Chadwick and Zvirin, 1974; Janowitz, 1968]. With the intention of calculating the drift volume for a passive particle settling in a density stratified fluid in the viscous limit, we characterize, in detail, the fluid velocity and density fields around such a particle. Specifically, we consider a sphere translating along the direction of stratification at small Reynolds ($Re = \frac{\rho_0 U a}{\mu}$) and viscous Richardson numbers (Ri_v), the translation assumed to be the result of a density difference. $Ri_v = \frac{\gamma a^3 g}{\mu U}$ measures the relative importance of viscous and buoyancy forces, and is therefore the key dimensionless parameter for motion of small particles in a stratified ambient; here, $\gamma = -\frac{d\rho}{dz}$ is the constant density gradient in the ambient ($\gamma > 0$ for stable stratification), a the sphere radius, ρ_0 the base state density within Boussinesq approximation, g the acceleration due to gravity, μ the fluid viscosity and U the speed of translation. Note that $Ri_v = \frac{Re}{Fr^2}$, where $Fr = \frac{U}{Na}$ is the Froude number that is the usual measure of the importance of stratification in the inviscid limit, $N = \sqrt{\frac{g\gamma}{\rho}}$ here being the Brunt-Vaisala frequency [Turner, 1979]. In a significant departure from most earlier efforts (discussed below), and keeping in mind the oceanic scenario, we consider the Peclet number, defined as $Pe = \frac{Ua}{D}$, D being the diffusivity of the stratifying agent (salt in the oceanic case) to be large.

Earlier efforts, particularly the ones devoted to analysis of the fluid motion around a moving particle (or) swimmer, have mostly been restricted to small Pe; an exception is the very recent effort of Shaik and Ardekani [2020b], and we discuss this in section 2.4. Motivated by the need to understand laminar jets in a stratified ambient, List [1971] was the first to characterize the analog of a Stokeslet (the limiting scenario of a small translating particle, for $Re = 0$, approximated as a point force) in a linearly stratified fluid, and for small Pe. The author considered both vertical and horizontal Stokeslet orientations in two and three dimensions; for the vertical orientation, relevant to the problem analyzed here, the motion although fore-aft symmetric was shown to decay away much more rapidly than the $O\left(\frac{1}{r}\right)$ decay characteristic of a Stokeslet in a three-dimensional homogeneous ambient. The resulting weak far-field motion, shown in the article only for the two-dimensional case, was in the form of recirculating cells stacked along the direction of stratification. 'Far-field' here refers to (in units of a) length scales of $O\left(Ri_v Pe\right)^{-\frac{1}{4}}$, the stratification screening length for $Pe \ll 1$; as will be seen below, the number of such cells is finite. Much later, Ardekani and Stocker [2010] considered the same problem, but for both passive and active particles modeled as point force and force-dipole singularities, respectively. The density and velocity fields were obtained numerically using a fast Fourier transform technique, the singularities being termed 'stratlets'. More recently, Fouxon and Leshansky [2014] examined the role of turbulence, within the Boussinesq framework, in disrupting the stratification-induced signatures on the flow field around passive particles and active swimmers. As part of their analysis, the authors derived an asymptotic expression for the far-field flow in the absence of turbulence, and that exhibited a rapid algebraic decay, consistent with the findings of the aforementioned studies. Candelier et al. [2014] calculated the correction to the Stokes drag on a sedimenting passive particle, for small Pe, arising from stratification effects in the outer region characterized by scales of $O\left(Ri_v Pe\right)^{-\frac{1}{4}}$; see discussion in the paragraph after the next one. The authors also determined the history force that characterizes the approach to the terminal settling regime. Wagner et al. [2014] examined the mixing efficiencies associated with the flow induced by micro-swimmers, for small Pe, finding them to be negligibly small.

While the aforementioned efforts have analyzed the fluid motion around both passive particles and active swimmers primarily in the small Pe regime, the motion of a typical particle or small-sized swimmer (zooplankton) in the oceanic ambient, relevant to the biogenic mixing hypothesis, pertains to large Pe; for instance, a zooplankton of size 0.1 mm moving at a speed of 1 mm/s in a typical oceanic stratification of $\gamma = 1.67 \times 10^{-3} \frac{\mathrm{kg}}{\mathrm{m}^4}$, yields $Re = 0.116$, $Ri_v = 1.84 \times 10^{-8}$ and $Pe = 100$. Note that the large Pe regime pertains generically to cases where salt is the stratifying agent, for particles larger than a few microns, the aforementioned oceanic ambient only being one such instance. The first theoretical effort in this regime is that of Zvirin and Chadwick [1975] who calculated the drag enhancement in what we term the Stokes stratification regime below, defined by $Re \ll Ri_v^{\frac{1}{3}} \ll 1$. The calculation was restricted to determining the drag enhancement arising from buoyancy effects in the outer region, on scales of $O(Ri_v^{-\frac{1}{3}})$, corresponding to the stratification screening length (this is the screening length for large Pe, in contrast to the $O(Ri_v Pe)^{-\frac{1}{4}}$ screening length above, for small Pe, that was obtained by List [1971] and Ardekani and Stocker [2010]). Similar to Childress's determination of the drag correction for the axial motion of a sphere in a rotating fluid [Childress, 1964], and Saffman's calculation of the inertial lift on a sphere in an ambient simple shear flow [Saffman, 1965], the analysis was done in Fourier space, with the enhancement to the Stokes drag coming out to be $O(Ri_v^{\frac{1}{3}})$, the inverse of the aforementioned screening length. Recently, Mehaddi et al. [2018] have extended the efforts of Candelier et al. [2014] and Zvirin and Chadwick [1975] for small and large Pe, respectively, with $Re = 0$, and have obtained the outer-region drag correction for any Pe, and for small but finite Re and Ri_v. In the process, the authors show that the Zvirin and Chadwick [1975] calculation remains valid over an unexpectedly large interval of Pe, corresponding to $Pe \gg Ri_v^{\frac{1}{3}}$, an aspect that is also mirrored in the torque calculation for sedimenting anisotropic particles that we consider in the Chapter 4 of this thesis. More recently, Zhang et al. [2019], by using detailed numerical calculations and an ingenious splitting procedure, showed that the enhancement in drag at low Reynolds numbers comes from the induced baroclinic torque and the resulting change in the flow structure. The enhancement was found to be proportional to $Ri_v^{\frac{1}{3}}$, in agreement with the Zvirin-Chadwick result above, but in opposition to the observations of Yick et al. [2009] who obtained a scaling closer to $Ri_v^{\frac{1}{2}}$; the latter mismatch is likely due to additional non-Boussinesq contributions arising from heavily deformed iso-pycnals close to the sphere; here, iso-pycnals denote the lines/surfaces along which the density is constant.

As discussed in Chapter 1 of this thesis, there have been very recent experiments (and computations) by Mercier et al. [2020] on the motion of anisotropic disk-shaped particles (and the resulting orientation dynamics) in a stably stratified fluid. The experiments pertain to finite Re and Ri_v, and highlight the existence of an edgewise-settling regime for sufficiently large Ri_v or small Fr; in this regard, also see the experiments of Mrokowska [2018, 2020a,b]) and the computations of Doostmohammadi and Ardekani [2014]. This is in contrast to the stable broadside-on settling regime known for small to moderate Re in a homogeneous ambient [Cox, 1965; Dabade et al., 2015b]. The experiments of Mercier et al. [2020] have motivated the recent theoretical effort of Dandekar et al. [2020] which evaluates the hydrodynamic force and torque on an arbitrarily shaped body in a linearly stratified ambient for arbitrary Pe, and finds a torque, arising from the ambient stratification, for chiral particles. The role of stratification in the orientation dynamics of achiral particles, such as the ones used in Mercier et al. [2020], has been analyzed in detail in the Chapter 4 of this thesis. In the present context, we only note that although the studies in this and the preceding paragraph, for both spherical and non-spherical particles, pertain to the large-Pe limit, the fluid motion induced by the translating particle was not examined in detail, which forms the basis for this and next chapter.

The primary motivation for our calculation is to eventually determine the drift volume in a stably stratified ambient, and thereby, estimate the importance of the biogenic mixing contribution. Now, as mentioned in Chapter 1, the infinite-time drift volume is divergent, for any finite Re, in a homogeneous ambient [Chisholm and Khair, 2017; Eames et al., 2003; Subramanian, 2010], this divergence arising from the slow $O(\frac{1}{r})$ decay of velocity field within the far-field wake, r being the distance downstream. For $Re = 0$, the velocity field decays as $O(\frac{1}{r})$ at large distances regardless of the direction, and as a result, the drift volume diverges for any finite time. This implies that the finiteness of the drift volume, for a weakly stratified ambient pertaining to the aforementioned Stokes stratification regime, must arise from the transition of the far-field fluid motion from an $O(\frac{1}{r})$ Stokesian decay to a more rapid decay beyond the $O(Ri_v^{-\frac{1}{3}})$ stratification screening length. Thus, for small Re, unlike the drag problem considered in Zvirin and Chadwick [1975], one expects the dominant contribution to the drift volume to arise from the fluid motion far from the sphere, or in other words, the outer region. It is with this in mind that the analysis here is restricted to the linearized equations in the far-field. One may nevertheless question the relevance of this linearization, given that the motion in the outer region is indirectly influenced by the heavily deformed iso-pycnals, close to the sphere, for large Pe. However, these deformed iso-pycnals contribute to a localized buoyant envelope around the sphere, and at large distances, one may regard the combination of the envelope and the sphere as an effective point force, albeit of a different magnitude, as far as the outer region is concerned; the linearity of the outer-region equations implies that the nature of fluid motion is independent of the magnitude of the force. More detailed scaling arguments pertaining to the velocity and density fields in the inner region (length scales of $O(a)$) are given in the conclusions section.

In the next section, we present the quasi-steady governing equations for the fluid motion under the Boussinesq approximation and a scaling analysis to determine the screening lengths arising from the effects of inertia and stratification, for both small and large Pe. Next, the linearized equations in the outer region are solved using a Fourier transform approach [Childress, 1964; Saffman, 1965], and the velocity and density field are written as Fourier integrals, in the aforementioned small and large-Pe limits, and in the so-called Stokes stratification regime, when buoyancy forces are dominant over inertial ones; this translates to $Re \ll (Ri_v Pe)^{1/4}$ for small Pe, and $Re \ll Ri_v^{1/3}$ for large Pe. In section 2.3, we contrast the streamline patterns and iso-pycnals obtained from a numerical evaluation of the Fourier integrals for $Pe = 0$ and $Pe \gg 1$; the numerical results are also compared to analytical approximations valid for distances much greater than the respective screening lengths. In the diffusion-dominant limit, for first time, we show analytically that there exist an algebraic decay of the velocity and density fields for any arbitrary transverse distance (r_t) from the sphere. In the Stokes-stratification regime in the convection-dominant limit, for first time, we present a detailed characterization of the velocity and density fields surrounding a sphere using both the exact and far-field calculations. It will be shown here that the motion at large distances of stratification screening length ($O(aRi_v^{-1/3})$) transforms from the familiar fore-aft symmetric Stokesian form to a fore-aft asymmetric pattern of recirculating cells with primarily horizontal motion within; except in the vicinity of the rear stagnation streamline. It will be also seen that, at larger distances, the motion is vanishingly small except within (a) an axisymmetric horizontal wake whose vertical extent grows as $O(r_t^{2/5})$, r_t being the distance in the plane perpendicular to translation and (b) a buoyant reverse jet behind the particle that narrows as the inverse square root of distance downstream. For large but finite Pe, the narrowing jet is smeared out beyond a secondary screening length of $O(aRi_v^{-1/2}Pe^{1/2})$, leading to an exponential decay of the aforementioned reverse flow. Even though the existence of jets in stratified fluids at moderate-to-high Reynolds numbers is known for sometime, This existence of a rearward jet in the far-field, even in the limit of $Re = 0$, is shown in this chapter for first time. We also present arguments for the transition from the far-field wake, to a different wake-regime, owing to effects of weak inertia. Similar arguments are presented for the diffusion-dominant limit for the transition from the far-field diffusion-dominant wake to different wake regimes. In the concluding section 2.4, we summarize our work, and follow this up with scaling arguments pertaining to the inner region dynamics.

2.2 The disturbance fields in a linearly stable stratified ambient

We consider a sphere moving vertically in an unbounded stably stratified fluid with a linear stratification profile $\frac{d\rho}{dz'} = -\gamma(\gamma > 0)$, z' being the vertical lab-fixed coordinate. The ambient density in the dimensional terms is given by $\rho = \rho_0 - \gamma z'$, ρ_0 being the reference density corresponding to $z' = 0$. We need to write the density equation in sphere-fixed coordinate system as we will solve our equations in this frame of reference. Considering a sphere of radius a, moving vertically downwards with a velocity of U, the density field in the sphere-fixed reference frame is given by $\rho = \rho_0(z_0) - \gamma z + \gamma U t$, z being the vertical coordinate in the new sphere-fixed reference frame, and z_0 being the initial vertical coordinate of the sphere at which the reference density ρ_0 is measured. Since the sphere perturbs the original linear density gradient, we have to include the density disturbance term (ρ_f) as well, leading to the expression being $\rho = \rho_0(z_0) - \gamma z + \gamma U t + \rho_f$. Using a, U and γa for the length, velocity and density scales, this expression then simplifies to $\rho = \rho_0 - z + t + \rho_f$; note that z, t and ρ_f in this expression are now non-dimensional quantities even though we use the same symbols as their dimensional counter parts.

Non-dimensionalizing the continuity equation, the Navier-Stokes equations using the aforementioned scales, and substituting the density expression given above, leads to the following set of equations in the sphere-fixed reference frame.

$$\nabla \cdot \mathbf{u} = 0, \tag{2.1}$$

$$Re[\mathbf{u} \cdot \nabla \mathbf{u}] = -\nabla p + \nabla^2 \mathbf{u} - Ri_v \rho_f \mathbf{1_z}, \tag{2.2}$$

$$1 - w + \mathbf{u} \cdot \nabla \rho_f = \frac{1}{Pe} \nabla^2 \rho_f, \tag{2.3}$$

with the boundary conditions:

$$\mathbf{u} = 0, \quad \mathbf{n} \cdot \nabla \rho_f = -\mathbf{n} \cdot \mathbf{1_z} \quad \text{at} \quad r = |\mathbf{x}| = 1, \tag{2.4}$$

$$\mathbf{u} \to \mathbf{1_z}, \quad \rho_f \to 0 \quad \text{as} \quad r = |\mathbf{x}| \to \infty, \tag{2.5}$$

where r is the non-dimensional distance from the sphere and w in (2.3) is the vertical velocity component [Candelier et al., 2014; Mehaddi et al., 2018; Shaik and Ardekani, 2020a]. The term involving $1 - w$ in (2.3) denotes the convection of the base-state stratification (along the vertical) by the perturbation velocity field. Note that the Boussinesq approximation has been used above to neglect the density disturbance in the convective terms of the equations of motion, so Re in (2.2) is based on an appropriate reference density. Further, in taking ρ_f in particular to be independent of time, we have assumed a quasi-steady state to be achieved, in the sphere-fixed reference frame, for long times. This assumption is examined in section 2.4.2 for both the inner ($r \sim O(a)$) and outer regions ($r \geq O(Ri_v^{-\frac{1}{3}})$).

As is well known, although we examine the limit $Re, Ri_v \ll 1$, the inertial and stratification terms in (2.2) cannot be neglected. The Stokes equations are not a uniformly valid approximation, and the aforementioned terms become comparable to the leading order viscous terms at sufficiently large distances [Lagerstrom, 2013; Proudman and Pearson, 1957; Van Dyke, 1975]. As discussed in the introduction of this chapter, the large length scales above are precisely the ones that control the drift volume that in turn underlies the biogenic mixing hypothesis. For a homogeneous fluid, the length scale (in units of a) at which inertial forces first become comparable to viscous forces is Re^{-1}, referred to here as the inertial screening length. Obtaining a similar estimate for the buoyancy forces requires one to obtain the far-field behavior of the density field which in turn depends on whether Pe is large or small.

For $Pe \to 0$, the density perturbation on length scales of $O(a)$ arises, at leading order, as a diffusive response to the no-flux boundary condition on the surface of the particle, and decays as $O(\frac{1}{r^2})$ at large distances. The convective correction to the density field satisfies $\frac{1}{Pe}\nabla^2\rho_f \sim (1-w)$; using $(1-w) \sim O(\frac{1}{r})$ for the Stokeslet field leads to $\rho_f \sim Pe\, r$. The buoyancy forces arising from the convective perturbation grow as $O(Ri_v Pe\, r)$. Equating them to the decaying viscous forces of $O(\frac{1}{r^3})$ leads to the small-Pe stratification screening length $l_c \sim (Ri_v Pe)^{-\frac{1}{4}}$. The equations governing the disturbance fields on scales of order the aforementioned screening length may be obtained by using the expansions: $\mathbf{u} = \mathbf{1_z} + (Ri_v Pe)^{1/4}\bar{\mathbf{u}}(\bar{\boldsymbol{r}})$, $p = p_\infty + (Ri_v Pe)^{\frac{1}{2}}\bar{p}(\bar{\boldsymbol{r}})$ and $\rho_f = Pe(Ri_v Pe)^{-\frac{1}{4}}\bar{\rho}_f(\bar{\boldsymbol{r}})$, with $\bar{\boldsymbol{r}} = (Ri_v Pe)^{\frac{1}{4}}\boldsymbol{r}$. Note that these scalings are based on the variation of the velocity, pressure and density disturbance as $\frac{1}{r}$, $\frac{1}{r^2}$ and $Pe\, r$, respectively, in the inner Stokesian region far away from the particle. The outer-region equations are given by

$$\bar{\nabla}.\bar{\mathbf{u}} = 0, \tag{2.6}$$

$$-\alpha_0\frac{\partial \bar{\mathbf{u}}}{\partial \bar{z}} = -\bar{\nabla}\bar{p} + \bar{\nabla}^2\bar{\mathbf{u}} - [\bar{\rho}_f + 6\pi\delta(\bar{\mathbf{r}})]\mathbf{1_z}, \tag{2.7}$$

$$-\mathbf{1_z}.\bar{u} + \beta_0\frac{\partial \bar{\rho}_f}{\partial \bar{z}} = \bar{\nabla}^2\bar{\rho}_f. \tag{2.8}$$

Here, α_0 and β_0 are given by $\frac{Re}{(Ri_v Pe)^{1/4}}$ and $\frac{Pe}{(Ri_v Pe)^{1/4}}$, respectively, and denote the ratios of the low-Pe stratification screening length to the inertial (Re^{-1}) and convective(Pe^{-1}) screening lengths. Note that the boundary condition on the particle surface has now been replaced by a point force on the RHS of (2.7).

Defining the relations between the physical space and Fourier transformed disturbance fields as:

$$\hat{f}(\mathbf{k}) = \int f(\mathbf{x})e^{i\mathbf{k}.\mathbf{r}}d\mathbf{k}, \tag{2.9}$$

$$f(\mathbf{x}) = \frac{1}{(2\pi)^3}\int \hat{f}(\mathbf{k})e^{-i\mathbf{k}.\mathbf{r}}d\mathbf{x}, \tag{2.10}$$

with $f(\mathbf{x})$ denoting the relevant disturbance field, and Fourier transforming (2.6-2.8), one obtains, after some algebra, the velocity and density disturbance fields as the following integrals with α_0 and β_0 as parameters:

$$\bar{\mathbf{u}}(\bar{\mathbf{r}}) = \frac{-3}{4\pi^2}\int \frac{k^2(ik_3\beta_0+k^2)(\mathbf{1_z}-\frac{k_3\mathbf{k}}{k^2})}{k^2(ik_3\alpha_0+k^2)(ik_3\beta_0+k^2)+k_t^2}e^{i\mathbf{k}.\bar{\mathbf{r}}}d\mathbf{k}, \tag{2.11}$$

$$\bar{\rho_f}(\bar{\mathbf{r}}) = \frac{-3}{4\pi^2}\int \frac{k_t^2}{k^2(ik_3\alpha_0+k^2)(ik_3\beta_0+k^2)+k_t^2}e^{i\mathbf{k}.\bar{\mathbf{r}}}d\mathbf{k}, \tag{2.12}$$

where $k_t = (k^2-{k_3}^2)^{\frac{1}{2}}$ is the magnitude of the wavevector projected onto the plane perpendicular to the translation direction.

For $Pe, Re \ll (Ri_v Pe)^{\frac{1}{4}}$, one may ignore the terms proportional to α_0 and β_0, with the velocity and density disturbance fields reducing to the following Fourier integrals

$$\bar{\mathbf{u}}(\bar{\mathbf{r}}) = \frac{-3}{4\pi^2}\int \frac{k^4(\mathbf{1_z}-\frac{k_3\mathbf{k}}{k^2})}{k^6+k_t^2}e^{i\mathbf{k}.\bar{\mathbf{r}}}d\mathbf{k}, \tag{2.13}$$

$$\bar{\rho_f}(\bar{\mathbf{r}}) = \frac{-3}{4\pi^2}\int \frac{k_t^2}{k^6+k_t^2}e^{i\mathbf{k}.\bar{\mathbf{r}}}d\mathbf{k}, \tag{2.14}$$

The above diffusion dominant limit has been considered previously (see [Ardekani and Stocker, 2010; Fouxon and Leshansky, 2014; List, 1971]), as indicated in the introduction of this chapter.

For $Pe \to \infty$, one neglects the diffusion term in (2.3) and thus $\mathbf{u}\cdot\nabla\rho_f \sim (1-w)$. Again, using $(1-w) \sim O(\frac{1}{r})$, one has $\rho_f \sim O(1)$, so the buoyancy forcing term in (2.2) is $O(Ri_v)$. Equating this to the $O(\frac{1}{r^3})$ viscous term, one obtains the large-*Pe* stratification screening length $l_c \sim Ri_v^{-\frac{1}{3}}$, as originally shown by Zvirin and Chadwick [1975]. Again, keeping in mind the Stokesian scalings in the inner region, the disturbance fields in the outer region may be expanded as: $\mathbf{u} = \mathbf{1_z} + Ri_v^{\frac{1}{3}}\tilde{\mathbf{u}}(\tilde{\mathbf{r}})$, $p = p_\infty + Ri_v^{\frac{2}{3}}\tilde{p}(\tilde{\mathbf{r}})$ and $\rho_f = \tilde{\rho_f}(\tilde{\mathbf{r}})$, with $\tilde{\boldsymbol{r}} = Ri_v^{\frac{1}{3}}\boldsymbol{r}$. One obtains the following outer-region equations:

$$\tilde{\nabla}.\tilde{\mathbf{u}} = 0, \tag{2.15}$$

$$-\alpha_\infty\frac{\partial\tilde{\mathbf{u}}}{\partial\tilde{z}} = -\tilde{\nabla}\tilde{p} + \tilde{\nabla}^2\tilde{\mathbf{u}} - [\tilde{\rho_f} + 6\pi\delta(\tilde{\mathbf{r}})]\mathbf{1_z}, \tag{2.16}$$

$$-\mathbf{1_z}.\tilde{u} + \frac{\partial\tilde{\rho_f}}{\partial\tilde{z}} = \beta_\infty\tilde{\nabla}^2\tilde{\rho_f}. \tag{2.17}$$

Here, $\alpha_\infty = \frac{Re}{Ri_v^{1/3}}$ is the large-*Pe* analog of α_0, with $\beta_\infty^{-1} = \frac{Pe}{Ri_v^{1/3}}$ being the analog of β_0 above.

As in the case of low Pe, Fourier transforming (2.15-2.17), one obtains the velocity and density fields as the following Fourier integrals with α_∞ and β_∞ as parameters given by

$$\tilde{\mathbf{u}}(\tilde{\mathbf{r}}) = \frac{-3}{4\pi^2}\int \frac{(ik_3+\beta_\infty k^2)k^2(\mathbf{1_z}-\frac{k_3\mathbf{k}}{k^2})}{(ik_3+\beta_\infty k^2)(ik_3\alpha_\infty+k^2)k^2+k_t^2} e^{i\mathbf{k}.\tilde{\mathbf{r}}} d\mathbf{k}, \tag{2.18}$$

$$\tilde{\rho_f}(\tilde{\mathbf{r}}) = \frac{-3}{4\pi^2}\int \frac{k_t^2}{(ik_3+\beta_\infty k^2)(ik_3\alpha_\infty+k^2)k^2+k_t^2} e^{i\mathbf{k}.\tilde{\mathbf{r}}} d\mathbf{k}. \tag{2.19}$$

In the Stokes stratification regime, corresponding to $Re \ll Ri_v^{\frac{1}{3}}$, one can set α_∞ in (2.16) to zero. Although our primary focus is on the limit $\beta_\infty \rightarrow 0\,(Pe \rightarrow \infty)$, retaining a small but finite β_∞ is important. While the structure of the disturbance fields, almost everywhere in the domain, is independent of β_∞ in this limit, in section 2.3.2, it is shown that a small but finite β_∞ crucially affects the structure of the fields right behind the translating sphere. Further, a non-zero β_∞ is also important for numerical convergence of the Fourier integrals below.

$$\tilde{\mathbf{u}}(\tilde{\mathbf{r}}) = \frac{-3}{4\pi^2}\int \frac{(ik_3+\beta_\infty k^2)k^2(\mathbf{1_z}-\frac{k_3\mathbf{k}}{k^2})}{(ik_3+\beta_\infty k^2)k^4+k_t^2} e^{i\mathbf{k}.\tilde{\mathbf{r}}} d\mathbf{k}, \tag{2.20}$$

$$\tilde{\rho_f}(\tilde{\mathbf{r}}) = \frac{-3}{4\pi^2}\int \frac{k_t^2}{(ik_3+\beta_\infty k^2)k^4+k_t^2} e^{i\mathbf{k}.\tilde{\mathbf{r}}} d\mathbf{k}. \tag{2.21}$$

2.3 Results and Discussion

Herein, we analyze the axial velocity and density disturbance fields, and the resulting streamline and iso-pycnal patterns in both the diffusion and convection dominant limits by using a combination of numerics (Gauss-Legendre quadrature integration) and far-field asymptotics. As already mentioned in the introduction, the results in both limits are for the case of buoyancy forces being dominant (the Stokes stratification regime), corresponding to $\alpha_0, \alpha_\infty \ll 1$. The role of weak inertial effects is discussed, via scaling arguments, towards the end of this section.

2.3.1 Diffusion-dominant limit ($Pe \ll 1$)

List [1971] used residue theory to enable the reduction of (2.13) and (2.14) to one-dimensional integrals for both the two and three-dimensional cases. We use a different method that reduces the disturbance fields to two-dimensional integrals instead, this being conveniently applicable in both the diffusion and convection dominant limits. The Fourier integrals are expressed in a spherical coordinate system with its polar axis aligned with the translation direction.

The integral over the azimuthal angle (ϕ) can be carried out analytically, and the resulting expressions are given by:

$$\bar{u}_z = \frac{-3}{2\pi}\int_0^\infty dk \int_0^\pi d\theta \frac{k^4 \sin^3\theta J_0(k\bar{r}_t \sin\theta) e^{ik\bar{z}\cos\theta}}{(k^4+\sin^2\theta)}, \tag{2.22}$$

$$\bar{\rho}_f = \frac{-3}{2\pi}\int_0^\infty dk \int_0^\pi d\theta \frac{k^2 \sin^3\theta J_0(k\bar{r}_t \sin\theta) e^{ik\bar{z}\cos\theta}}{(k^4+\sin^2\theta)}, \tag{2.23}$$

where $J_0(x)$ is the zeroth order Bessel function of the first kind. Note that since the problem is axisymmetric, the fields are written as functions of $(\bar{r}_t, \bar{z})$ with $\bar{z}$ and $\bar{r}_t$ being the distances along and orthogonal to the direction of translation. Not including the complex exponential, the Fourier integrand for the density disturbance field in (2.23) decays as $\frac{1}{k^{5/2}}$ for large k, while that for the axial velocity in (2.22) only decays as $\frac{1}{k^{1/2}}$; the latter slow decay reflects the $\frac{1}{r}$-decay of the Stokeslet for small r. As a result, an accurate evaluation of (2.22) relies essentially on cancellation induced by the complex Fourier exponential. To facilitate numerical evaluation, we therefore separate out the Stokeslet contribution, writing the axial velocity integral above as:

$$\bar{\mathbf{u}}_z = \frac{-3(2+\frac{\bar{r}_t^2}{\bar{z}^2})}{4|\bar{z}|\,(1+\frac{\bar{r}_t^2}{\bar{z}^2})^{\frac{3}{2}}} + \frac{3}{2\pi}\int_0^\infty dk \int_0^\pi d\theta \frac{\sin^5\theta J_0(k\bar{r}_t \sin\theta)\cos(k\bar{z}\cos\theta)}{(k^4+\sin^2\theta)}, \tag{2.24}$$

where the integrand in (2.24) now decays as $\frac{1}{k^{9/2}}$ for large k. The Stokes streamfunction may be found using the relation $\bar{u}_z = \frac{1}{\bar{r}_t}\frac{\partial\bar{\psi}}{\partial\bar{r}_t}$ and is given by:

$$\bar{\psi}_s = \frac{-3\bar{r}_t^2}{4(\bar{r}_t^2+\bar{z}^2)^{\frac{1}{2}}} + \frac{3\bar{r}_t}{2\pi}\int_0^\infty dk \int_0^\pi d\theta \frac{\sin^4\theta J_1(k\bar{r}_t \sin\theta)\cos(k\bar{z}\cos\theta)}{k(k^4+\sin^2\theta)}. \tag{2.25}$$

The density disturbance and axial velocity fields, and the Stokes streamfunction, given by (2.23), (2.24) and (2.25), respectively, are evaluated using Gaussian quadrature. This numerical evaluation of the above integrals is carried out after first using $k = \tan\hat{k}_f$ to transform the original k-interval to a finite one in $\hat{k}_f$; a large number of quadrature points($\sim$ 50000) for both the dimensions are used to ensure convergence. Even larger number of quadrature points are required for the large-Pe integrals that will be discussed later in the section. The instantaneous streamline and iso-pycnal patterns, in a reference frame with a far-field quiescent ambient, are shown in figure 2.1, and are seen to be fore-aft symmetric, as may also be inferred from the cosine in (2.24) and (2.25). As originally found by List [1971] and Ardekani and Stocker [2010], buoyancy forces suppress the long-ranged vertical motion associated with the Stokeslet at large distances, leading to the development of recirculating cells aligned with the direction of stratification, and wherein the motion is predominantly horizontal. Interestingly and perhaps surprisingly (if one's intuition is based on the cellular disturbance flow fields set up internal gravity waves in an unbounded stratified ambient), the far-field analysis in the next subsection shows the number of such cells to be finite, likely on account of the neglect of inertial/convection effects.

Far-field analysis

At large distances, as already mentioned, one expects largely horizontal motion. As a consequence, the characteristic length scale in the vertical direction will be much smaller than that along the horizontal - this is already evident from the rather small aspect ratios of the recirculating cells in figure 2.1. Thus, the Fourier integrals in (2.13) and (2.14), for length scales large compared to $O(Ri_v Pe)^{-1/4}$, may be simplified using $k_3 \gg k_t$, leading to:

$$\bar{\mathbf{u}}(\bar{\mathbf{r}}) = -\frac{3}{4\pi^2}\int \frac{k^4(\mathbf{1_z} - \frac{k_3\mathbf{k}}{k^2})}{(k_3^6 + k_t^2)} e^{i\mathbf{k}.\bar{\mathbf{r}}} d\mathbf{k}, \tag{2.26}$$

$$\bar{\rho}_f(\bar{\mathbf{r}}) = -\frac{3}{4\pi^2}\int \frac{k_t^2}{(k_3^6 + k_t^2)} e^{i\mathbf{k}.\bar{\mathbf{r}}} d\mathbf{k}, \tag{2.27}$$

which can be reduced to one-dimensional integrals only involving the similarity variable $\eta = \frac{\bar{z}}{\bar{r}_t^{\frac{1}{3}}}$ via contour integration in the complex-k_3 plane as shown below.

In a cylindrical coordinate system aligned with the translation direction, and after carrying out the ϕ integration, the expressions for the axial and transverse velocities, and the density disturbance, reduce to

$$\bar{u}_z = \frac{-3}{2\pi}\int_{-\infty}^{\infty} dk_3 \int_0^{\infty} dk_t \frac{k_3^2 k_t^3 J_0(k_t \bar{r}_t) e^{ik_3\bar{z}}}{(k_3^6 + k_t^2)}, \tag{2.28}$$

$$\bar{u}_{r_t} = \frac{3i}{2\pi}\int_{-\infty}^{\infty} dk_3 \int_0^{\infty} dk_t \frac{k_3^3 k_t^2 J_1(k_t \bar{r}_t) e^{ik_3\bar{z}}}{(k_3^6 + k_t^2)}, \tag{2.29}$$

$$\bar{\rho}_{f_1} = \frac{-3}{2\pi}\int_{-\infty}^{\infty} dk_3 \int_0^{\infty} dk_t \frac{k_t^3 J_0(k_t \bar{r}_t) e^{ik_3\bar{z}}}{(k_3^6 + k_t^2)} \tag{2.30}$$

Now, we use contour integration to first evaluate the k_3-integral. Contributions arise from the existence of six poles in the complex-k_3 plane, with these poles being symmetrically

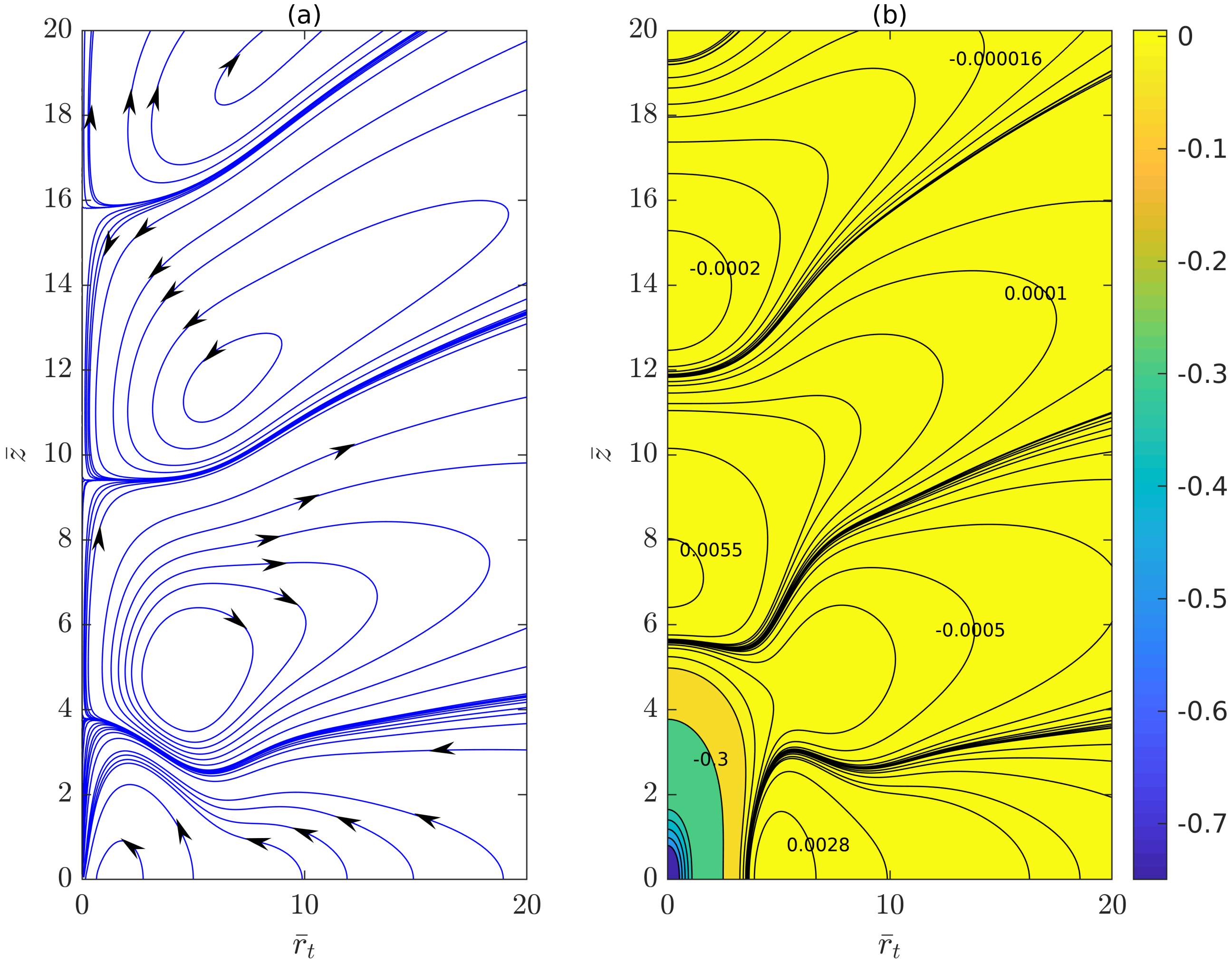

Fig. 2.1 (a) Streamlines and (b) Isopycnals (Lines/surfaces along which density is constant) for a translating sphere in a linearly stratified fluid in the diffusion dominant limit ($Pe = 0$); in the point-particle approximation used, the sphere is at the origin and moving vertically downward.

disposed about the real k_3-axis, consistent with the fore-aft symmetry of the disturbance fields. The contour integration yields the following one-dimensional integrals

$$\bar{u}_z = -3i\int_0^\infty k_t^2 J_0(k_t\bar{r}_t)\left(lq_1^2 e^{iq_1k_t^{\frac{1}{3}}|\bar{z}|} + mq_2^2 e^{iq_2k_t^{\frac{1}{3}}|\bar{z}|} + nq_3^2 e^{iq_3k_t^{\frac{1}{3}}|\bar{z}|}\right) dk_t, \tag{2.31}$$

$$\bar{u}_{r_t} = -3\,\mathrm{sgn}\,\bar{z}\int_0^\infty k_t^{\frac{4}{3}} J_1(k_t\bar{r}_t)\left(lq_1^3 e^{iq_1k_t^{\frac{1}{3}}|\bar{z}|} + mq_2^3 e^{iq_2k_t^{\frac{1}{3}}|\bar{z}|} + nq_3^3 e^{iq_3k_t^{\frac{1}{3}}|\bar{z}|}\right) dk_t, \tag{2.32}$$

$$\bar{\rho}_f = -3i\int_0^\infty k_t^{\frac{4}{3}} J_0(k_t\bar{r}_t)\left(le^{iq_1k_t^{\frac{1}{3}}|\bar{z}|} + me^{iq_2k_t^{\frac{1}{3}}|\bar{z}|} + ne^{iq_3k_t^{\frac{1}{3}}|\bar{z}|}\right) dk_t. \tag{2.33}$$

Here q_1, q_2, q_3, l, m and n are complex-valued constants given by

$$\begin{aligned}
[q_1,q_2,q_3,q_4,q_5,q_6] &= [e^{\frac{\pi i}{6}}, e^{\frac{\pi i}{2}}, e^{\frac{5\pi i}{6}}, e^{\frac{7\pi i}{6}}, e^{\frac{9\pi i}{6}}, e^{\frac{11\pi i}{6}}],\\
l &= \frac{1}{(q_1-q_2)(q_1-q_3)(q_1-q_4)(q_1-q_5)(q_1-q_6)},\\
m &= \frac{1}{(q_2-q_1)(q_2-q_3)(q_2-q_4)(q_2-q_5)(q_2-q_6)},\\
n &= \frac{1}{(q_3-q_1)(q_3-q_2)(q_3-q_4)(q_3-q_5)(q_3-q_6)}.
\end{aligned}$$

Setting $(k_t\bar{r}_t)^{\frac{1}{3}} = p$ as the integration variable, and using $\eta = \frac{\bar{z}}{\bar{r}_t^{\frac{1}{3}}}$, with some simplification, yields the following expressions for the disturbance fields

$$\bar{u}_z = \frac{-9i}{\bar{r}_t^3}\int_0^\infty p^8 J_0(p^3)\left(lq_1^2 e^{iq_1p|\eta|} + mq_2^2 e^{iq_2p|\eta|} + nq_3^2 e^{iq_3p|\eta|}\right) dp, \tag{2.34}$$

$$\bar{\rho}_f = \frac{-9i}{\bar{r}_t^{\frac{7}{3}}}\int_0^\infty p^6 J_0(p^3)\left(le^{iq_1p|\eta|} + me^{iq_2p|\eta|} + ne^{iq_3p|\eta|}\right) dp, \tag{2.35}$$

$$\bar{u}_{r_t} = \frac{-9\,\mathrm{sgn}(\eta)}{\bar{r}_t^{\frac{7}{3}}}\int_0^\infty p^6 J_1(p^3)\left(lq_1^3 e^{iq_1p|\eta|} + mq_2^3 e^{iq_2p|\eta|} + nq_3^3 e^{iq_3p|\eta|}\right) dp. \tag{2.36}$$

These integrals are functions of $|\eta|$, consistent with fore-aft symmetry. Thus, the above self-similar forms point to a thin axisymmetric wake bracketing the horizontal plane containing the settling sphere, in the far-field, whose vertical extent grows as $z \propto (Ri_vPe)^{-\frac{1}{6}} r_t^{\frac{1}{3}}$, where z and r_t are now in units of a; the self-similarity is also evident from figure 2.1 where the number and shapes of recirculating cells is invariant for large r_t, with their vertical extents alone increasing with increasing r_t. Even within the self-similar wake, it can be seen from

(2.34-2.36) that the disturbance fields decay more rapidly compared to the $O(1/r)$ decay of the Stokeslet, reinforcing the fact that buoyancy forces screen the originally long-ranged Stokesian fields. The one dimensional integrals in (2.34-2.36) are readily evaluated numerically, and furthermore, the large-η asymptotes, obtained from using the small argument approximation for the Bessel function, are given by $\bar{u}_z \approx \frac{181440}{\bar{r}_t^3 |\eta|^9}$, $\bar{u}_{r_t} \approx \operatorname{sgn}(\eta) \frac{816480}{\bar{r}_t^{7/3} |\eta|^{10}}$, and $\bar{\rho}_f \approx \frac{-3240}{\bar{r}_t^{7/3} |\eta|^7}$.

The comparison between one-dimensional profiles of the axial velocity field, obtained from the exact calculations above (that led to the streamline pattern in figure 2.1), and those obtained from the far-field self-similar approximation given by (2.34) is shown in figure 2.2 for various $\bar{r}_t$'s. The plots correspond to $\bar{r}_t^3 \bar{u}_z$ as a function of $|\eta|$, as a result of which the far-field approximation shown remains invariant to a change in $\bar{r}_t$. In the log-log plots shown, the zero-crossings of the axial velocity (which roughly correlate to the boundaries between recirculating cells) appears as sharp dips (to negative infinity). There exist significant differences between the numerical and far-field predictions for $\bar{r}_t$'s of order unity; for instance, the number of zero crossings in the numerical field depends upon $\bar{r}_t$, being 7 for $\bar{r}_t = 1$, 6 for $\bar{r}_t = 4$ and increasing to 8 (the same as the far-field approximation) for $\bar{r}_t \geq 15$. The agreement improves with increasing $\bar{r}_t$, and there is near-quantitative agreement for the largest $\bar{r}_t$ $(= 25)$; note that the streamline pattern in figure 2.1a includes only three of the eight zero crossings for $\bar{r}_t = 25$. Finally, for $\bar{r}_t$'s greater than that corresponding to the final zero crossing, the axial velocity profiles conform to the algebraic asymptote above viz. $\bar{r}_t^3 \bar{u}_z \approx \frac{181440}{|\eta|^9}$, and shown as the dashed orange line in figure 2.2. An analogous scenario prevails for the density disturbance field as can be seen from figure 2.3.

As one approaches the translation axis (the stagnation streamline corresponding to $\bar{r}_t = 0$), η becomes asymptotically large for any finite $\bar{z}$, and only the large-η asymptotes are of relevance. On substituting for η, the large-η asymptotes for the axial velocity and density fields above are seen to be functions of only $|\bar{z}|$, suggesting that these asymptotes remain valid far-field (large $|\bar{z}|$) approximations even along the translation axis. The radial velocity is, of course, zero along the stagnation streamline, with the large-η approximation above being $O(\bar{r}_t)$ for small $\bar{r}_t$. In figure 2.4, we compare the exact axial velocity field for $\bar{r}_t = 0$, again obtained numerically, with the large-η asymptote that is now proportional to $\bar{z}^{-9}$. Although the locations of the (seven) zero-crossings of the exact profile can no longer be predicted, the far-field algebraic decay nevertheless conforms to the asymptote above. For $\bar{r}_t = 0$ alone, the velocity field given by (2.20) is expressible in terms of a one-dimensional integral that again yields the aforementioned large-$\bar{z}$ asymptote [Fouxon and Leshansky, 2014].

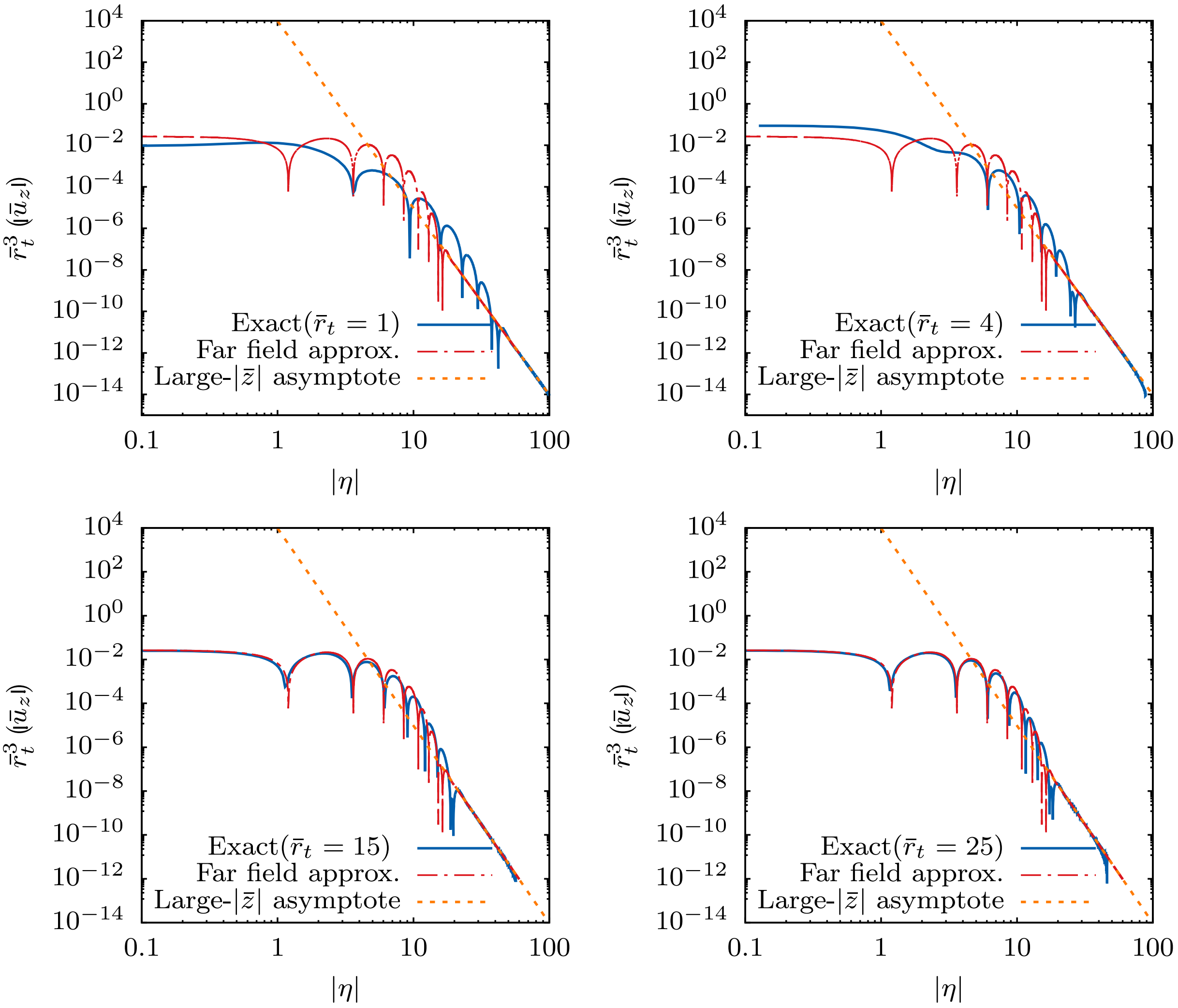

Fig. 2.2 The axial velocity profiles in the diffusion-dominant limit ($Pe = 0$): comparison between the exact numerical profiles and the far-field approximation (given by (2.34) for various $\bar{r}_t$'s; in each of the plots, the large-η analytical asymptote is shown as a dashed orange line.

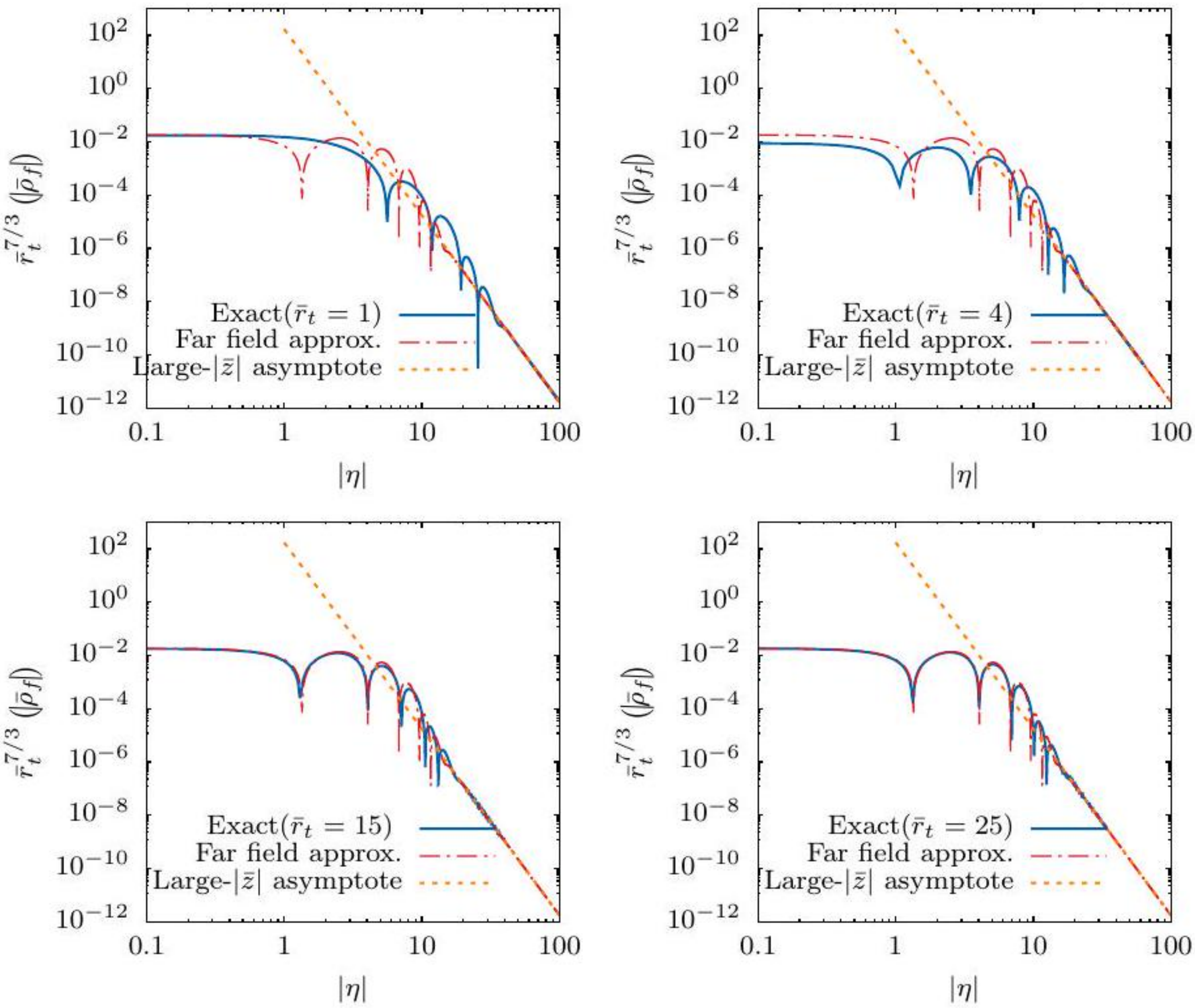

Fig. 2.3 The density disturbance profiles in the diffusion-dominant limit ($Pe = 0$): comparison between the exact numerical profiles and the far-field approximation (given by (2.34) for various $\bar{r}_t$'s; in each of the plots, the large-η analytical asymptote is shown as a dashed orange line.

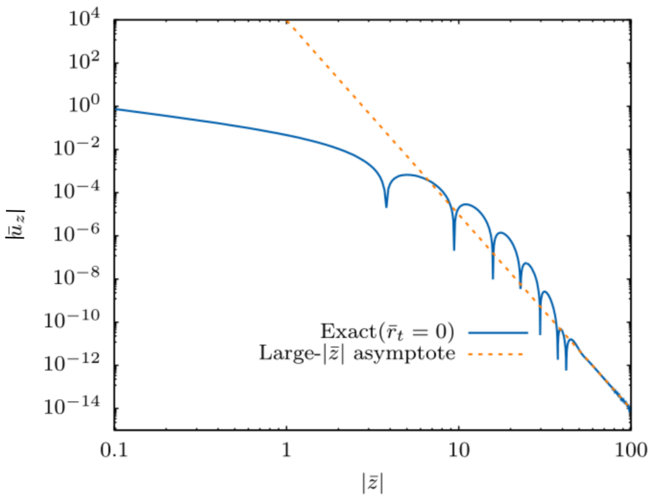

Fig. 2.4 Axial velocity, as a function of $|\tilde{z}|$, for $\tilde{r}_t = 0$ (the translation axis), in the diffusion dominant limit ($Pe = 0$); the large-$\tilde{z}$ asymptote is shown as a dashed orange line.

2.3.2 Convection dominant limit ($Pe \gg 1$)

The simplification of the Fourier integrals in the convection dominant limit, given by (2.20) and (2.21), is analogous to the diffusion dominant case above. In a spherical coordinate system aligned with the translation direction, and after integration over the azimuthal angle, the disturbance fields are given by

$$\tilde{u}_z = \frac{-3\left(2+\frac{\tilde{r}_t^2}{\tilde{z}^2}\right)}{4|\tilde{z}|\left(1+\frac{\tilde{r}_t^2}{\tilde{z}^2}\right)^{\frac{3}{2}}} + \frac{3}{2\pi}\int_0^\infty dk \int_0^\pi d\theta \, \frac{\sin^5\theta J_0(k\tilde{r}_t \sin\theta)e^{ik\tilde{z}\cos\theta}}{(ik^3\cos\theta + \beta_\infty k^4 + \sin^2\theta)}, \tag{2.37}$$

$$\tilde{p}_f = \frac{-3}{2\pi}\int_0^\infty dk \int_0^\pi d\theta \, \frac{k^2\sin^3\theta J_0(k\tilde{r}_t\sin\theta)e^{ik\tilde{z}\cos\theta}}{(ik^3\cos\theta + \beta_\infty k^4 + \sin^2\theta)}, \tag{2.38}$$

where we have again separated out the Stokeslet contribution in (2.37) for purposes of numerical convergence. The Stokes streamfunction is given by

$$\tilde{\psi}_s = \frac{-3\tilde{r}_t^2}{4(\tilde{r}_t^2+\tilde{z}^2)^{\frac{1}{2}}} + \frac{3\tilde{r}_t}{2\pi}\int_0^\infty dk \int_0^\pi d\theta \, \frac{\sin^4\theta J_1(k\tilde{r}_t\sin\theta)e^{ik\tilde{z}\cos\theta}}{k(ik^3\cos\theta + \beta_\infty k^4 + \sin^2\theta)}. \tag{2.39}$$

Note from (2.37) and (2.38) that, although our interest is in the limit $\beta_\infty = 0$, corresponding to convection effects being infinitely dominant, we have retained the terms proportional to β_∞ in the integrands. One reason is ease of numerical evaluation (as can be seen below). The second reason is the sensitive dependence of the structure of both the velocity and

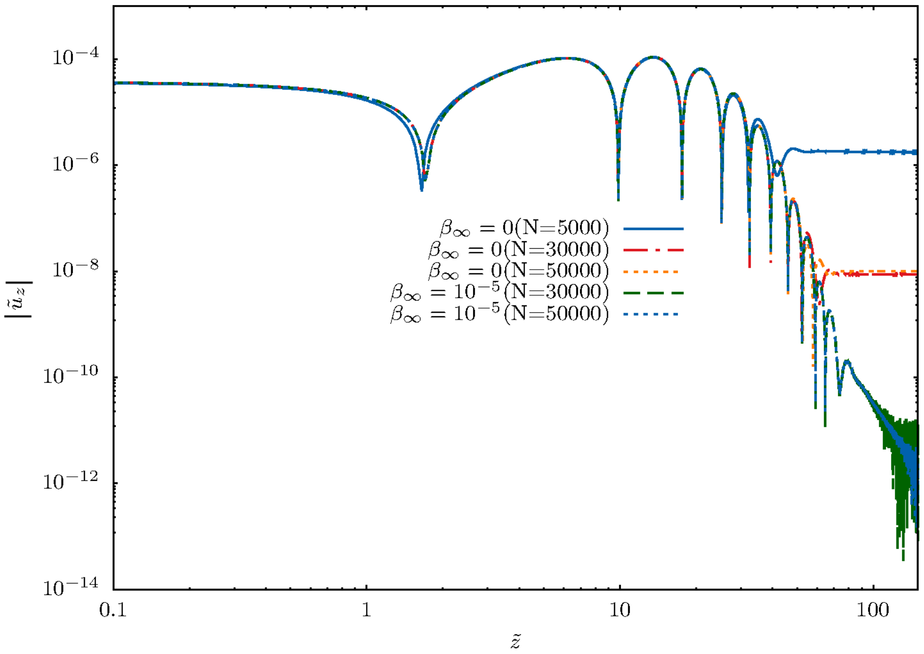

Fig. 2.5 The comparison given highlights the importance of weak diffusive effects (small but finite β_∞) in obtaining an accurate representation of the disturbance fields in the convection-dominant limit. The profiles for $\beta_\infty = 0$ asymptote to a spurious plateau regardless of N; here, N represents the number of quadrature points used for numerical integration. The axial velocity calculations shown here are performed for $r_t = 25$.

density fields, in the neighorhood of the rear stagnation streamline, on β_∞; the density field in particular diverges for $\beta_\infty = 0$.

The rationale behind the retention of weak diffusion effects (small but finite β_∞) is illustrated in Figure 2.5 where we compare the numerically evaluated axial velocity profiles at $r_t = 25$ for $\beta_\infty = 0$ and 10^{-5} for varying number of quadrature points. The $\beta_\infty = 0$ profile deviates from the true profile, asymptoting instead to a spurious plateau beyond a certain $\tilde{z}$. Further, there is only a modest effect of quadrature resolution on this threshold $\tilde{z}$, and as a result, for $\beta_\infty = 0$, the eventual algebraic decay regime remains numerically inaccessible regardless of the number of quadrature points. On the other hand, the profile for $\beta_\infty = 10^{-5}$ does access the algebraic decay regime, and the numerical error does reduce with increase (from 30000 to 50000) in the number of quadrature points).

Figure 2.6 shows the streamline pattern and the isycnalopycnal contours for the smallest $\beta_\infty (= 10^{-5})$ accessed in our calculations. The limited spatial extent here, in comparison to figure 2.1, is on account of the numerical difficulties involved in calculating the farfield isopycnals; the streamline pattern alone, over a larger spatial extent, appears below in figure

2.14a. Nevertheless, the profound asymmetry of both the streamline and iso-pycnals patterns is readily evident from Figure 2.5, and is in contrast to those in the diffusion-dominant limit (Figure 2.1). This asymmetry may be anticipated from the integral expressions in (2.37-2.39) where, unlike the $Pe = 0\,(\beta_\infty = \infty)$ limit, one can no longer replace the complex exponential by a Cosine. Apart from the different shapes and numbers of the recirculating cells in front of and behind the translating sphere, there is also the appearance of a radially localized but vertically extended structure, in the streamline pattern, in the rear. As will be seen below, this corresponds to a buoyant reverse jet that develops behind the particle with decreasing β_∞ (see figure 2.14f). It can be noted that the streamline pattern in Figure 2.5*a* is, in fact, quite analogous to Figure 2*d* in Zhang et al. [2019] which, although it pertains to the region around a finite sphere of order its own size, corresponds to a relationship between Re and Riv consistent with the Stokes-stratification regime. The far-field analysis in the subsections below points to both a stratification-induced wake in the convection-dominant limit with a structure that is insensitive to β_∞ (for $\beta_\infty \ll 1$); and the buoyant reverse jet mentioned above whose structural features depend essentially on β_∞.

Far-field wake analysis

Similar to the diffusion-dominant case analyzed in section 2.3.1, the expected dominance of horizontal motion for distances large compared to $Ri_v^{-\frac{1}{3}}$ points to the assumption $k_3 \gg k_t$ in the Fourier integrals in (2.20) and (2.21), when characterizing a far-field wake region. The integrals, in this limit, reduce to

$$\tilde{\mathbf{u}}(\tilde{\mathbf{r}}) = \frac{-3}{4\pi^2}\int \frac{ik_3k_t^2}{(ik_3^5+k_t^2)}e^{i\mathbf{k}.\tilde{\mathbf{r}}}d\mathbf{k}, \tag{2.40}$$

$$\tilde{\rho_f}(\tilde{\mathbf{r}}) = \frac{-3}{4\pi^2}\int \frac{k_t^2}{ik_3^5+k_t^2}e^{i\mathbf{k}.\tilde{\mathbf{r}}}d\mathbf{k}, \tag{2.41}$$

where we have set $\beta_\infty = 0$. The integrals in (2.40) and (2.41) can be reduced to one-dimensional integrals, written in terms of the similarity variable $\eta = \frac{\bar{z}}{\bar{r}_t^{\frac{2}{5}}}$, via contour integration as shown below.

Starting from 2.40 and 2.41, in a cylindrical coordinate system aligned with the translation direction, and after carrying out the ϕ integration, the expressions for the axial and transverse velocities, and the density disturbance, reduce to

$$\bar{u}_z = \frac{-3i}{2\pi}\int_{-\infty}^{\infty} dk_3 \int_0^{\infty} dk_t \frac{k_3k_t^3J_0(k_t\bar{r}_t)e^{ik_3\bar{z}}}{(ik_3^5+k_t^2)}, \tag{2.42}$$

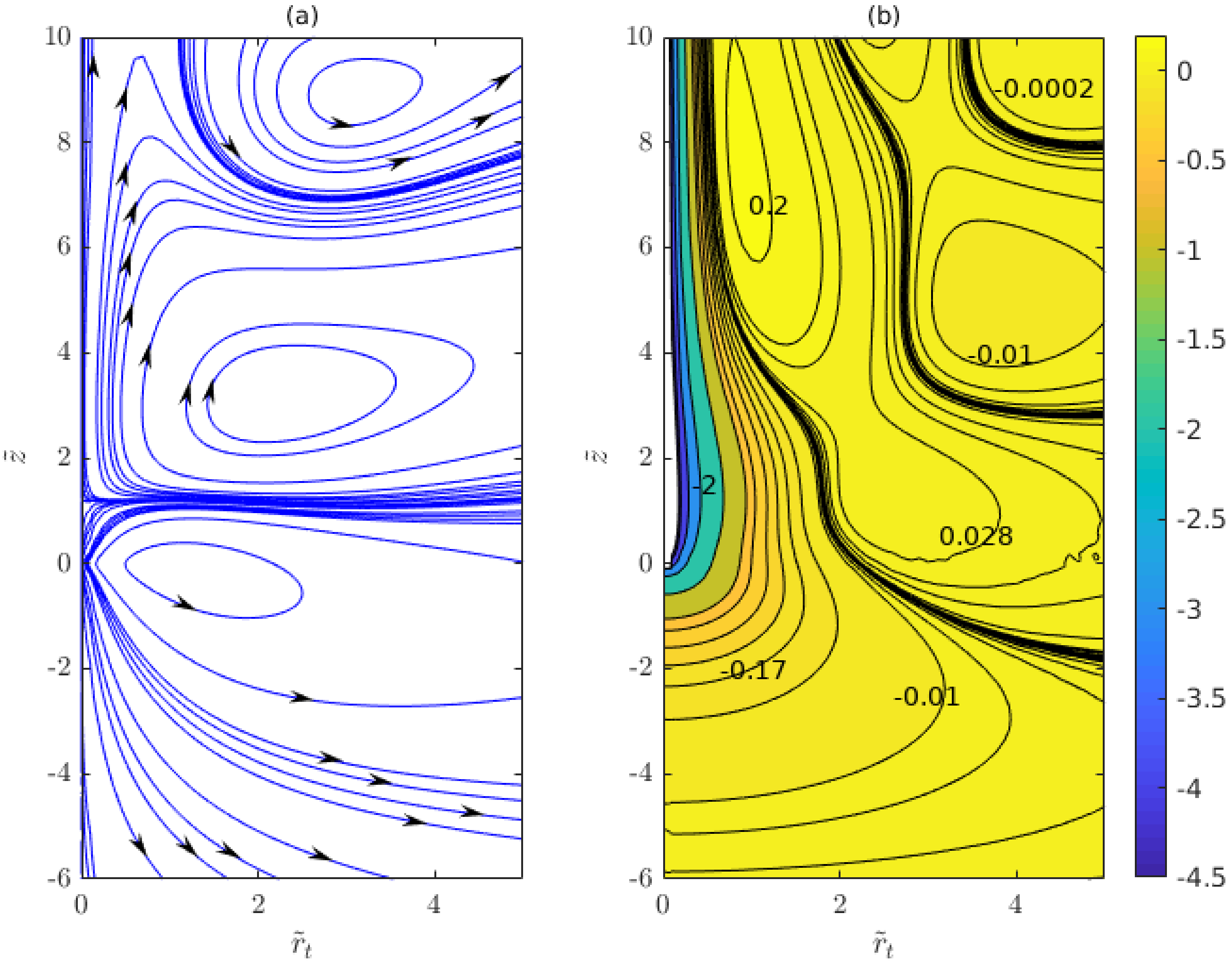

Fig. 2.6 (a) Streamlines and (b) Iso-pycnals for a translating sphere in a linearly stratified fluid, in the convection dominant limit ($\beta_\infty = 10^{-5}$), in the Stokes stratification regime ($Re \ll Ri_v^{\frac{1}{3}}$); in the point-particle approximation used, the sphere is at the origin and moving vertically downward.

$$\bar{u}_{r_t} = \frac{3i}{2\pi} \int_{-\infty}^{\infty} dk_3 \int_0^{\infty} dk_t \frac{k_3^2 k_t^2 J_1(k_t \bar{r}_t) e^{ik_3 \bar{z}}}{(ik_3^5 + k_t^2)}, \tag{2.43}$$

$$\bar{\rho}_{f_1} = \frac{-3}{2\pi} \int_{-\infty}^{\infty} dk_3 \int_0^{\infty} dk_t \frac{k_t^3 J_0(k_t \bar{r}_t) e^{ik_3 \bar{z}}}{(ik_3^5 + k_t^2)}. \tag{2.44}$$

As for the diffusion dominant case analyzed before, we first evaluate the k_3-integral using contour integration. There now exist five poles in the complex-k_3 plane with two poles in the lower half and three poles in the upper half of the complex plane; the differing number of poles in the two halves of the plane translates to fore-aft asymmetry of the axial velocity and density disturbance fields. The residue integration then yields the following 'one-dimensional' integrals for positive and negative $\tilde{z}$

$$\begin{aligned}\tilde{u}_z &= -3i \int_0^{\infty} k_t^{\frac{9}{5}} J_0[k_t r_t][Q_1 q_1 e^{iq_1 k_t^{\frac{2}{5}} \tilde{z}} + Q_2 q_2 e^{iq_2 k_t^{\frac{2}{5}} \tilde{z}} + Q_3 q_3 e^{iq_3 k_t^{\frac{2}{5}} \tilde{z}}] dk_t \text{ (for } \tilde{z} > 0) \\ &= 3i \int_0^{\infty} k_t^{\frac{9}{5}} J_0[k_t r_t][Q_4 q_4 e^{iq_4 k_t^{\frac{2}{5}} \tilde{z}} + Q_5 q_5 e^{iq_5 k_t^{\frac{2}{5}} \tilde{z}}] dk_t \text{ (for } \tilde{z} < 0),\end{aligned} \tag{2.45}$$

$$\begin{aligned}\tilde{u}_{r_t} &= -3 \int_0^{\infty} k_t^{\frac{6}{5}} J_0[k_t r_t][Q_1 q_1^2 e^{iq_1 k_t^{\frac{2}{5}} \tilde{z}} + Q_2 q_2^2 e^{iq_2 k_t^{\frac{2}{5}} \tilde{z}} + Q_3 q_3^2 e^{iq_3 k_t^{\frac{2}{5}} \tilde{z}}] dk_t \text{ (for } \tilde{z} > 0) \\ &= 3 \int_0^{\infty} k_t^{\frac{6}{5}} J_0[k_t r_t][Q_4 q_4^2 e^{iq_4 k_t^{\frac{2}{5}} \tilde{z}} + Q_5 q_5^2 e^{iq_5 k_t^{\frac{2}{5}} \tilde{z}}] dk_t \text{ (for } \tilde{z} < 0),\end{aligned} \tag{2.46}$$

$$\begin{aligned}\tilde{\rho}_f &= -3 \int_0^{\infty} k_t^{\frac{7}{5}} J_0[k_t r_t][Q_1 e^{iq_1 k_t^{\frac{2}{5}} \tilde{z}} + Q_2 e^{iq_2 k_t^{\frac{2}{5}} \tilde{z}} + Q_3 e^{iq_3 k_t^{\frac{2}{5}} \tilde{z}}] dk_t \text{ (for } \tilde{z} > 0) \\ &= 3 \int_0^{\infty} k_t^{\frac{7}{5}} J_0[k_t r_t][Q_4 e^{iq_4 k_t^{\frac{2}{5}} \tilde{z}} + Q_5 e^{iq_5 k_t^{\frac{2}{5}} \tilde{z}}] dk_t \text{ (for } \tilde{z} < 0).\end{aligned} \tag{2.47}$$

Here q_1, q_2, q_3, q_4, q_5, Q_1, Q_2, Q_3, Q_4 and Q_5 are complex-valued constants given by

$$
\begin{aligned}
[q_1, q_2, q_3, q_4, q_5] &= [e^{\frac{\pi i}{10}}, e^{\frac{\pi i}{2}}, e^{\frac{9\pi i}{10}}, e^{-\frac{7\pi i}{10}}, e^{-\frac{3\pi i}{10}}],\\
Q_1 &= \frac{1}{(q_1-q_2)(q_1-q_3)(q_1-q_4)(q_1-q_5)},\\
Q_2 &= \frac{1}{(q_2-q_1)(q_2-q_3)(q_2-q_4)(q_2-q_5)},\\
Q_3 &= \frac{1}{(q_3-q_1)(q_3-q_2)(q_3-q_4)(q_3-q_5)},\\
Q_4 &= \frac{1}{(q_4-q_1)(q_4-q_2)(q_4-q_3)(q_4-q_5)},\\
Q_5 &= \frac{1}{(q_5-q_1)(q_5-q_2)(q_5-q_3)(q_5-q_4)}.
\end{aligned}
$$

Setting $k_t \bar{r}_t = p$ as the integration variable, and using $\eta = \frac{\tilde{z}}{\tilde{r}_t^{\frac{2}{5}}}$ yields the following expressions for axial velocity, density disturbance and transverse velocity

$$
\begin{aligned}
\tilde{u}_z &= -\frac{15i}{2\tilde{r}_t^{14/5}} \int_0^\infty m^6 J_0[m^{5/2}][Q_1 q_1 e^{iq_1 m\eta} + Q_2 q_2 e^{iq_2 m\eta} + Q_3 q_3 e^{iq_3 m\eta}]dm \ (\tilde{\eta} > 0),\\
&= \frac{15i}{2\tilde{r}_t^{14/5}} \int_0^\infty m^6 J_0[m^{5/2}][Q_4 q_4 e^{iq_4 m\eta} + Q_5 q_5 e^{iq_5 m\eta}]dm \ (\tilde{\eta} < 0),
\end{aligned}
\tag{2.48}
$$

$$
\begin{aligned}
\tilde{\rho_f} &= -\frac{15}{2\tilde{r}_t^{12/5}} \int_0^\infty m^5 J_0[m^{5/2}][Q_1 e^{iq_1 m\eta} + Q_2 e^{iq_2 m\eta} + Q_3 e^{iq_3 m\eta}]dm \ (\tilde{\eta} > 0),\\
&= \frac{15}{2\tilde{r}_t^{12/5}} \int_0^\infty m^5 J_0[m^{5/2}][Q_4 e^{iq_4 m\eta} + Q_5 e^{iq_5 m\eta}]dm \ (\tilde{\eta} < 0),
\end{aligned}
\tag{2.49}
$$

$$
\begin{aligned}
\tilde{u}_{r_t} &= -\frac{15}{2\tilde{r}_t^{11/5}} \int_0^\infty m^{9/2} J_1[m^{5/2}][Q_1 q_1^2 e^{iq_1 m\eta} + Q_2 q_2^2 e^{iq_2 m\eta} + Q_3 q_3^2 e^{iq_3 m\eta}]dm \ (\tilde{\eta} > 0),\\
&= \frac{15}{2\tilde{r}_t^{11/5}} \int_0^\infty m^{9/2} J_1[m^{5/2}][Q_4 q_4^2 e^{iq_4 m\eta} + Q_5 q_5^2 e^{iq_5 m\eta}]dm \ (\tilde{\eta} < 0).
\end{aligned}
\tag{2.50}
$$

The fore-aft asymmetry implies that one has different asymptotic approximations depending on the sign of $\tilde{\eta}$ (or $\tilde{z}$). Nevertheless, the above self-similar forms point to a far-field wake, that includes the horizontal plane containing the settling sphere, and whose vertical extent grows as $z \propto Ri_v^{-\frac{1}{5}} r_t^{\frac{2}{5}}$, with z and r_t being measured in units of a. The axial and radial velocity profiles, and the density disturbance profiles, obtained from a numerical evaluation of the one-dimensional integrals above, are shown both on the linear and logarithmic scales in figure 2.7, with the logarithmic plot clearly highlighting the zero-crossings at larger distances. The logarithmic plot also shows that while there are still only a finite number of zero crossings, similar to $Pe = 0$, they differ in number for negative and positive $\tilde{\eta}$, with there being fewer zero crossings for negative $\tilde{\eta}$. This implies fewer recirculating cells below the settling sphere, and is consistent with the streamline pattern in figure 2.6 (also see figure 2.14 below). Similar to the diffusion-dominant limit, one may obtain the large-η asymptotic forms from (2.48-2.50) which govern the eventual algebraic decay of the disturbance fields beyond the final zero crossing; these are given by $[\frac{3240}{\frac{14}{r_t}^5\tilde{\eta}^7}, -\frac{2160}{\frac{14}{r_t}^5\tilde{\eta}^7}]$ for the axial velocity, $[\frac{11340}{\frac{11}{r_t}^5\tilde{\eta}^8}, -\frac{7560}{\frac{11}{r_t}^5\tilde{\eta}^8}]$ for the radial velocity, and $[-\frac{540}{\frac{12}{r_t}^5\tilde{\eta}^6}, \frac{360}{\frac{12}{r_t}^5\tilde{\eta}^6}]$ for the density disturbance, with the members of each ordered pair corresponding to positive and negative $\tilde{\eta}$, respectively. These asymptotes, and the above approximate profiles based on the one-dimensional integrals above will be compared to the exact (numerical) fields below.

The structure of the far-field wake may also be characterized in terms of the $\tilde{\eta}$-moments of the disturbance fields above. The motion being largely horizontal, it is the moments of the radial velocity field that are the most important. A calculation using the far-field approximation above (equation (2.50)) shows that the zeroth and first moments of the radial velocity field in the wake vanish, and that the second moment, defined as $\int_{-\infty}^{\infty} \tilde{\eta}^2 \tilde{u}_{r_t} d\tilde{\eta} = 6$, is the first non-trivial member of the moment hierarchy (interestingly, this may also be seen from direct neglect of the viscous term ik_3k^4 in the original Fourier integral (2.20), and additionally setting $\beta_\infty = 0$; the radial velocity may now be obtained in terms of generalized functions as $\tilde{u}_{r_t} = \frac{3}{\tilde{r}_t}\delta''(z)$, which yields the same value for the second moment). The moment-based characterization above offers an interesting contrast to the known solution for the motion induced by a sphere settling through a linearly stratified ambient in the linearized inviscid approximation, when stratification forces are (infinitely) dominant. As shown in (Vladimirov and Li'in [1991]), the motion is strictly horizontal and restricted to an infinite horizontal slab whose upper and lower planes bound the sphere. Within this slab, the fluid moves radially inward (outward) in the rear (front) half of the translating sphere. The nature of this motion is easily understood from the changing size of the sphere cross-section in a given horizontal plane, and the requirement of satisfying the impenetrability condition at the sphere surface. In two dimensions (that is, a settling cylinder), the horizontal velocity field is a constant, while in three dimensions (a settling sphere), the motion would have a $1/r_t$-dependence consistent with incompressibility. Such a motion corresponds has a dipolar character with a non-trivial first moment for the radial velocity. In contrast, as already seen, the structure of the far-field wake above does not exhibit the aforementioned structure. This is because although the

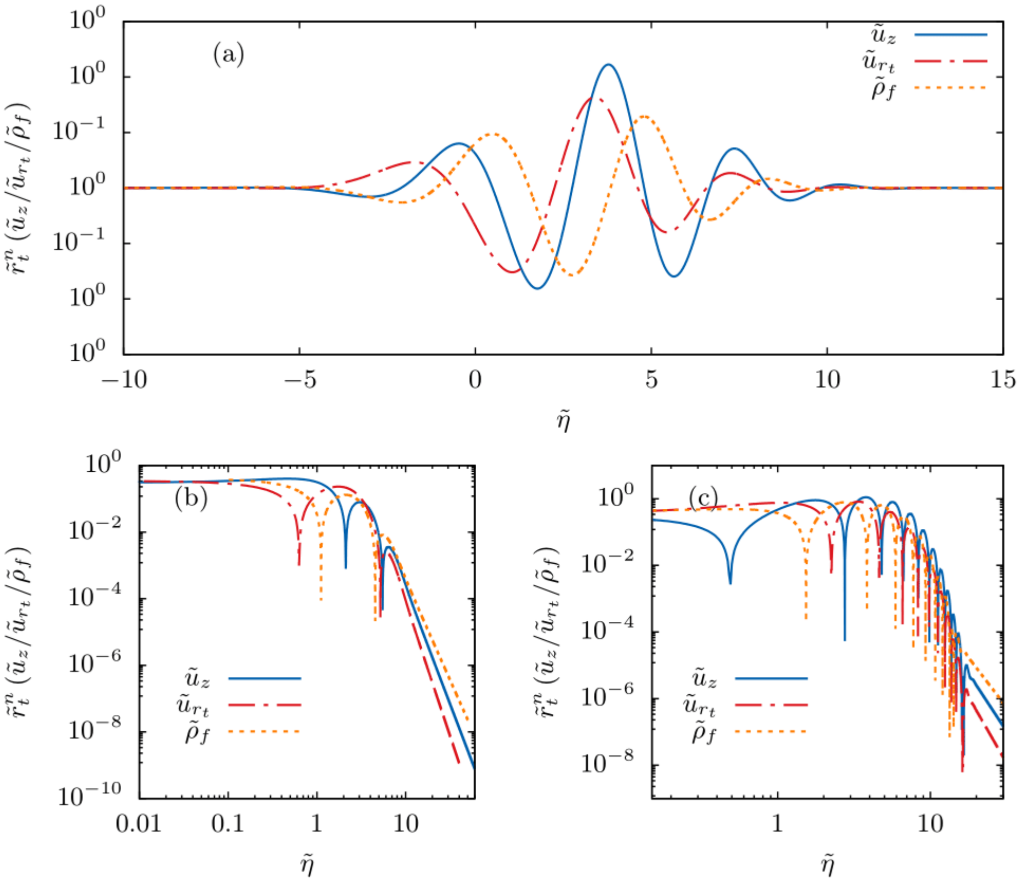

Fig. 2.7 The axial velocity, the radial velocity and density disturbance profiles, within the far-field wake region, in the convection dominant limit ($Pe \gg 1$) pertaining to the Stokes stratification regime: (a) the disturbance fields on a linear scale; the absolute value of the disturbance fields on a logarithmic scale for (b) negative $\tilde{\eta}$ and (c) for positive $\tilde{\eta}$; here, $n = 14/5$, $11/5$ and $12/5$ for u_z, u_{r_t} and ρ_f, respectively. The aforementioned wake includes the plane of the settling sphere, and grows in vertical extent as $z \propto Ri_v^{\frac{2}{15}} r_t^{\frac{2}{5}}$.

Stokeslet in the inner region has a radial component consistent with the symmetry of the linearized inviscid solution above (directed inward behind the sphere and outward in front of it), the Stokeslet is screened by the buoyancy forces induced in a surrounding volume with a linear dimension of $O(Ri_v^{-\frac{1}{3}})$. As a result, the wake velocity field on length scales much larger than $O(Ri_v^{-\frac{1}{3}})$, has the symmetry pertaining to a force-dipole consisting of the original Stokeslet and an effective upward force arising from the volumetric distribution of induced buoyancy forces.

Far-field jet analysis

As for the diffusion-dominant case, the large-η asymptotes for the axial velocity and density disturbance fields in the convection-dominant limit, given in (2.48-2.50), are seen to be independent of $\bar{r}_t$, with the radial disturbance field being $O(\bar{r}_t)$ for $\tilde{z} \to 0$. Thus, one expects the large-η asymptotes to continue to remain valid at sufficiently large distances (large $\tilde{z}$) along the stagnation streamline ($\tilde{z} = 0$). This remains true for the front stagnation streamline, with $\tilde{u}_z = -\frac{2160}{\tilde{z}^7}$ and $\rho_f = \frac{360}{\tilde{z}^6}$ for large negative $\tilde{z}$.

The wake approximation in the earlier subsection, and therefore, the large-η approximations derived from it, are no longer valid in the vicinity of the rear stagnation streamline. The pronounced asymmetry in the streamline pattern in figure 2.1, and the predominantly vertical motion behind the sphere, are already indicative of the breakdown of this approximation.The neighborhood of the rear stagnation streamline, at large distances, corresponds to large positive $\tilde{z}$ and small $\tilde{r}_t$ which, in Fourier space, is equivalent to $k_3 \ll k_t$ - the opposite of the wake-approximation above. The resulting integrals are

$$\tilde{\mathbf{u}}(\tilde{\mathbf{r}}) = -\frac{6\pi i}{8\pi^3} \int \frac{k_3 k_t^2 (\mathbf{1_z} - \frac{k_3 \mathbf{k}}{k^2})}{(i k_3 k_t^4 + k_t^2 + \beta_\infty k_t^6)} e^{i\mathbf{k}.\tilde{\mathbf{r}}} d\mathbf{k}, \tag{2.51}$$

$$\tilde{\rho}_f(\tilde{\mathbf{r}}) = -\frac{6\pi}{8\pi^3} \int \frac{k_t^2}{(i k_3 k_t^4 + k_t^2 + \beta_\infty k_t^6)} e^{i\mathbf{k}.\tilde{\mathbf{r}}} d\mathbf{k}, \tag{2.52}$$

where, unlike the wake-approximation above, we retain the $O(\beta_\infty)$ terms in the integrands, in anticipation of the fact that the reverse jet we find below has a structure that crucially depends on β_∞ even in the limit $\beta_\infty \ll 1$. The integrals in (2.51-2.52) can be further simplified by contour integration in the complex-k_3 plane. From the denominator of the integrand in (2.51-2.52) one notes that the only pole exists in the upper half of the complex plane, being given by $k_3 = i\frac{\beta_\infty k_t^4 + 1}{k_t^2}$, and contributes for positive z. Performing the integral over the azimuthal angle, and accounting for the contribution of the aforementioned pole in the k_3-integration, the disturbance fields reduce to the following one-dimensional integrals

$$\tilde{u}_z = 3 \int_0^\infty \frac{J_0(k_t \tilde{r}_t) e^{-\tilde{z}(\beta_\infty k_t^2 + \frac{1}{k_t^2})}}{k_t^3} dk_t, \tag{2.53}$$

$$\tilde{\rho}_f = -3 \int_0^\infty \frac{J_0(k_t \tilde{r}_t) e^{-\tilde{z}(\beta_\infty k_t^2 + \frac{1}{k_t^2})}}{k_t} dk_t. \tag{2.54}$$

For $\tilde{r}_t = 0$, the integrals in (2.53) and (2.54) may be evaluated analytically, giving:

$$\tilde{u}_z = 3\sqrt{\beta_\infty}K_1[2\sqrt{\beta_\infty \tilde{z}}], \tag{2.55}$$

$$\tilde{\rho}_f = -3K_0[2\sqrt{\beta_\infty \tilde{z}}]. \tag{2.56}$$

Here, K_0 and K_1 are the zeroth and first order modified Bessel functions of the second kind, respectively. The crucial role of weak diffusion on the jet structure may now be seen. On using $K_1(2\sqrt{\beta_\infty \tilde{z}}) \approx \frac{1}{2\sqrt{\beta_\infty \tilde{z}}}$ in the limit $\beta_\infty \to 0$, (2.55) is found to be independent of β_∞ at leading order, reducing to $\tilde{u}_z \approx \frac{3}{2\tilde{z}}$. Rather remarkably, this implies that the axial velocity, although pointing in the reverse direction (that is, opposite to the translating sphere) decays in the exact same manner as the Stokeslet on length scales much larger than $O(Ri_v^{-\frac{1}{3}})$ - this is the infinite-Pe reverse jet. On using the small argument form $K_0(2\sqrt{\beta_\infty \tilde{z}}) \approx -\ln(2\sqrt{\beta_\infty \tilde{z}})$, the density disturbance given by (2.56) is seen to be logarithmically singular all along the rear stagnation streamline for $Pe = \infty$. We comment further on this singular behavior in the context of Figure 2.9.

The far-field behavior above changes fundamentally for any small but finite β_∞. Now, there exists a second screening length across which the buoyant jet transitions from the $\frac{1}{z}$ decay above to a much faster exponential one, this arising from the exponentially decaying forms of the large-argument asymptotes of the modified Bessel functions above; likewise, the density disturbance transitions from the logarithmic form above, again to a far-field exponential decay. From (2.55) and (2.56), this second screening length is seen to be $O(\beta_\infty^{-\frac{1}{2}})$, in units of $aRi_v^{-\frac{1}{3}}$, or $O(Ri_v^{-\frac{1}{2}}Pe^{\frac{1}{2}})$ in units of a. The radial extent of the reverse-Stokeslet behavior, that may be interpreted as the width of the jet region, can be inferred from (2.51) and (2.52). Setting $\beta_\infty = 0$, one notes that $\tilde{z} \sim O(k_t^2) \sim O(\tilde{r}_t^{-2})$ for the argument of the exponential integrand to be of order unity. Thus, the reverse-Stokeslet behavior above is valid in a region $\tilde{r}_t \propto \tilde{z}^{-\frac{1}{2}}$ for $\beta_\infty = 0$; the buoyant jet narrows as $O(\tilde{z}^{-\frac{1}{2}})$, with increasing downstream distance, until the effects of diffusion become important. The diffusive smearing of the jet, and the transition to an exponentially decaying reverse flow, occurs across a second screening length of $O(\beta_\infty^{-\frac{1}{2}})$ when the jet has a width of $O(\beta_\infty^{\frac{1}{4}})$, both in units of $aRi_v^{-\frac{1}{3}}$; interestingly, this transition width is $O(Ri_vPe)^{-\frac{1}{4}}$, the small Pe screening length in units of a. At moderate to large Reynolds numbers, the observation of a rearward vertical columnar structure behind a particle moving through density stratified fluid goes back to the studies of Ochoa and Van Woert [1977]. It is confirmed in the experimental and numerical studies of Hanazaki et al. [2009a] that these vertical structures behind the particle are indeed rearward jets. Previously, this appearance of jets has been primarily attributed to the inertial effects (for instance, see Eames and Hunt [1997]). It is even safely assumed that the rearward jet behind the particle vanishes at small enough Reynolds numbers due to lack of any theoretical evidence [Okino et al., 2021]. Thus, the existence of such a jet in the Stokes stratification regime comes as a surprise, and shows the non-trivial signature of stratification even at zero Reynolds number. Even though all the earlier studies on the jets in stratified fluids are at moderate-to-high Re [Akiyama et al., 2019; Hanazaki et al., 2009a,b, 2015; Okino et al., 2017, 2021], we make a qualitative comparison with our results here. Our finding that the width of the jet at secondary screening length is $O(Ri_vPe)^{-1/4}(= Re^{-1/2}Pr^{-1/4}Fr^{1/2})$ is consistent with the findings of Akiyama et al. [2019] that the jet radius scales as $Fr^{1/2}$. It is also qualitatively consistent with their finding that the jet radius decreases as Pr is increased. Finally, it is also worth emphasizing that, unlike the usual case of the laminar (or turbulent) wake or jet, the buoyant jet in a density stratified fluid does not conserve momentum flux; the implication of the jet region for the drift volume in a stratified fluid is briefly discussed in section 3.2.

Figures 2.8 and 2.9 show plots of the axial velocity and density disturbance fields evaluated numerically at points along the stagnation streamline, based on (2.37) and (2.38), with $\bar{r}_t = 0$. In figure 2.8, the right hand side plot shows the transition of the axial velocity field, for negative $\tilde{z}$, from an $O(1/\tilde{z})$ Stokeslet decay in the inner region, to the more rapid $O(1/\tilde{z}^7)$ decay of the large-η asymptote derived earlier (see section 2.3.2), on length scales greater than the (primary) screening length. Note that this transition is accompanied by a reversal in direction, as evident from the sharp dip around $|\tilde{z}| \approx 8.85$ ($z \approx -8.85Ri_v^{-1/3}$) in the aforementioned logarithmic plot. Thus, the axial flow in the neighborhood of the front stagnation streamline, and at distances larger than the screening length, points towards the sphere. Importantly, the axial velocity profiles are virtually coincident for $\beta_\infty \leq 10^{-2}$, implying that the flow pattern in the vicinity of the front stagnation streamline converges to a limiting form for $Pe \to \infty$ that is characterized by the primary screening length of $O(Ri_v^{-\frac{1}{3}})$. In contrast, the plot on the left hand side, for positive $\tilde{z}$, shows a transition from the inner region Stokeslet decay to an eventual exponential decay at the largest distances, with this transition being postponed to progressively larger $\tilde{z}$ with decreasing β_∞. For the smallest $\beta_\infty' s (= 10^{-4}$ and $10^{-5})$, one can see the emergence of an intermediate asymptotic regime, corresponding to $1 \ll \tilde{z} \ll \beta_\infty^{-\frac{1}{2}}$, where the velocity conforms to the reverse-Stokeslet behavior predicted above. Note that both the Stokeslet and reverse-Stokeslet behavior appear as the same asymptote (the black dot-dashed line), since the plot is for the absolute value of the velocity field on a logarithmic scale, and the indication of the reversal in direction is again the intervening sharp dip corresponding to $\tilde{z} \approx 1.15$ ($z \approx 1.15Ri_v^{-\frac{1}{3}}$). The inset in this plot shows that the axial velocity profiles collapse onto a universal exponential behavior, when the ordinate and abscissa are rescaled with $\beta_\infty^{\frac{1}{2}}$ and $\beta_\infty^{-\frac{1}{2}}$, respectively, the latter corresponding to the axial distance being scaled by the secondary screening length. This collapse is consistent with (2.55) above; although, since the distance corresponding to the reversal in direction scales with the primary screening length, the dips of the curves in the inset plot, are no longer coincident for varying β_∞.

The plots in figure 2.9 again highlight the contrast between the density disturbance fields along the front and rear stagnation streamlines. The plot on the right hand side, for negative $\tilde{z}$, shows that the density disturbance converges to a limiting form for $\beta_\infty \leq 10^{-2}$, with an $O(1/\tilde{z}^6)$ far-field decay, consistent with the large$-\eta$ asymptote obtained earlier in the far-field wake analysis of the present section; although, the numerics break down beyond a certain $|\tilde{z}|$ that is a function of the number of quadrature points used. In contrast, the left hand side plot shows that the density disturbance transitions from a near-field plateau to a far-field exponential decay, with this plateau increasing in magnitude logarithmically with decreasing β_∞, consistent with (2.56), and thereby precluding a collapse of the density profiles for small β_∞. The inset in this figure plots the density profiles as a function of the rescaled abscissa, $\beta_\infty^{\frac{1}{2}}\tilde{z}$, so as to highlight their collapse onto a common curve (the modified Bessel function asymptote given by (2.56)). The individual curves deviating from this common asymptote on account of the near-field plateauing behavior, with this deviation occurring at a progressively smaller distance with decreasing β_∞; for $\beta_\infty \to 0$, the said plateau regime becomes vanishingly small, while the exponential decay is pushed off to infinitely large distances (in units of the primary screening length), so the density field becomes logarithmically singular along the entire rear stagnation streamline. While the singularity itself is an expected consequence (for $Pe = \infty$) of the steady state assumption, the nature of the divergence is an artifact of the outer region analysis. The logarithmic singularity implies that the density disturbance, obtained from a time dependent analysis, should diverge logarithmically for long times. The density along the rear stagnation streamline of a finite-sized sphere must instead diverge linearly in time, this divergence arising due to the asymptotically large residence time of fluid elements in the immediate neighborhood of the rear stagnation point. There is no notion of a stagnation point in an outer-region analysis, and therefore, unlike the velocity field given by (2.55), the density field given by (2.56) is not valid exactly on the rear stagnation streamline ($\tilde{r}_t = r_t = 0$). One must instead interpret (2.56) as being valid for $\tilde{r}_t \ll 1$, but with r_t still being much greater than a. The (negative) logarithmic divergence for $\beta_\infty \to 0$ can then be attributed to the logarithmically divergent (in time) downward drift displacements arising from the $O(1/z)$ Stokesian disturbance field.

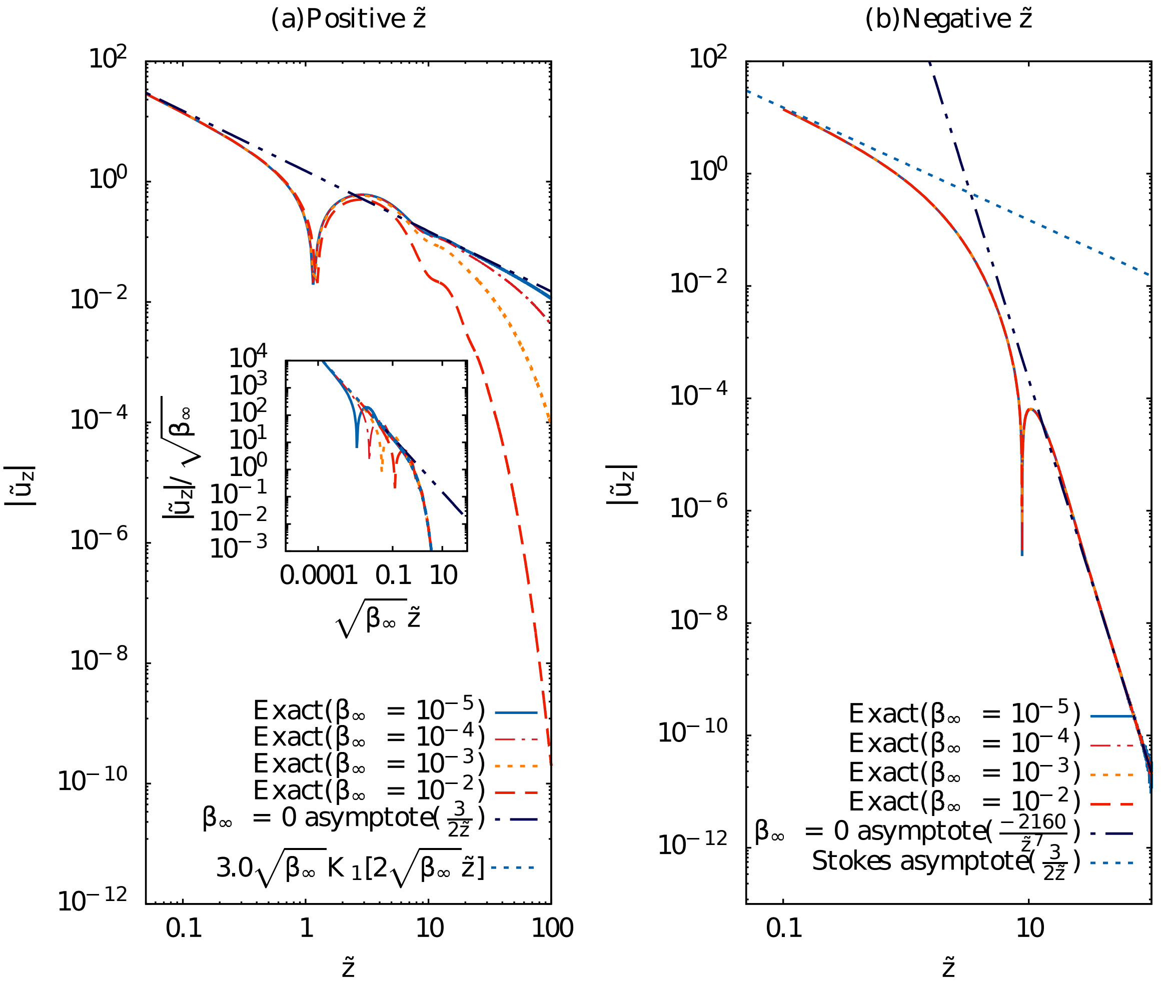

Fig. 2.8 The axial velocity field plotted along the stagnation streamline for both positive (Figure (a)) and negative $\tilde{z}$ (Figure (b)), and for different small β_∞. In the Figure (a), both the Stokeslet and reverse-Stokeslet asymptotes appear as the black dot-dashed line; the inset shows the collapse of the far-field profiles onto a common far-field decay, when plotted as a function of $\beta_\infty^{\frac{1}{2}}\tilde{z}$, consistent with (2.55). The Figure (b) shows the transition from the near-field Stokeslet decay (blue dashed line) to the far-field decay given by $-\frac{2160}{\tilde{z}^7}$ (the black dash-dotted line).

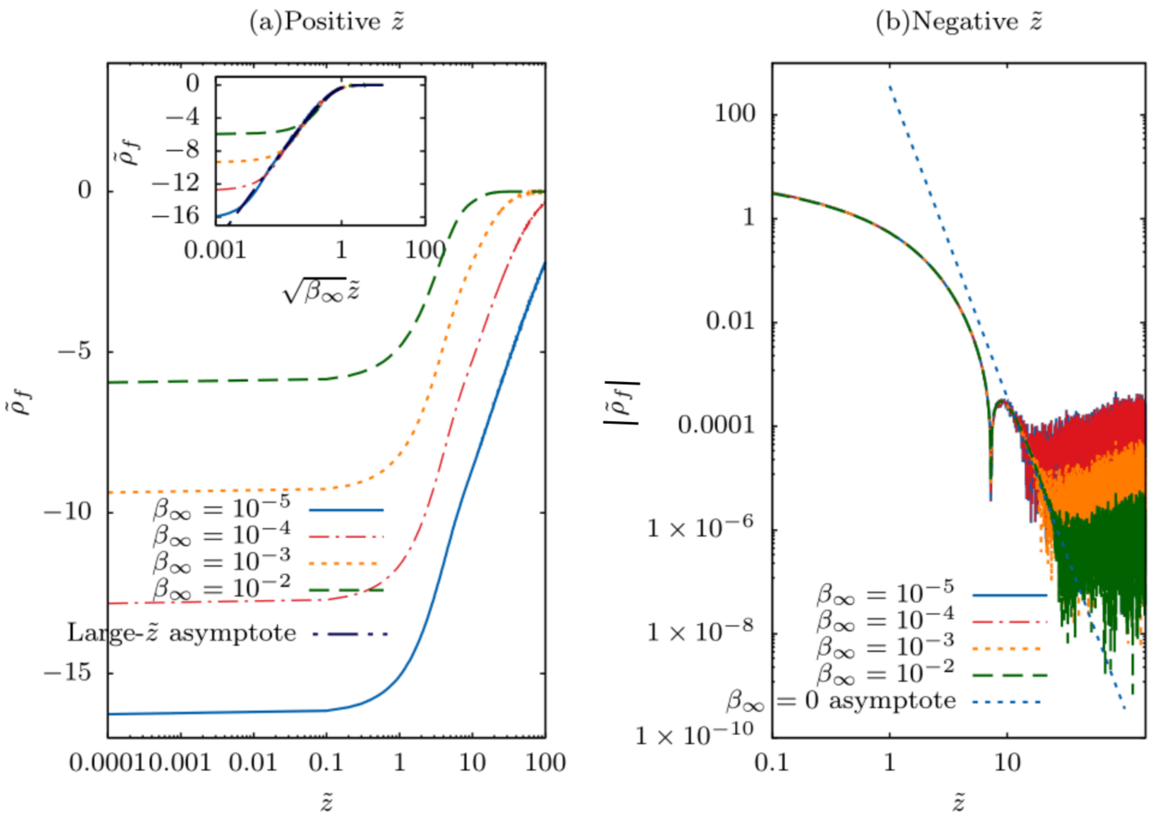

Fig. 2.9 The density disturbance field plotted along the stagnation streamline for both positive (Figure (a)) and negative $\tilde{z}$ (Figure (b)), and for different small β_∞. The inset plot in the Figure (a) shows the collapse of the density disturance profiles onto a common far-field asymptote, given by (2.56), when plotted as a function of $\beta_\infty^{\frac{1}{2}}\tilde{z}$. The Figure (b) shows that the small-β_∞ density profiles converging to a common limiting form given by $\frac{360}{\tilde{z}^6}$; although in agreement with the farfield asymptote, the numerical approximations (with $\tilde{N} = 1,50,000$) break down for large axial distances, with this breakdown being delayed the most for $\beta_\infty = 10^{-2}$.

Comparison of numerical profiles with the far-field approximations: Transition from the jet to the wake regimes

Having characterized the far-field approximations for the disturbance fields in both the buoyant jet and wake regions in (section 2.3.2) above, we now compare the exact results for the axial velocity, obtained from a numerical evaluation of (2.37), for $\beta_\infty = 10^{-5}$, with these approximations. The comparison is shown in Figures 2.10 and 2.11 for negative and positive $\tilde{\eta}$, respectively. Motivated by the self-similar one-dimensional integral approximation given by (2.48), both figures plot $\bar{r}_t^{\frac{14}{5}} |\tilde{u}_z|$ as a function of $\tilde{\eta}$. Only the wake-similarity profile (2.48) is relevant for negative $\tilde{\eta}$, and is shown alongside the exact numerical profiles in figure 2.10 for different $\bar{r}_t$, together with its large-η asymptotic form given by $2160/\tilde{\eta}^7$. The comparison here is similar to the diffusion dominant case, the agreement being poor for small to order unity $\bar{r}_t$, with the number of zero crossings also being in disagreement, but improving with increasing $\bar{r}_t$. There is good agreement for $\bar{r}_t = 6$, and almost a perfect match between the analytical and numerical profiles for $\bar{r}_t = 25$.

The comparison for positive $\tilde{\eta}$ is more elaborate since one now has both far-field wake and jet approximations in different regions of the half-space. One expects the axial velocity profile to transition from a jet-like profile to a wake-like one as one moves away from the rear stagnation streamline, that is, for a fixed $\tilde{z}$ and with increasing $\bar{r}_t$. This is seen in figure 2.11 where the numerically determined axial velocity profiles are shown for six different $\bar{r}_t$'s ranging from 0.05 to 25, together with the far-field wake and jet approximations developed in the earlier two subsections. For the smallest $\bar{r}_t$ $(= 0.05)$, the exact calculation matches the far field jet approximation for $\tilde{z}$ greater than about 10; for the chosen β_∞, this jet approximation is virtually identical (in magnitude) to a Stokeslet decay over the range of $\tilde{\eta}$ examined. For the aforementioned $\bar{r}_t$, similar to figure 2.8, the numerical profile has a zero-crossing at a smaller $\tilde{z} \approx 1.15$, and continues to diverge at smaller $\tilde{z}$, in accordance with the expected Stokeslet behavior in the inner region, with there being the beginning of a plateau at the smallest $\tilde{z}$'s. For $\bar{r}_t = 0.25$, the plateauing tendency for small $\tilde{z}$ is more readily evident, with there still being a good agreement with the jet approximation for large $\tilde{z}$. The plateauing behavior arises for any finite $\bar{r}_t$ since the disturbance velocity field is now finite in the plane $\tilde{z} = 0$; the continued divergence down to $\tilde{z} = 0$ only occurs along the rear stagnation streamline (see figure 2.8). For $\tilde{r}_t$ values greater than unity, the exact profile starts to agree better with with the wake approximation, and for $r_t = 25$ this agreement is near-perfect, with the jet approximation being virtually irrelevant. Analogous comparisons for the density disturbance profiles, for both negative and positive $\tilde{z}$, are shown in figures 2.12 and 2.12 respectively, even though numerical convergence issues arise for large $\tilde{r}_t$and $\tilde{z}$due to the slower decay of the associated density disturbance integral for large k. Importantly, a jet-to-wake like transition for the density disturbance for positive $\tilde{z}$ can nevertheless be seen with increasing $\tilde{r}_t$.

From figures 2.8 and 2.11, one sees that although the axial profile velocity exhibits only a single zero crossing along the rear stagnation streamline (corresponding to the Stokeslet-reverse-Stokeslet transition for $\beta_\infty = 0$), the jet-approximation for any non-zero $\tilde{r}_t$ (the expression (2.53)) appears to exhibit multiple zero crossings (likely, a denumerable infinity of them) as evident from the plots in the latter figure for $\tilde{r}_t = 6$ and $\tilde{r}_t = 25$. These zero-crossings suggest additional recirculating cells in the region $\tilde{z} \gg \tilde{r}_t$ for $\tilde{z}, \tilde{r}_t \gg 1$. In fact, with $\beta_\infty = 0$ and $\hat{k}_t = k_t/\tilde{z}^{\frac{1}{2}}$ as a rescaled wavenumber, (2.53) is easily shown to be of the form $\tilde{z}^{-1}F(\tilde{r}_t\tilde{z}^{\frac{1}{2}})$, with F having an oscillatory character, implying that the reverse Stokeslet identified above is only the central part of a far more elaborate axial flow structure behind the particle, one that exhibits multiple reversals as one proceeds outward from the rear stagnation streamline, with successive reversals separated by a distance that decreases as $\tilde{z}^{\frac{1}{2}}$. Note that this predominantly vertical flow structure is not in conflict with the finite number of zero-crossings predicted by the wake approximation, since the latter is restricted to the region $\tilde{z} \ll \tilde{r}_t$. Thus, although the self-similar profiles in the wake predict an eventual algebraic decay, this decay might not extend to indefinitely large distances. Instead, with increasing $\tilde{z}$, one will again have zero-crossings in the region $\tilde{z} \gg \tilde{r}_t$. As of now, however, this is difficult to verify, given the near-impossibility of accurate numerical evaluation at such large distances. Nevertheless, and although not evident from figures 2.6 and 2.7, the implication is that the flow-field in the convection-dominant limit exhibits an infinite number of recirculating cells (unlike the diffusion-dominant limit).

Finally, figures 2.14 and 2.15 show the streamline and iso-pycnal patterns, respectively, for β_∞ varying over the range $10^{-5} - 10$. The departure of both patterns from fore-aft symmetry, with decreasing β_∞, is evident, with the buoyant jet clearly evident in the streamline patterns for $\beta_\infty \leq 10^{-2}$. The spatial extent of all the streamline patterns shown corresponds to $|\tilde{z}|, \tilde{r} \leq 20$, with these intervals measured in units of $aRi_v^{-\frac{1}{3}}$. For $\beta_\infty = 10^{-5}$, this implies that the streamline pattern includes the first two zero crossings that appear in the large-$\tilde{r}_t$ axial velocity profile in figure 2.11, while including both the zero crossings that appear in the profiles in figure 2.10. Note that the length scale characterizing the pattern changes from $Ri_v^{-\frac{1}{3}}$ to $(Ri_vPe)^{-\frac{1}{4}}$ with increasing β_∞. In units of $aRi_v^{-\frac{1}{3}}$, this corresponds to the characteristic length scale increasing as $\beta_\infty^{\frac{1}{4}}$. Thus, for the same range in $\tilde{z}$ and $\tilde{r}_t$, one samples a proportionately smaller region of the streamline pattern with increasing β_∞. This reduction in the spatial extent is evident from a comparison of the streamline pattern for $\beta_\infty = 10$ to the one in figure 2.1. In figure 2.15, the iso-pycnals are seen to become heavily compressed and distorted for the smallest β_∞'s, in a manner consistent with the density disturbance approaching being

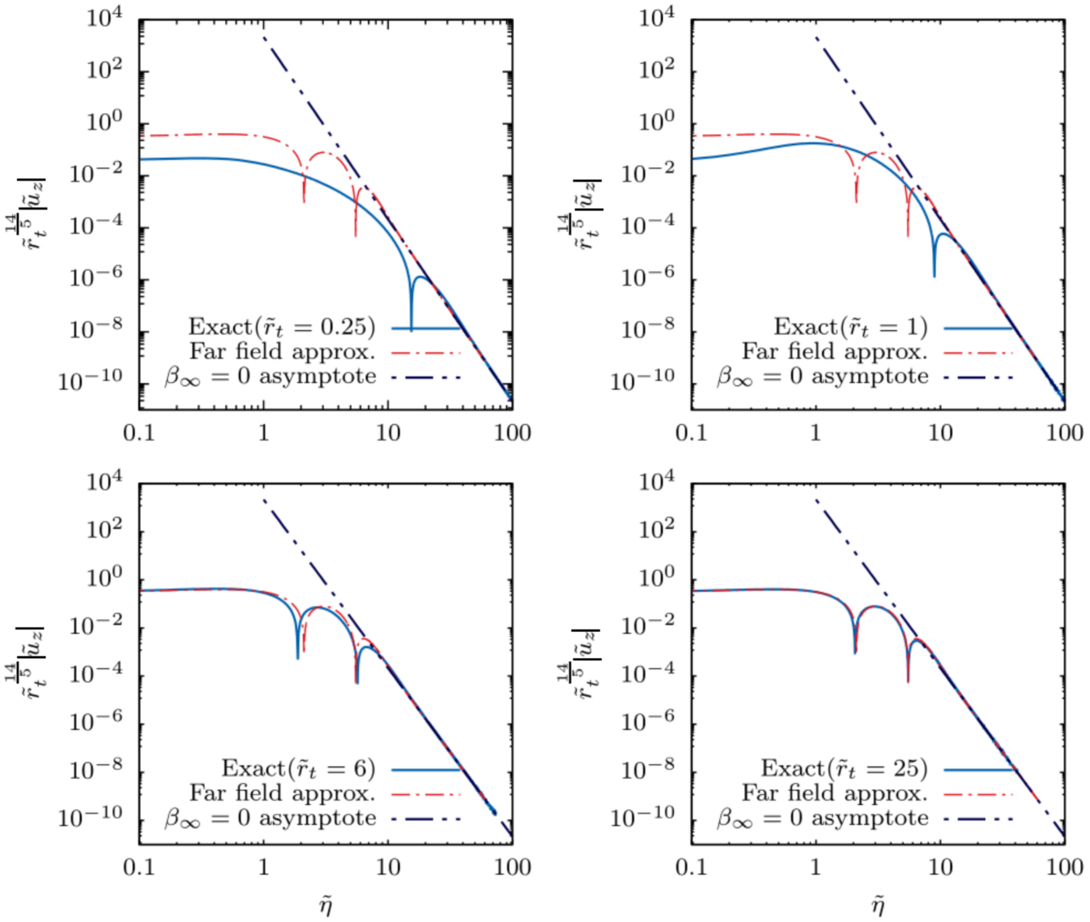

Fig. 2.10 The comparison, for negative $\tilde{z}$, between the numerically evaluated axial velocity profile, and the far-field wake-approximation given by (2.48), in the convection dominant limit, and in the Stokes stratification regime ($Re \ll Ri_v^{\frac{1}{3}}$); the exact profile is obtained from a numerical integration of (2.37) with $\beta_\infty = 10^{-5}$.

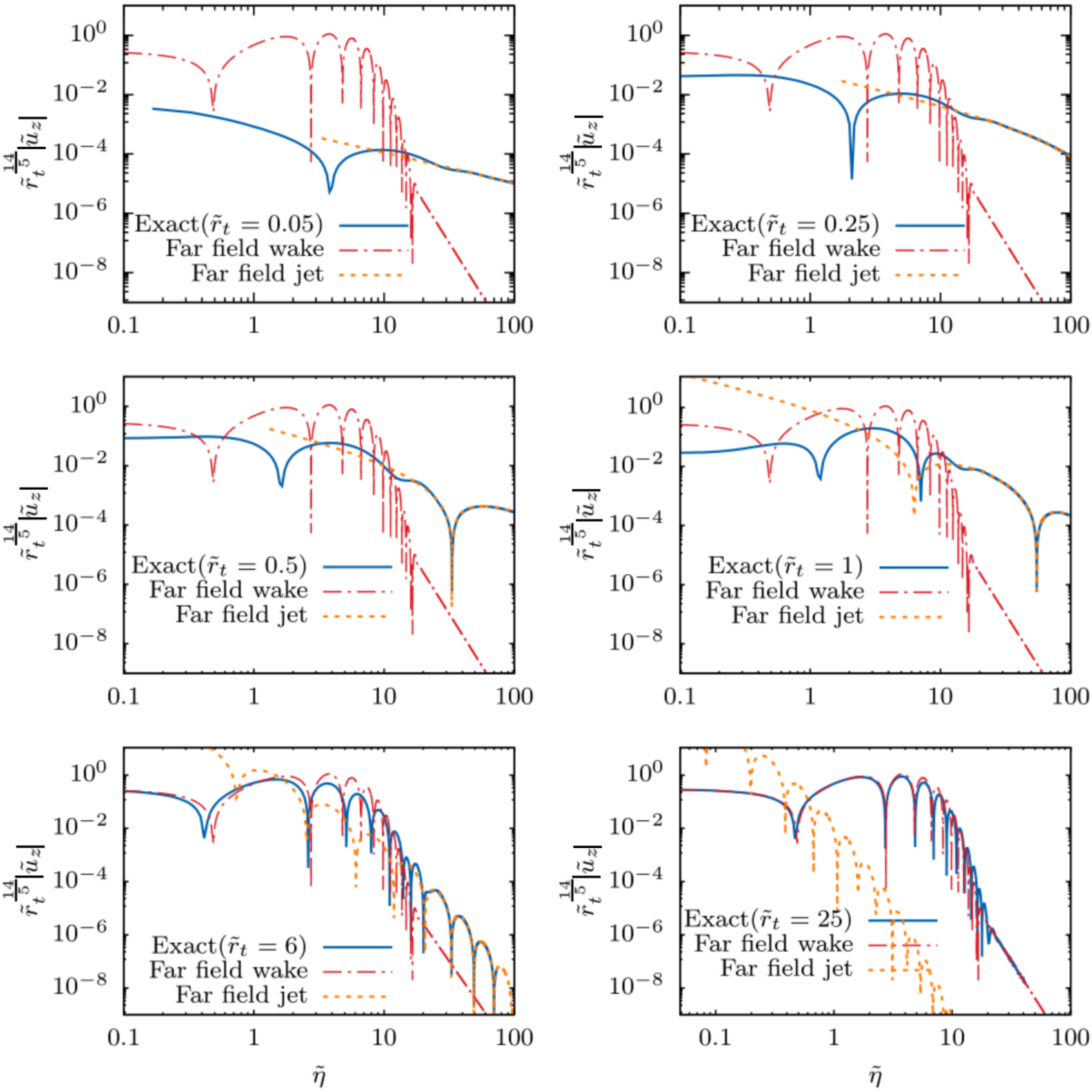

Fig. 2.11 The comparison, for positive $\tilde{z}$, between the numerically evaluated axial velocity profile, and both the far-field jet and wake-approximations given by (2.53) and (2.48), respectively. The profiles pertain to the convection dominant limit and the Stokes stratification regime ($Re \ll Ri_v^{\frac{1}{3}}$); the numerical profile is obtained from an integration with $\beta_\infty = 10^{-5}$.

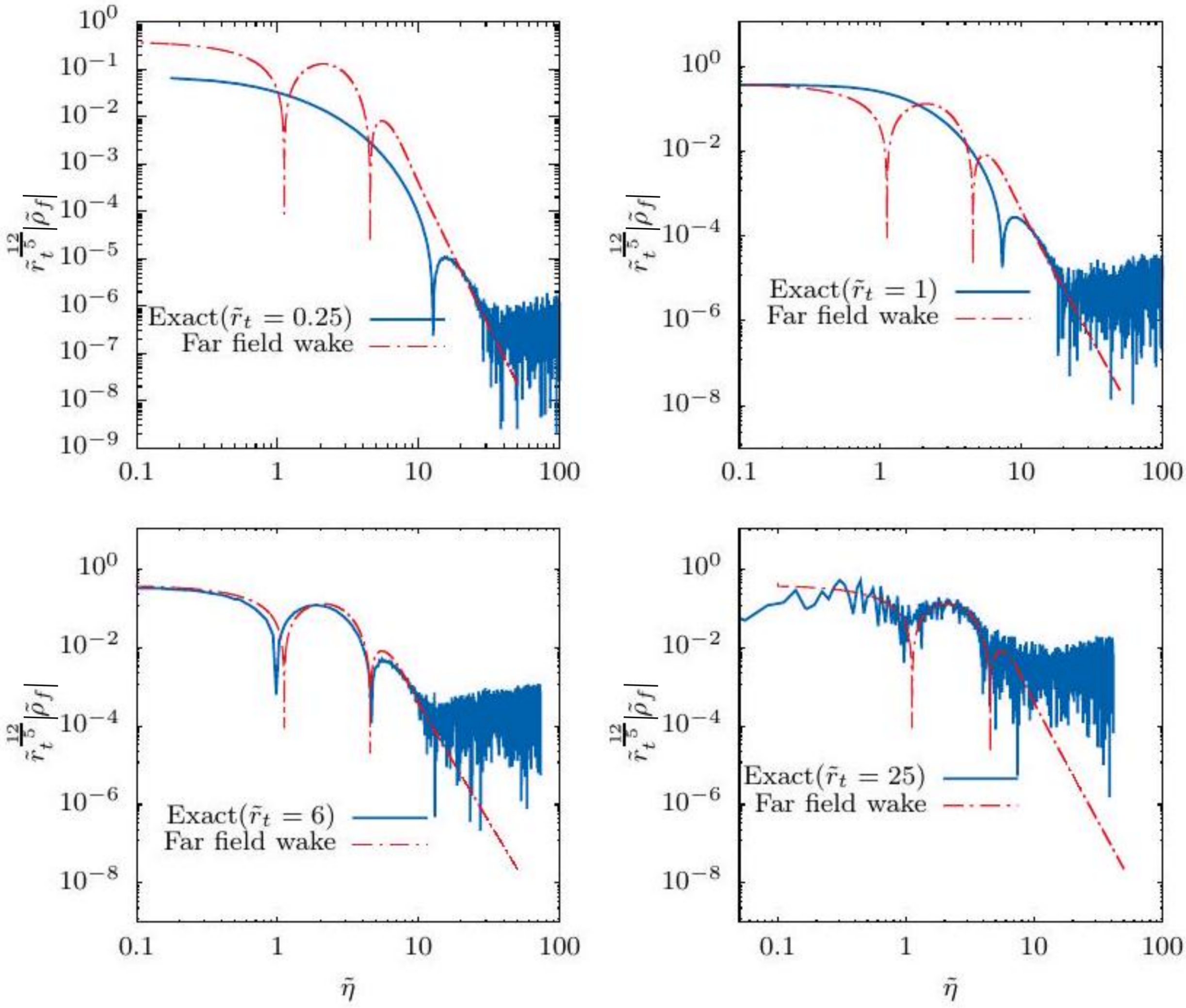

Fig. 2.12 The comparison, for negative $\tilde{z}$, between the numerically evaluated density disturbance profile, and the far-field wake-approximation given by (2.49), in the convection dominant limit, and in the Stokes stratification regime ($Re \ll Ri_v^{\frac{1}{3}}$); the exact profile is obtained from a numerical integration of (2.38) with $\beta_\infty = 10^{-5}$.

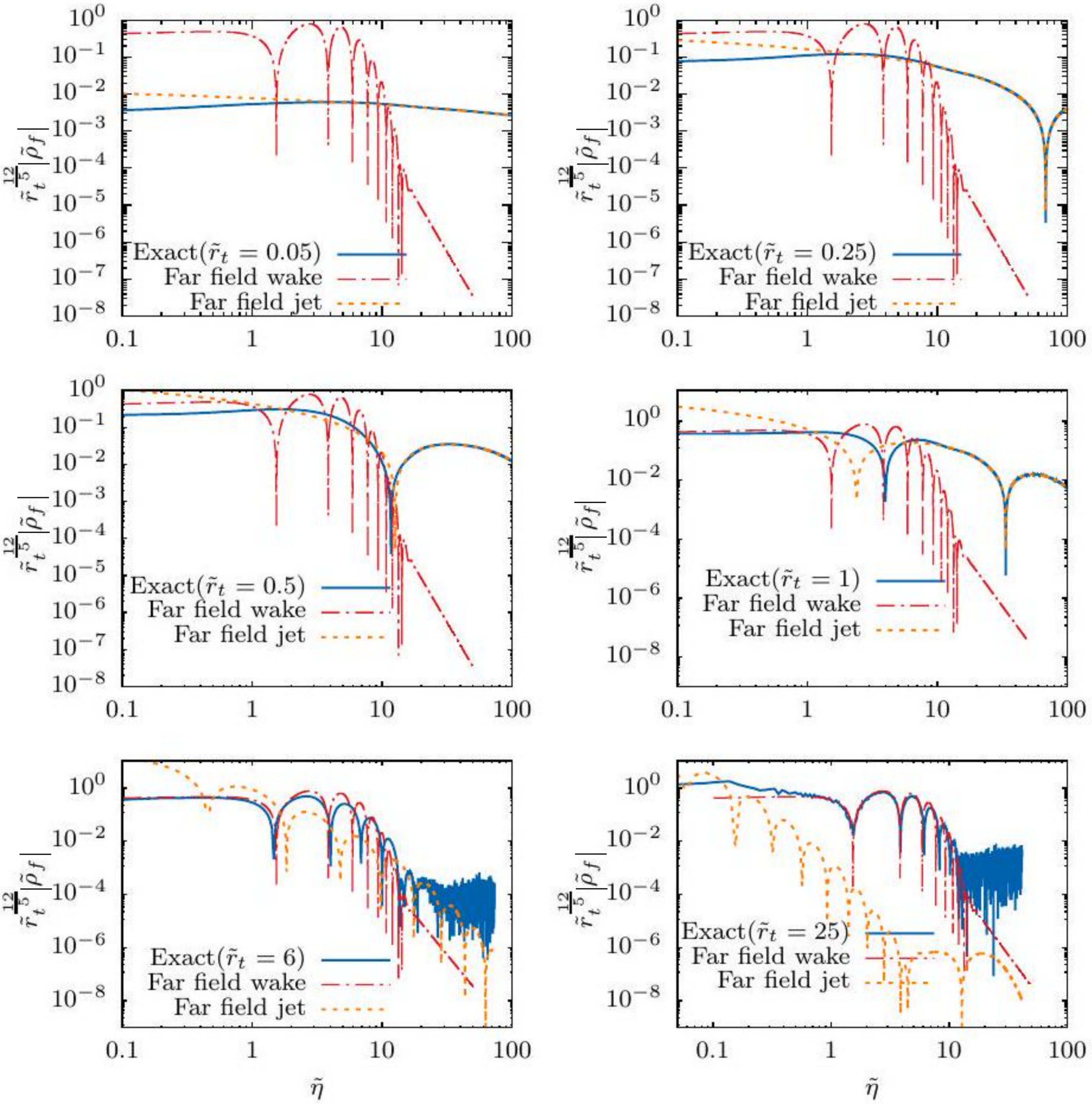

Fig. 2.13 The comparison, for positive $\tilde{z}$, between the numerically evaluated density disturbance profile, and both the far-field jet and wake-approximations given by (2.54) and (2.49), respectively. The profiles pertain to the convection dominant limit and the Stokes stratification regime ($Re \ll Ri_v^{\frac{1}{3}}$); the numerical profile is obtained from an integration with $\beta_\infty = 10^{-5}$.

infinitely large (and negative) along the rear stagnation streamline ($\tilde{r}_t = 0, \tilde{z} > 0$) and as a result, numerically resolving the iso-pycnal becomes very difficult; this difficulty is reflected in the range of accessible $\tilde{r}_t$ and $\tilde{z}$ in figure 2.15 progressively decreasing with decreasing β_∞ (this isn't an issue for the streamline patterns, given that the axial velocity remains finite along the rear stagnation streamline even for $\beta_\infty = 0$).

2.3.3 Effects of weak inertia or convection

In our calculations thus far, we have completely neglected the role of inertia. This is equivalent to assuming the inertial screening length (of $O(Re^{-1})$) to be much larger than the relevant stratification screening length, the latter being $(Ri_v Pe)^{-\frac{1}{4}}$ for $Pe \ll 1$ and $O(Ri_v^{-\frac{1}{3}})$ for $Pe \gg 1$, with this ordering of the screening lengths corresponding to the Stokes stratification regime. With regard to the calculations above, this is equivalent to setting $\alpha_0 = 0$ in (2.7) and $\alpha_\infty = 0$ in (2.16), for small and large Pe, respectively. While the detailed calculation of the flow field in the presence of competing effects of inertia and buoyancy is beyond the scope of the present work, the effect of weak inertia on the larger-scale structure of the velocity field may nevertheless be inferred via scaling arguments.

We begin with the diffusion-dominant case ($Pe \ll 1$) where, for small but finite α_0, the denominator of the Fourier integrals for the disturbance fields, obtained from Fourier transforming (2.6)-(2.8), takes the form $\alpha_0\beta_0 k_3^2 k^2 + \mathrm{i}k_3(\alpha_0+\beta_0)k^4 + k^6 + k_t^2$, with k here being scaled by $(Ri_v Pe)^{\frac{1}{4}}$. Note that the term proportional to $\beta_0 k_3 k^4$ denotes effects arising from the (weak) convection of the density disturbance field, and is typically associated with a screening length of $O(Pe^{-1})$ [Leal, 2007]; the fore-aft asymmetry in the far-field arising from this term alone was already seen in the streamline and iso-pycnal patterns corresponding to the largest β_∞'s in figures 2.14 and 2.15. Assuming buoyancy forces to first become important with increasing distance from the settling sphere, we now know from section 2.3.1 that the dominant motion is restricted to an axisymmetric wake on distances greater than $O(Ri_v Pe)^{-\frac{1}{4}}$, and is primarily horizontal. Thus, in order to examine inertia-induced transitions in the wake-scaling at larger distances, one may set $k_3 \gg k_t$, whence the aforementioned Fourier-space expression takes the form $\alpha_0\beta_0 k_3^4 + i(\alpha_0+\beta_0)k_3^5 + k_3^6 + k_t^2$. For $\alpha_0 = \beta_0 = 0$, one obtains the balance $k_3^6 \approx k_t^2$, and the vertical extent of the aforesaid wake growing as $z \propto (Ri_v Pe)^{-\frac{1}{6}} r_t^{\frac{1}{3}}$ (in units of a), as shown in section 2.3.1. For α_0, β_0 small but finite, the neglected terms invariably become important, and balance buoyancy forces (instead of viscosity) on larger lengthscales, corresponding to smaller k's. For $\alpha_0 \ll \beta_0$ (or $Re \ll Pe$), one obtains the balance $\beta_0 k_3^5 \approx k_t^2$ beyond a radial length scale of $O(Ri_v^{\frac{1}{2}} Pe^{-\frac{5}{2}})$; this balance is the same as that in section 2.3.2, and therefore, implies a wake that grows as $z \propto Ri_v^{-\frac{1}{5}} r_t^{\frac{2}{5}}$. Thus, even for

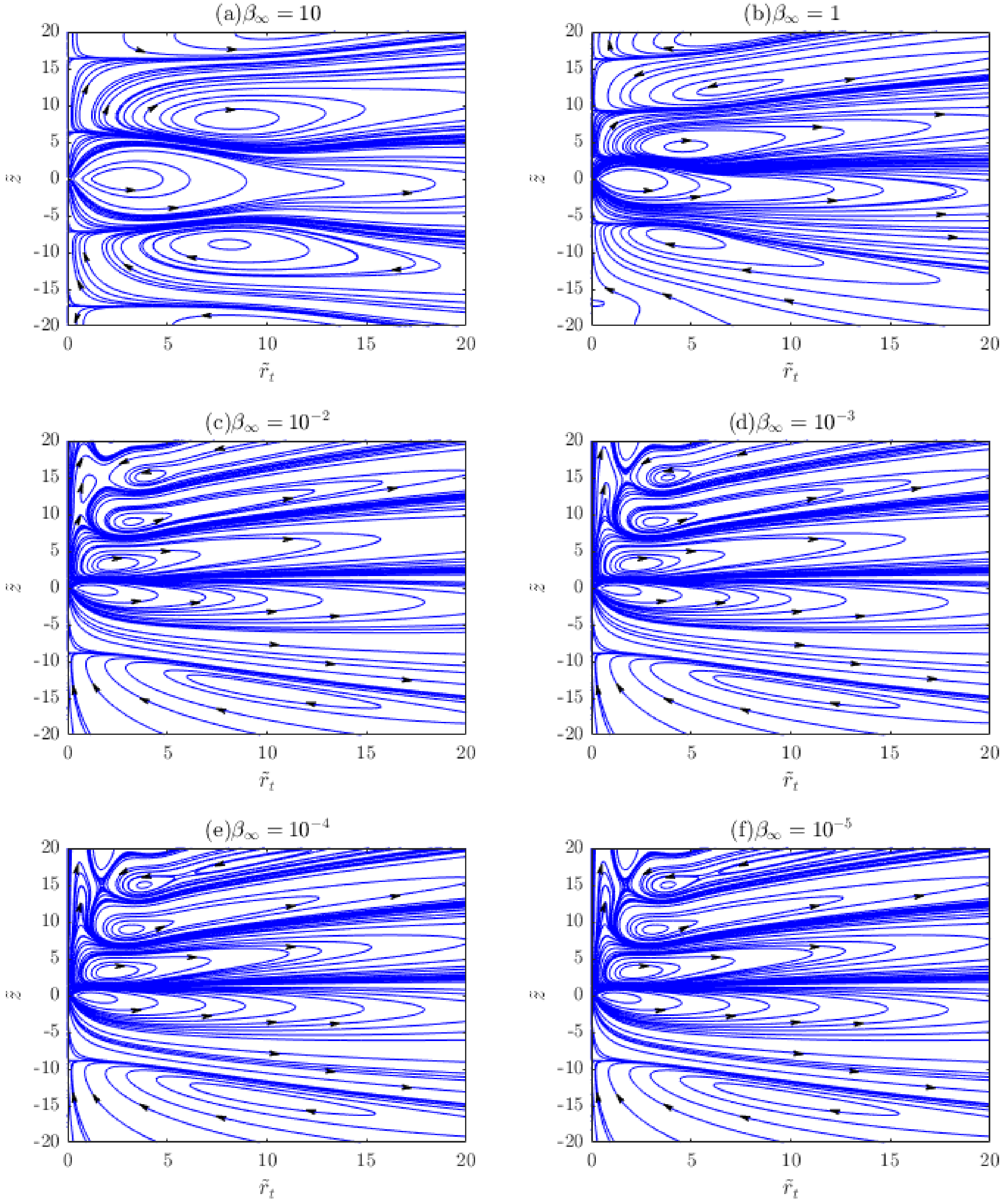

Fig. 2.14 Streamline patterns, pertaining to the Stokes-stratification regime (defined by the stratification screening length being the smallest of all relevant scales), for various β_∞. The first plot for $\beta_\infty = 10$ is in the diffusion-dominant limit and nearly fore-aft symmetric; the plot for $\beta_\infty = 10^{-5}$ shows the buoyant reverse jet in the rear.

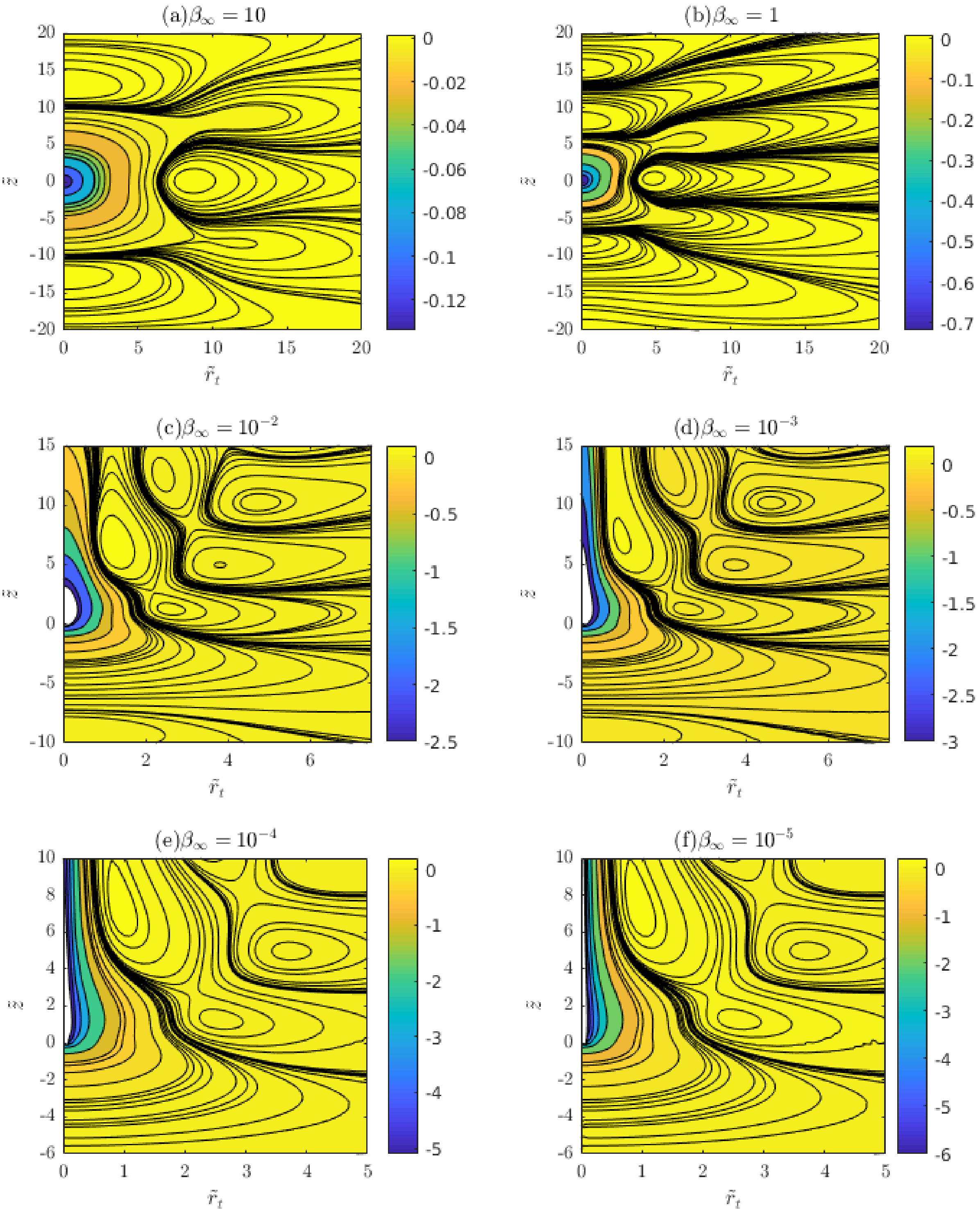

Fig. 2.15 Isopycnals pertaining to the Stokes-stratification regime for various β_∞. The first plot for $\beta_\infty = 10$ is in the diffusion-dominant limit and nearly fore-aft symmetric; the plots for the smallest β_∞'s are suggestive of a developing singularity along the rear stagnation streamline.

$Pe \ll 1$, one obtains the large-Pe wake-scaling derived in section 2.3.2, but only beyond the aforementioned secondary screening length. Note, however, that there is no buoyant jet on these scales, implying that the jet structure seen in Figure 2.14(c) does not 'come in' from infinity with decreasing β_∞. Finally, on the largest scales, the leading order balance is between inertial and buoyancy forces, and takes the form $\alpha_0\beta_0 k_3^4 \approx k_t^2$, leading to a wake that grows as $z \propto Re^{\frac{1}{4}} Ri_v^{-\frac{1}{4}} r_t^{\frac{1}{2}}$ beyond a radial scale of $Re^{-\frac{5}{2}} Ri_v^{\frac{1}{2}}$ that may be termed a tertiary screening length, again for $Re \ll Pe$. Thus, in the diffusion-dominant limit, weak convection (small but finite Pe) and inertia effects (small but finite Re) alter the far-field wake-scaling, causing it grow progressively faster beyond the screening lengths obtained above. Although the difference in the growth exponents is marginal ($1/3 \rightarrow 2/5 \rightarrow 1/2$), one expects a more significant alteration of the wake structure; the change in structure accompanying the first transition in growth exponent ($1/3 \rightarrow 2/5$) involves a departure from fore-aft symmetry, and the details may already be inferred from sections 2.3.1 and 2.3.2. Provided the stratification screening length, $(Ri_v Pe)^{-\frac{1}{4}}$, remains the smallest of the three possible primary screening lengths viz. $(Ri_v Pe)^{-\frac{1}{4}}$, Re^{-1} and Pe^{-1}, an assumption that defines the Stokes stratification regime for small Pe, the screening lengths derived above remain well ordered under the assumption $Re \ll Pe$. If we allow for convection and inertial effects to be small but of comparable importance ($Re \sim Pe$), so that $\alpha_0/\beta_0 \sim O(1)$, then the growth exponents found above remain the same, but the secondary and tertiary screening lengths are now given by $max(Re,Pe)^{-3}(Ri_v Pe)^{\frac{1}{2}}$ and $min(Re,Pe)^{-5/2} max(Re,Pe)^{-\frac{1}{2}}(Ri_v Pe)^{\frac{1}{2}}$. A schematic of the different wake-scaling regimes in the diffusion-dominant limit is given in figure 2.16; fluid motion outside the wake remains negligibly small.

The effects of inertia in the convection dominant limit, corresponding to $Pe \gg 1$, is based on the same expression as that in the preceding paragraph, except that k is now scaled with $Ri_v^{\frac{1}{3}}$, and accordingly, one has the form $-\alpha_\infty k_3^2 k^2 + i\alpha_\infty \beta_\infty k_3 k^4 + \mathrm{i} k_3 k^4 + \beta_\infty k^6 + k_t^2$. Outside of the buoyant jet, one may neglect $\beta_\infty k^6$ and use $k_3 \gg k_t$ implying the dominance of horizontal motion. Setting $\alpha_\infty = \beta_\infty = 0$ then leads to the balance $k_3^5 \approx k_t^2$ which, as already seen in section 2.3.2, and again in the analysis of the diffusion-dominant case above, yields the wake scaling $z \approx Ri_v^{-\frac{1}{5}} r_t^{\frac{2}{5}}$. At length scales larger than a radial threshold of $O(Re^{-\frac{5}{2}} Ri_v^{\frac{1}{2}})$, the balance is between inertial and buoyancy forces, leading to the same square-root scaling $z \propto r_t^{\frac{1}{2}}$ seen above. Thus, the difference with regard to the wake-scalings, in relation to the diffusion-dominant limit analyzed above, is that the initial scaling regime $z \propto r_t^{\frac{1}{3}}$ is now absent, and one directly transitions to the $z \propto r_t^{\frac{2}{5}}$ scaling regime at distances much greater than the stratification screening length of $O(Ri_v^{-\frac{1}{3}})$. As already mentioned in section 2.3.2, a novel feature in the large-Pe regime is the emergence of a buoyant jet that is smeared out by

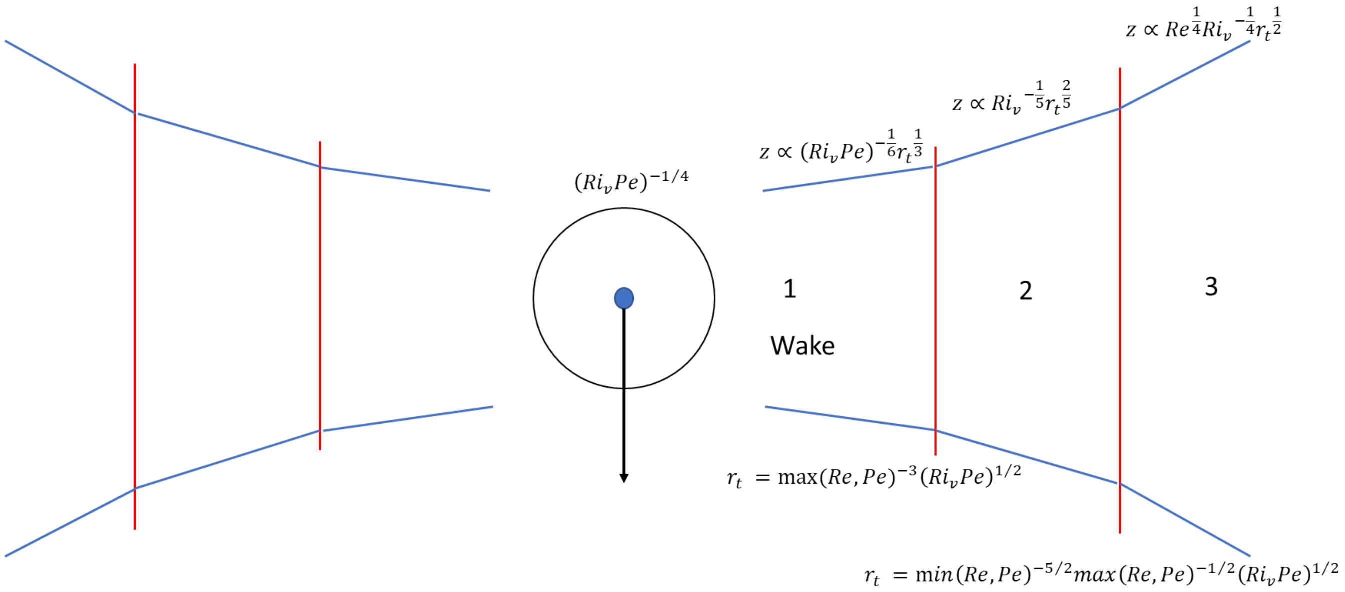

Fig. 2.16 Schematic of the different wake-growth regimes in the diffusion-dominant limit ($Pe \ll 1$).

diffusion beyond a length scale of $O(Ri_v^{-\frac{1}{2}} Pe^{\frac{1}{2}})$. The diffusion-screening length for the jet is asymptotically smaller than the secondary screening length, of $O(Re^{-\frac{5}{2}} Ri_v^{\frac{1}{2}})$ above, provided $Re \ll Ri_v^{\frac{2}{5}} Pe^{-\frac{1}{5}}$. A schematic of the various scaling regimes, in the convection-dominant limit, is given in figure 2.17.

While the discussion in this chapter has been restricted to the Stokes stratification regime, we briefly mention the screening lengths relevant to the inertia-stratification regime that, for large Pe, is defined by $Ri_v^{\frac{1}{3}} \ll Re$, or $\alpha_\infty \gg 1$; the inertial screening length of $O(Re^{-1})$ is now the primary screening length. For $Re \ll 1$, the fore-aft symmetric flow field in the inner Stokesian region first transitions, on scales of $O(Re^{-1})$, to a far-field structure consisting of an $O(1/r^2)$ source flow everywhere except for a viscous wake behind the translating sphere that acts as a directed sink [Batchelor, 1967; Subramanian, 2010]. In terms of the Fourier-space expression given in the preceding paragraph, the viscous wake corresponds to the balance $\mathrm{i}k_3 k^4 \sim \alpha_\infty k_3^2 k^2$, leading to the familiar scaling $r_t \sim (z/Re)^{\frac{1}{2}}$ for the wake growth in physical space. This source-wake structure is expected to be modified by buoyancy forces when k_t^2 becomes comparable to the terms in the aforementioned balance. This happens for $k \sim O(\alpha_\infty^{-\frac{1}{2}})$, which gives a secondary screening length of $O(Re^{\frac{1}{2}} Ri_v^{-\frac{1}{2}})$ in the inertia-stratification regime [Zhang et al., 2019]. The structure of the flow field on these length scales is currently under investigation.

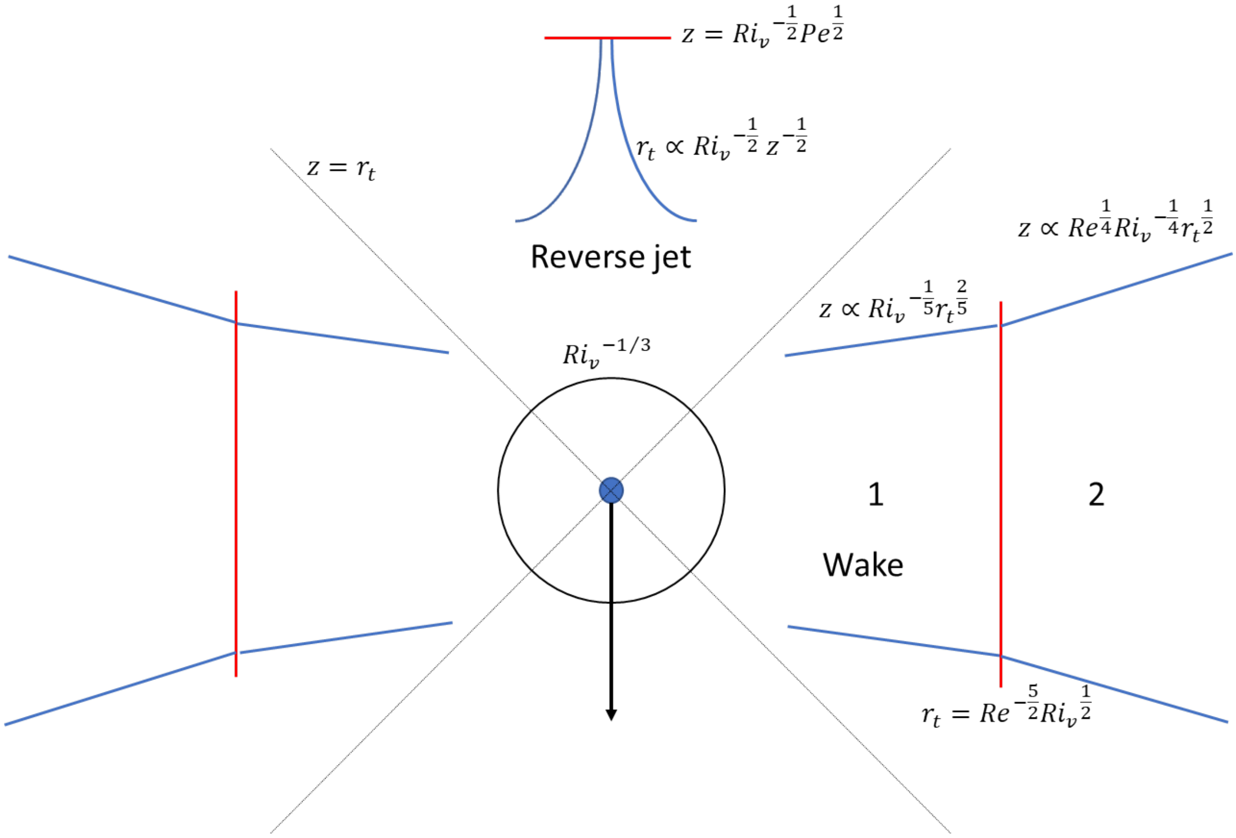

Fig. 2.17 Schematic of various regions in the convection dominant limit for non-zero Reynolds and Péclet numbers in the Stokes-stratification regime

2.4 Conclusions

2.4.1 Summary of main results

We have analyzed in detail both the disturbance velocity and density fields induced by a sphere translating in a linearly stratified ambient fluid otherwise at rest. The analysis pertains to the Stokes stratification regime when buoyancy forces are dominant over inertial ones, so the transition from the well known Stokesian behavior, in the inner region, first occurs across a screening length determined by a balance between viscous and buoyancy forces. While we analyze the fluid motion in the diffusion-dominant limit (section 2.3.1), this scenario has also been the focus of earlier work [Ardekani and Stocker, 2010; List, 1971], and our main focus is therefore on the convection dominant limit ($Pe \gg 1$) when the screening length is $Ri_v^{-\frac{1}{3}}$. In the latter limit, and within the Stokes stratification regime defined by $Re \ll Ri_v^{\frac{1}{3}} \ll 1$, we show through both computations (section 2.3.2) and asymptotic analysis (section 2.3.2), that the far-field fluid motion consists of an axisymmetric wake surrounding the sphere whose vertical extent grows as $z \propto Ri_v^{-\frac{1}{5}} r_t^{\frac{2}{5}}$, and wherein the fluid motion is predominantly horizontal; an analog of this wake also exists in the diffuson dominant limit, in which case it grows as $z \propto (Ri_v Pe)^{-\frac{1}{6}} r_t^{\frac{1}{3}}$; z and r_t here being scaled by a. Although not obvious from the figures in earlier sections,the amplitude of fluid motion at a given non-dimensional distance (measured in units of the relevant screening length) is significantly greater for $Pe \gg 1$. In sharp contrast to the diffusion dominant limit, we have shown (section 2.3.2) that there also exists a buoyant reverse jet in the vicinity of the rear stagnation streamline for $Pe \gg 1$. Unlike the usual laminar or turbulent jets which broaden with increasing distance downstream on account of the momentum flux being conserved, the buoyant jet region above narrows down with increasing distance downstream as $r_t \propto Ri_v^{-\frac{1}{6}} z^{-\frac{1}{2}}$, with a velocity field that, although oppositely directed, decays in the same manner as a Stokeslet for $Pe = \infty$; the jet is screened by diffusion beyond a length scale of $O(Ri_v^{-\frac{1}{2}} Pe^{\frac{1}{2}})$ for large but finite Pe. The recent effort of Shaik and Ardekani [2020b] has investigated the flow pattern due to a particle settling in the aforementioned 'convection dominant' limit, based on a numerical fast Fourier transform technique. Although the primary emphasis was on calculating the drift volume, their examination of the fluid motion shows the existence of a strong reverse flow along the rear stagnation streamline, consistent with our findings. Finally, in section 2.3.3, we comment briefly on the role of weak inertial (and convection) effects on the structure of the fluid motion beyond the primary buoyancy-induced screening length.

The fore-aft asymmetry of the large-Pe disturbance velocity field found here has implications for pair-interactions. A vertically oriented particle-pair will experience a repulsive interaction for sufficiently large separations (on scales of $O(Ri_v^{-\frac{1}{3}})$). This is in contrast to the Stokesian scenario where the particle-pair separation remains invariant with time, as may be established using reversibility arguments; note that the fore-aft symmetry of the $Pe = 0$ velocity field, obtained in section 2.3.1, implies that the particle-pair separation, in a stratified fluid, is conserved to leading order in the diffusion dominant limit. For $Pe \gg 1$, the aforementioned repulsive pair-interaction is initially controlled by the greater magnitude of the velocity field along the front stagnation streamline, this because the zero-crossing along the front stagnation streamline ($\approx 8.85Ri_v^{-\frac{1}{3}}$) occurs at a greater distance than that on the rear stagnation streamline ($\approx 1.15Ri_v^{-\frac{1}{3}}$). However, for distances a little beyond approximately $2Ri_v^{-\frac{1}{3}}$, the more rapid $O(1/z^7)$ decay of the disturbance velocity in front of the particle implies that the repulsion is controlled by the slowly decaying $O(1/z)$ disturbance along the rear stagnation streamline. Succinctly put, the rear particle pushes the one in front for smaller separations, while the opposite is true at larger separations. The range of repulsion is limited to a length scale of $O(Ri_v^{-\frac{1}{2}} Pe^{\frac{1}{2}})$ by the effects of diffusion. The above repulsive interaction is also in contrast to the homogeneous inertial case (Re finite, $Ri_v = 0$), where the well-known drafting-kissing-tumbling scenario prevails, implying that a vertically oriented particle-pair experiences an initial attraction [Joseph et al., 1994]. For a horizontally oriented particle-pair in the large Pe limit, the inward radial velocities (not shown) imply an attractive interaction, again in contrast to the respulsion in the homogeneous inertial case (that leads to a self-similar expansion of sedimenting clusters; see Daniel et al. [2009]; Subramanian and Koch [2008]), but consistent with the recent work of Doostmohammadi and Ardekani [2013] for a stratified medium, although the pair separations in this latter study were of $O(a)$. It is worth adding that the more complicated structure of the large-Pe velocity field (see Figure 2.14) implies that, unlike the homogeneous case, considering horizontal and vertically-aligned particle-pairs alone does not really encompass the spectrum of pair-interactions possible for other orientations.

2.4.2 Discussion: the inner-region scaling estimates

It was indicated in the introduction as to how the validity of a linearized approximation is not obvious at large Pe, given that the ambient iso-pycnals in the inner region are severely distorted by the sphere velocity field. An examination of the density disturbance in the inner region for large Pe should help identify possible restrictions on the results obtained in this chapter, and a few comments in this regard are in order. We begin with the simpler case of small Pe when the density perturbation around the sphere, on length scales of $O(a)$ (the inner region), quickly approaches a finite quasi-steady state for all subsequent times. The no-flux condition on the sphere surface causes the ambient iso-pycnals to tilt, so as to meet the sphere in a normal orientation. This tilting effect is significant in a region of $O(a^3)$, implying that the density perturbation associated with the aforementioned quasi-steady state is $O(\gamma a)$. The resulting baroclinically induced vorticity drives a flow of $O(\gamma a^3 g/\mu)$, or $O(Ri_v)$ in non-dimensional terms (scaled by U; see Varanasi et al. [2021]). For $Ri_v \ll 1$, this weak flow may evidently be neglected compared to the primary Stokesian field. On larger length scales, convection of the base-state stratification by the perturbation Stokeslet field leads to a density perturbation that grows as $O(Pe\,r)$ in the inner region. The buoyancy forcing due to this density perturbation becomes comparable to viscous forces on length scales of $O(Ri_v Pe)^{-\frac{1}{4}}$, the small-*Pe* stratification screening length screening length identified first by List [1971] and Ardekani and Stocker [2010]. Importantly, for small *Pe* and Ri_v, the Stokesian flow remains a valid leading order approximation in the inner region for all times.

For large *Pe*, the density perturbation in the inner region can become much larger than the nominal $O(\gamma a)$ estimate above. This may be seen by considering the limiting case of $Pe = \infty$, when the iso-pycnals are affinely convected by the sphere velocity field, there being no steady state. The sphere, as it settles through the stably stratified medium, continuously entrains positively buoyant fluid in a quasi-spherical annular region that extends behind it in a narrow wake that lengthens with time. The amplitude of the density perturbation near the sphere increases linearly with time as $O(\gamma U t)$, leading to a buoyancy forcing per unit volume of $O(\gamma U t g)$. Clearly, for large enough times, this buoyancy forcing will become comparable to the viscous terms even in the inner region, and for $Ri_v \ll 1$. Since the viscous terms in the equations of motion are $O(\frac{\mu U}{a^2})$ in the inner region, the threshold time at which buoyancy forces are of a comparable magnitude is $O(\frac{\mu}{\gamma a^2 g})$, or $O(\frac{a}{U} Ri_v^{-1})$. This is therefore the time at which the flow in the inner region must deviate from the leading Stokesian approximation on account of buoyancy forces; as mentioned in the introduction, it is still possible for the structure of the fluid motion to remain similar to that detailed in this chapter, but for a buoyancy-induced renormalization of the force exerted by the particle, although only a detailed examination of the inner region would confirm this. Moving to the outer region, in the Stokes stratification regime, the time scale associated with the development of the flow field in this region may be estimated as the time required for momemtum to diffuse to a distance of $O(a Ri_v^{-1/3})$, which is $O(\frac{a^2}{\nu} Ri_v^{-2/3})$. The ratio of this latter time to the time scale estimated above, for the inner region to depart from a homogeneous Stokesian evolution, is $O(Re Ri_v^{1/3})$, and therefore, asymptotically small for $Re, Ri_v \ll 1$. Thus, there is an asymptotically long interval of time corresponding to $\frac{a^2}{\nu} Ri_v^{-2/3} \ll t \ll \frac{a}{U} Ri_v^{-1}$, where one has a quasi-steady response in the outer region, with the motion in the inner region still governed by the Stokes equations at leading order. The findings with regard to the nature of the fluid motion, detailed in section 2.3.2, are certainly valid in this time period. Note that for any finite Pe, however large, the distortion of the isopycnals will not continue indefinitely. Instead, there will eventually be a steady state boundary layer, of thickness $O(aPe^{-\frac{1}{3}})$, as far as the density gradient is concerned (although not for the density itself which will continue to increase with time for an assumed constant U).

Scaling arguments similar to those in the preceding paragraph may also be used to assess the possibility of observing quasi-steady dynamics on scales beyond the primary screening length, and thereby, examine the relevance of the wake-scaling regimes sketched in section 2.3.3; see figures 2.16 and 2.17. Focusing on the Stokes stratification regime for large Pe, the arguments in section 2.3.3 pointed to a secondary screening length of $O(aRe^{-\frac{5}{2}}Ri_v^{\frac{1}{2}})$ across which the dominant balance shifted from one between buoyancy and viscous forces to one between buoyancy and inertial forces. Given that the inertial forces enter the dominant balance, the time scale for a quasi-steady wake to be established on the aforementioned secondary screening length may be estimated as $\frac{aRe^{-\frac{5}{2}}Ri_v^{\frac{1}{2}}}{U}$. The ratio of this time scale to $\frac{aRi_v^{-1}}{U}$ gives us $Re^{-\frac{5}{2}}Ri_v^{\frac{3}{2}}$, with this ratio needing to be much less than unity in order for a quasi-steady analysis of the fluid motion to hold; this yields $Re \gg Ri_v^{\frac{3}{5}}$. Combining this with the primary criterion for the large-Pe Stokes stratification regime gives $Ri_v^{\frac{3}{5}} \ll Re \ll Ri_v^{\frac{1}{3}}$ for the dynamics in both the primary and secondary outer regions to be quasi-steady, in the time that the inner region region has a Stokesian character.

Chapter 3

Fluid drift due to a settling sphere in a stratified fluid

In the last chapter, we have examined the translation of a sphere in a stably stratified ambient in the limit of small Reynolds ($Re \ll 1$) and viscous Richardson numbers ($Ri_v \ll 1$) and characterized in detail the velocity and density fields around the particle in both the diffusion dominant (small Pe) and convection dominant (large Pe) limits. For large Pe, the characterization pertains to what we termed the Stokes stratification regime, defined by $Re \ll Ri_v^{\frac{1}{3}} \ll 1$, and corresponding to the dominance of buoyancy over inertial forces (both nevertheless being small in comparison to viscous forces). In this chapter, by using this velocity field in the convection dominant limit (large Pe), we obtain the associated fluid pathlines, drift displacements and drift volume for different viscous Richardson(Ri_v) and Peclet(Pe) numbers. In the next two sections, we briefly introduce the previous literature on fluid drift in a homogeneous ambient, its relevance to the drift in a density-stratified environment, and then present scaling estimates for the drift volume in a viscous density-stratified fluid. Next, we formulate the framework for the actual calculation of the fluid pathlines, the drift displacements, and the corresponding drift volume.

3.1 Introduction

The idea of drift in fluids and pathlines goes back to the study of Maxwell [1869]. In an Eulerian description of the fluid, one is concerned about the flow field in space at a fixed point as time progresses. Maxwell [1869] realized that one could draw important observations by looking instead at the velocities of individual fluid elements and the paths traced by these fluid elements. This pertains to the Lagrangian description in fluid mechanics. Specifically, Maxwell studied the problem of a two-dimensional cylinder (a potential dipole in two dimensions) translating through an ideal fluid, and numerically calculated the trajectories traced by the individual fluid elements as they are convected by the disturbance velocity field [see also Rankine [1864]]. Much later, Darwin [1953], apparently unaware of Maxwell's work, found closed-form solutions for the fluid element trajectories, for the above problem, in terms of elliptic functions. He also noted that an analogous closed-form solution is not possible for the case of a sphere moving through an ideal fluid (a potential dipole in three dimensions) due to the existence of hyper-elliptic integrals [see also Lighthill [1956]]. Thus, one must resort to a numerical evaluation of the pathlines for this latter case.

Darwin [1953], in his work, also introduced the concept of drift volume, now known as 'Darwin' drift Eames et al. [2003]; Eames and McIntyre [1999]; Pushkin et al. [2013]; Yih [1997]; this is in contrast to 'Stokes' drift of fluid elements that arises in the context of irrotational water waves Craik [2005]; Stokes [1847]. Darwin's definition of the drift volume is as follows. He considers a solid body moving through an ideal fluid from far upstream (say, $x = -\infty$) of an unbounded plane of fluid elements (given by $x = 0$), oriented perpendicular to the translation direction. As this solid body moves far downstream ($x = \infty$), the plane of fluid elements under consideration gets deformed. The volume contained between the initial and final (deformed) material planes is defined as the drift volume. Darwin [1953] showed that this drift volume is given in terms of a conditionally convergent integral; the conditional convergence arises from, in effect, integrating the disturbance velocity field that decays as $O(1/r^D)$ over volume that increases as r^D, r being the distance from the translating particle, and D being the embedding dimension. One gets the answer to be half the volume of a body for the case of a translating sphere in a volume whose horizontal extent is much larger than the vertical extent; this being equivalent to choosing the particular order of integration where the integration over the coordinate aligned with the translation is carried out first, so as to evaluate the drift displacements [see also Benjamin [1986]; Yih [1985]], before integrating over the plane of upstream offsets. For the order of integration above, Darwin showed that the volume of displaced fluid, for a general body, equals half the added mass divided by the fluid density. Recently, Yih [1995] has shown that the integral for the drift volume becomes absolutely convergent on including a weak compressibility, and the answer obtained is the same as that originally found by Darwin. For the case of incompressible ideal fluid, Eames and coworkers Eames et al. [1994] generalized the concept of drift volume to define the partial drift volume, and examined Lagrangian reflux and drift in a detailed manner. A similar study of the drift displacements and drift volume for the case of a droplet moving in a viscous fluid in the Stokes regime has also been carried out by Eames and coworkers Eames et al. [2003]; the concept of the partial drift volume developed in the earlier

Eames effort above is crucial to the Stokesian regime, since the total drift volume, as defined by Darwin, is divergent in the Stokes limit. Indeed, Eames and coworkers found both the drift displacements and the drift volume to be divergent quantities due to the slow $O(1/r)$ decay of the velocity field; note that the potential flow field used by Darwin in his original calculation decays as $O(1/r^3)$ allowing for a finite drift volume. For the case of small but finite inertia (non-zero Reynolds number), one would still have a divergent drift volume due to the presence of the viscous wake behind the translating particle where the velocity field still decays as $O(1/r)$, as is the case for entire velocity field in the Stokes limit Subramanian [2010]; the drift volume diverges logarithmically for large times. More recently, closed-form asymptotic expressions have been found for the partial drift volume, for both the passive and active particles moving in an unbounded homogeneous fluid domain,with the use of a flux interepretation by Chisholm and Khair [2017, 2018].

The concept of fluid drift has also been used and interpreted in a variety of other scenarios. For instance, Eames and McIntyre [1999] have established connections between the Darwin drift and the so-called Stokes drift exhibited by fluid elements due to the progression of small amplitude irrotational water waves. The idea of drift has been used in multiphase and multibody problems Eames [2003], mixing in gas-fluidized beds Eames and Gilbertson [2005], fluid transport due to vortex motion Dabiri [2006]; Eames and Flor [1998], and protein transport in membranes Prasad et al. [2007]. However, as mentioned in Chapter 1, the idea of drift has most recently been invoked in the context of biogenic mixing of oceans Katija and Dabiri [2009] to understand the possible missing energy contributions to the meridional overturning circulation Munk and Wunsch [1998]; Munk [1966]. It is in this context that we intend to calculate the drift volume for a passive particle settling in a density stratified fluid in the present chapter.

This chapter is divided into different sections. In section 3.2, scaling estimates for the drift volume in a density stratified fluid are provided for both the Stokes-stratification ($Re \ll Ri_v^{1/3}$;$\alpha \ll 1$) and Inertia-stratification ($Re \gg Ri_v^{1/3}$; $\alpha_\infty \gg 1$) regimes. The methodology and details of exact calculation of the pathlines, drift displacements and drift volume, which pertain to the Stokes stratification regime, are given in section 3.3. The results of the numerical calculations are discussed in section 3.4, along with the drift volume scalings obtained from the numerical evaluation. Through rigorous calculations, we show, for first time, that the drift volume in a density stratified fluid in the convection-dominant limit is convergent (and is of $O(Ri_v^{-1/3})$), and is of reflux in nature. The drift displacement plots in our results clearly point to this convergence as will be seen in this section. Finally, in section 3.5, revised estimates for drift volume are proposed along with the summary of the main results of the current chapter. We also discuss the relevance of the current studies on drift volume to the oceanic mixing towards the end.

3.2 Estimates for drift volume scalings in a density stratified fluid

In this section, we estimate the drift volume for a sphere settling in a viscous density-stratified fluid whose calculation, as mentioned in the introduction of the Chapter 1, was one of the motivations of this thesis. The rapid algebraic decay of the far-field velocity disturbance (as shown in Chpater 2), induced by buoyancy forces, implies that the drift volume ($\mathscr{D}$) will be finite in presence of an ambient stratification, as originally argued by Subramanian [2010]. Estimates for $\mathscr{D}$ as a function of Ri_v and Re, in the Stokes and inertia-stratification regimes, are obtained below.

For the homogeneous Stokesian scenario, the $O(1/r)$ decay of the disturbance field implies a divergent drift volume for any finite time. As originally shown by Eames et al. [2003], it therefore becomes necessary to define a partial drift volume ($\mathscr{D}_p$) where, in contrast to Darwin [1953], one only considers an initial material plane of a finite spatial extent. The partial drift volume for the case of a sphere moving in an unbounded viscous fluid is defined as

$$\mathscr{D}_p = 2\pi \int_0^h r_t dr_t \int_{-t}^{t} dt' u_z(r_t, Z-t) \tag{3.1}$$

Here, u_z is the axial velocity, (r_t,Z) are coordinates of the fluid element in the lab reference frame, ($-t$,t) the time interval, and h the radius of material plane. Taking the limits $t \to \infty$ and $h \to \infty$ in the above expression gives the full drift volume. In a recent effort, Chisholm and Khair [2017] have shown that, at leading order in a/h, $\mathscr{D}_p \sim ah^2 \sinh^{-1}(Ut/h)$, t and h here being the time and radius of the aforementioned material plane, respectively; the h-scaling clearly points to the finite-time divergence of $\mathscr{D}$ $(= \lim_{h\to\infty} \mathscr{D}_p)$ in the Stokesian limit. In the limits $Ut/h \ll 1$ and $Ut/h \gg 1$, the authors find $\mathscr{D}_p$ to be $O(ahUt)$ and $O[ah^2 \ln(Ut/h)]$, respectively. These scalings may be readily obtained without a detailed calculation: for $Ut \ll h$, the flux through the original plane is independent of time, and due to the U-component of the Stokesian field, in the transverse plane containing the sphere. This component is $3Ua/(4r_t)$, and the flux through a circular section of radius h is therefore given by $\int_0^h 3U(a/4r_t)2\pi r_t dr_t \approx (3\pi/2)Uah$, implying $\mathscr{D}_p \approx (3\pi/2)Uaht$; here, the lower limit of the integral is taken to be 0 since the leading contribution comes from r_t of $O(h)$ (this is also the reason why a Stokeslet approximation suffices for the leading order estimate).

In the long-time limit of interest, when the distance of the material plane from the sphere is much larger than its radial extent, the flux is primarily due to the velocity $u_z \approx 3U/az$ along the rear stagnation streamline. The drift displacement due to this disturbance velocity field may be estimated as $\int^t dt\, u_z = \int^{Ut}(dz'/U)u_z = \int^{Ut} dz'(3a/2z') \sim (3a/2)\ln(Ut)$, and is logarithmically divergent in time. A subtle point here is with regard to the argument of the logarithm; the approximate estimate above gives a dimensional argument for the logarithm, and one needs an additional length with respect to which Ut in the logarithm is measured. Although an obvious choice would be a, the correct choice is h (as also evident from the exact result above), and this is because the onset of the logarithmic divergence is dependent on the transverse radial location of the fluid element. The decreasing magnitude of the disturbance field implies that it takes a progressively longer time for an element, further off from the translation axis, to be displaced through a distance of $O(a)$; evidently, the logarithmic divergence in time can only begin after the drift displacement has attained a magnitude of $O(a)$. For an element at a transverse distance of $O(h)$, the scales that contribute dominantly to $\mathscr{D}_p$, this time is $O(h/U)$, implying that the argument of the logarithm, in the expression for the drift displacement above, should be $t/(h/U)$; multiplication by πh^2 gives the estimate $\mathscr{D}_p \approx \frac{3\pi}{2} a h^2 \ln(Ut/h)$. In the Stokes-stratification regime, one expects the dominant contribution to the drift volume to come from the range $h \sim l_c$, l_c being the relevant stratification screening length; $l_c \sim O[(Ri_v Pe)^{-\frac{1}{4}}]$ for $Pe \ll 1$, and $O(Ri_v^{-\frac{1}{3}})$ for $Pe \gg 1$. However, for elements at these distances (from the translation axis), the drift displacement attains a magnitude of $O(a)$ only in the $O(l_c/U)$ time taken for the sphere to translate through a screening length. Since the velocity field decays faster for larger separations, there cannot be the analog of the aforementioned logarithmic-in-time behavior, for larger times, that occurred in the homogeneous case. This implies that $\mathscr{D}$ for the Stokes drift displacement can be obtained from the aforementioned long-time estimate for the Stokesian case by replacing h with l_c, but removing the logarithm. One therefore obtains $\mathscr{D} \sim O[a^3(Ri_v Pe)^{-\frac{1}{2}}]$ and $O(a^3 Ri_v^{-\frac{2}{3}})$, for small and large Pe, in the Stokes stratification regime, the latter estimate being relevant to the oceanic scenario [Katija and Dabiri, 2009; Subramanian, 2010]; both estimates diverge in the limit of a homogeneous ambient ($Ri_v \to 0$), as must be the case. The numerical pre-factors in these estimates would require a detailed calculation of the drift displacements on length scales of order the stratification screening length; the large-Pe case is considered in 3.4. Note that fluid elements that start off at distances of $h \ll l_c$ from the translation axis will suffer drift displacements of $O(a \ln Ri_v^{-\frac{1}{3}})$, and one therefore expects higher-order terms involving logarithms in a small Ri_v expansion of $\mathscr{D}$ in the limit $Re \ll Ri_v^{\frac{1}{3}} \ll 1$. Recent efforts by Shaik and Ardekani [2020a] and Shaik and Ardekani [2020b] have obtained $\mathscr{D}_p$ numerically, in both the small and large Pe limits, Consistent

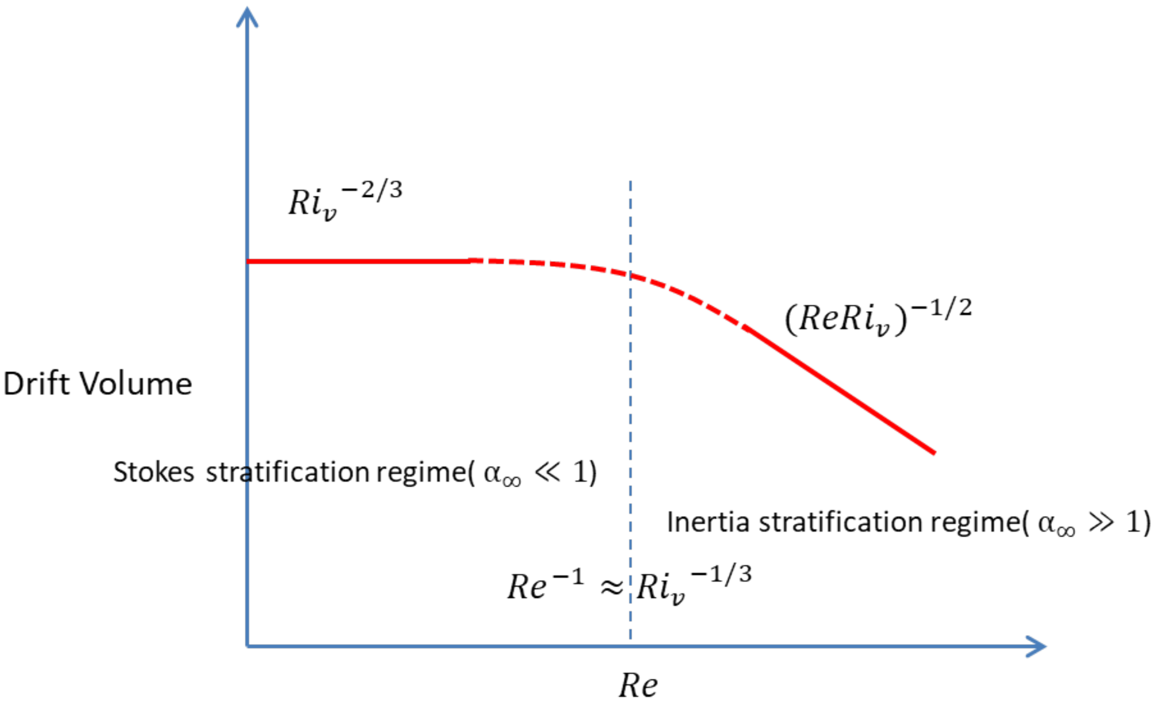

Fig. 3.1 Schematic for scaling estimates of drift volume in a density straified fluid: In the Stokes stratification regime the scaling for the drift is given by $Ri_v^{-2/3}$ whereas in the inertia-stratification regime, the drift scales as $(ReRi_v)^{-1/2}$. One expects a smooth transitions between Stokes and Inertia stratification regimes.

with the results of Chisholm and Khair [2017], $\mathscr{D}_p$ exhibits an $O(h^2)$ scaling with the radial extent of the material plane under consideration. The scaling arguments above imply that this algebraic divergence must be cut off once $h \sim O(l_c)$. It is also important to note that the narrowing down of the buoyant jet as $1/z^{\frac{1}{2}}$ with downstream distance implies that the $O(1/z)$ Stokesian decay of the axial velocity field within this jet region will not lead to divergent drift displacements, and thereeore does not affect the above drift volume estimates.

In the inertia-stratification regime ($Ri_v \ll Re \ll 1$), discussed briefly towards the end of section 2.3.3 in Chapter 2, the disturbance velocity field attains the familiar source-sink structure on length scales larger than the primary (inertial) screening length of $O(aRe^{-1})$ [Batchelor, 1967]. It is well known that the presence of a viscous wake leads to $\mathscr{D}$ diverging linearly in time for the homogeneous scenario [Chisholm and Khair, 2017; Subramanian, 2010]. This divergence is readily seen from the constant flux through a fixed plane driven by the viscous wake. This flux is given by $u_z(r_t^{wake})^2$, where $r_t^{wake} \sim (az/Re)^{\frac{1}{2}}$, and is $O(Ua^2/Re)$, leading to $\mathscr{D} \sim (Ua^2/Re)t$ for the homogeneous case. For the stratified case, and for $Pe \gg 1$, this viscous wake only persists until the secondary screening length of $O(Re/Ri_v)^{-\frac{1}{2}}$ obtained in section 2.3.3, and therefore the linear divergence above will be cut off for $t \sim O(\frac{a(Re/Ri_v)^{-\frac{1}{2}}}{U})$, when stratification forces screen the wake velocity field, and one obtains $\mathscr{D} \sim a^3(ReRi_v)^{-\frac{1}{2}}$ in the inertia-stratification regime. Note that this scaling is consistent with the scaling obtained above in the Stokes-stratification regime, in that it reduces to $O(Ri_v^{-2/3})$ for $Re = Ri_v^{1/3}$. In summary, for a fixed $Ri_v \ll 1$, $\mathscr{D}$ starts off being $O(a^3 Ri_v^{-\frac{2}{3}})$ until an Re of $O(Ri_v^{\frac{1}{3}})$, decreasing thereafter as $O(a^3 Re^{-\frac{1}{2}} Ri_v^{-\frac{1}{2}})$ for $Re \gg Ri_v^{\frac{1}{3}}$. The estimates mentioned above for both the Stokes stratification and Inertia stratification regimes can be summarized in figure 3.1 where the drift estimates are plotted against Re. A detailed examination of pathlines and drift volume, to verify the scaling arguments above, is carried out in the remaining sections of this chapter. This detailed examination pertains to the Stokes stratification regime; the Inertia stratification regime is beyond the scope of this thesis

3.3 Evaluation of drift volume in a density stratified fluid

The numerical evaluation of the fluid pathlines, drift displacements, and drift volume requires the use of the velocity field obtained in the Chapter 2. Note that in a density stratified fluid in the limit of $Re = 0$, the velocity field, when expressed in inner coordinates, is a function of Ri_v and Pe. Thus, the drift volume given by 3.1 is expected to be a function of both the above mentioned dimensionless numbers in the Stokes stratification regime. As derived in the last chapter, for the convection dominant limit, the velocity field, in outer coordinates, in the Stokes stratification regime ($\alpha_\infty = 0$), is given by the following Fourier intergal

$$\bar{\mathbf{u}}_{\mathbf{1}} = -\frac{3}{4\pi^2}\int \frac{\left(ik_3 + k^2\beta_\infty\right)k^2\mathbf{1}_z.\left(\underline{\underline{\mathbf{I}}} - \hat{\mathbf{k}}\hat{\mathbf{k}}\right)}{\left(ik_3k^4 + \beta_\infty k^6 + k_t^2\right)} e^{i\mathbf{k}.\mathbf{r}} d\mathbf{k} \tag{3.2}$$

Note that we have retained the $O(\beta_\infty)$ term which, as mentioned above, renders the drift volume a function of *Pe*; Although, one expects the drift volume to approach a *Pe*-independent value in the limit $\beta_\infty \ll 1$ despite the Pe-dependent reverse jet region.

To obtain fluid pathlines in the Stokes stratification regime in the convection-dominant limit ($Re = 0$, $Ri_v \ll 1$ and $Pe \gg 1$), we find the axial and transverse velocities after separating the Stokeslet contributions, and taking only the real part. The expressions for both the velocity components in outer coordinates are now given by

$$\bar{u}_z = -\frac{3\left(r_t^2+2z^2\right)}{4\left(r_t^2+z^2\right)^{\frac{3}{2}}} + \frac{3}{\pi}\int_0^\infty dk \int_0^{\frac{\pi}{2}} d\theta \frac{\sin^5\theta J_0(kr_t\sin\theta)\left[\cos(kz\cos\theta)(\beta_\infty k^4+\sin^2\theta)+k^3\cos\theta\sin(kz\cos\theta)\right]}{(\beta_\infty k^4+\sin^2\theta)^2+k^6\cos^2\theta} \tag{3.3}$$

$$\bar{u}_{r_t} = -\frac{3r_tz}{4\left(r_t^2+z^2\right)^{\frac{3}{2}}} + \frac{3}{\pi}\int_0^\infty dk \int_0^{\frac{\pi}{2}} d\theta \frac{\cos\theta\sin^4\theta J_1(kr_t\sin\theta)\left[k^3\cos\theta\cos(kz\cos\theta)-(\beta_\infty k^4+\sin^2\theta)\sin(kz\cos\theta)\right]}{(\beta_\infty k^4+\sin^2\theta)^2+k^6\cos^2\theta} \tag{3.4}$$

As the above expressions are written for the case of a point-particle approximation, they are only valid at large distances ($r \gg a$) from the sphere. To obtain the pathlines of fluid elements over the entire range of distances from the sphere, and thence, the drift volume, uniformly valid expressions for both the axial and transverse velocities are required. This can be done by writing down the additive composite velocity field, obtained by adding the inner region Stokes velocity field to the outer region velocity field, while removing the matching region contribution to avoid double-counting Van Dyke [1975]. This leads to the following composite expressions for both the components of velocity written in the inner coordinates.

$$\bar{u}_z^C = -\frac{r_t^2-2z^2}{4(r_t^2+z^2)^{\frac{5}{2}}} + -\frac{3\left(r_t^2+2z^2\right)}{4\left(r_t^2+z^2\right)^{\frac{3}{2}}} + \frac{3}{\pi}\int_0^\infty dk \int_0^{\frac{\pi}{2}} d\theta \frac{\sin^5\theta J_0(kr_t\sin\theta)\left[\cos(kz\cos\theta)(\beta_\infty k^4+\sin^2\theta)+k^3\cos\theta\sin(kz\cos\theta)\right]}{(\beta_\infty k^4+\sin^2\theta)^2+k^6\cos^2\theta} \tag{3.5}$$

$$\bar{u}_{r_t}^C = \frac{3r_tz}{4(r_t^2+z^2)^{\frac{5}{2}}} - \frac{3r_tz}{4\left(r_t^2+z^2\right)^{\frac{3}{2}}} + \frac{3}{\pi}\int_0^\infty dk \int_0^{\frac{\pi}{2}} d\theta \frac{\cos\theta\sin^4\theta J_1(kr_t\sin\theta)\left[k^3\cos\theta\cos(kz\cos\theta)-(\beta_\infty k^4+\sin^2\theta)\sin(kz\cos\theta)\right]}{(\beta_\infty k^4+\sin^2\theta)^2+k^6\cos^2\theta} \tag{3.6}$$

For evaluating the pathlines of fluid elements, we now take $\bar{u}_z^C = \frac{dz}{dt}$ and $\bar{u}_{r_t}^C = \frac{dr_t}{dt}$, and therefore have to solve coupled ODE's for z and r_t with given initial coordinates at $t = 0$. We choose the plane of fluid elements to be given by $z = 0$ at $t = 0$ with an additional constraint given by $r_t > a$. Note that, on account of axisymmetry, it suffices to choose an initial line of fluid elements transverse to the direction of translation - this line corresponds to the intersection of the aforementioned initial plane with a vertical plane passing through the axis of symmetry (the direction of translation). The initial interval of r_t 's is $(1, 2Ri_v^{-1/3})$; the largest r_t is chosen to be twice the large-Pe stratification screening length to ensure convergence. Having chosen the r_t -interval, forward and backward integrations are carried out for large times for a given pair (Ri_v, Pe). We use a fourth order Runge-Kutta method for integration with the axial and transverse velocities (and the associated Fourier integrals) evaluated at each time instant to update the position of the fluid elements. The backward integration in time mentioned above implies the sphere moves upward from $z = 0$ to large positive z (corresponding to a large negative time). Similarly, a forward integration implies that the sphere moves from $z = 0$ to a large negative z (corresponding to a large positive time). The above procedure helps us calculate the pathlines of individual fluid elements, with the associated drift displacements being given by difference between the z coordinates of the particular fluid element corresponding to large positive and negative times. The magnitudes of these positive and negative times is chosen to be $T_{max} \sim Ri_v^{-1/2} Pe^{1/2}$, corresponding to the sphere translating through a secondary screening length (where diffusion effects become important), which must ensure convergence of the drift displacements, and thereby ensure that the initial plane above converges to asymptotic upstream and downstream deformed surfaces for the largest negative and positive times. Having calculated the upstream and downstream drift surfaces by way of backward and forward integrations, respectively, the upstream drift volume component is calculated by evaluating the volume between the initial plane of fluid elements at $t = 0$; the downstream drift volume component is calculated in an analogous manner.

3.4 Results and Discussion

To begin with, we briefly consider the homogeneous Stokesian scenario - that is, of a sphere translating with $Re = Ri_v = 0$ - and calculate the pathlines of fluid elements and drift surfaces. Note that we do not perform a detailed calculation of the drift displacements and drift volume in the above case as these aspects are treated in the previous literature [Chisholm and Khair, 2017; Eames et al., 2003] as explained in the introduction of this chapter. Since the instantaneous streamlines in the lab reference frame associated with the homogeneous Stokes flow are open, one obtains open pathlines irrespective of the transverse distance(r_t) of the fluid element from the sphere at time $t = 0$ (note that the pathlines for the original potential problem have a looped character, with the loop size approaching the size of the

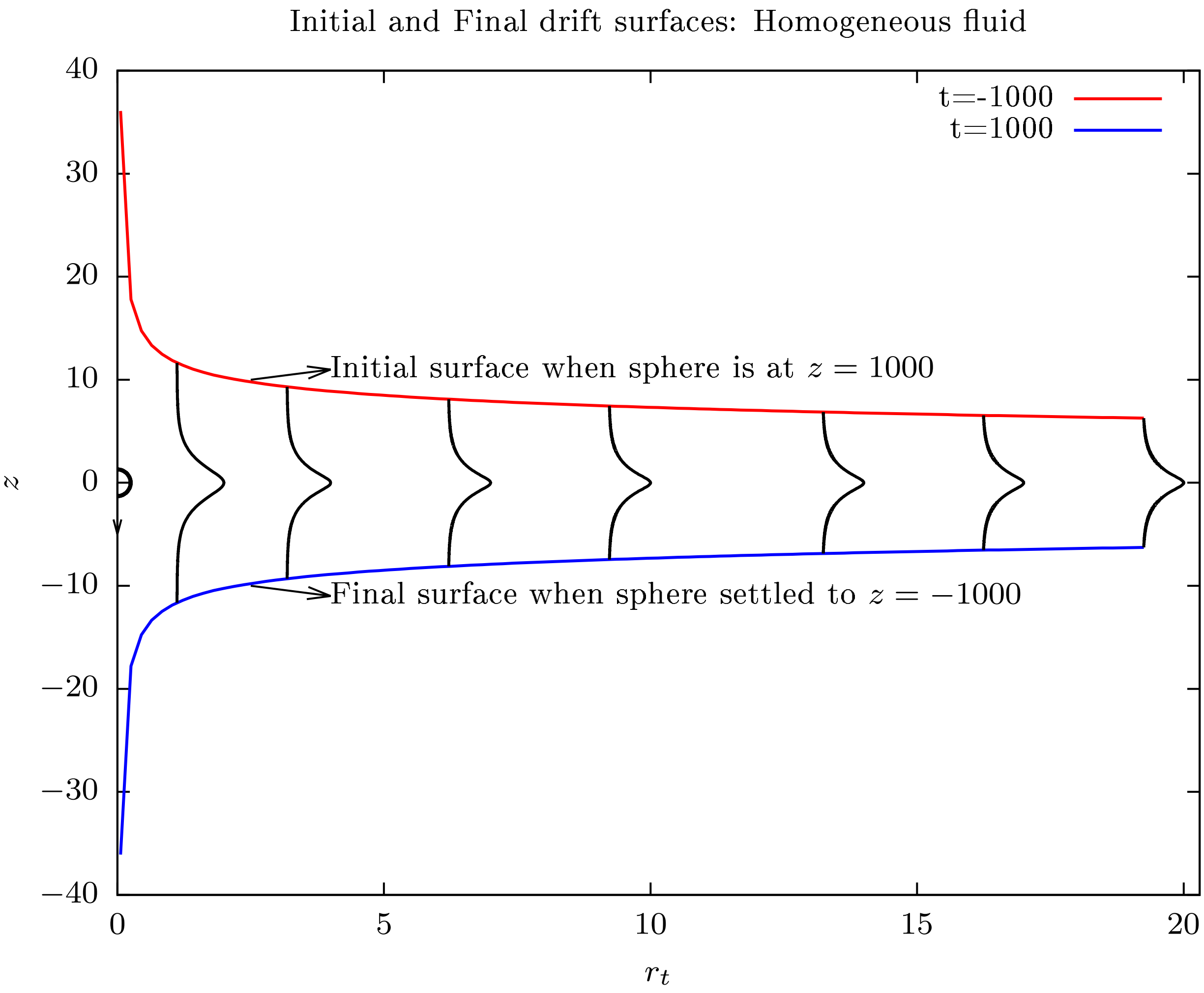

Fig. 3.2 Fluid pathlines (depicted as black lines in the figure) due to a translating sphere in a homogeneous viscous fluid without stratification at $Re = 0$. The initial plane of fluid elements, at time t=-1000, is depicted as red deformed curve whereas the the final plane of fluid elements, at time t=1000, is in blue; the sphere is at the origin, at time t=0, and moving vertically downward.

whole pathline with increasing r_t - see Darwin [1953]). These Stokesian pathlines are shown as black curves for different r_t 's in figure 3.2. The logarithmic-in-time divergence of the drift displacements due to the slow $O(1/r)$ decay of the velocity field in the homogeneous viscous case implies that the integrations can be carried out only for finite times. The forward and backward integrations in figure 3.2 are carried out up until a maximum time of $T_{max} = 1000$. The plane of fluid elements given by the red curve is the result of the backward integration in time, and denotes the initial drift surface when the sphere starts far upstream at $z = 1000$ for $t = -1000$. The symmetrically located blue curve is likewise the final drift surface when the sphere ends up far downstream at $z = -1000$ for $t = 1000$. The partial drift volume enclosed between these two surfaces (extending up to $r_t = 20$) is already large compared to the volume of the sphere (a^3) itself. This largeness is, of course, related to the divergence of the Stokesian drift volume (for any finite time) discussed in section 3.1, and is in sharp contrast to the homogeneous potential flow case where the drift volume remains of order the volume of the transating particle. Now we turn to the detailed calculations for the case of a density stratified fluid.

Figures 3.3a and 3.3b show the pathlines of the fluid elements in a stratified fluid at a fixed viscous Richardson number $Ri_v = 10^{-3}$ and for two different Peclet numbers ($Pe = 50$ & 1000 respectively). The effect of the rapid algebraic decay of the axial velocity, on the pathlines of fluid elements that are located at transverse distances of $r \geq Ri_v^{-1/3}$ at time $t = 0$, is evident. The spatial extent of the pathlines is much smaller for these transverse distances (this will be again illustrated via drift displacement plots that we consider later in this section). Note that for calculating the drift surfaces at $Ri_v = 10^{-3}$, we have chosen $T_{max} = 1000$ since this is the secondary screening length ($Ri_v^{-1/2} Pe^{1/2}$) for this Ri_v and the largest of Pe considered here. We will come back to this in detail in this section when we discuss the drift displacement plots.

As can be seen from the figures, the pathlines are strongly affected by weak stratification and are evidently different from their counterparts in the homogeneous Stokesian scenario. This is a consequence of the streamlines in the instantaneous frame of reference, in a density stratified fluid, not exhibiting the open configuration, as already seen in Chapter 2. Fluid elements outside the region corresponding to the reverse buoyant jet exhibit primarily horizontal motion for transverse distances much larger than stratification screening length ($Ri_v^{-1/3}$); the fluid elements located in the region of the buoyant jet do exhibit a reversal of fluid motion. For the symmetric time intervals considered here, the pathlines are seen to be fore-aft asymmetric, unlike the homogeneous viscous case or the case of the diffusion dominant limit (recall that, in the latter case the velocity field is fore-aft symmetric leading to fore-aft symmetric pathlines over any symmetric time interval; the detailed calculations of pathlines in $Pe = 0$ limit are not shown in this thesis). From figure 3.3a and 3.3b corresponding to $Pe = 50$ and $Pe = 1000$ respectively, we note that the pathlines and drift surface patterns are almost similar underlining the fact that the drift volume is independent of Pe for $Pe \gg 1$. However, it can also be seen that the reversed motion of fluid elements starting at smaller transverse distances from the line of translation of the sphere is slightly weaker for $Pe = 50$, which may be anticipated due to smaller secondary diffusion screening length for $Pe = 50$ in comparison to $Pe = 1000$.

Now we turn to the variation of drift displacements with time, for different Pe, which is ultimately related to the convergence of the drift volume in the limit $Pe \gg 1$. Figure 3.4 shows the evolution of the drift displacement of a fluid element that is located close to the sphere, at (r_t,z) = $(1.005, 0)$, at time $t = 0$, over a range of Pe from 10 to 1000. The plot shows both the upstream and downstream drift displacements as a function of time. This plot (and the others after it) includes several vertical lines. The first (black) vertical line indicates the axial distance where the zero crossing in the axial velocity field exists ($1.1 Ri_v^{-1/3}$, in the units of sphere radius a).In this particular case of $Ri_v = 10^{-3}$, this zero-crossing turns out to be 11 (in the units of a). We expect the Stokeslet field to dominate for distances much smaller than this. This behavior is also reflected in the drift displacement evolution for times $t < 11a$, which suggests there is logarithmic divergence (to plus and minus infinity for the upstream and downstream displacements). This logarithmic divergence gets cut off for times $t > 11a$. However, due to the asymmetric influence of stratification on the instantaneous velocity field (already seen in Chapter 2), at distances larger than the stratification screening length, the upstream and downstream drift displacement evolution differs significantly for times $t > 11a$. The upstream drift displacement is seen to reach a plateau for times $t \sim 50a$ as the velocity field (for negative z) exhibits a rapid algebraic decay. Further the convergence of the upstream drift displacment with increasing Pe is again quite rapid, with the displacement curve being virtually independent of Pe for $Pe \geq 10$ (smaller values of Pe have not been shown). However, the evolution of downstream drift displacements is more sensitive to Pe, which correlates to the sensitivity of the jet region behind the sphere (in the instantaneous streamline pattern) to increasing Pe. The convergence of downstream drift displacements is only seen to happen for times $t > O(Ri_v Pe^{-1/2})$, which is essentially the secondary screening length in the large Pe limit. The multiple vertical lines (in different colors) are drawn to emphasize the above fact. The second black vertical line in figure 3.4 indicates the time (or distance) for the onset of the $O(1/z)$ decay of the axial velocity field (corresponding to the reverse Stokeslet behavior) in the jet region. The remaining vertical lines correspond to the secondary diffusion screening lengths, for each of the Pe's considered, beyond which

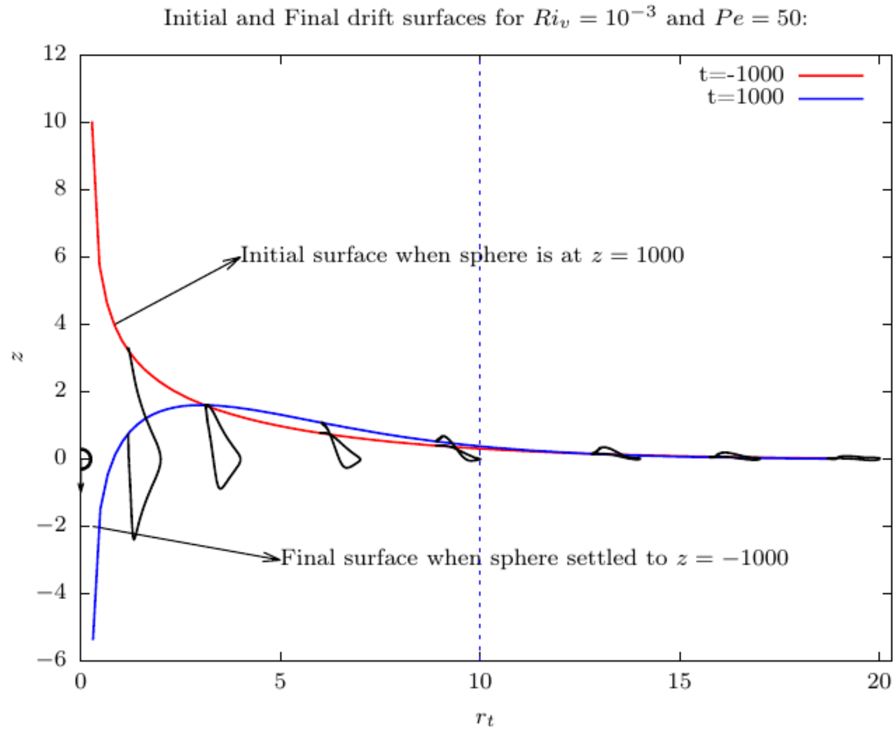

(a) Pathlines and Drift surfaces for $Pe = 50$

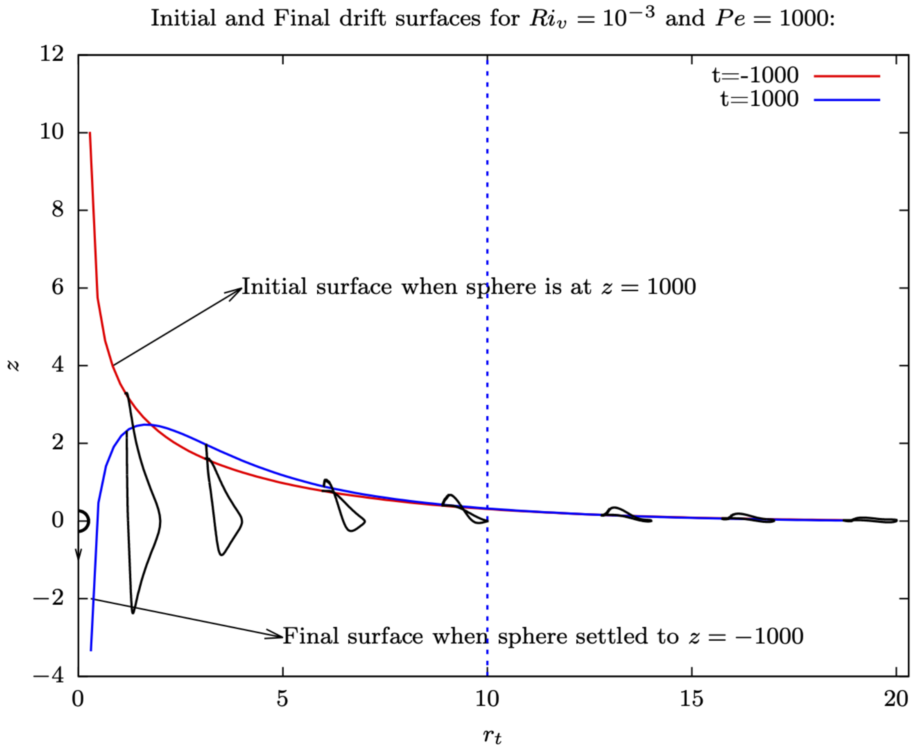

(b) Pathlines and Drift surfaces for $Pe = 1000$

Fig. 3.3 Fluid pathlines (depicted as black lines in the figure) due to a translating sphere in a viscous stratified fluid at $Re = 0$ and $Ri_v = 10^{-3}$ for two different Pe ($= 50, 1000$). The initial plane of fluid elements, at time t=-1000, is depicted as red deformed curve whereas the the final plane of fluid elements, at time t=1000, is in blue; the sphere is at the origin, at time t=0, and moving vertically downward. The blue dotted vertical lines indicate the stratification screening length.

there is an exponential decay of the axial velocity. It can be seen that the downstream drift displacements converge and reach a plateau beyond the secondary diffusion screening length.

The evolution of the drift displacements for fluid elements that begin at transverse distances of $O(Ri_v^{-1/3})$ at $t = 0$ (for $Ri_v^{-1/3}$, this is $r_t = 10$) at $t = 0$) is shown in figure 3.5. The time variation of the drift displacements for this case is different from those of fluid elements starting at smaller transverse distances (an instance of which was shown in figure 3.4 above). The downstream drift displacements still show a sensitive dependence on *Pe*; however, more importantly, the fluid elements exhibit a Lagrangian reflux (that is, a net displcement in the direction opposite to the translating particle) rather than Lagrangian drift. This behavior clearly suggests the strong role of stratification on the drift in the convection-dominant limit. As will be seen later in this section, this has implications for the drift volume. From figure 3.6, for fluid elements that have started at two times the stratification screening length, we observe that the drift displacements are approximately independent of *Pe* in the convection dominant limit (especially $Pe \geq 50$). This implies that the convergence of upstream drift displacements is no longer a function of secondary screening length (the fluctuations in drift displacements at these distances are due to numerical convergence issues as we need much larger number of quadrature points to resolve this which is beyond the scope of the present work). Finally, Figure 3.7 shows the drift displacements for fluid elements starting at different transverse distances at $t = 0$ and clearly suggest the convergence, for large times, for the case of $Ri_v = 10^{-3}$ and $Pe = 1000$. We draw analogous conclusions from drift displacements and pathlines for any other viscous Richardson and Peclet numbers (whose calculations are not shown here).

With the above results having established the convergence of the fluid drift displacements, we now move on to calculate the drift volume. For this purpose, we first calculate the upstream and downstream drift surfaces for large negative and positive times, respectively, by virtue of backward and forward integrations over a whole range of r_t values until twice the primary screening length. For $Ri_v = 10^{-3}$ and $Pe = 1000$, the evolution of these drift surfaces with time is shown in the figures 3.8*a* and 3.8*b*. While the evolution of the upstream drift surfaces in figure 3.8*a* corresponds to the fluid elements being dragged along in the same direction as the translating sphere, a change in the evolution of the downstream drift surfaces, arising from a reversal in the fluid element trajectories can be seen in figure 3.8*b* for times $t \geq Ri_v^{-1/3}$. For different Ri_v and *Pe*, the upstream drift volume is evaluated by calculating the volume between the large (negative) time upstream drift surface and the plane of fluid elements at time $t = 0$. Similarly, the downstream drift is evaluated by considering the large (positive) time drift surface. Figures 3.9*a* and 3.9*b* show the upstream and downstream drift volumes, respectively, against Ri_v for different *Pe* (≥ 50). Our results indicate that both the

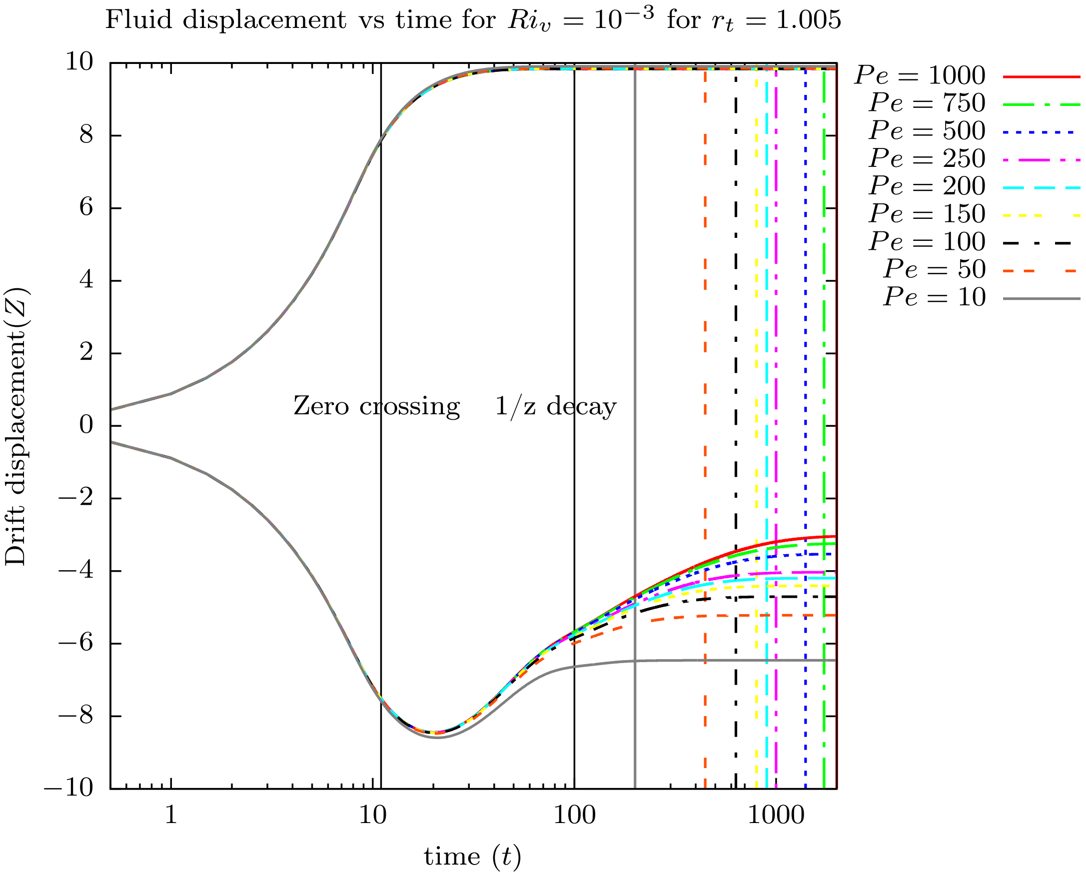

Fig. 3.4 Drift displacement against time for a fluid element located at $(1.005, 0)$ at time $t = 0$ in viscous density stratified fluid at $Re = 0$ and $Ri_v = 10^{-3}$ for different Pe values. Drift displacements are plotted by doing both the backward and forward integration. The upstream drift displacement plots start at small positice Z for small times, whereas the downstream drift displacement plots start at small negative Z for small times.

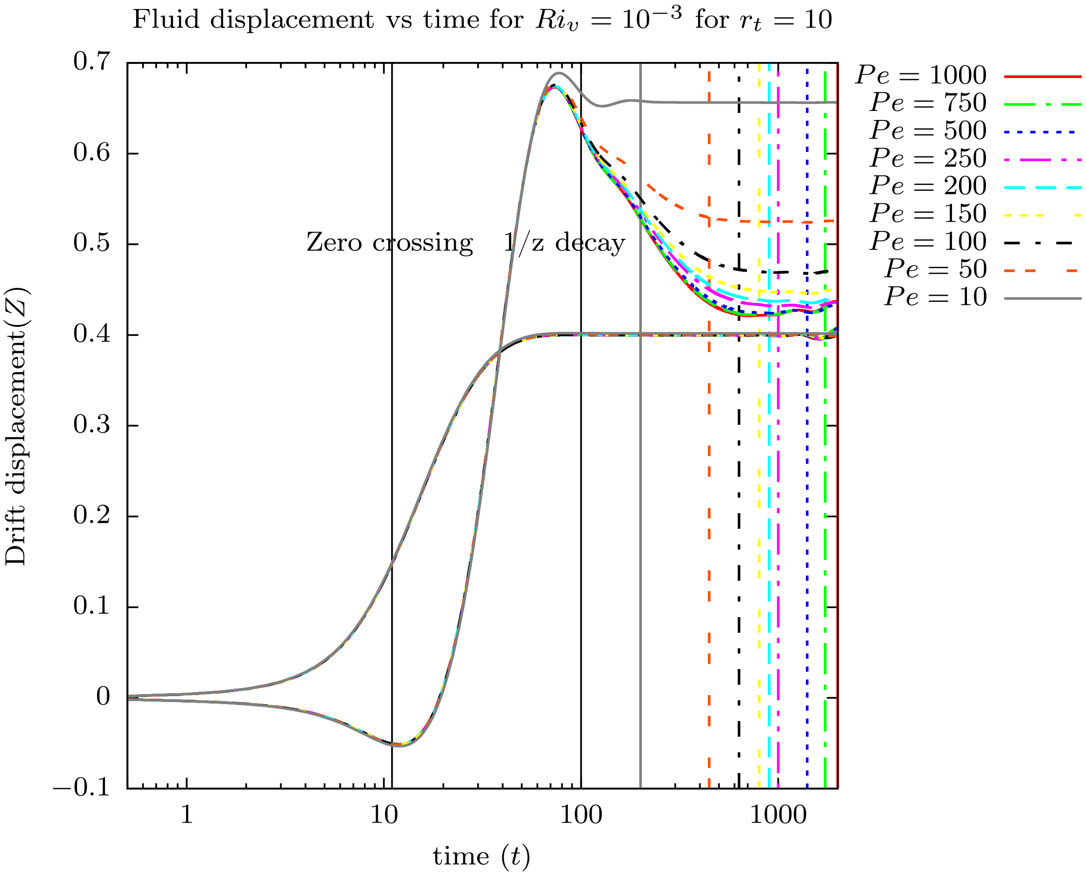

Fig. 3.5 Drift displacement against time for a fluid element located at $(10,0)$ at time $t = 0$ in viscous density stratified fluid at $Re = 0$ and $Ri_v = 10^{-3}$ for different Pe values.

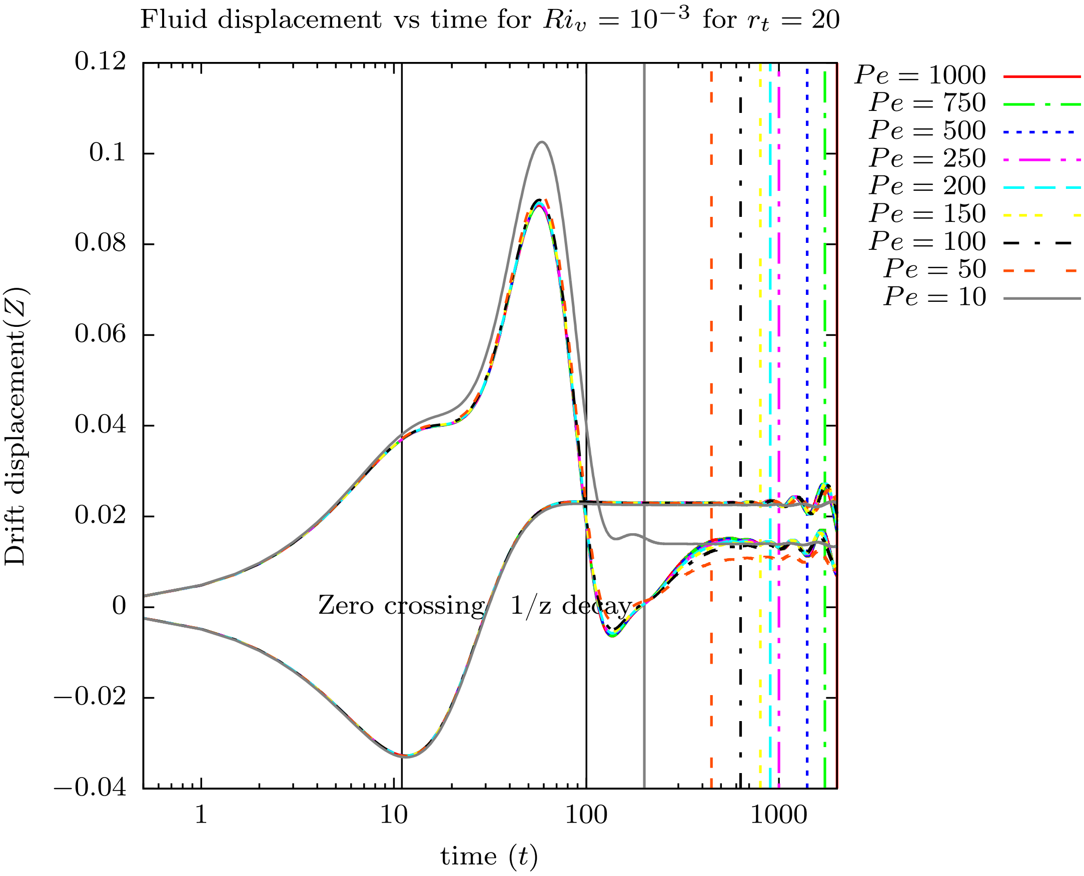

Fig. 3.6 Drift displacement against time for a fluid element located at $(20,0)$ at time $t = 0$ in viscous density stratified fluid at $Re = 0$ and $Ri_v = 10^{-3}$ for different Pe values.

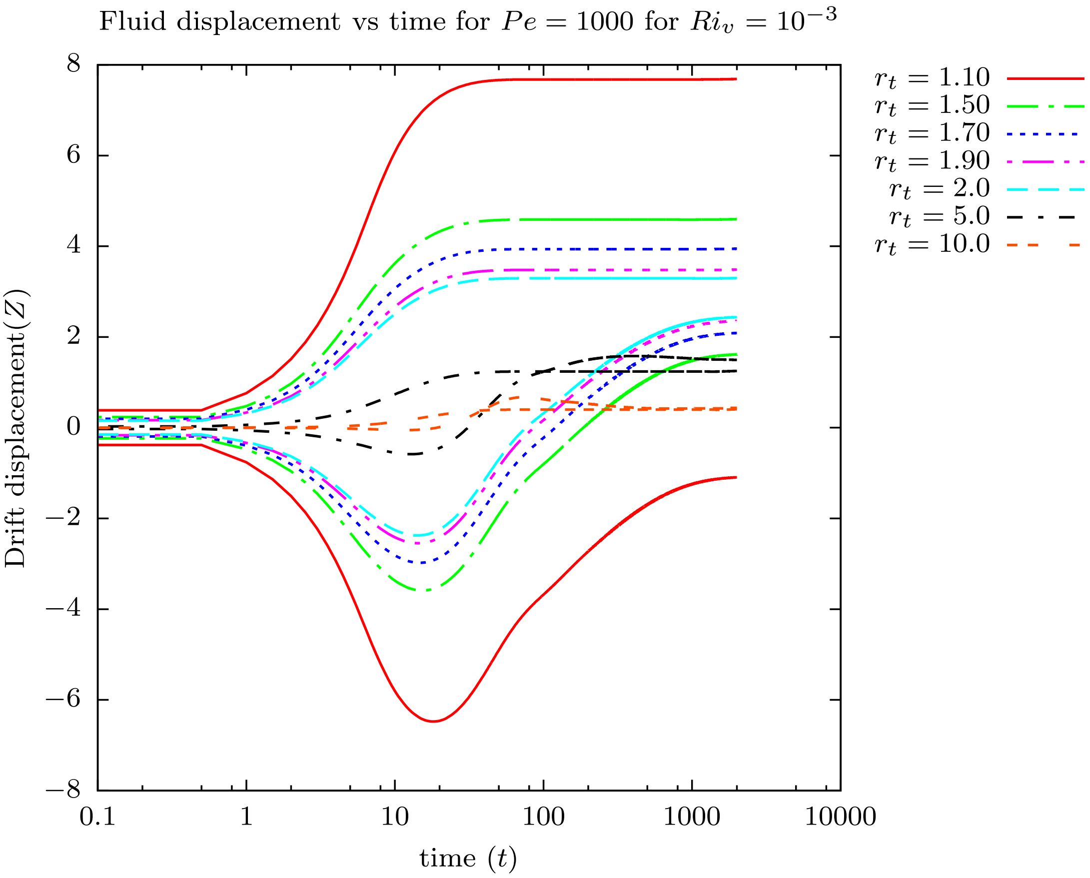

Fig. 3.7 Upstream and downstream drift displacements of fluid elements starting at different transverse distances against time in a viscous density stratified fluid at $Re = 0$ and $Ri_v = 10^{-3}$, and $Pe = 1000$. As before, drift displacements are plotted for both the backward and forward integration(upstream and downstream).

upstream and downstream drift volume components scale as $Ri_v^{-2/3}$. However, while the upstream drift is a positive quantity ($= 3.71 Ri_v^{-2/3}$) indicating a net Lagrangian drift, the downstream drift is a negative quantity ($= -3.79 Ri_v^{-2/3}$) indicating a net Lagrangian reflux.

For different $Pe (\geq 50)$, the total drift volume (found by adding upstream and drift volumes) is plotted as a function of Ri_v in figure 3.10. The total drift volume evidently does not scale as $Ri_v^{-2/3}$; instead, the scaling appears to be closer to $Ri_v^{-1/3}$ (although, one needs to go to even smaller Ri_v in order to be certain of this exponent); the black line in the figure corresponds to $1.4 Ri_v^{-1/3}$. Importantly, the total drift has the character of a Lagrangian reflux (instead of a net Lagrangian drift) in the convection dominant limit. This can clearly be attributed to the negative downstream drift discussed earlier. The scaling arguments presented in section 3.2 suggested that the drift volume ina density stratified fluid in the convection-dominant limit scales as $Ri_v^{-2/3}$. Although the numerical calculations for the upstream and downstream drift volume agree with our scalings, the cancellation between the reflux and drift contributions implies that the scaling for the total (net) drift volume does not conform to the expected scaling; instead, the total drift volume turns out to be closer to being $O(Ri_v^{-1/3})$.

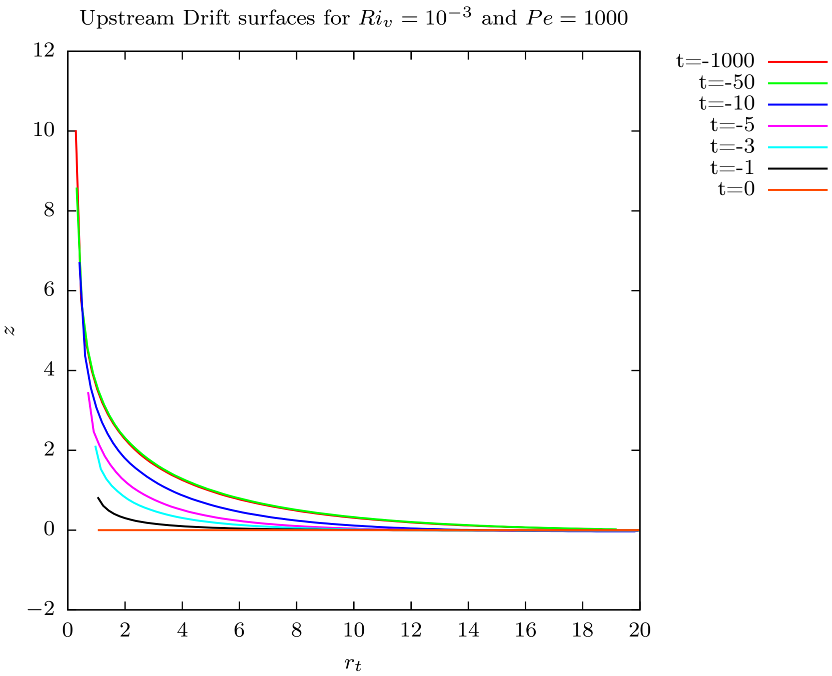

(a) Upstream drift surfaces in a density stratified fluid

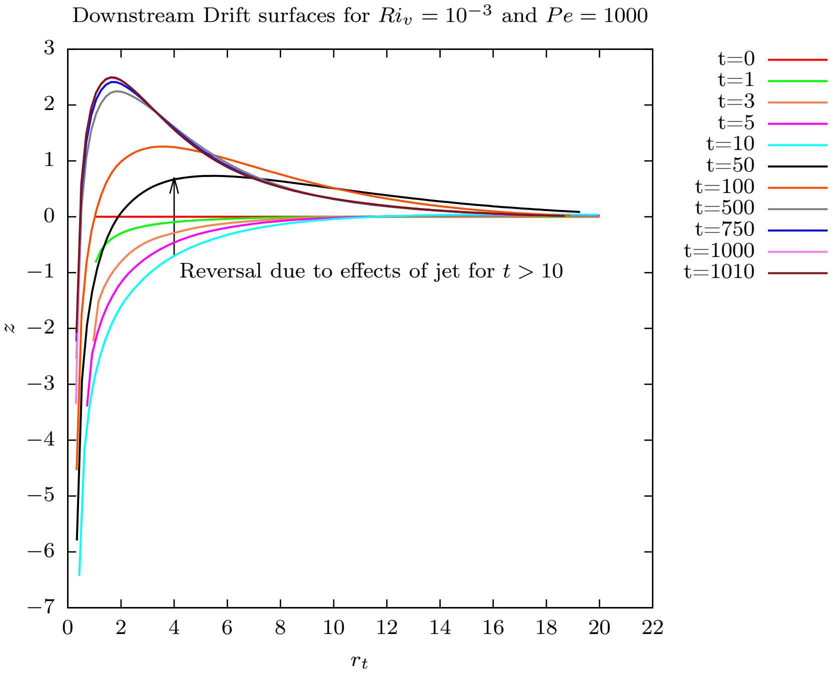

(b) Downstream drift surfaces in a density stratified fluid

Fig. 3.8 Evolution of upstream and downstream drift surfaces, for negative and positive times respectively, for the the plane of fluid elements that has a radius $r_t = 20$ at time $t = 0$, in a viscous density stratified fluid, at $Re = 0$, $Ri_v = 10^{-3}$, and $Pe = 1000$. For $t \geq 10$, a reversal in the trajectories of the fluid elements can be seen.

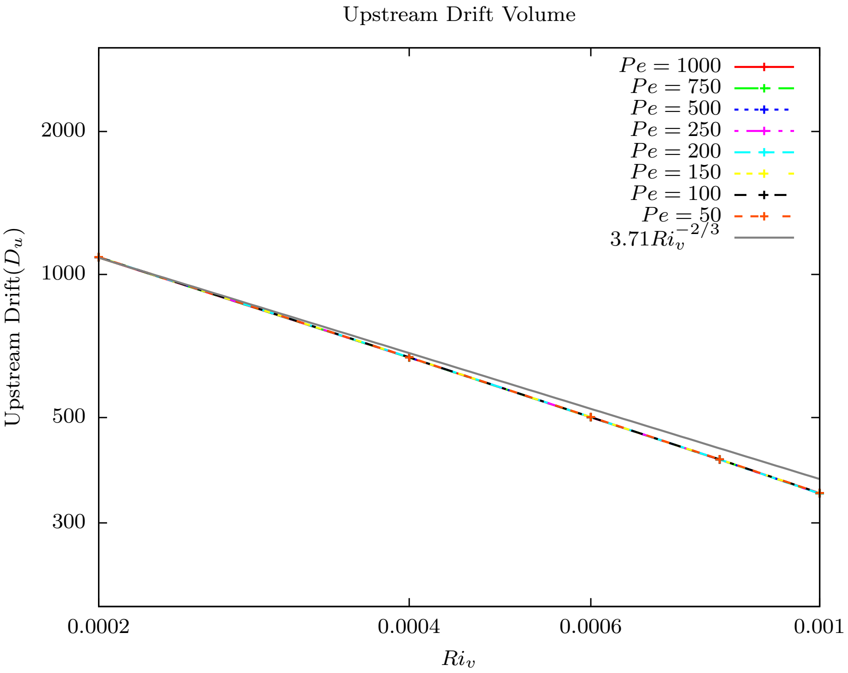

(a) Upstream drift surfaces in a density stratified fluid

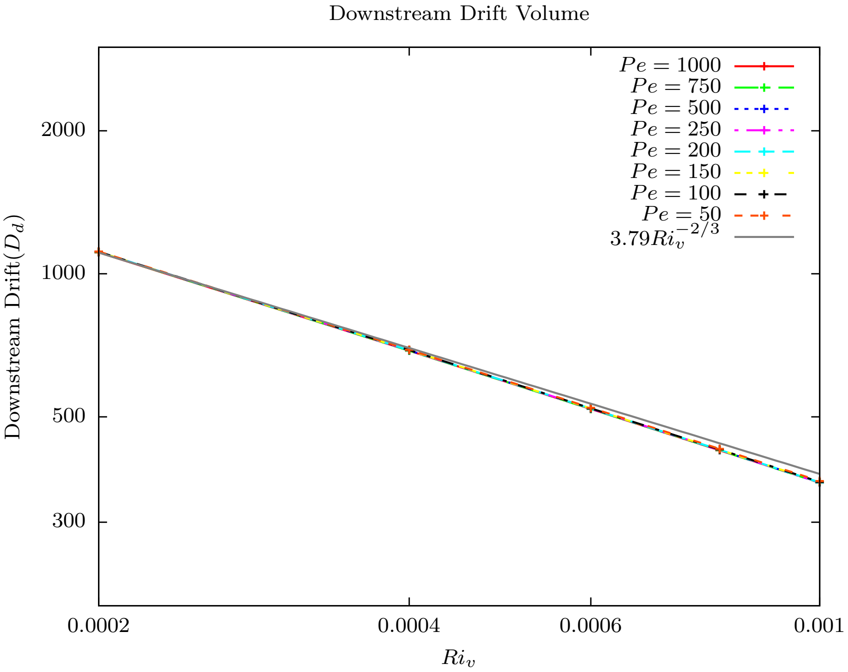

(b) Downstream drift surfaces in a density stratified fluid

Fig. 3.9 The upstream and downstream drift volumes plotted against Ri_v for different Pe ($\gg 1$). The upstream drift volume scaling, for $Pe \gg 1$, approaches $3.71Ri_v^{-2/3}$ for $Ri_v \to 0$ (a Lagrangian drift). The downstream drift volume scaling, for $Pe \gg 1$, approaches $3.79Ri_v^{-2/3}$ and is negative (a Lagrangian reflux).

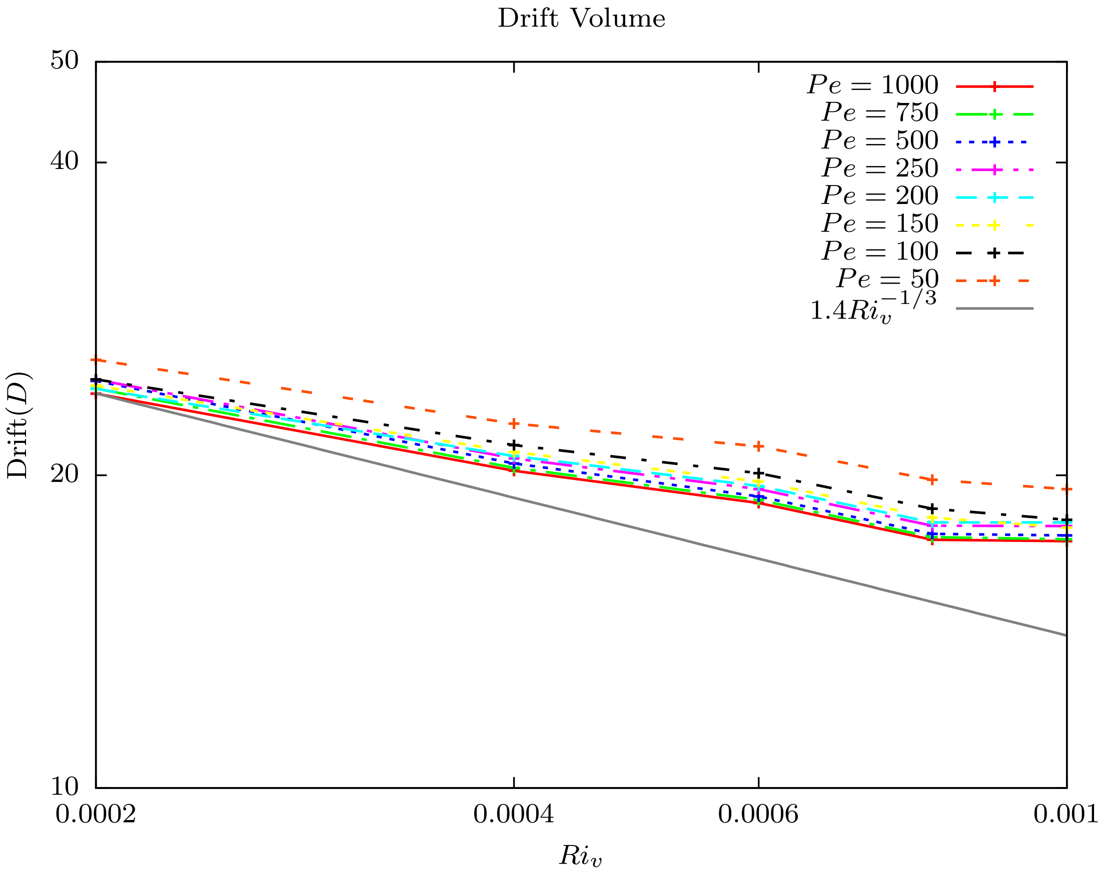

Fig. 3.10 The absolute drift volume plotted against viscous Richardson number for different Peclet numbers. The drift volume scaling in the convection dominant limit appears close to that of $1.4Ri_v^{-1/3}$. Note that as mentioned in the text, the total drift volume is negative indicating a net Lagrangian reflux

3.5 Conclusions

In this chapter, we have carried out a detailed numerical evaluation of the pathlines, drift displacements, drift surfaces and drift volume by using a composite velocity field that remains valid over length scales from r of $O(a)$ to $O(aRi_v^{-1/3})$. A few comments are in the order with regard to comparison between the detailed numerical calculations performed in section 3.4 and the drift estimates made in section 3.2. We also discuss the relevance of drift volume with regard to the mixing in a density stratified fluid towards the end.

We know that the 'full' drift volume calculation, corresponding to the volume enclosed between the surfaces at $t = -\infty$ and ∞, is not possible numerically. Thus, it makes sense to calculate the partial drift volume corresponding to the time interval $(-T_{max}, T_{max})$ with the radius of plane of fluid elements being truncated at h_{max}. For T_{max} and h_{max} much larger than the primary stratification screening length $(aRi_v^{-1/3})$, one expects this partial drift volume to approach the 'full' drift volume. Theoretical arguments mentioned in section 3.2 suggest that the drift volume in the Stokes stratification regime must diverge as $Ri_v^{-2/3}$ for Ri_v going to zero. We find such a divergence (with an exponent close to $-2/3$), but only for the upstream and downstream drift volumes corresponding to the time intervals $(-T_{max}, 0)$ and $(0, T_{max})$ respectively. However, when we add both the upstream and downstream drift volumes to obtain the drift volume over the entire time interval, there appears to be a cancellation at leading order, and thereby, we find a reduced divergence with an exponent that is closer to $-1/3$. With the present numerical results it is difficult to say whether this corresponds to what is presumably the next term in the asymptotic series (in Ri_v) for the drift volume in the Stokes stratification regime, or if the reduced divergence is only an apparent one, and reflecting of a very small numerical prefactor multiplying $Ri_v^{-2/3}$. Nevertheless, and interestingly, the total drift volume is negative corresponding to a net reflux in the opposite direction to translation. This reflux arises for times much longer than that taken for the sphere to translate a distance equal to the stratification screening length, suggesting a strongly singular role of buoyancy forces.

The finding that the drift volume (or rather Lagrangian reflux) in the Stokes stratification regime is indeed smaller than expected, and apparently of $O(Ri_v^{-1/3})$ implies that the original estimates mentioned in the section 3.2 need to be revised. Recall that the drift volume was predicted to plateau at $O(Ri_v^{-2/3})$ in the Stokes stratification regime, and until an Re of $O(Ri_v^{1/3})$. It should then transition to an algebraic decay regime of $O(ReRi_v)^{-1/2}$ for larger Re, corresponding to the inertia-stratification regime. Thus, the simplest expectation is for the drift volume to decrease monotonically, with increasing Re, from an initial plateau value of $O(Ri_v^{-2/3})$. In light of the cancellation above, we examine the contribution to the drift volume at the next order. The general form of the drift volume (in units of a^3) may be written as

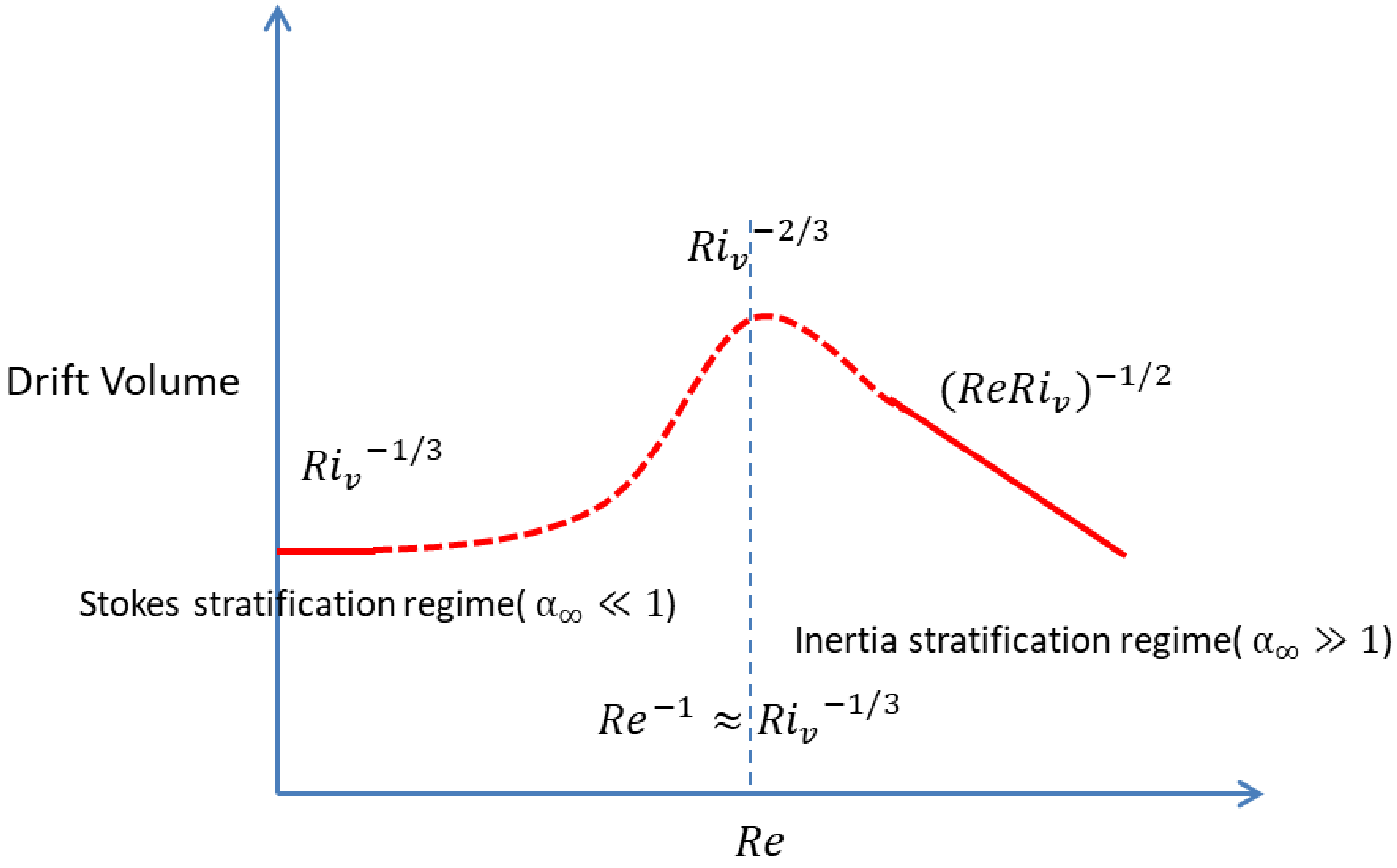

Fig. 3.11 Schematic for revised scaling estimates of drift volume in a density straified fluid as discussed in section 3.5: In the Stokes stratification regime the scaling for the drift is now given by $Ri_v^{-1/3}$ whereas in the inertia-stratification regime, the drift still scales as $(ReRi_v)^{-1/2}$. The drift volume maximum will still scales as $Ri_v^{2/3}$ as described in the text.

$Ri_v^{-2/3}F(Re/Ri_v^{1/3})$. In the Stokes stratification regime, it is natural to expect a correction to the leading $O(Ri_v^{-2/3})$ estimate to arise at $O(Re/Ri_v^{1/3})$ due to inertial effects (assuming that the correction due to inertial effects scales linearly with the ratio of the respective screening lengths); this is equivalent to assuming an expansion for F to be of the form $c_1 + c_2 Re/Ri_v^{1/3}$ in the limit $Re/Ri_v^{1/3} \ll 1$, where c_1 and c_2 are constants of order unity. This leads to an inertial correction of $O(ReRi_v^{-1})$ to the leading order estimate of $O(Ri_v^{-2/3})$. There will, of course, be higher order corrections within the Stokes stratification regime, and one expects the leading correction to be $O(Ri_v^{-1/3})$. In light of the absence of the leading $O(Ri_v^{-2/3})$ contribution, one only has the two smaller contributions of $O(ReRi_v^{-1})$ and $O(Ri_v^{-1/3})$, With increasing Re, therefore, one expects the drift volume to begin from a plateau of $O(Ri_v^{-1/3})$ until an Re of $O(Ri_v^{-2/3})$, and then increase as $ReRi_v^{-1}$ for $Ri_v^{2/3} \ll Re \ll Ri_v^{1/3}$, attaining a maximum value of $O(Ri_v^{-2/3})$ for $Re/Ri_v^{1/3} \sim O(1)$, before decreasing as $O(ReRi_v)^{-1/2}$ for $Re \gg Ri_v^{1/3}$. Thus, the consequence of the (numerical) cancellation found at leading order, in section 3.4 is that the drift volume likely exhibits a non-monotonic dependence on Re as explained above. Note that any other algebraic scaling for F (not the linear one assumed above) would lead to the drift volume still being non-monotonic, although the value of the initial plateau, and the Re at which the drift volume starts increasing first, will scale differently with Ri_v.

We briefly discuss the relation between drift volume presented in this section and the mixing in a density stratified fluid. Katija and Dabiri [2009] suggested that the divergent drift volume in the viscous limit can be an essential contribution to the mixing of oceans. The underlying idea is that this divergent drift amounts to an indefinite increase in the *available potential energy* [Lorenz, 1955; Vallis, 2017; Winters et al., 1995] of the oceans, which can be released elsewhere (via instabilities) to contribute to the mixing of the oceans. Our calculations in the Stokes-stratification regime (large Pe limit) clearly showed that there would be a convergent drift volume with the incorporation of a weak density stratification. Although not a direct measure of the mixing, the convergent drift volume in a density stratified fluid implies that the available potential energy cannot be an arbitrarily large quantity at any instant of time. This available potential energy is intimately related to the drift displacements and the perturbed density disturbance fields calculated in the present thesis. The concept of the available potential energy was first introduced by Lorenz [1955] in the context of atmospheric circulation. Available potential energy is defined as the energy released by the fluid as it undergoes adiabatic rearrangement to move towards a minimum energy state. It is important to note that the available potential energy is only an indicator the energy made available for fluid motion; this can be released as the kinetic energy of the fluid via different mechanisms such as instabilities, and subsequent wave generation and interactions.

Wagner et al. [2014] calculated the mixing efficiency defined as the ratio of gravitational potential energy created and the rate of work done by the swimmer; the mixing efficiencies were, however, found to be asymptotically small, as expected for small Pe. However, one will expect a larger mixing efficiency in the convection-dominant limit. This calculation of available potential energy using the disturbance fields evaluated in the present thesis, and thereby the determination of the mixing efficiency, will be considered in future work.

Chapter 4

The rotation of a sedimenting spheroidal particle in a linearly stratified ambient

In this chapter, we obtain the expression for the angular velocity of a torque-free sedimenting spheroid in a linearly stratified fluid in the limit of $Re \ll 1$, $Ri_v \ll 1$,using a reciprocal theorem formulation. The interest is in the contribution to the angular velocity arising from the perturbation of the ambient stratification, that is, the hydrodynamic component of the stratification torque. In what follows, we present a brief introduction to the literature, before formulating the problem and presenting the detailed results.

4.1 Introduction

The present study is specifically motivated by very recent experiments involving cylindrical and disk-shaped particles (Mrokowska [2018],Mercier et al. [2020],Mrokowska [2020a],Mrokowska [2020b]) that are among the first to systematically explore the role of shape anisotropy for sedimenting particles in a heterogeneous stably stratified fluid ambient. The experiments and computations reported by Mercier et al. [2020] pertain to a linearly stratified ambient, while the experiments reported in Mrokowska [2018],Mrokowska [2020a] and Mrokowska [2020b] pertain to a non-linearly stratified fluid layer sandwiched between homogeneous upper and lower layers (mimicking the well-known three-layered verical structure of the ocean away from the poles). While the detailed results obtained for the two sets of experiments differ on account of the differing nature of the ambient stratification, one of the most important findings, common to both sets of experiments, pertains to the ability of the torque due to buoyancy forces to oppose, and even overwhelm the aforementioned inertial torque that acts in a homogeneous setting, thereby turning the particle longside-on (see Figures 4.1 and 4.2 illustrating broadside-on and longside-on configurations for prolate and oblate spheroids respectively). It is worth mentioning here that the rotation of an anisotropic particle (a prolate spheroid of aspect ratio 2) towards the edgewise configuration, in a stratified setting, was originally discovered in the numerical simulations of Doostmohammadi and Ardekani [2014]. Such a rotation was found to occur for both a linear and a discontinuous stratification (a density interface). This study of anisotropic particle reorientation was in turn motivated by an earlier work, of the same authors, where they found analogous behavior in the context of pair-interactions of sedimenting spherical particles; particle-pairs in close contact were found to rotate at a slower rate in a stratified ambient, implying a stratification-induced torque favoring a long-side orientation of the resulting dumbbell-shaped configuration [Doostmohammadi and Ardekani, 2013]. A recent theoretical study [Dandekar et al., 2020] has analytically determined the stratification-induced corrections to the force and torque acting on a non-spherical particle settling in a viscous linearly stratified ambient. While a correction to the force was determined in terms of the viscous Richardson number (Ri_v defined below in section 4.2) for both chiral and achiral particles, a hydrodynamic torque was found to arise from buoyancy forces only for chiral particles, the origin of this torque being the translation-rotation coupling that already exists for such particles in a homogeneous ambient. As will be seen later, the hydrodynamic torque for the spheroids (achiral particles) considered here, arises at an order higher than that explored in the above study. Thus, the said analysis does not explain one of the principal observations in the aforementioned experiments, and simulations, involving the stratification-induced transition of a sedimenting anisotropic but achiral particle from a broadside-on to an edgewise configuration.

In this chapter, we show that buoyancy forces associated with the ambient stratification do lead to a torque even for achiral particles modeled as prolate and oblate spheroids of an arbitrary aspect ratio. This stratification-induced torque consists of both hydrostatic and hydrodynamic components; the former contribution has been given in [Dandekar et al., 2020] for a slender cylindrical rod of a circular cross-section, and acts to orient the rod broadside-on. Consistent with this finding, it is shown here (also see [Varanasi et al., 2021]) that the hydrostatic contribution turns a spheroid broadside-on regardless of whether its prolate or oblate, and regardless of its aspect ratio. However, the hydrodynamic component of the stratification-induced torque is shown to be asymptotically larger than the hydrostatic one for large Pe, and orients spheroids edgewise, thereby offering the first theoretical explanation of the experimental observations above - that of edgewise settling of an anisotropic particle in a stratified fluid.

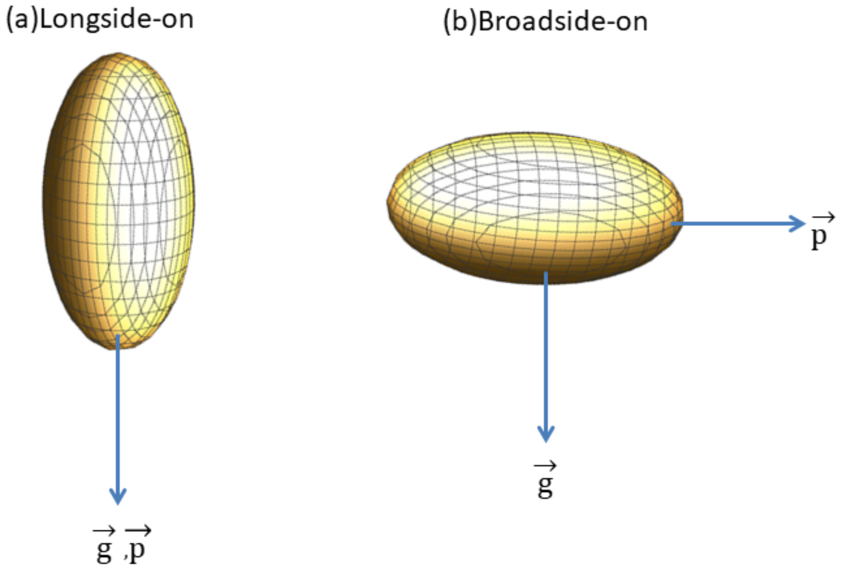

Fig. 4.1 Figures (a) and (b) depict the prolate spheroid’s longside-on and broadside-on orientations, respectively.

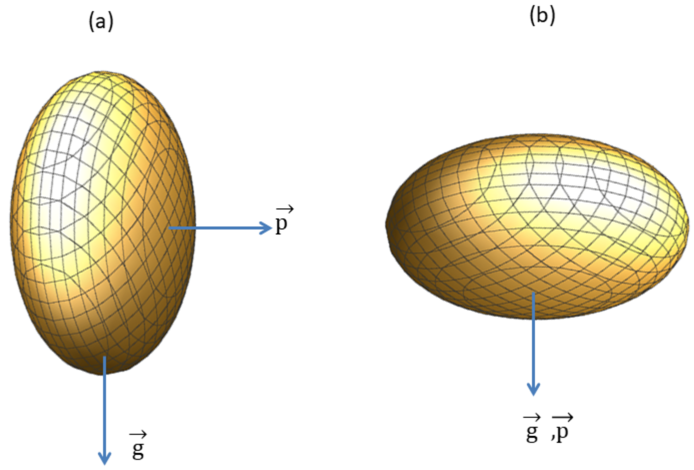

Fig. 4.2 Figures (a) and (b) depict the oblate spheroid's longside-on and broadside-on orientations, respectively.

The layout of the chapter is as follows. In section 4.2, we describe the reciprocal theorem formulation which yields the angular velocity of a spheroid sedimenting in a linearly stratified viscous fluid in terms of distinct contributions originating from the effects of fluid inertia and the buoyancy forces associated with the ambient stratification. The angular velocity contributions arising from the fluid inertial torque, and the hydrostatic component of the stratification torque, are readily evaluated on account of their regular character; the former has been given in [Dabade et al., 2015b]. We summarize these results briefly in section 4.3. The calculation of the hydrodynamic component of the stratification torque is more involved, being sensitively dependent on *Pe*. The regular contributions arising in the small Pe limit Varanasi et al. [2021] are briefly summarized in section 4.4.1. Certain aspects pertaining to singular contributions in the small-*Pe* regime are discussed in section 4.4.1 and in appendix B.1; specifically, the derivation of an outer-region torque contribution in the latter appendix helps demarcate the regime of validity of the results summarized in section 4.4.1. The large Pe calculation which forms the main part of the present chapter is presented in section 4.4.2. Finally, section 4.5 discusses the transition from broadside-on to edgewise settling that arises due to the competing influences of the inertial and hydrodynamic components of the stratification torque, at large *Pe*, and ends with a qualitative comparison with recent experiments. In section 4.6, we briefly summarize our results.

4.2 A sedimenting spheroid in a linearly stratified ambient: The generalized reciprocal theorem formulation

The torque acting on a spheroid, sedimenting in a stably stratified fluid ambient, is derived below using the generalized reciprocal theorem (see Kim and Karrila [1991];Dabade et al. [2015a, 2016]). The theorem relates two pairs of stress and velocity fields, and may be stated in the form:

$$\int_{S_p} \sigma_{ij}^{(2)} u_i'^{(1)} n_j dS - \int_{S_p} \sigma_{ij}^{(1d)} u_i^{(2)} n_j dS = \int \frac{\partial \sigma_{ij}^{(1d)}}{\partial x_j} u_i^{(2)} dV, \tag{4.1}$$

where S_p denotes the surface of the spheroid, and with the neglect of the surface integrals at infinity, the volume integral on the right hand side of (4.1) is over the unbounded fluid domain external to the spheroid. In (4.1), the pair $(\boldsymbol{\sigma}^{(1d)}, \boldsymbol{u}'^{(1)})$ denotes the dynamic stress and velocity fields associated with the problem of interest viz. a torque-free spheroid sedimenting under gravity in an ambient linearly stratified medium for small Reynolds (Re) and viscous Richardson (Ri_v) numbers, with $\boldsymbol{u}'^{(1)}$ corresponding to the lab reference frame with a quiescent far-field ambient (the prime indicates that the velocity field has a disturbance-like character in this reference frame, and decays away in the far-field). The Reynolds and viscous Richardson numbers measure the relative importance of inertial and buoyancy forces relative to viscous forces, respectively, and the aforementioned smallness of these parameters corresponds therefore to the case where inertia and stratification act as weak perturbing influences about a leading order Stokesian approximation; note, however, that the result for the stratification torque obtained below in section 4.4.1 is an exception to this general assumption, in that it continues to be valid for finite values of the Richardson number. The Reynolds and Richardson numbers are defined later in this section when writing down the non-dimensional system of governing equations; the precise definition of the dynamic stress field, $\boldsymbol{\sigma}^{(1d)}$, is also provided at the same place.

The pair $(\boldsymbol{\sigma}^{(2)}, \boldsymbol{u}^{(2)})$, that defines the test problem in (4.1), corresponds to the stress and velocity fields associated with inertialess ($Re = 0$) rotation of the same spheroid, about an axis orthogonal to its axis of symmetry, in a homogeneous and otherwise quiescent ambient with the same (assumed constant) viscosity as the medium in the actual problem. The equations governing the test problem may be written as

$$\frac{\partial u_i^{(2)}}{\partial x_i} = 0, \tag{4.2}$$

$$\mu \frac{\partial^2 u_i^{(2)}}{\partial x_j^2} - \frac{\partial p^{(2)}}{\partial x_i} = 0, \tag{4.3}$$

with the boundary condition $\boldsymbol{u}^{(2)} = \boldsymbol{\Omega}^{(2)} \wedge \boldsymbol{x}$ on S_p, $\boldsymbol{\Omega}^{(2)}$ being the angular velocity of the spheroid in the test problem, and far-field decay conditions for both $\boldsymbol{u}^{(2)}$ and $p^{(2)}$. Note that the test velocity ($\boldsymbol{u}^{(2)}$) and stress ($\boldsymbol{\sigma}^{(2)}$) fields decay as $O(\frac{1}{r^2})$ and $O(\frac{1}{r^3})$, respectively, r being the distance away from the spheroid; this decay, together with the decaying (dynamic) stress field in the problem of interest, justifies the neglect of the surface integrals at infinity in (4.1). Use of the aforementioned surface boundary condition in (4.1) leads to

$$\int_{S_p} \sigma_{ij}^{(2)} u_i'^{(1)} n_j dS - \Omega_j^{(2)} \int_{S_p} \varepsilon_{ijk} x_k \sigma_{il}^{(1d)} n_l dS = \int \frac{\partial \sigma_{ij}^{(1d)}}{\partial x_j} u_i^{(2)} dV \tag{4.4}$$

where the second integral on the left hand side in (4.4) now denotes the torque due to the dynamic stress field $\boldsymbol{\sigma}^{(1d)}$. We postpone further simplification of (4.4) until after we define the pair $(\boldsymbol{\sigma}^{(1d)}, \boldsymbol{u}'^{(1)})$ below.

As mentioned above, problem 1 corresponds to an arbitrarily oriented spheroid, sedimenting under the action of a gravitational force $F\hat{\boldsymbol{g}}$, in an ambient fluid that is linearly stratified (along $\hat{\boldsymbol{g}}$) in the absence of the fluid motion induced by the spheroid. The unit vector $\hat{\boldsymbol{g}}$ is aligned along gravity, with g denoting the magnitude of the gravitational acceleration, and $F = \frac{4\pi}{3} L b^2 \Delta\rho g$ $(\frac{4\pi}{3} L^2 b \Delta\rho g)$ denoting the buoyant weight for a prolate (oblate) spheroid. Here, L and b are the semi-major and semi-minor axes of the spheroid, with $\kappa = L/b$ and b/L being the aspect ratios of prolate and oblate spheroids, respectively; thus, $\kappa > 1$ and < 1 for the prolate and oblate cases. The density difference that enters the buoyant weight above is $\Delta\rho = \rho_s - \rho_\infty^{(1)}(\boldsymbol{x}_c)$, with ρ_s being the density of the spheroid (assumed homogeneous), and $\rho_\infty^{(1)}(\boldsymbol{x}_c) = \rho_0$ being the ambient fluid density at the center of the spheroid. The latter simplification arises because of the linear stratification and the fore-aft symmetry of the spheroid, both of which imply that the weight of the equivalent stratified spheroidal fluid blob that gives the buoyant force, within an Archimedean interpretation, is the same as the weight of a homogeneous fluid blob with density equal to the ambient value at the spheroid center. In a lab-fixed reference frame, the ambient density field in problem 1 may be written in the form:

$$\rho_\infty^{(1)}(\boldsymbol{x}^L) = \rho_0 + \gamma x_i^L \hat{g}_i \tag{4.5}$$

where $\boldsymbol{x}^L$ denotes the position vector in laboratory coordinates with the spheroid center as the origin, and $\gamma > 0$ is the constant density gradient that characterizes the stable ambient stratification. The calculations for the torque are, however, best done in a reference frame translating with the spheroid where a quasi-steady state is assumed to prevail at leading order. The latter assumption is motivated by the asymptotically weak rotation of the sedimenting spheroid in the limit $Re, Ri_v \ll 1$. The precise condition for the quasi-steady state assumption to hold depends on Pe, being more restrictive for large Pe, and is stated later alongside the results for the spheroid angular velocity for small and large Pe, obtained below.

The ambient density in the particle-fixed reference frame takes the form:

$$\rho_\infty^{(1)}(\boldsymbol{x}) = \rho_0 + \gamma(x_i + U_i t)\hat{g}_i, \tag{4.6}$$

$\boldsymbol{x}$ being the position vector in the new reference frame. In (4.6), $\boldsymbol{U}$ is the spheroid settling velocity, and related to the force $(F\hat{\boldsymbol{g}})$ via a mobility tensor that is a known function of the spheroid aspect ratio κ. In terms of the spheroid orientation vector $\boldsymbol{p}$, one may write $\boldsymbol{U} = \frac{1}{\mu L}[X_A^{-1}\boldsymbol{pp} + Y_A^{-1}(\boldsymbol{I} - \boldsymbol{pp})] \cdot (F\hat{\boldsymbol{g}})$, $X_A(\kappa)$ and $Y_A(\kappa)$ being the non-dimensional axial and transverse translational resistance functions. The aspect ratio dependence of these functions is well known (see Kim and Karrila [1991]), and is given in Appendix A.1 for convenient reference. Note that the ambient density at the center of the spheroid $(\boldsymbol{x} = 0)$ is given by $\rho_0 + \gamma(U_i\hat{g}_i)t$, the time dependence arising from the spheroid translation. The equations of motion for problem 1, within a Boussinesq framework where the fluid density multiplying the inertial terms is taken as a constant ρ_0 (say), may be written as

$$\frac{\partial u_i^{(1)}}{\partial x_i} = 0, \tag{4.7}$$

$$\mu\frac{\partial^2 u_i^{(1)}}{\partial x_j^2} - \frac{\partial p^{(1)}}{\partial x_i} = \rho_0 u_j^{(1)}\frac{\partial u_i^{(1)}}{\partial x_j} - \rho^{(1)} g_i, \tag{4.8}$$

$$\frac{\partial \rho^{(1)}}{\partial t} + u_j^{(1)}\frac{\partial \rho^{(1)}}{\partial x_j} = D\nabla^2\rho^{(1)}, \tag{4.9}$$

where D is the diffusivity of the stratifying agent (Candelier et al. [2014]; Mehaddi et al. [2018]; Shaik and Ardekani [2020b]). One now defines the perturbation density $(\rho'^{(1)})$ via $\rho^{(1)} = \rho_0 + \gamma(x_i + U_i t)\hat{g}_i + \rho'^{(1)}$. Next, using the scales $U = F/(\mu L X_A)$ for the velocity, L

for the length, $\mu U/L$ for the pressure and γL for $\rho'^{(1)}$, one obtains the following system of non-dimensional equations:

$$\frac{\partial u_i^{(1)}}{\partial x_i} = 0, \tag{4.10}$$

$$\frac{\partial^2 u_i^{(1)}}{\partial x_j^2} - \frac{\partial p^{(1)}}{\partial x_i} + \frac{\rho_0 g L^2}{\mu U}\hat{g}_i + Ri_v(\hat{U}_j t + x_j)\hat{g}_j\hat{g}_i = Re\, u_j^{(1)}\frac{\partial u_i^{(1)}}{\partial x_j} - Ri_v \rho'^{(1)}\hat{g}_i, \tag{4.11}$$

$$u_j^{(1)}\frac{\partial \rho'^{(1)}}{\partial x_j} + (\hat{U}_j + u_j^{(1)})\hat{g}_j = \frac{1}{Pe}\nabla^2 \rho'^{(1)}, \tag{4.12}$$

where $Re = \rho_0 UL/\mu$, $Ri_v = \gamma L^3 g/(\mu U)$ and $Pe = UL/D$ are the Reynolds, viscous Richardson and Peclet numbers, respectively; note that $Ri_v = Re/Fr^2$, where Fr is the Froude number, and the usual measure of the importance of stratification in the inviscid limit (Turner [1979]). In (4.10-4.12), we continue to use the same notation for the dimensionless fields for simplicity. The velocity fields, in the lab reference frame used in (4.1), and in the particle-fixed reference frame adopted in (4.10-4.12) are related as $\boldsymbol{u}'^{(1)} = (\hat{\boldsymbol{U}} + \boldsymbol{u}^{(1)})$, with $\hat{\boldsymbol{U}} = \left[p_i p_j + X_A/Y_A(\delta_{ij} - p_i p_j)\right]\hat{g}_j$, now being a dimensionless vector along the direction of settling, and $-\hat{\boldsymbol{U}}$ therefore being the far-field ambient flow in the particle-fixed frame; note that $\hat{\boldsymbol{U}}$ is not a unit vector for an arbitrarily oriented spheroid, and reduces to one only for a spheroid aligned with gravity. Thus, the combination $(\hat{\boldsymbol{U}} + \boldsymbol{u}^{(1)}) \cdot \hat{\boldsymbol{g}}$ in (4.12) denotes the convection of the (constant) base-state density gradient by the component of the disturbance velocity field ($u_3'^{(1)}$) along gravity. Finally, the time dependence of $\boldsymbol{u}^{(1)}$ in (4.11), and that of $\rho'^{(1)}$ in (4.12) in particular, that arise from the (slow) rotation of the spheroid, have been neglected owing to the quasi-steady state assumption made in (4.10-4.12); the time dependence of the density multiplying the inertial terms, on account of spheroid translation, has already been neglected within the Boussinesq approximation.

One now defines a disturbance pressure field ($p'^{(1)}$) via $p^{(1)} = p_0^{(1)} + p'^{(1)}$ with

$$\frac{\partial p_0^{(1)}}{\partial x_i} = \frac{\rho_0 g L^2}{\mu U}\hat{g}_i + Ri_v(\hat{U}_j t + x_j)\hat{g}_j\hat{g}_i, \tag{4.13}$$

so that $p_0^{(1)}$ defines the baseline hydrostatic contribution arising from the ambient linear stratification. Having incorporated the baseline hydrostatic variation in $p_0^{(1)}$, one may write the governing equations above in terms of the disturbance velocity, pressure and density fields as follows:

$$\frac{\partial u_i'^{(1)}}{\partial x_i} = 0, \tag{4.14}$$

$$\frac{\partial \sigma_{ij}^{(1d)}}{\partial x_j} = Re(-\hat{U}_j + u_j'^{(1)}) \frac{\partial u_i'^{(1)}}{\partial x_j} - Ri_v \rho'^{(1)} \hat{g}_i, \tag{4.15}$$

$$(-\hat{U}_j + u_j'^{(1)}) \frac{\partial \rho'^{(1)}}{\partial x_j} = -u_j'^{(1)} \hat{g}_j + \frac{1}{Pe} \nabla^2 \rho'^{(1)}. \tag{4.16}$$

where the left hand side of (4.11) has been written in terms of the dynamic stress field $\boldsymbol{\sigma}^{(1d)}$ defined by $\boldsymbol{\sigma}^{(1d)} = -p'^{(1)}\boldsymbol{I} + (\boldsymbol{\nabla u}'^{(1)} + \boldsymbol{\nabla u}'^{(1)\dagger})$. Thus, one has the relation $\boldsymbol{\sigma}^{(1)} = -p_0^{(1)}\boldsymbol{I} + \boldsymbol{\sigma}^{(1d)}$ between the total $(\boldsymbol{\sigma}^{(1)})$ and the dynamic stress fields of problem 1.

Assuming the spheroid in problem 1 to rotate with an angular velocity $\boldsymbol{\Omega}^{(1)}$, one has the boundary condition $\boldsymbol{u}'^{(1)} = \boldsymbol{\Omega}^{(1)} \wedge \boldsymbol{x}$ on S_p. Using this in the first surface integral in (4.4), and substituting the divergence of the dynamic stress from (4.15) in the volume integral in (4.1), one obtains

$$\Omega_j^{(1)} \mathscr{L}_j^{(2)} - \Omega_j^{(2)} \mathscr{L}_j^{\sigma(1)d} = Re \int u_i^{(2)} (-\hat{U}_j + u_j'^{(1)}) \frac{\partial u_i'^{(1)}}{\partial x_j} dV - Ri_v \int \rho'^{(1)} \hat{g}_i u_i^{(2)} \, dV, \tag{4.17}$$

where $\mathscr{L}^{\sigma(1)d}$ now denotes the torque contribution due to the dynamic stress $\boldsymbol{\sigma}^{(1d)}$. Now, the particle in problem 1 is torque-free. In light of the above relation between $\boldsymbol{\sigma}^{(1)}$ and $\boldsymbol{\sigma}^{(1d)}$, the total torque $(\mathscr{L}^{(1)})$ may be written as $\mathscr{L}^{(1)} = \mathscr{L}^{\sigma(1)d} + \mathscr{L}^{\sigma(1)s}$, where the dynamic torque component $\mathscr{L}^{\sigma(1)d}$ includes both inertia and stratification-induced contributions, while $\mathscr{L}^{\sigma(1)s}$ is the hydrostatic contribution due to the pressure field $p_0^{(1)}$ associated with the linearly varying density field of the stably stratified ambient, and defined by (4.13). Thus, $\mathscr{L}^{(1)} = 0 \Rightarrow \mathscr{L}^{\sigma(1)d} = -\mathscr{L}^{\sigma(1)s}$, and the relation involving the spheroid angular velocity in problem 1 takes the following form:

$$\Omega_j^{(1)} \mathscr{L}_j^{(2)} = Re \int u_i^{(2)} (-\hat{U}_j + u_j'^{(1)}) \frac{\partial u_i'^{(1)}}{\partial x_j} dV - \left[\Omega_j^{(2)} \mathscr{L}_j^{\sigma(1)s} + Ri_v \int \rho'^{(1)} \hat{g}_i u_i^{(2)} \, dV \right], \tag{4.18}$$

where

$$\mathscr{L}_i^{\sigma(1)s} = -\varepsilon_{ijk} \int_{S_p} p_0^{(1)} x_j n_k dS, \tag{4.19}$$

with $p_0^{(1)}$ being defined in (4.13). Since the buoyancy force in a homogeneous ambient acts through the centre of the spheroid, only the linearly varying term in (4.13) contributes to the hydrostatic torque, which may therefore be written as

$$\mathscr{L}_i^{\sigma(1)s} = -Ri_v\,\varepsilon_{ijk}\int_{S_p}\frac{1}{2}(x_l\hat{g}_l)^2 x_j n_k dS, \tag{4.20}$$

the contribution above remaining the same regardless of the choice of reference frame ($\boldsymbol{x}$ or $\boldsymbol{x}^L$). On substitution of the above expression for $\mathscr{L}_k^{\sigma(1)s}$, and using the relation $\boldsymbol{u}_i^{(2)} = \boldsymbol{U}_{ij}^{(2)}\boldsymbol{\Omega}_j^{(2)}$ (on account of the linearity of the Stokes equations), the second order tensor $\boldsymbol{U}_{ij}^{(2)}$ being known in closed form (see Dabade et al. [2015a], and section 4.3 below), (4.18) takes the form:

$$\begin{aligned}\Omega_j^{(1)}\mathscr{L}_j^{(2)} =&\,\Omega_k^{(2)}\left\{Re\int U_{jk}^{(2)}\,(-\hat{U}_l + u_l'^{(1)})\frac{\partial u_j'^{(1)}}{\partial x_l}dV\right.\\ &\left.-Ri_v\left[-\frac{1}{2}\varepsilon_{klm}\int_{S_p}(x_j\hat{g}_j)^2 x_l n_m dS + \int \rho'^{(1)}\hat{g}_j U_{jk}^{(2)}\,dV\right]\right\},\end{aligned} \tag{4.21}$$

Again, on account of linearity, one may write the torque on the rotating spheroid in the test problem, in the form $\mathscr{L}^{(2)} = [X_C\boldsymbol{pp} + Y_C(\boldsymbol{I}-\boldsymbol{pp})]\cdot\boldsymbol{\Omega}^{(2)}$, where $X_C(\kappa)$ and $Y_C(\kappa)$ are the non-dimensional axial and transverse rotational resistance functions, and are known functions of κ (Kim and Karrila [1991]), whose expressions are given in Appendix A.1. By symmetry, the sedimenting spheroid cannot spin about its axis regardless of its orientation, and therefore without loss of generality, the test problem 2 can be taken as that of a tranverse rotation in the inertialess limit ($\boldsymbol{\Omega}^{(2)}\cdot\boldsymbol{p} = 0$), in which case the test-torque-angular-velocity relation takes the simpler form $\mathscr{L}^{(2)} = Y_C\boldsymbol{\Omega}^{(2)}$. Finally, accounting for the fact that the test angular velocity $\boldsymbol{\Omega}^{(2)}$ can point in an arbitrary direction in a plane perpendicular to $\boldsymbol{p}$, one obtains the following relation for the spheroid angular velocity in problem 1:

$$\begin{aligned}\Omega_i^{(1)} = \frac{1}{Y_C}&\left\{Re\int U_{ji}^{(2)}(-\hat{U}_l + u_l'^{(1)})\frac{\partial u_j'^{(1)}}{\partial x_l}dV + Ri_v\left[\varepsilon_{ilm}\int_{S_p}\frac{1}{2}(x_j\hat{g}_j)^2 x_l n_m dS\,.\right.\right.\\ &\left.\left.-\int \rho'^{(1)}\hat{g}_j U_{ji}^{(2)}\,dV\right]\right\}.\end{aligned} \tag{4.22}$$

Since a settling spheroid in a homogeneous ambient must retain its initial orientation in the Stokes limit on account of reversibility, expectedly, the rotation of the spheroid, as given by

(4.22), arises due to the combined (weak) effects of fluid inertia and the ambient stratification. The first term within the curly brackets in (4.22) corresponds to the inertial torque, while the second and third terms which have been grouped together (within square brackets) correspond to the hydrostatic and hydrodynamic components of the stratification torque, respectively. The hydrostatic torque only involves knowledge of the ambient density field, and is easily evaluated. The inertial torque has a regular character in that the dominant contributions to the $O(Re)$ volume integral in (4.22) arise from a volume of $O(L^3)$ around the sedimenting spheroid, and therefore, the integral may again readily be determined at leading order using the Stokesian approximations for the velocity fields involved, as has been done in Dabade et al. [2015a]. The evaluation of these two simpler contributions is detailed in the next section. The nature of the hydrodynamic torque arising from the perturbed stratification depends crucially on Pe, and this more complicated calculation is given in sections 4.4.1 and 4.4.2, for small and large Pe, respectively.

4.3 The spheroidal angular velocity due to the inertial and hydrostatic torque contributions

The $O(Re)$ inertial angular velocity in (4.22) has recently been calculated for spheroids, both prolate and oblate, of an arbitrary aspect ratio (see Dabade et al. [2015a]). Although the analysis in Dabade et al. [2015a] pertains to the limit $Re \ll 1$, the results have been shown to remain qualitatively valid even for Re's of order unity (see Jiang et al. [2020]). As mentioned above, this angular velocity has a regular character, as may be seen from the convergence of the inertial volume integral in (4.18) based on the leading order Stokesian estimate for the integrand. As argued in Dabade et al. [2015a], the inertial acceleration $\boldsymbol{u}^{(1)} \cdot \nabla \boldsymbol{u}'^{(1)} \sim \hat{\boldsymbol{U}} \cdot \nabla \boldsymbol{u}'^{(1)} \sim O(1/r^2)$ for distances large compared to L, or $r \gg 1$ in dimensionless terms, on using $\boldsymbol{u}'^{(1)} \sim O(1/r)$ for the Stokeslet field due to the translating spheroid. The test velocity field $\boldsymbol{u}^{(2)}$ due to the rotating spheroid has the character of a rotlet-cum-stresslet in the far-field, and is therefore $O(1/r^2)$. This leads to an integrand that decays as $\hat{\boldsymbol{U}} \cdot \nabla \boldsymbol{u}'^{(1)} \cdot \boldsymbol{u}^{(2)} \sim O(1/r^4)$ for $r \gg 1$, implying a convergent volume integral. This volume integral has been evaluated in closed form using spheroidal coordinates in Dabade et al. [2015a]. For the prolate case, the spheroidal coordinates (ξ, η, ϕ) are defined by the relations: $x_1 + \mathrm{i}x_2 = d\bar{\xi}\bar{\eta}\exp(i\phi)$, $x_3 = d\xi\eta$, with the 3-axis of the Cartesian system ($\mathbf{1}_3$) aligned with the spheroid axis of symmetry. Here, $1 \leq \xi < \infty$, $|\eta| \leq 1$ and $0 \leq \phi < 2\pi$, with $\bar{\xi} = (\xi^2 - 1)^{\frac{1}{2}}$ and $\bar{\eta} = (1 - \eta^2)^{\frac{1}{2}}$. The constant-$\xi$ surfaces correspond to confocal prolate spheroids and the constant-η surfaces to confocal two-sheeted hyperboloids, both with the interfoci distance $2d$, and the constant-ϕ

surfaces are planes passing through the axis of symmetry. The corresponding expressions for the oblate case may be obtained by the substitutions $d \leftrightarrow -\mathrm{i}d$, $\xi \leftrightarrow \mathrm{i}\bar{\xi}$, the constant-$\xi$ and η surfaces now being confocal oblate spheroids and single-sheeted hyperboloids, respectively. In either case, the spheroid is the surface $\xi = \xi_0$, its aspect ratio being given by $\kappa = \frac{\xi_0}{\bar{\xi}_0}$ and $\frac{\bar{\xi}_0}{\xi_0}$ for prolate and oblate spheroids; thus, the near-spherical limit ($\kappa \to 1$) for either prolate or oblate spheroids corresponds to $\xi_0 \to \infty$, while the slender fiber ($\kappa \to \infty$) and flat disk ($\kappa \to 0$) limits correspond to $\xi_0 \to 1$. The fluid domain in the volume integrals in (4.22) corresponds to $\xi \geq \xi_0$.

For a prolate spheroid, the volume integration can be carried out analytically which is detailed in Dabade et al. [2015b];Varanasi et al. [2021], and the inertial angular velocity ($\Omega^{(1)I}$) is given by

$$\Omega_i^{(1)I} = Re\left[\frac{F_I^p(\xi_0)X_A}{Y_C Y_A}(\varepsilon_{ijk}\hat{g}_j p_k \hat{g}_l p_l)\right], \tag{4.23}$$

for prolate spheroids. The corresponding expression for the oblate case may be obtained by the aforementioned substitutions viz. $d \leftrightarrow -\mathrm{i}d$, $\xi_0 \leftrightarrow \mathrm{i}\bar{\xi}_0$ in the dimensional angular velocity, and is given by

$$\Omega_i^{(1)I} = Re\left[\frac{F_I^o(\xi_0)X_A}{Y_C Y_A}(\varepsilon_{ijk}\hat{g}_j p_k \hat{g}_l p_l)\right]. \tag{4.24}$$

The expressions for $F_I^p(\xi_0)$ and $F_I^o(\xi_0)$, as functions of the spheroid eccentricity ($e = 1/\xi_0$), were first obtained by Dabade et al. [2015a], and are given in Appendix A.1. The inertial angular velocity given by (4.23) and (4.24) orients sedimenting spheroids broadside-on regardless of κ. The combination of the aspect-ratio-dependent functions, $F_I^{p/o}(\xi_0)X_A/(Y_C Y_A)$, that multiplies $Re(\hat{\boldsymbol{g}} \cdot \boldsymbol{p})(\hat{\boldsymbol{g}} \wedge \boldsymbol{p})$, and that determines the κ-dependence of the inertial angular velocities above, is plotted as a function of the eccentricity in 4.3, for both the prolate and oblate cases. One obtains the expected $O(1/\xi_0^2)$ scaling in the near-sphere limit ($\xi_0 \to \infty$); at the other extreme($\xi_0 \to 1$), the inertial angular velocity approaches zero as $O[\ln(\xi_0 - 1)]^{-1}$ in the slender fiber limit, consistent with viscous slender body theory (Khayat and Cox [1989],Subramanian and Koch [2005]), while remaining finite in the limit of a flat disk.

The calculation of the hydrostatic component of the stratification torque in spheroidal coordinates is easily performed, and the angular velocity due to the hydrostatic torque is found to be

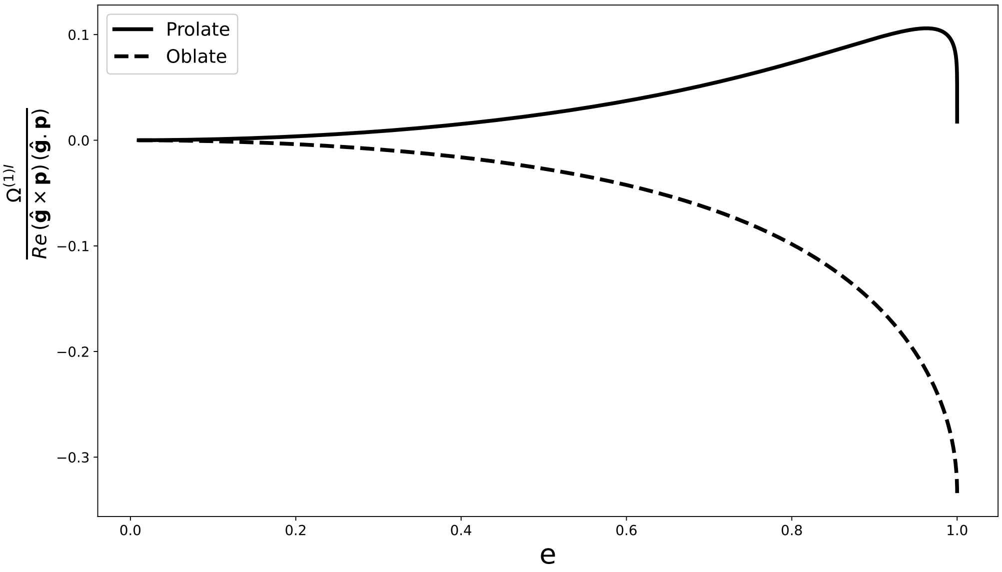

Fig. 4.3 The functions $\frac{F_I^p(\xi_0)X_A}{Y_C Y_A}$ and $\frac{F_I^o(\xi_0)X_A}{Y_C Y_A}$, that characterize the aspect-ratio-dependence of the inertial contributions to the angular velocities of prolate and oblate spheroids, plotted as a function of the spheroid eccentricity. (Reproduced with permission from Varanasi et al. [2021])

,

$$\Omega_i^{(1)s} = Ri_v \frac{4\pi}{15Y_C} \frac{1-\xi_0^2}{\xi_0^4} (\varepsilon_{ijk}\hat{g}_j p_k)(\hat{g}_l p_l), \tag{4.25}$$

for the prolate case, and using the transformations mentioned above,

$$\Omega_i^{(1)s} = Ri_v \frac{4\pi}{15Y_C} \frac{\sqrt{\xi_0^2-1}}{\xi_0^3} (\varepsilon_{ijk}\hat{g}_j p_k)(\hat{g}_l p_l), \tag{4.26}$$

for the oblate case. The angular velocities given by (4.25) and (4.26) also orient the spheroid broadside-on like the inertial torque above. The aspect-ratio-dependent functions that multiply $Ri_v(\hat{\boldsymbol{g}}\cdot\boldsymbol{p})(\hat{\boldsymbol{g}}\wedge\boldsymbol{p})$ in (4.25)and (4.26) are plotted as functions of ξ_0 in Fig. 4.4. Since the hydrostatic torque is only a function of the particle geometry, these aspect ratio functions are algebraically small in both the near-sphere, and the slender fiber and flat-disk limits.

The inertial and hydrostatic angular velocities above have an identical angular dependence, of the form $(\hat{\boldsymbol{g}} \cdot \boldsymbol{p})(\hat{\boldsymbol{g}} \wedge \boldsymbol{p})$, one which is easily inferred based on the requirement that the angular velocity be a pseudovector quadratic in $\hat{\boldsymbol{g}}$ (Dabade et al. [2015a]). The dependence implies that the maximum angular velocity occurs midway between the horizontal ($\hat{\boldsymbol{g}} \cdot \boldsymbol{p} = 0$) and vertical ($\hat{\boldsymbol{g}} \cdot \boldsymbol{p} = 1$) orientations. The hydrostatic torque arises because the point of action of the upward buoyant force, the center of mass of the equivalent stratified fluid blob (in the Archimedean interpretation), lies below the geometric center through which the weight of the (homogeneous) spheroid acts vertically downward. The two forces therefore constitute a couple that turns the spheroid broadside-on. The broadside-on nature of the inertial torque is on account of 'wake-shielding' - the wake associated with the front portion of the spheroid shields the rear, which catches up with the front as a result. As pointed out in Dabade et al. [2015a], this is not literally true for small Re. A signature of the wake arises only on length scales greater than $O(LRe^{-1})$, the Oseen region, in contrast to the scaling arguments above which show that the $O(Re)$ inertial torque arises from fluid inertial forces in a region of $O(L^3)$ (the inner region) around the sedimenting spheroid. Nevertheless, the velocity field in the inner region, at $O(Re)$, reflects the asymmetry of the outer Oseen field, and the sense of rotation remains the same for small Re. Importantly, the broadside-on nature of the inertial and hydrostatic torques imply that the transition from broadside-on to edgewise settling, observed in the recent experiments (see Mercier et al. [2020]) discussed in the introduction, must depend entirely on the hydrodynamic component of the stratification torque, that is, the second term within square brackets on the right hand side in (4.22). While the calculation above shows the hydrostatic component to be $O(Ri_v)$, consistent with the nominal order in (4.22), this is not true of the hydrodynamic component. As will be shown in section 4.4 below, the hydrodynamic component scales as $O(Ri_v)$ only for sufficiently small $Pe\,(\ll Ri_v^{\frac{3}{5}}$ for $Ri_v \ll 1$; see section 4.4.1), when the dominant contribution to the associated torque integral comes from length scales of $O(L)$ similar to the inertial torque above. In the opposite limit of $Pe \gg 1$, and for the so-called Stokes stratification regime corresponding to $Re \ll Ri_v^{\frac{1}{3}}$ (see Mehaddi et al. [2018], Varanasi and Subramanian [2021]), the dominant contributions to the torque integral arise from much larger length scales of $O(LRi_v^{-\frac{1}{3}})$, and the hydrodynamic component scales as $O(Ri_v^{\frac{2}{3}})$, being much larger than the hydrostatic component above. Before proceeding with the calculation of the hydrodynamic component of the stratification torque, it is worth remarking on the nature of the coupling between the inertial and stratification torque contributions that is not obvious from the formal result (4.22) above, where they appear as separate additive contributions. On account of the convergent volume integral, the $O(Re)$ inertial angular velocity, as given by (4.23) and (4.24), only involves the Stokesian fields in a homogeneous ambient, and is evidently independent

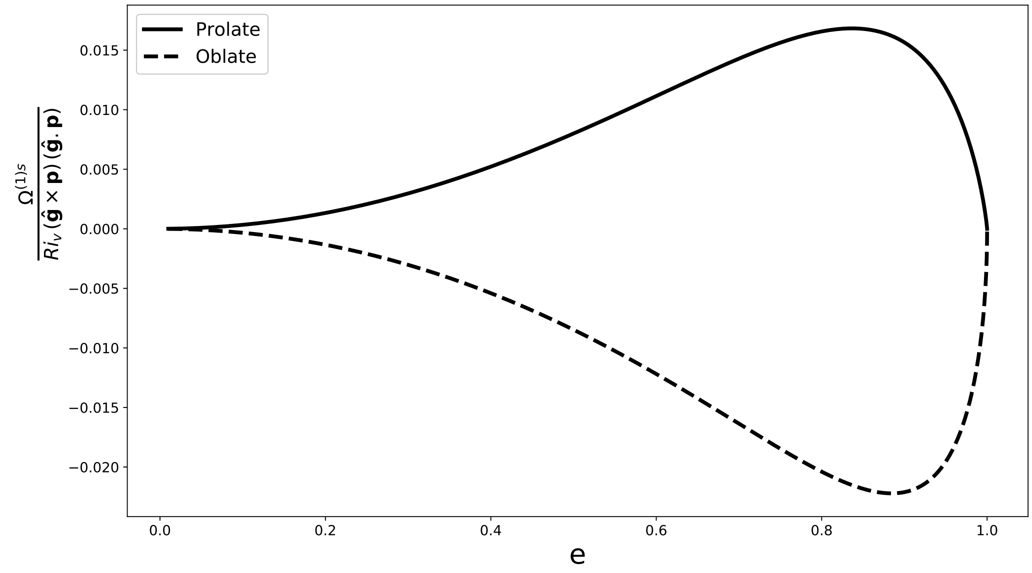

Fig. 4.4 The aspect-ratio-dependent functions multiplying $Ri_v(\hat{\boldsymbol{g}}\cdot\boldsymbol{p})(\hat{\boldsymbol{g}}\wedge\boldsymbol{p})$ in (4.25) and (4.26) for prolate and oblate spheroids that arise from hydrostatic contributions, plotted as a function of the spheroid eccentricity. (Reproduced with permission from Varanasi et al. [2021])

of the ambient stratification. The correction to this leading order estimate is dependent on the nature of the ambient stratification, however, even within the Boussinesq framework. To see this, we return to the inertial volume integral, and estimate the next correction. Recall that the angular velocities in (4.23) and (4.24) were based on the approximating the volume integral by Stokesian estimates, and the torque contribution at the next order requires one to examine the next term in the small-*Re* expansion for the velocity field in problem 1. Writing $\boldsymbol{u}'^{(1)} = \boldsymbol{u}'^{(10)} + Re\,\boldsymbol{u}'^{(11)}$, $\boldsymbol{u}'^{(10)}$ is the Stokesian approximation whose solution is detailed in Dabade et al. [2015b] (see equation 3.20 therein), and is $O(1/r)$ for $r \gg 1$, while $\boldsymbol{u}'^{(11)}$ remains $O(1)$ in the far-field. The latter, of course, implies that the above regular expansion breaks down at length scales of $O(LRe^{-1})$, a manifestation of the singular nature of inertia in an unbounded domain (the so-called Whitehead's paradox; see Leal [1992]). Provided one assumes buoyancy forces to dominate the inertial ones on scales much smaller than the inertial screening length (of $O(LRe^{-1})$), the above far-field estimate of $\boldsymbol{u}'^{(11)}$ may still be used to estimate the correction to the leading $O(Re)$ contribution. The $O(Re^2)$ inertial acceleration is now $\hat{\boldsymbol{U}} \cdot \nabla \boldsymbol{u}'^{(11)} \sim O(1/r)$, and using $\boldsymbol{u}^{(2)} \sim O(1/r^2)$, the resulting volume integral, at $O(Re^2)$, is logarithmically divergent. The divergence will be cut off at the stratification screening length that is $O(Ri_v Pe)^{-\frac{1}{4}}$ for $Pe \ll 1$ (Ardekani and Stocker [2010],List [1971]), and $O(Ri_v^{-\frac{1}{3}})$ for $Pe \gg 1$ (Mehaddi et al. [2018],Varanasi and Subramanian [2021]), implying that the next correction to the inertial angular velocity is $O[Re^2 \ln(Ri_v Pe)^{-\frac{1}{4}}]$ for $Pe \ll 1$ and $O(Re^2 \ln Ri_v^{-\frac{1}{3}})$ for $Pe \gg 1$, and is thereby a function of the ambient stratification. For self consistency, one requires that both of the aforementioned stratification screening lengths be less than $O(Re^{-1})$, which translates to the requirement $Ri_v \gg Pe^{-1}Re^4$ for small *Pe*, and for one to be in the aforementioned Stokes stratification regime ($Ri_v^{\frac{1}{3}} \gg Re$) for large *Pe*.

4.4 The spheroidal angular velocity due to the hydrodynamic component of the stratification contribution

Owing to the differing character of the hydrodynamic component in the limits of small and large *Pe*, the calculations in these two asymptotic regimes are carried out in separate subsections below. Keeping in mind that $Pe = RePr$, *Pr* being the Prandtl number, the small *Pe* case doesn't necessarily place a restriction on *Pr* which may either be small or large (although, large *Pr* imposes a greater restriction on the smallness of *Re* since *Re* must now be smaller than $O(Pr^{-1})$). However, the assumption of small *Re* implies that the large *Pe* case necessarily requires a large *Pr* which may be realized in experiments that use salt as a stratifying agent.

4.4.1 The hydrodynamic stratification torque in the diffusion-dominant limit ($Pe \ll 1$)

In the limit $Pe \ll 1$, one may neglect the convective terms in the advection diffusion equation (4.16), and the density perturbation $\rho'^{(1)}$ in the stratification torque integral therefore arises as a diffusive response to the no-flux condition that must be satisfied on the spheroid surface. As a result, the spheroid acts as a concentration-dipole singularity in the far-field ($r \gg 1$), implying that $\rho'^{(1)}$ must decay as $O(1/r^2)$. Since the test velocity field $\boldsymbol{u}^{(2)}$ corresponding to the rotating spheroid also decays as $O(1/r^2)$, the integrand is $O(1/r^4)$ for $r \gg 1$. This decay is the same as that of the inertial integrand estimated above, and the integral for the hydrodynamic stratification torque is therefore convergent for small Pe, based on the leading order diffusive estimates above. Thus, the effects of stratification arise as a regular perturbation for small Pe, or said differently, the dominant contribution to the hydrodynamic component of the stratification torque arises from buoyancy forces in a volume of $O(L^3)$ around the sedimenting spheroid. As a consequence and as is shown below, for small Pe, the hydrodynamic component is $O(Ri_v)$ similar to the hydrostatic component given in (4.25) and (4.26) above. It turns out that there is, in fact, a more severe constraint on the Peclet number; as explained below under a separate subheading, the $O(Ri_v)$ scaling for the hydrodynamic component holds only when $Pe \ll Ri_v^{\frac{3}{5}} \ll 1$.

To determine the detailed dependence of the $O(Ri_v)$ hydrodynamic component on κ, one needs to solve for the density perturbation $\rho'^{(1)}$ which satisfies

$$\nabla^2 \rho'^{(1)} = 0. \tag{4.27}$$

in the fluid domain $\xi \geq \xi_0$. The no-flux boundary condition on the spheroid surface ($\xi = \xi_0$) may be written as $\mathbf{1}_\xi \cdot \boldsymbol{\nabla} \rho'^{(1)} = -\mathbf{1}_\xi \cdot \hat{\boldsymbol{g}}$ where we have used that $\boldsymbol{n} = \mathbf{1}_\xi$, and the right hand side of the boundary conditon arises from the gradient of the linearly varying ambient density; there is the additional requirement of far-field decay viz. $\rho'^{(1)} \to 0$ for $\xi \to \infty$. Note that the linearity of the governing equation (4.27) and the boundary conditions in $\rho'^{(1)}$, and the linear dependence on $\hat{\boldsymbol{g}}$ of the surface boundary condition above, imply that $\rho'^{(1)}$ must be linear in $\hat{\boldsymbol{g}}$ at leading order for small Pe. From (4.22), the hydrodynamic component of the stratification torque must therefore be quadratic in $\hat{\boldsymbol{g}}$. This implies that the hydrodynamic torque must have an angular dependence identical to the inertial and hydrostatic contributons, of the form $(\hat{\boldsymbol{g}} \wedge \boldsymbol{p})(\hat{\boldsymbol{g}} \cdot \boldsymbol{p})$, with a multiplicative pre-factor that is a function of κ. Thus, for small Pe, the ratio of the hydrostatic and hydrodynamic components of the stratification torque is independent of the spheroid orientation and Ri_v, and only a function of κ.

The solution for the density perturbation can be found by solving 4.27 with the no-flux boundary condition mentioned above [see Varanasi et al. [2021] for details]. This solution together with the test velocity field can be substituted in the integral for the hydrodynamic stratification torque in 4.22. The volume integration leads to the following expression for the angular velocity in the $Pe = 0$ limit

$$\Omega_i^{(1)d} = Ri_v \frac{F_s^{p/o}(\xi_0)}{Y_C} \left(\varepsilon_{ijk}\hat{g}_j p_k\right)\left(\hat{g}_l p_l\right), \tag{4.28}$$

with

$$F_s^p(\xi_0) = 2\pi\bar{\xi}_0^{\,2} \frac{\left(\left(7\xi_0^5 - 7\xi_0^3 - 2\xi_0\right) + \bar{\xi}_0^{\,2} C_p \left(-12\xi_0^4 + 6\xi_0^2 + \xi_0 C_p \left(3\xi_0^4 + 2\left(\xi_0^5 - \xi_0\right) C_p - 6\xi_0^2 + 7\right) - 2\right)\right)}{15\xi_0^5 \left(\xi_0 - \bar{\xi}_0^{\,2} C_p\right)\left(-\xi_0^2 + \bar{\xi}_0^{\,2}\xi_0 C_p + 2\right)\left(\left(\xi_0^2 + 1\right) C_p - \xi_0\right)}, \tag{4.29}$$

for prolate spheroids, where $C_p = \coth^{-1}\xi_0$. Using the transformation mentioned in section 4.3, one obtains

$$F_s^o(\xi_0) = 2\pi \frac{\left(\left(7\xi_0^4 - 7\xi_0^2 - 2\right)\bar{\xi}_0 + 2\left(\xi_0^4 - 3\xi_0^2 + 2\right)\xi_0^4 C_o^3 - 2\left(6\xi_0^4 - 9\xi_0^2 + 4\right)\xi_0^2 C_o + \left(3\xi_0^4 + 4\right)\bar{\xi}_0\xi_0^2 C_o^2\right)}{15\xi_0^3\left(\xi_0^2 C_o) - \bar{\xi}_0\right)\left(\left(\xi_0^2 - 2\right)(C_o) - \bar{\xi}_0\right)\left(-\xi_0^2 + \bar{\xi}_0\xi_0^2 C_o - 1\right)}, \tag{4.30}$$

for the oblate case, where $C_o = \cot^{-1}\bar{\xi}_0$. Fig. 4.5 shows a plot of the aspect-ratio-dependent functions given by (4.29) and (4.30), divided by Y_C. The hydrodynamic component of the stratification torque given by (4.29) always orients a prolate spheroid edgewise for small Pe. Interestingly, Fig. 4.5 shows that (4.30) changes sign below a critical aspect ratio $\kappa_c \approx 0.41$ ($e \approx 0.9$), and therefore, the hydrodynamic component acts to orient oblate spheroids, with aspect ratios lower than the aforementioned threshold, broadside on.

The hydrodynamic stratification torque arises due to the flow associated with the baroclinic source of vorticity, although the reciprocal theorem formulation used here bypasses the explicit calulation of this flow. The vorticity arises from the tilting of the iso-pycnals to the

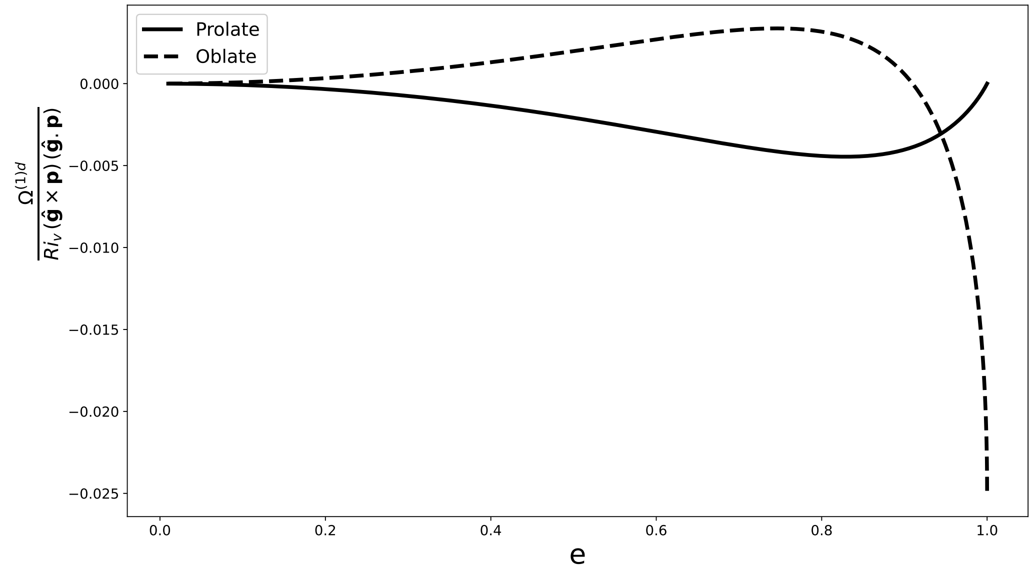

Fig. 4.5 The aspect-ratio-dependent functions given by (4.29) and (4.30), divided by Y_c, for prolate and oblate spheroids that arise from hydrodynamic contributions in the small *Pe* limit, plotted as a function of the spheroid eccentricity. (Reproduced with permission from Varanasi et al. [2021])

vertical (the direction of gravity) due to the requirement that they meet the spheroidal surface in a normal orientation, consistent with a no-flux constraint. A sketch of the deformed iso-pycnals in the plane $\phi = 0, \pi$, and the resulting sign of the baroclinc vorticity field ($\propto \nabla\rho \wedge \hat{\boldsymbol{g}}$) in different regions of the fluid domain, appears in Figure 4.6, for both prolate and oblate spheroids. The baroclinically induced flow has a dipolar character in the Stokes limit, and the relative sizes of the different flow quadrants are set by the pair of singular iso-pycnals that meet the spheroid surface in the points S_1 and S_2. This pair separates the iso-pycnals that do not meet the spheroid surface from those that do. The baroclinically induced flow on account of diffusive iso-pycnal tilting has been known for a long time, having originally been proposed in the oceanic context where the induced flow has a boundary layer character on account of the dominance of inertia (Phillips [1970],Wunsch [1970]). Such a flow has also been examined in a Stokesian scenario more recently (Anis Alias and Page [2017]), although only for the case of a horizontal circular cylinder wherein symmetry precludes a torque contribution. That there must be a torque on an inclined spheroid, due to the aforementioned baroclinic flow, is obvious. While the sense of the torque (broadside-on vs edgewise) is not readily evident, one may nevertheless rationalize the scalings observed for the extreme aspect ratio cases. Figure 4.5 shows that the angular velocity remains finite in the limit of a flat disk ($\kappa \rightarrow 0$) which is consistent with the iso-pycnals being perturbed in a volume of $O(L^3)$ around the spheroid in this limit, with the density perturbation being $O(\gamma L)$, and the test velocity field $\boldsymbol{U}^{(2)}$ being $O(1)$ in this region; the points S_1 and S_2 remain bounded away from the edges of the flat disk. On the other hand, the angular velocity approaches zero as $O(\xi_0 - 1)$ in the limit of a slender fiber, with the points S_1 and S_2 now moving towards the ends of the fiber. The dominant contribution continues to come from a volume of $O(L^3)$. But, while $\boldsymbol{U}^{(2)}$ is $O[\ln(\xi_0 - 1)]^{-1}$, the density perturbation in this region is algebraically small. The slender fiber only perturbs the iso-pycnals in a thin $O(d^2 L)$ shell around itself, with the density perturbation being $O(\gamma d)$ in this region. Further, each cross-section of the fiber acts as a 2D concentration dipole, implying that the density perturbation decays as $O(1/r)$ for r much greater than d, and is therefore $O(\gamma d)(d/L)$ for $r \sim O(L)$. Using these estimates, and dividing by the $O[\ln(\xi_0 - 1)]^{-1}$ rotational resistance for a slender fiber leads to the aforementioned scaling for the fiber rotation due to the hydrodynamic contribution of the stratification torque.

A closer look at the $Pe \ll 1$ analysis

Although the O(Ri_v) angular velocity given by (4.28) was said to be valid for small Pe, there are, in fact, multiple contributions to the stratification-induced rotation for $Pe \ll 1$; the more detailed arguments herein, and the analysis in Appendix B, yield a precise estimate of the

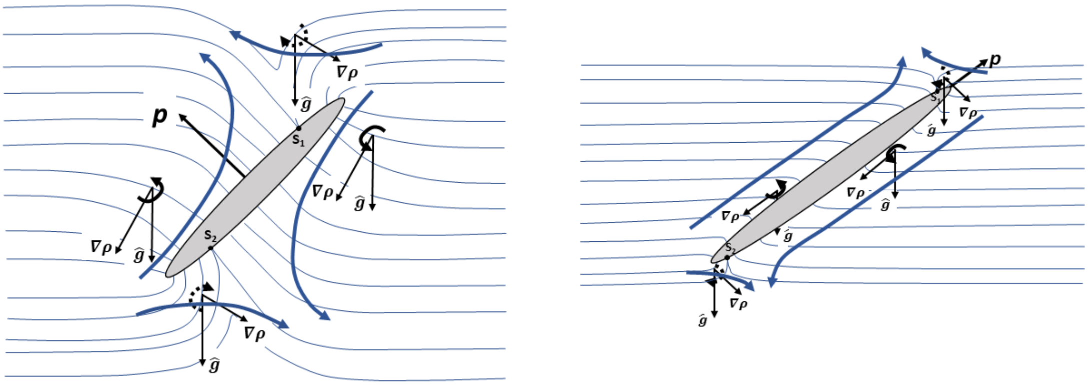

(a)

(b)

Fig. 4.6 Figures (a) and (b) depict the baroclinically-driven flow, for small *Pe*, that is responsible for the rotation of an (a) oblate, and a (b) prolate spheroid, in a stably stratified ambient. The curved blue arrows denote the sense of the baroclinically induced vorticity in the different quadrants of the fluid domain, with vorticities corresponding to anticlockwise and clockwise senses of rotation being denoted by solid and dashed lines; the blue contours denote the deformed iso-pycnals around each of the spheroids.

Pe-interval of validity. While the dominant contribution to (4.28) arose from buoyancy forces on length scales of $O(L)$, as will be seen in section 4.4.2 below, the dominant length scale contributing to the hydrodynamic component of the stratification torque changes to $O(LRi_v^{-\frac{1}{3}})$ with increasing Pe; one therefore expects the singular effect of convection to already be evident for small but finite Pe. To see this, we note that, for small Pe, besides the density perturbation driven by the no-flux condition on the spheroid surface that has been analyzed above, an independent contribution arises from perturbation of the ambient stratification on much larger length scales due to weak convection effects. To obtain an estimate for this latter torque contribution, we consider the correction to the leading order density perturbation, now denoted as $\rho'^{(10)}$, in a manner similar to the velocity field examined at the end of the earlier section; thus, one writes $\rho'^{(1)} = \rho'^{(10)} + Pe\,\rho'^{(11)}$, with $\nabla^2\rho'^{(11)} \sim \boldsymbol{u}'^{(1)}\cdot\hat{\boldsymbol{g}}$. With $\boldsymbol{u}'^{(1)} \sim 1/r$ on length scales smaller than $O(LRe^{-1})$, one obtains $\rho'^{(11)} \sim r$. The stratification torque at the next order is proportional to $Ri_v Pe\int\rho'^{(11)}\hat{\boldsymbol{g}}\boldsymbol{u}^{(2)}dV$, which turns out to diverge as $O(r^2)$, on using the above estimate for $\rho'^{(11)}$. Cutting off the divergence at the small-Pe stratification screening length of $O[L(Ri_v Pe)^{-\frac{1}{4}}]$ (Ardekani and Stocker [2010],List [1971]) would seem to lead to an $O(Ri_v Pe)^{\frac{1}{2}}$ torque contribution. However, it is shown in Appendix B.1 that this contribution is identically zero for a spheroid, on account of the fore-aft symmetry of the disturbance density field on scales of $[L(Ri_v Pe)^{-\frac{1}{4}}]$ (Ardekani and Stocker [2010],Varanasi and Subramanian [2021]).

The fore-aft asymmetry of the density perturbation, necessary for a non-trivial torque contribution, requires inclusion of the $O(Pe)$ convective term $(\boldsymbol{u}\cdot\nabla\rho')$ in (4.12). It is well known that, for Pe small but finite, this convective term becomes comparable to the diffusive term on length scales of $O(LPe^{-1})$, the mass/heat transfer analog of the inertial screening length (Leal [1992]), and the angular velocity scaling therefore depends on the relative magnitudes of the convective (LPe^{-1}) and stratification $(L(Ri_v Pe)^{-\frac{1}{4}})$ screening lengths, which in turns depends on the relative magnitudes of Pe and $Ri_v^{\frac{1}{3}}$; this criterion being analogous to the classification into Stokes $(Re \ll Ri_v^{\frac{1}{3}})$ and inertia $(Re \geq Ri_v^{\frac{1}{3}})$-stratification regimes based on the structure of the large-Pe disturbance velocity field (Mehaddi et al. [2018],Varanasi and Subramanian [2021]), except that Pe now replaces Re. For $Pe \ll Ri_v^{\frac{1}{3}}$, fore-aft asymmetric buoyancy forces acting on scales of $O[L(Ri_v Pe)^{-\frac{1}{4}}]$ lead to an $O(Ri_v^{\frac{1}{4}}Pe^{\frac{5}{4}})$ hydrodynamic torque contribution, an exact expression for which is obtained in Appendix B. In the opposite limit of $Pe \gg Ri_v^{\frac{1}{3}}$, the dominant contribution to the torque integral arises on scales of $O(Ri_v^{-\frac{1}{3}})$, and the resulting torque comes out to be $O(Ri_v^{\frac{2}{3}})$! Thus, the arguments above, and those in Appendix B, show that, for small Pe, in addition to the $O(Ri_v)$ torque contribution given by (4.29) and (4.30), there exists a second independent contribution that increases with

Pe as $O(Ri_v^{\frac{1}{4}}Pe^{\frac{5}{4}})$ for $Pe \ll Ri_v^{\frac{1}{3}}$, but is independent of Pe, being $O(Ri_v^{\frac{2}{3}})$ for $Ri_v^{\frac{1}{3}} \ll Pe \ll 1$. This far-field hydrodynamic contribution, arising from a weak convective distortion of the stratified ambient, can evidently exceed the hydrostatic contribution, possibly leading to an edgewise settling regime even for small Pe. In light of this additional contribution, the dominance of the $O(Ri_v)$ hydrostatic contribution and the prevalence of broadside-on settling requires $Ri_v \gg Ri_v^{\frac{1}{4}}Pe^{\frac{5}{4}}$, which translates to the stricter criterion $Pe \ll Ri_v^{\frac{3}{5}} \ll 1$, instead of $Pe \ll 1$, as originally assumed.

It is important to point out that the $O(Ri_v)$ scaling in (4.25), (4.26) and (4.28) implies that the associated (dimensional) angular velocities are independent of U. While this must be the case for the hydrostatic contributions, it turns out to be the case for the hydrodynamic component too, at small Pe, since the leading order density perturbation arises as a diffusive response, and is therefore independent of the ambient flow. Despite this U-independence, the torque associated with (4.28) does have a hydrodynamic character, in that it still arises from the flow induced by buoyancy forces. Using the $O(\gamma L)$ density perturbation produced by the diffusive response, one obtains a buoyancy-driven velocity scale of $O(\gamma L^3 g/\mu)$, implying a spheroidal angular velocity of $O(\gamma L^2 g/\mu)$; the latter is $O(Ri_v)$ in units of U/L, this being the scale used in the reciprocal theorem formulation in section 4.2. Importantly, the U-independence implies that this torque contribution is not necessarily limited to small Ri_v. Instead, it is limited by the assumption of a quasi-steady density perturbation set up on scales of $O(L)$ by diffusion alone, which requires an appropriate Peclet number (based on the aforementioned $O(\gamma L^3 g/\mu)$ velocity scale) to be small; an analogously defined Reynolds number must also be small for the baroclinic flow to be obtained from the Stokes equations. These two requirements translate to $Ri_vPe, Ri_vRe \ll 1$, which also ensures that the spheroid rotation may be neglected when deriving the disturbance fields. Thus, (4.28) remains valid even when $Ri_v \sim O(1)$ provided $Re, Pe \ll 1$. Note, however, that a genuine dependence, of the hydrodynamic component of the angular velocity contribution, on U arises due to contributions from the outer region, and an estimate of this contribution was obtained in the preceding paragraph (also see Appendix B.1).

To summarize then, for sufficiently small Pe, all three contributions that appear in (4.22) have a regular character, and therefore, the same dependence on the spheroid orientation viz. $\sin\psi\cos\psi$ with ψ being the angle between $\boldsymbol{p}$ and $\boldsymbol{g}$ as defined above; the Pe-interval of validity depends on Ri_v, being $Pe \ll 1$ for $Ri_v \sim O(1)$, and $Pe \ll Ri_v^{\frac{3}{5}}$ for $Ri_v \ll 1$. The inertial contribution is $O(Re)$, while both hydrodynamic and hydrostatic components of the stratification contribution are $O(Ri_v)$, with the hydrodynamic component alone acting to orient the spheroid edgewise for prolate spheroids of arbitrary κ and oblate spheroids with $\kappa > 0.41$. Therefore, oblate spheroids with $\kappa < 0.41$ will certainly orient broadside-on for

$Pe \ll 1$. Further, it is seen from Fig. 4.4 and Fig. 4.5 that the hydrodynamic component always remains smaller in magnitude than the hydrostatic one in the edgewise-rotation regime, and therefore, a sedimenting spheroid, either prolate or oblate, is expected to settle in the broadside-on configuration, regardless of κ, for sufficiently small Pe.

4.4.2 The angular velocity due to the hydrodynamic torque in the convection-dominant limit ($Pe \gg 1$)

In contrast to the small Pe limit, for $Pe \gg 1$, the dominant contribution to the integral for the stratification-induced hydrodynamic torque in (4.21) comes from length scales of $O(LRi_v^{-\frac{1}{3}})$, the stratification screening length in the Stokes stratification regime ($Re \ll Ri_v^{\frac{1}{3}} \ll 1$). To see this, we note from the right hand side of the advection diffusion equation (4.16) that, for large Pe, the density perturbation is driven by the convection of the base-state stratification of order unity by the vertical component of the Stokeslet field, $u_3'^{(1)}$. Since $u_3'^{(1)} \sim O(1/r)$, one finds $\rho'^{(1)} \sim O(1)$ for $r \gg 1$. This, along with the far-field $O(1/r^2)$ decay of the test velocity field, implies that the integrand in the stratification torque integral decays as $O(1/r^2)$, and that the volume integral therefore diverges as $O(r)$. This divergence is expected to be resolved only when the slow $O(1/r)$ decay of the Stokeslet is accelerated by stratification that, for large Pe, occurs on length scales of $O(LRi_v^{-\frac{1}{3}})$. It has recently been shown in the Chapter 2 of the present thesis that, for a sedimenting sphere at large Pe, the density and velocity fields are indeed asymptotically small on length scales larger than $O(Ri_v^{-\frac{1}{3}})$, except within a horizontal wake whose vertical extent grows as $O(r_t^{\frac{2}{5}})$, r_t being the distance in the plane transverse to gravity, where the density and axial velocity perturbation decay as $r_t^{-\frac{12}{5}}$ and $r_t^{-\frac{14}{5}}$, respectively; and a buoyant jet in the rear where u_3 reverses sign, but continues to exhibit an $O(1/r)$ Stokesian decay. Despite the latter slow decay, the asymptotically narrow character of the buoyant jet implies that the torque integral does converge on length scales of $O(LRi_v^{-\frac{1}{3}})$, and is $O(Ri_v^{-\frac{1}{3}})$. The pre-factor of Ri_v in front of the integral in (4.21) implies that the torque and the angular velocity scale as $O(Ri_v^{\frac{2}{3}})$ for $Pe \to \infty$.

Since the dominant contribution to the torque integral comes from length scales much larger than $O(L)$, of $O(LRi_v^{-\frac{1}{3}})$, the calculation requires one to rewrite the integral involving $\rho'^{(1)}$, in (4.21), in outer coordinates (defined below), with the sedimenting spheroid in problem 1 now regarded as a point force, and the rotating spheroid in the test problem acting as a combination of rotlet and stresslet singularities (see Marath and Subramanian [2017]). The details of this calculation are provided below; a similar calculation, but for low Pe, with the outer region being characterized by a length scale of $O(Ri_vPe)^{-\frac{1}{4}}$, has been given in Appendix B.1 and the resulting O($Ri_v^{\frac{1}{4}}Pe^{\frac{5}{4}}$) torque contribution was discussed above in section 4.4.1.

Before delving into the large-*Pe* analysis, it is worth noting that a reciprocal theorem formulation to determine the stratification-induced correction to the force (that would include both drag and lift components for an arbitrarily oriented spheroid) would involve the test problem of a translating spheroid instead. Since the test velocity field now decays as $O(1/r)$ in the far-field, this would lead to a stronger $O(r^2)$ divergence of the force integral, leading to a scaling of $O(Ri_v^{-\frac{2}{3}})$ on truncation of the divergence, and thence, an $O(Ri_v^{\frac{1}{3}})$ stratification-induced correction to the Stokes drag. Such a correction was originally calculated for a spherical particle by Zvirin and Chadwick [1975]. A similar calculation was done by Candelier et al. [2014] for the small-*Pe* regime, the drag contribution from the outer region now being $O(Ri_vPe)^{\frac{1}{4}}$; a later effort has connected this outer-region drag calculation across the different asymptotic regimes (Mehaddi et al. [2018]). In a very recent study, Dandekar et al. [2020] have examined the force and torque acting on an arbitrarily shaped particle sedimenting in a linearly stratified ambient. For anisotropic particles lacking a handedness (that includes the spheroids examined here), the authors find a correction to the force at $O(Ri_v^{\frac{1}{3}})$ similar to the case of a spherical particle mentioned in the above efforts, but end up not finding a torque at this order, a result that is not surprising in light of the above scaling arguments which show the torque to be $O(Ri_v^{\frac{2}{3}})$. Within the framework of the matched asymptotics expansions approach used by the said authors, the $O(Ri_v^{\frac{1}{3}})$ correction to the drag appears as a response of the particle to an 'ambient uniform flow' that is the limiting form of the outer solution in the matching region ($1 \ll r \ll Ri_v^{-\frac{1}{3}}$); the uniformity of this flow is consistent with the absence of a torque at this order. Incidentally, the existence of an inertial torque induced by a uniform flow suggests a higher $O(ReRi_v^{\frac{1}{3}})$ inner-region contribution to the leading $O(Re)$ inertial angular velocity, in response to the aforementioned $O(Ri_v^{\frac{1}{3}})$ uniform flow that would again orient the spheroid broadside-on; this is in addition to the outer-region correction obtained in section 4.3.

As mentioned above, the stratification torque integral in (4.22) needs to be evaluated in outer coordinates which are related to the coordinates in the particle-fixed reference frame as $\tilde{\boldsymbol{x}} = Ri_v^{\frac{1}{3}}\boldsymbol{x}$, so an $O(1)$ change in $\tilde{\boldsymbol{x}}$ corresponds to $\boldsymbol{x}$ changing by an amount of order the stratification screening length. However, as originally shown by Childress [1964] and Saffman [1965], a Fourier space approach turns out to be much more convenient for a calculation involving the outer region, and we therefore consider the Fourier transformed equations of continuity and motion, and the advection diffusion equation for the density field, obtained from (4.14-4.16), and given by

$$k_i \hat{u}_i'^{(1)} = 0, \tag{4.31}$$

$$-4\pi^2 k^2 \hat{u}_i'^{(1)} - 2\pi \mathrm{i} k_i \hat{p}'^{(1)} = -Ri_v(\hat{\rho}'^{(1)} \hat{g}_i) + \tilde{F}\hat{g}_i, \tag{4.32}$$

$$2\pi \mathrm{i} k_j \hat{U}_j \hat{\rho}'^{(1)} = \hat{u}_j'^{(1)} \hat{g}_j + \frac{1}{Pe} 4\pi^2 k^2 \hat{\rho}'^{(1)} + \frac{1}{Pe} i2\pi k_i D_i^s, \tag{4.33}$$

for problem 1. Here, we have used the definition $\hat{f}(\boldsymbol{k}) = \int d\boldsymbol{x} e^{-2\pi \mathrm{i}\boldsymbol{k}\cdot\boldsymbol{x}} f(\boldsymbol{x})$ for the Fourier transform, and the sedimenting spheroid has been replaced by a point force, $\tilde{\boldsymbol{F}}\delta(\boldsymbol{x})$, on the right hand side of the physical space equations of motion viz. (4.15), with $\tilde{\boldsymbol{F}} = \tilde{F}\hat{\boldsymbol{g}}$, $\tilde{F}$ being the non-dimensional buoyant force (in units of μUL) exerted by the spheroid; the corresponding dimensional expression has been given in section 4.2 (given that U is itself defined in terms of F, this re-scaling of F merely amounts to multiplication by X_A). Note that the inertial term in the original equation of motion, (4.15), has now been omitted in (4.32) since, as already argued earlier, the leading $O(Re)$ inertial torque is dominated by the inner region, with the outer region contribution being only $O(Re^2 \ln Ri_v^{-\frac{1}{3}})$ (see end of section 4.3), and not considered here. Further, on large length scales relevant to the outer region, the spheroid, on account of the no-flux boundary condition at its surface, appears as a concentration-dipole forcing in the advection-diffusion equation. In physical space, this corresponds to a term of the form $\boldsymbol{D}^s.\boldsymbol{\nabla}\delta(\boldsymbol{x})$, and the Fourier transform of this term appears on the RHS of (4.33); $\boldsymbol{D}^s$ here is the Pe-dependent strength of the dipole forcing; this can be neglected for the same reason as the inertial term above, its contribution being asymptotically small compared to that arising from the distortion of the base-state stratification (the first term on the RHS of (4.33)).

Thus, neglecting the term proportional to the concentration-dipole forcing in (4.33), for large Pe , one obtains

$$\hat{\rho}'^{(1)} = \frac{\hat{u}_j'^{(1)} \hat{g}_j}{2\pi \mathrm{i} k_l \hat{U}_l - \frac{4\pi^2 k^2}{Pe}}. \tag{4.34}$$

Using (4.34) in (4.32), and operating on both sides with $(\delta_{ij} - \hat{k}_i \hat{k}_j)$ to eliminate the pressure field, one obtains

$$4\pi^2 k^2 \hat{u}_i'^{(1)} = Ri_v \hat{g}_j (\delta_{ij} - \hat{k}_i \hat{k}_j) \frac{\hat{u}_l'^{(1)} \hat{g}_l}{(2\pi \mathrm{i} k_p \hat{U}_p - \frac{4\pi^2 k^2}{Pe})} + \tilde{F}\hat{g}_j(\delta_{ij} - \hat{k}_i \hat{k}_j). \tag{4.35}$$

Contracting with $\hat{\boldsymbol{g}}$ gives:

$$\hat{u}_i'^{(1)}\hat{g}_i = \frac{\tilde{F}\hat{g}_i\hat{g}_j(\delta_{ij}-\hat{k}_i\hat{k}_j)}{\left[4\pi^2k^2 - Ri_v\frac{\hat{g}_m\hat{g}_n(\delta_{mn}-\hat{k}_m\hat{k}_n)}{2\pi \mathrm{i}(k_l\hat{U}_l)}\right]}, \tag{4.36}$$

which, on using in (4.34), yields the following final expression for $\hat{\rho}'^{(1)}$:

$$\hat{\rho}'^{(1)}(\boldsymbol{k}) = \frac{\tilde{F}Pe[1-(\hat{k}_i\hat{g}_i)^2]}{\{8\pi^3Pe\mathrm{i}k^3(\hat{k}_n\hat{U}_n) - 16\pi^4k^4 - Ri_vPe[1-(\hat{k}_m\hat{g}_m)^2]\}}, \tag{4.37}$$

which will be used in the Fourier-space torque integral that is defined below.

The test velocity field $u_i^{(2)} = U_{ij}^{(2)}\Omega_j^{(2)}$ satisfies the Stokes equations, with the rotating spheroid, on length scales of $O(LRi_v^{-\frac{1}{3}})$, acting as a force-dipole singularity that includes both stresslet and rotlet contributions. Thus, the equations of motion may be written in the form (see Marath and Subramanian [2017]):

$$\frac{\partial^2 u_i^{(2)}}{\partial x_j^2} - \frac{\partial p^{(2)}}{\partial x_i} = S_{ij}^{(2)}\frac{\partial}{\partial x_j}[\delta(\boldsymbol{x})], \tag{4.38}$$

where

$$S_{ij}^{(2)} = B_1[(\varepsilon_{ilm}\Omega_l^{(2)}p_m)p_j + (\varepsilon_{jlm}\Omega_l^{(2)}p_m)p_i] + B_3\varepsilon_{ijk}\Omega_k^{(2)} \tag{4.39}$$

with

$$B_1 = \frac{8\pi}{\xi_0^3(-3\xi_0 + 3\coth^{-1}\xi_0(1+\xi_0^2))}, \tag{4.40}$$

$$B_3 = \frac{8\pi(1-2\xi_0^2)}{\xi_0^3(-3\xi_0 + 3\coth^{-1}\xi_0(1+\xi_0^2))}, \tag{4.41}$$

for prolate spheroids. There is an additional contribution that is neglected in (4.39), on account of the test spheroid rotating about an axis transverse to $\boldsymbol{p}$, that is, since $\boldsymbol{\Omega}^{(2)}\cdot\boldsymbol{p} = 0$. The term proportional to B_3 in (4.39) is the rotlet singularity (due to transverse rotation), while that involving B_1 is the stresslet singularity. Thus, for $\xi_0 \to \infty$, $B_3 = -4\pi$ and B_1 is $O(1/\xi_0^2)$, consistent with a rotating sphere acting as a pure rotlet singularity; note that $B_3 = Y_C/2$, the latter being the resistance function mediating the torque-angular-velocity relation for transverse rotation defined earlier.

Fourier transforming (4.38), and contracting with the projection operator $(\boldsymbol{I}-\hat{\boldsymbol{k}}\hat{\boldsymbol{k}})$, one obtains

$$\hat{u}_i^{(2)} = -\frac{\mathrm{i}}{2\pi k}\{B_1[(\varepsilon_{mqr}\Omega_q^{(2)}p_r)p_n + (\varepsilon_{nqr}\Omega_q^{(2)}p_r)p_m] + B_3\varepsilon_{mnq}\Omega_q^{(2)}\}\hat{k}_n(\delta_{im}-\hat{k}_i\hat{k}_m), \quad (4.42)$$

so the second-order tensor $\boldsymbol{U}^{(2)}$ is given by

$$U_{ij}^{(2)}(\boldsymbol{k}) = -\frac{\mathrm{i}}{2\pi k}\{B_1[(\varepsilon_{mjr}p_r)p_n + (\varepsilon_{njr}p_r)p_m] + B_3\varepsilon_{mnj}\}\hat{k}_n(\delta_{im}-\hat{k}_i\hat{k}_m). \quad (4.43)$$

Now, using the convolution theorem, the integral for the angular velocity contribution due to the hydrodynamic component of the stratification-induced torque in (4.21) may be written as

$$Ri_v\int \rho'^{(1)}\hat{g}_j U_{ji}^{(2)}dV = Ri_v\int d\boldsymbol{k}\hat{\rho}'^{(1)}(\boldsymbol{k})\hat{g}_j U_{ji}^{(2)}(-\boldsymbol{k}), \quad (4.44)$$

where, in applying the convolution theorem, we have assumed the volume integral on the left hand side of (4.44) to extend over the entire domain, and thereby, have neglected the $O(L^3)$ volume of the spheroid. Since the dominant contribution arises from length scales of $O(LRi_v^{-\frac{1}{3}})$, this neglect only amounts to an error of $O(Ri_v)$ in the torque integral, and $O(Ri_v^2)$ in the resulting angular velocity.

Using (4.37) and (4.43) in the Fourier space torque integral in (4.44), and after some simplification which includes defining a rescaled wavevector $2\pi\boldsymbol{k}$, one obtains the angular velocity induced by the hydrodynamic stratification torque as

$$\begin{aligned}\Omega_i^{(1)d} = &Ri_v Pe\frac{\mathrm{i}\tilde{F}}{8\pi^3 Y_C}\int d\boldsymbol{k}\frac{[1-(\hat{k}_x\hat{g}_x)^2]}{\{\mathrm{i}k^3 Pe(\hat{k}_y\hat{U}_y) - k^4 - Ri_v Pe[1-(\hat{k}_z\hat{g}_z)^2]\}k}\Big[B_1\Big\{(\varepsilon_{irj}p_r\hat{g}_j)(\hat{k}_m p_m)\\ &+(\varepsilon_{irj}p_r\hat{k}_j)(\hat{g}_m p_m) - 2(\hat{k}_m\hat{g}_m)(\hat{k}_j p_j)(\varepsilon_{irl}p_r\hat{k}_l)\Big\} + B_3\varepsilon_{ijr}\hat{g}_j\hat{k}_r\Big], \end{aligned} \quad (4.45)$$

the terms proportional to B_1 and B_3 being the stresslet and rotlet-induced torque contributions, respectively. Redefining the new wavevector to be $Ri_v^{-\frac{1}{3}}\boldsymbol{k}$, so it remains of order unity on length scales of order the stratification screening length (and thereby, pertains to the outer region in Fourier space), and considering only the real part of the integral above, one obtains

$$\begin{aligned}\Omega_i^{(1)d} = & Ri_v^{\frac{2}{3}} \frac{\tilde{F}}{8\pi^3 Y_C}\Bigg[B_1 \int d\boldsymbol{k} \frac{[1-(\hat{k}_x\hat{g}_x)^2]k^2(\hat{k}_v\hat{U}_v)}{\{k^6(\hat{k}_y\hat{U}_y)^2+[\beta_\infty k^4+1-(\hat{k}_z\hat{g}_z)^2]^2\}}\Bigg[\Big\{(\varepsilon_{irj}p_r\hat{g}_j)(\hat{k}_m p_m)+(\varepsilon_{irj}p_r\hat{k}_j)(\hat{g}_m p_m) \\ & -2(\hat{k}_m\hat{g}_m)(\hat{k}_j p_j)(\varepsilon_{irl}p_r\hat{k}_l)\Big\}\Bigg] + B_3\int d\boldsymbol{k}\frac{[1-(\hat{k}_x\hat{g}_x)^2]k^2(\hat{k}_v\hat{U}_v)}{\{k^6(\hat{k}_y\hat{U}_y)^2+[\beta_\infty k^4+1-(\hat{k}_z\hat{g}_z)^2]^2\}}\varepsilon_{ijr}\hat{g}_j\hat{k}_r\Bigg],\end{aligned} \tag{4.46}$$

where the angular velocity due to the hydrodynamic stratification torque finally comes out to be $O(Ri_v^{\frac{2}{3}})$, as anticipated by the scaling arguments above, and the convergent Fourier integrals in (4.46) are evaluated below; note that the imaginary part of (4.45), neglected in (4.46), may be shown to equal zero by symmetry. β_∞ in the above expression is given by $\frac{Ri_v^{1/3}}{Pe}$ as introduced in Chapter 2 of this thesis, and denotes the importance of diffusion effects. Before evaluating the integrals above using a specific coordinate system, we note that the force-velocity relationship for a sedimenting spheroid, for the scalings used here, is given by

$$\hat{U}_i = [p_i p_j + \frac{X_A}{Y_A}(\delta_{ij} - p_i p_j)]\hat{g}_j. \tag{4.47}$$

Defining the aspect-ratio-dependent resistance ratio $An(\kappa) = X_A/Y_A$, (4.47) may be written as

$$\hat{U}_i = [(1-An)p_i p_j + An\delta_{ij}]\hat{g}_j. \tag{4.48}$$

where An decreases monotonically from unity for a sphere to a minimum of $1/2$ for an infinitely slender prolate spheroid ($\kappa \to \infty$); on the oblate side, An increases from unity to a maximum of $3/2$ for a flat disk ($\kappa \to 0$). Both of these may be readily verified based on the expressions given in Appendix A.

To evaluate the above Fourier integrals, we choose a spherical coordinate system with its polar axis along $\hat{\boldsymbol{g}}$. After expressing $\hat{\boldsymbol{U}}$ in terms of $\hat{\boldsymbol{g}}$, $\boldsymbol{p}$ and $An(\kappa)$ as in 4.48, the unit wave vector $\hat{\boldsymbol{k}}$ and $\boldsymbol{p}$ may be written in the form $-\cos\theta\hat{\boldsymbol{g}} + \sin\theta\cos\phi\mathbf{1}_{g^{\perp 1}} + \sin\theta\sin\phi\mathbf{1}_{g^{\perp 2}}$ and $-\cos\psi\hat{\boldsymbol{g}} + \sin\psi\mathbf{1}_{g^{\perp 1}}$, respectively, in a $\hat{\boldsymbol{g}}$-aligned coordinate system; θ and ϕ here being the polar and azimuthal angles, with the polar axis being along $-\hat{\boldsymbol{g}}$. After substituting the above, the integral in 4.46 can be simplified to a three dimensional Fourier integral with β_∞ as a parameter. These three dimensional integrals are then evaluated using Gaussian quadrature with sufficient number of quadrature points to ensure convergence for different (small) β_∞ values in the convection-dominant limit. Numerical evaluation in the $\hat{\boldsymbol{g}}$-aligned coordinate system presented here turns out to more involved. The individual integrals multiplying B_1 and

B_3 in 4.46 diverge as Pe in the limit $\beta_\infty \to 0$ with the divergence arising due to the buoyant jet mentioned in the Chapter 2 of the thesis (see also Varanasi and Subramanian [2021]). We have verified that the divergences of the individual contributions cancel out, and the total angular velocity integral is nevertheless convergent and independent of Pe for $Pe \to \infty$. The ψ-dependence of the large-Pe hydrodynamic angular velocity is seen to be more complicated than the $\cos\psi \sin\psi$ dependence obtained earlier for the inertial and hydrostatic contributions in section 4.3, and for the hydrodynamic component, in the limit $Pe \ll Ri_v^{3/5}$, in section 4.4.1. This is along expected lines since the large Pe limit examined in this section is a singular perturbation problem, as evident from the outer region contributing at leading order (this aspect is also seen in the outer-region contribution to the torque at low Pe, derived in Appendix B.1). Another feature of the singular character is that, unlike the earlier angular velocity contributions, the large-Pe hydrodynamic stratification angular velocity is in general a non-separable function of ψ and κ.

Figures **??** and **??** show plots of the angular velocity ($\Omega^{(1)d}$), due to the hydrodynamic component of the stratification torque, versus ψ for prolate and oblate spheroids, respectively. As evident from Figure **??**, for prolate spheroids, the magnitude of the angular velocity is expectedly small in the near-sphere limit, increasing monotonically with κ to a (finite) maximum in the limit of a slender fiber. Figures **??** shows plots of the angular velocity scaled with the square of the eccentricity (ξ_0^{-2}), so as to obtain a collapse in the near-sphere limit. Note that the finite value of the stratification-induced angular velocity in the limit of a slender fiber ($\xi_0 \to 1$) is in contrast to the $O[\ln(\xi_0 - 1)]^{-1}$ scaling exhibited by the inertial angular velocity calculated in section 4.3 (also see Dabade et al. [2015a]), and implies that, for fixed Re and Ri_v, the stratification torque invariably becomes dominant for large aspect ratios. Figure **??** confirms the squared-eccentricity scaling for oblate spheroids with near-unity aspect ratios; expectedly, the angular velocity approaches a finite value in the limit of a flat disk. Importantly, for both prolate and oblate spheroids, the sign of $\Omega^{(1)d}$ is such as to rotate the spheroid onto an edgewise orientation.

The non-trivial orientation dependence of the angular velocity referred to in the previous paragraph is also evident from the plots in figures **??** and **??**. For near-unity aspect ratios, the angular velocity curve is nearly symmetric about $\psi = \frac{\pi}{4}$; that the angular dependence in this limit is indeed of the form $\sin\psi \cos\psi$ may be shown based on the fact that for $An \to 1$, $\psi_U \approx \psi$. The asymmetry about $\psi = \frac{\pi}{4}$ increases as the aspect ratio departs from unity, with the location of the maximum angular velocity moving to ψ's greater than, and less than, $\frac{\pi}{4}$ for prolate and oblate spheroids, respectively, as shown in figure 4.9. To see the deviation of the angular dependence from the aforementioned simple form more clearly, in figures 4.10a and 4.10b we plot the angular velocity scaled by the inertial angular velocity (which is

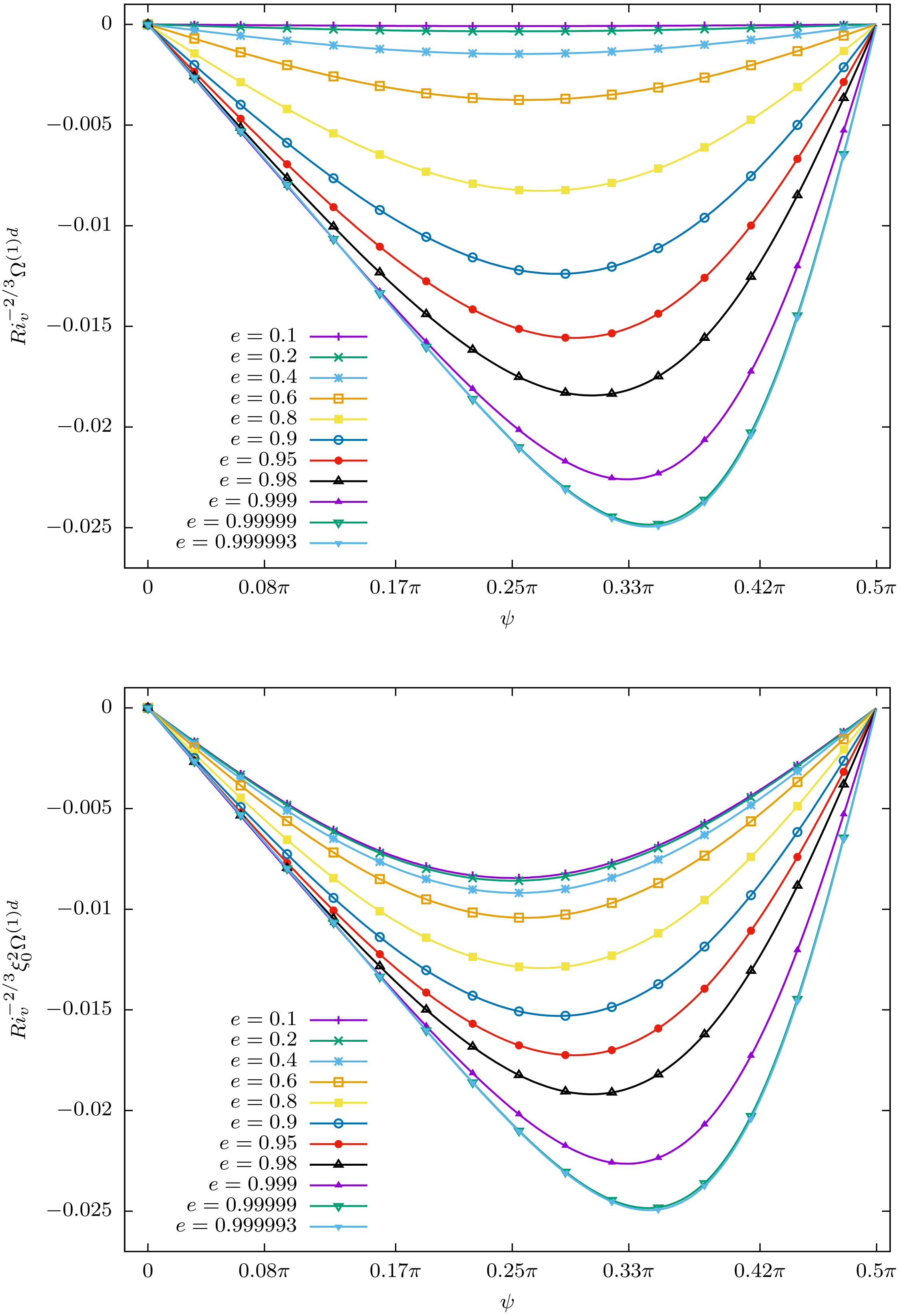

Fig. 4.7 The angular velocity due to the hydrodynamic component of the stratification torque, for prolate spheroids of different aspect ratios. The figure shows $Ri_v^{-2/3}\Omega^{(1)d}$, (a) plotted as a function of the spheroid inclination with gravity, and (b) normalized by the near-sphere scaling $(1/\xi_0^2)$ plotted as a function of the spheroid inclination with gravity.

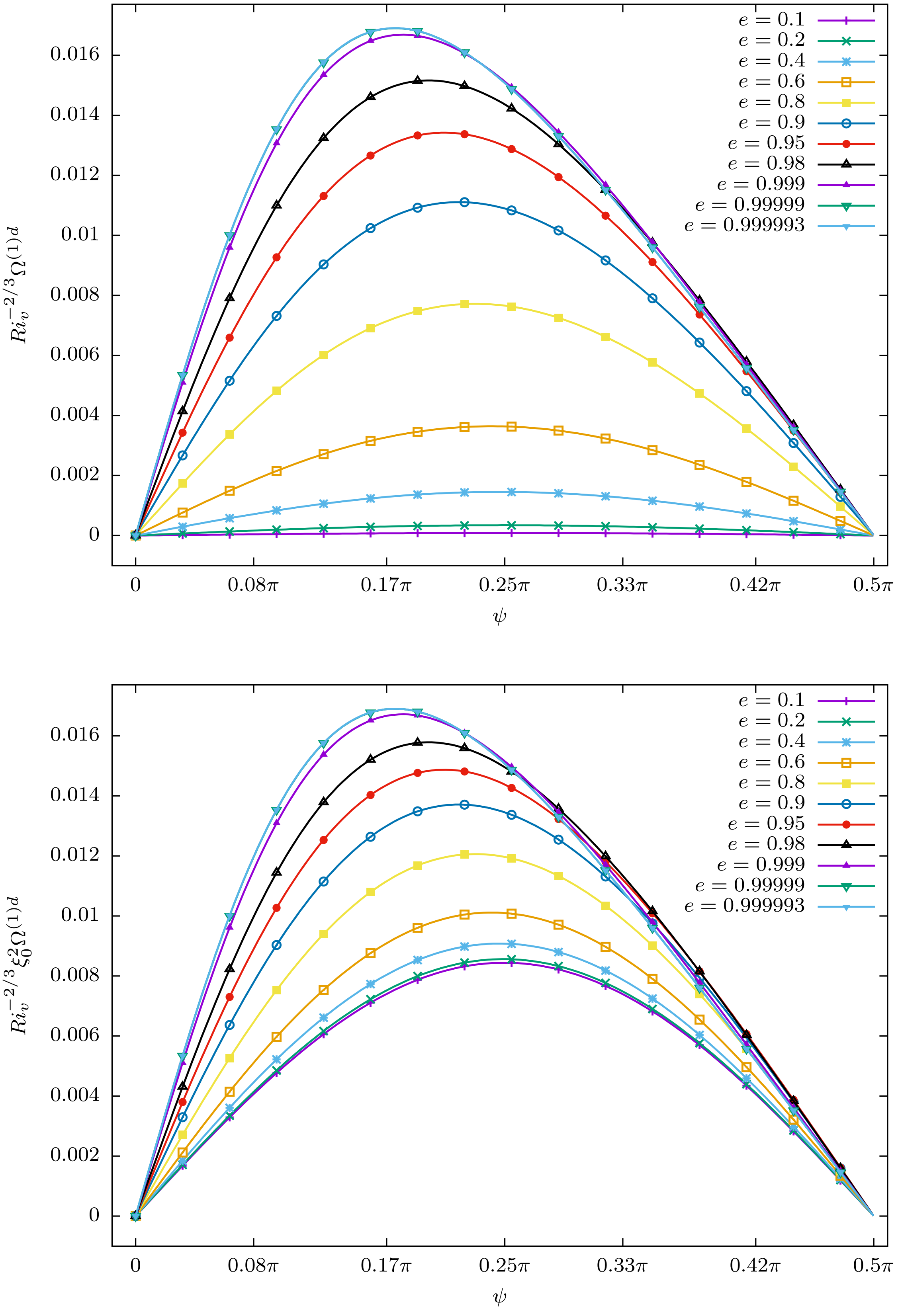

Fig. 4.8 The angular velocity due to the hydrodynamic component of the stratification torque, for oblate spheroids of different aspect ratios. The figure shows $Ri_v^{-2/3}\Omega^{(1)d}$, (a) plotted as a function of the spheroid inclination with gravity, and (b) normalized by the near-sphere scaling $(1/\xi_0^2)$ plotted as a function of the spheroid inclination with gravity.

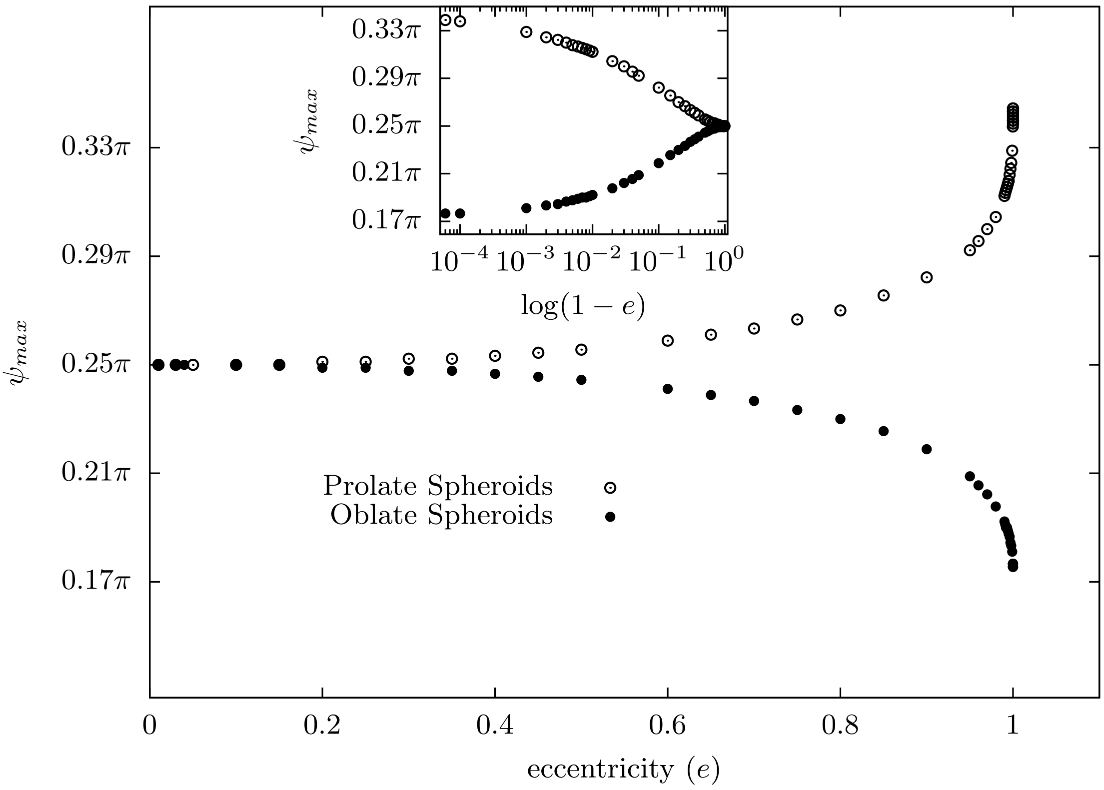

Fig. 4.9 The angle corresponding to the maximum angular velocity, arising from the hydrodynamic component of the stratification torque, plotted as a function of the spheroid aspect ratio (both prolate and oblate spheroids); the inset shows the variation of this angle on a log-log scale, emphasizing the approach to finite values for extreme aspect ratios ($\kappa = 0$ and ∞).

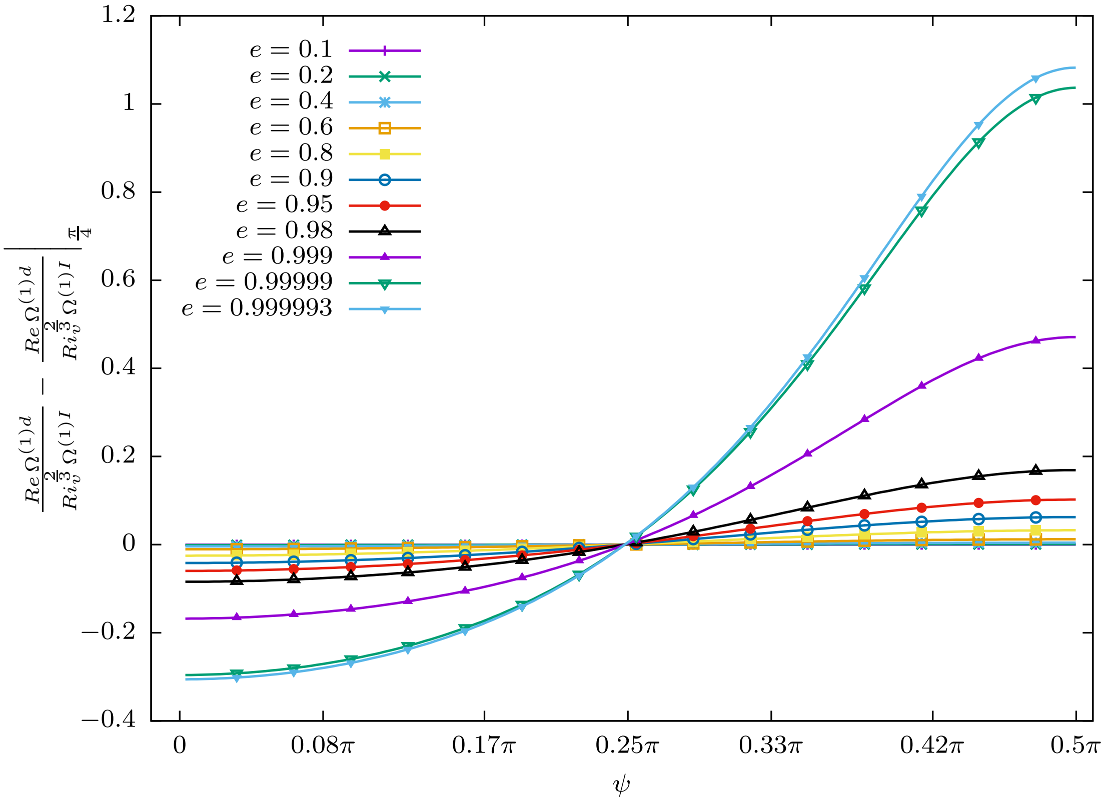

(a) Prolate Spheroid

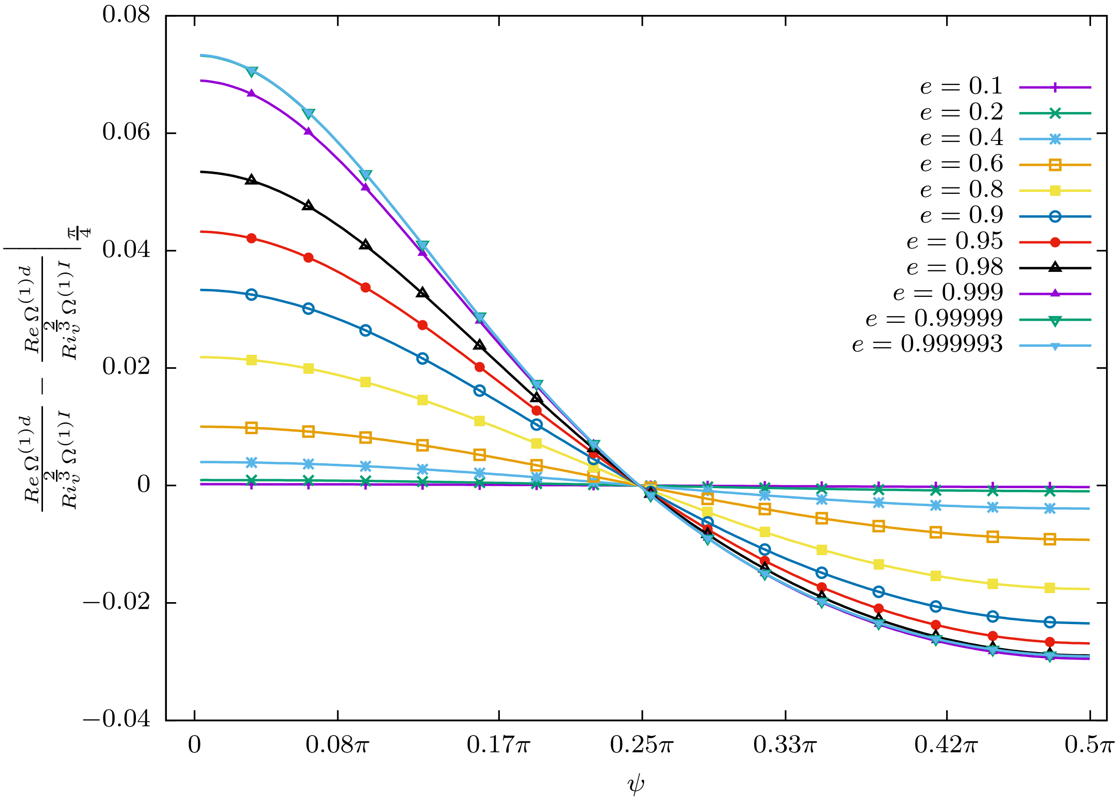

(b) Oblate Spheroid

Fig. 4.10 Ratio of the angular velocities due to the hydrodynamic-stratification and inertial torques. The stratification-induced rotation is higher for the near-vertical and near-horizontal orientations for prolate and oblate spheroids, respectively; note that the angular velocity ratio at $\psi = \pi/4$ has been subtracted for convenient depiction.

proportional to $sin\psi cos\psi$) minus its value at $\pi/4$, as a function of ψ. For near-unity aspect ratios, one obtains a horizontal line, while for both larger and smaller aspect ratios, this renormalized angular velocity asymptotes from one plateau for $\psi \to 0$ to a second one for $\psi \to \frac{\pi}{2}$.

A closer look at the $Pe \gg 1$ analysis

In contrast to the inertial contribution determined in section 4.3, which was independent of the ambient stratification at leading order, the stratification-induced torque can, in principle, be coupled to inertial forces even in the limit $Re, Ri_v \ll 1$. For sufficiently small Pe ($Pe \ll Ri_v^{\frac{3}{5}}$ as argued in section 4.4.1), the density perturbation that determines the stratification torque arises from a diffusive response to the no-flux condition on the surface of the sedimenting spheroid, and is therefore independent of the fluid motion. As a result, a non-trivial coupling between stratification and inertia occurs primarily for large Pe. Since the dominant length scales contributing to the stratification torque in this limit are much larger than $O(L)$, the magnitude of the density perturbation is controlled by the convection of the ambient stratification by the far-field disturbance fluid motion. The nature of this convection is therefore dependent on the form of the disturbance velocity field, and this in turn depends on the relative magnitudes of the inertial (LRe^{-1}) and stratification ($LRi_v^{-\frac{1}{3}}$) screening lengths. The calculation of the angular velocity due to the hydrodynamic stratification torque detailed above pertains to the Stokes stratification regime, with $Re \ll Ri_v^{\frac{1}{3}}$, where the disturbance velocity field directly transitions from the Stokeslet form to a more rapid decay on length scales of $O(LRi_v^{-\frac{1}{3}})$ (Varanasi and Subramanian [2021]) and is therefore independent of Re. In the Stokes stratification regime therefore, the stratification-induced rotation, both in the limit of small and large Pe, is independent of Re, and the inertial and stratification angular velocity contributions are additive. This will no longer true when $Re \geq O(Ri_v^{\frac{1}{3}})$, corresponding to the so-called inertia-stratification regime, in which case the leading order stratification-induced rotation for large Pe will be a function of $Re/Ri_v^{\frac{1}{3}}$. In the limit $Ri_v^{\frac{1}{3}} \ll Re \ll 1$, opposite to the one analyzed above, the disturbance velocity transitions from an $O(1/r)$ to an $O(1/r^2)$ decay (outside of a viscous wake) across length scales of order the inertial screening length. This leads to the stratification torque integrand decaying as $O(1/r^3)$ for length scales much larger than $O(LRe^{-1})$, and the torque integral in (4.22) continues to exhibit a logarithmic divergence. This (milder) divergence is only eliminated when buoyancy forces become comparable to inertial forces at a secondary screening length that was estimated in Varanasi and Subramanian [2021] to be $O(Re/Ri_v)^{\frac{1}{2}}$. Accounting for the aforementioned cut-off of the logarithmic divergence, the angular velocity arising from the hydrodynamic stratification torque is expected to have a leading $O[Ri_v Re^{-1}\ln(Re/Ri_v^{\frac{1}{3}})]$ contribution arising from a region between the primary and secondary screening lengths (that is, due to the logarithmic growth for $Re^{-1} \ll r \ll (Re/Ri_v)^{\frac{1}{2}}$), with logarithmically smaller $O(Ri_v Re^{-1})$ contributions arising from length scales of order the two screening lengths. Assuming this angular velocity to rotate the spheroid towards an edgewise configuration, and equating it to the $O(Re)$ inertial contribution, one obtains $Re \leq Ri_v^2$ for a transition to an edgewise-settling regime. This, however, contradicts the requirement $Re \gg Ri_v^{\frac{1}{3}}$ characterizing the inertia-stratification regime, implying that the inertial angular velocity contribution remains dominant in this regime. Thus, one concludes that, in the limit of small *Re* and Ri_v, a broadside-on-edgewise transition is possible only in the Stokes stratification regime.

To end this subsection, we again examine the validity of a quasi-steady state assumed in the analysis above for large *Pe*. As already argued in section 4.3, momentum diffusion occurs asymptotically fast for small *Re*, and therefore, the quasi-steady assumption used to evaluate the stratification torque integral relies on the time scale for the density disturbance to approach a steady state being much shorter than that characterizing spheroid rotation. The former time scale may be regarded as that required to convect the density perturbation through the $O(LRi_v^{-\frac{1}{3}})$ stratification screening length, and is therefore $O(L/URi_v^{-\frac{1}{3}})$. The time scale of rotation is $O(L/URe^{-1})$ or $O(L/URi_v^{-\frac{2}{3}})$, depending on which of *Re* or $Ri_v^{\frac{2}{3}}$ is greater. In either case the time scale for the development of a steady density perturbation is smaller, provided one remains in the Stokes stratification regime $Re \ll Ri_v^{\frac{1}{3}} \ll 1$. Note that the perturbation density field, for $Pe = \infty$, is expected to be logarithmically singular along the rear stagnation streamline, as has been shown for the case of a spherical particle (see Varanasi and Subramanian [2021]), with this singularity either being resolved on a larger diffusive time scale (that is, due to *Pe* being regarded as large but finite), or on account of the unsteadiness arising from the rotation of the settling spheroid. However, the convergence of the Fourier integrals involved in the stratification torque above implies that the contribution of the transiently developing region in the immediate neighborhood of the rear stagnation streamlilne is irrelevant as far as the leading order hydrodynamic stratification torque is concerned, and a quasi-steady analysis of this torque remains valid for $Re \ll Ri_v^{\frac{1}{3}}$.

4.5 Results and Discussion

In earlier sections, we have derived expressions for the angular velocity of a spheroid settling in a viscous linearly stratified ambient. The spheroid angular velocity is the sum of three components; the inertial and hydrostatic contributions are given by (4.23) and (4.25)[(4.24)

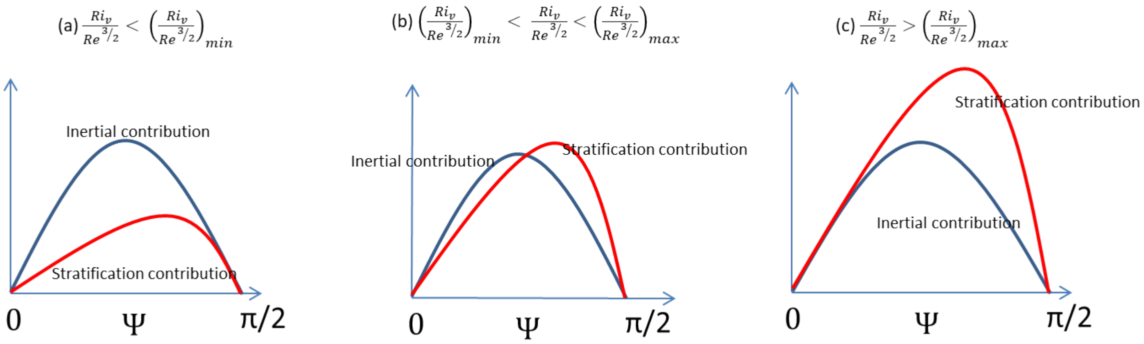

Fig. 4.11 Figures (a),(b) and (c) illustrate the competition between inertia and stratification in the large *Pe* limit for the case of a prolate spheroid; the absolute values of angular velocity contributions from inertia and stratification are plotted against ψ for different $\frac{Ri_v}{Re^{3/2}}$ values. The non-trivial dependence of stratification contribution to the angular velocity on the orientation implies the possibility of the intermediate orientation as shown in (b). It is also easy to see that this intermediate orientation is stable as explained in the main text.

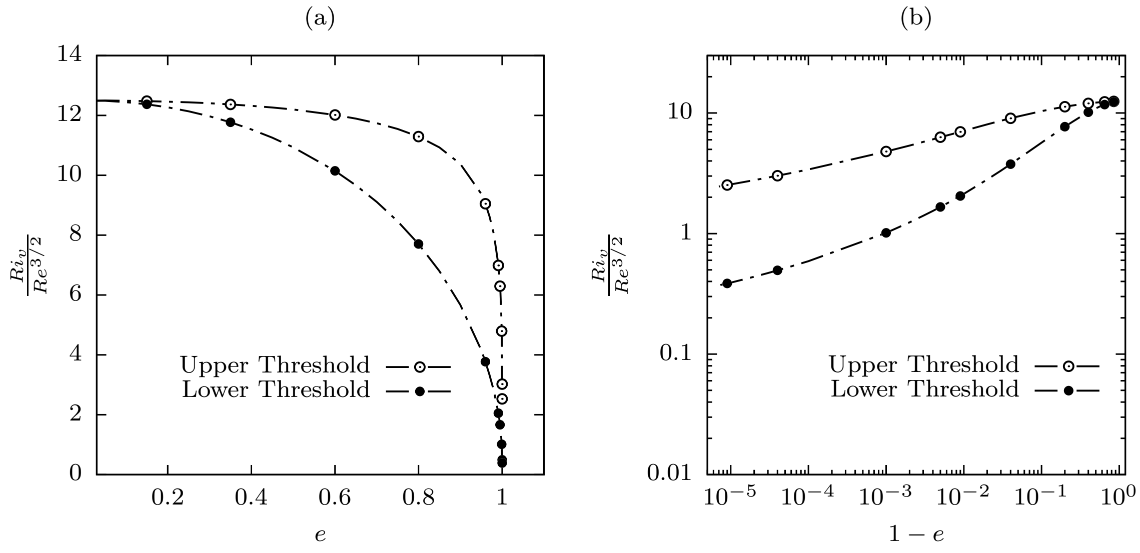

Fig. 4.12 The upper and lower threshold curves that demarcate the regimes of broadside-on settling (below), edgewise settling (above) and intermediate equilibrium orientations (in between), plotted as a function of eccentricity, for a prolate spheroid; the plot on the right presents a magnified view of the thresholds near the slender-fiber limit.

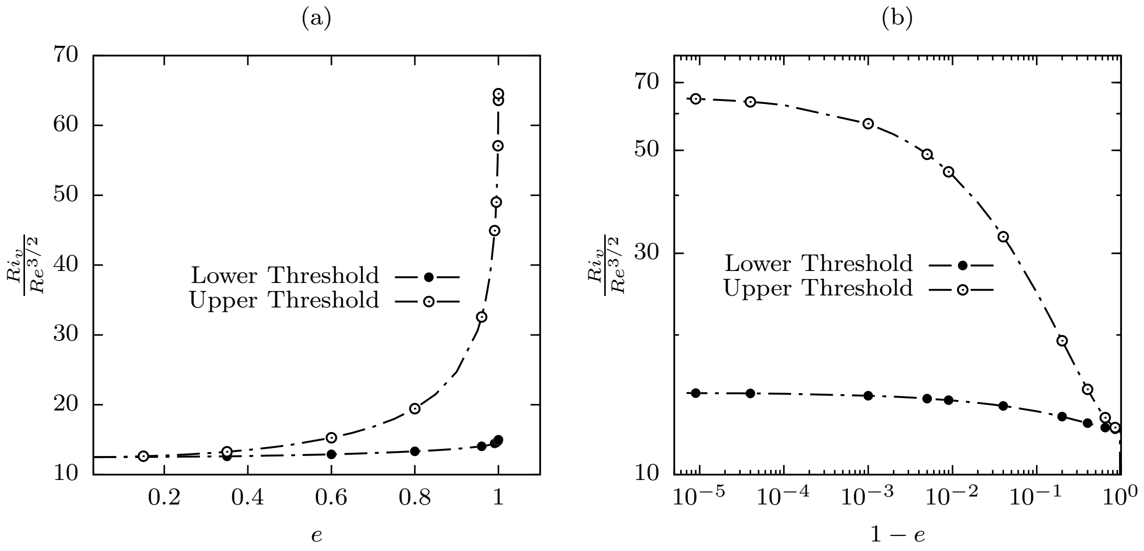

Fig. 4.13 The upper and lower threshold curves that demarcate the regimes of broadside-on settling (below), edgewise settling (above) and intermediate equilibrium orientations (in between), plotted as a function of eccentricity, for an oblate spheroid; the plot on the right presents a magnified view of the thresholds near the flat-disk limit.

and (4.26)] for prolate [oblate] spheroids; the hydrodynamic contribution arising from the stratification is given by (4.29) and (4.30) for prolate and oblate spheroids, respectively, in the limit of small *Pe*; and is obtained from the numerical evaluation of (4.46) for $Pe \gg 1$. As already argued in section 4.4.1, both prolate and oblate spheroids will settle broadside-on for sufficiently small *Pe* regardless of κ. Herein, we therefore focus on the transition from broadside-on to edgewise settling that becomes possible for large *Pe*. In this limit, the hydrodynamic stratification component is $O(Ri_v^{\frac{2}{3}})$ and rotates the spheroid towards an edgewise orientation regardless of κ. It is dominant over the $O(Ri_v)$ hydrostatic component that favors the broadside-on orientation. Thus, the transition from broadside-on to edgewise settling, at leading order, depends on the relative magnitudes of the inertial and hydrodynamic stratification angular velocities, and for a fixed κ, the transition threshold is determined by the ratio $Ri_v/Re^{\frac{3}{2}}$ in the limit $Re, Ri_v \ll 1$. However, the differing orientation dependence of the inertial and stratification angular velocities, as evident from figure 4.10a, for instance, implies that the transition cannot be characterized by $Ri_v/Re^{\frac{3}{2}}$ equalling a single κ-dependent threshold. An instance of the latter scenario, that of a single threshold demarcating differing orientation dynamics regimes, occurs when the competing physical effects are inertia and viscoelasticity, both of which lead to angular velocities with a $\sin\psi\cos\psi$ dependence, so that the edgewise and broadside-on settling regimes are demarcated by a single critical curve in the $De/Re-\kappa$ plane, De here being the Deborah number, a dimensionless measure of elasticity (see Dabade et al. [2015a]).

Writing the leading order hydrodynamic stratification component in the general form $Ri_v^{\frac{2}{3}}F_s(\kappa,\psi)$, for large Pe, and equating it to the inertial component, of the form $ReF_I(\kappa)\sin\psi\cos\psi$, the threshold criterion for the broadside-on-edgewise transition is determined by the ratio $Ri_v/Re^{\frac{3}{2}} = [(\sin\psi\cos\psi)F_I(\kappa)/F_s(\kappa,\psi)]^{\frac{3}{2}}$. Recall from figure 4.10 that, for all $\kappa > 1\,(\kappa < 1)$, $F_s(\kappa,\psi)/(F_I(\kappa)\sin\psi\cos\psi)$ approaches its minimum and maximum values for $\psi\to 0\,(\pi/2)$ and $\pi/2\,(0)$, respectively, varying monotonically in between these limits. Now, define $(Ri_v/Re^{\frac{3}{2}})_{max} = \lim_{\psi\to 0(\psi\to\frac{\pi}{2})}[(F_I(\kappa)\sin\psi\cos\psi)/F_s(\kappa,\psi)]^{\frac{3}{2}}$ and $(Ri_v/Re^{\frac{3}{2}})_{min} = \lim_{\psi\to\frac{\pi}{2}(\psi\to 0)}[(F_I(\kappa)\sin\psi\cos\psi)/F_s(\kappa,\psi)]^{\frac{3}{2}}$ for prolate (oblate) spheroids, both of which are finite and only functions of κ. One then has the following behavior for the orientation of either a sedimenting prolate or an oblate spheroid. For $Ri_v/Re^{\frac{3}{2}} < (Ri_v/Re^{\frac{3}{2}})_{min}$, the broadside-on orientation is the only equilibrium; likewise, for $Ri_v/Re^{\frac{3}{2}} > (Ri_v/Re^{\frac{3}{2}})_{max}$ the longside-on orientation is the only equilibrium. For $Ri_v/Re^{\frac{3}{2}}$ between the aforementioned thresholds, the inertial and stratification angular velocity curves must intersect at an orientation, ψ_i (say), intermediate between 0 and $\pi/2$. It is easily seen that this equilibrium is a stable one for both the prolate and oblate cases; for example, in the prolate case, the stratification-induced angular velocity is greater than the inertial one for $\psi_i < \psi < \pi/2$, with the converse being true $0 < \psi_i < \psi$, implying that a prolate spheroid with its orientation in either of these intervals is rotated towards $\psi = \psi_i$; this is graphically illustrated for the prolate spheroid in figure 4.11. As $Ri_v/Re^{\frac{3}{2}}$ increases from the lower $[(Ri_v/Re^{\frac{3}{2}})_{min}]$ to the upper threshold $[(Ri_v/Re^{\frac{3}{2}})_{max}]$, the intermediate equilibrium orientation, ψ_i, decreases from $\frac{\pi}{2}$ to zero. Figures 4.12 and 4.13 show the aforementioned pair of threshold curves, $(Ri_v/Re^{\frac{3}{2}})_{min}(\kappa)$ and $(Ri_v/Re^{\frac{3}{2}})_{max}(\kappa)$, plotted in the $Ri_v/Re^{\frac{3}{2}}-\kappa$ plane for prolate and oblate spheroids, respectively. Both the threshold values in figure 4.12 approach zero in the limit of large aspect ratios because, as already noted in section 4.4.2, the stratification-induced torque remains finite in this limit, in contrast to the inertial torque which becomes logarithmically small (see figure 4.3). As seen from the log-log plot in figure 4.12, the convergence of the thresholds to zero is slow on account of the aforementioned logarithmic scaling. For oblate spheroids, the lower and upper thresholds approach distinct finite values in the limit of a flat disk. Since the angular velocity due to the hydrodynamic stratification torque approaches a $\sin\psi\cos\psi$ dependence for $\kappa\to 1$ from either the prolate or oblate side, the two threshold curves towards a common albeit finite critical value in the near-sphere limit in both figures 4.12 and 4.13. In effect, for a prolate spheroid, the thresholds diverge from a common finite value for $\kappa = 1$, tending to a maximum separation for $\kappa\approx 4.11\,(e\approx 0.94)$, before approaching zero in the limit $\kappa\to\infty$. For flat disks, the threshold curves diverge away monotonically from a common value as κ increases from unity, approaching a maximum separation in the limit of a flat disk.

In order to connect to experiments, we now discuss the implication of the aforementioned predictions, within a quasi-steady framework, for a spheroid that starts off with an arbitrary initial orientation and sediments through a stratified fluid at large Pe; arguments in sections 4.4.1 and 4.4.2 show that the quasi-steady assumption remains rigorously valid in the Stokes stratification regime, regardless of Pe, provided Re and Ri_v are small. The experiments reported in Mercier et al. [2020] correspond to an ambient linear stratification that includes a neutral buoyancy level. The latter would correspond to the equilibrium location of the sedimenting spheroid for long times, and for the viscous overdamped regime under consideration, one expects the spheroid velocity U to decrease monotonically to zero as it approaches this level. In dimensionless terms, Re and Pe decrease with time, while Ri_v increases with time. If the spheroid starts off sufficiently far above neutral buoyancy level, then the initial terminal velocity is likely large enough for the ratio $Ri_v/Re^{\frac{3}{2}} \sim U^{-\frac{5}{2}}$ to be below the lower κ-dependent threshold in figure 4.13 (note that the particles used in the experiments were disk-shaped, and maybe likened to thin oblate spheroids). As a result, the spheroid starts off rotating towards a broadside-on orientation. The spheroid will slow down as it approaches the neutral buoyancy level, and the resulting increase in $Ri_v/Re^{\frac{3}{2}}$ will eventually cause it to exceed the aforementioned lower threshold, leading to the broadside-on orientation becoming an unstable equilibrium. Assuming the spheroid to have had sufficient time prior to this point, to have already attained a near-broadside-on orientation, one expects the onset of a reversal in rotation. Strictly speaking, the arguments in the previous paragraph, with regard to the existence of an intermediate stable equilibrium, only pertain to a truly steady setting (where the neutral buoyancy level corresponds to an infinitely great depth). For the experimental scenario, assuming a sufficiently slow decrease in $Ri_v/Re^{\frac{3}{2}}$ with time, the spheroid would progress quasi-statically through a sequence of intermediate orientation equilibria, on its way to an edgewise configuration. Finally, in the immediate neighborhood of the neutral buoyancy level, the dynamics would appear to be slow enough for one to be in the small-Pe regime analyzed in section 4.4.1, and the resulting dominance of the hydrostatic component of the stratification torque, over the $O(Ri_v)$ hydrodynamic component, should again reverse the spheroid rotation, causing it to finally approach its equilibrium location in a broadside-on configuration. The aforementioned sequence of events is broadly consistent with the observations in Mercier et al. [2020]. Note that since $U \to 0$ for long times in the vicinity of the neutral buoyancy level, Ri_v becomes arbitrarily large in the vicinity of the neutral buoyancy level, in turn leading to an apparent breakdown of the analysis. As discussed in section 4.4.1, the expressions (4.29) and (4.30), for the hydrodynamic component of the stratification angular velocity remain valid, even for Ri_v of order unity or greater provided $Ri_v Pe \ll 1$ (for sufficiently small Re). The magnitude of $Ri_v Pe$, which is independent of U, therefore determines if the small-Pe analysis remains valid close to the neutral buoyancy level. For large $Ri_v Pe$, the small-Pe screening length of $O[L(Ri_v Pe)^{-\frac{1}{4}}]$ would be much less than L, implying that the baroclinic flow driving spheroid rotation is likely restricted to a thin boundary layer on the surface of the spheroid, this boundary-layer character being similar to the original analysis of Phillips [1970]; the resulting magnitude of the hydrodynamic stratification component is not known. It must also be emphasized that both Re and Ri_v for the disks in the said experiments are of order unity, and a direct quantitative comparison with the experimental trajectories is therefore not possible. Such a comparison would require the analogs of the thresholds in Figures 4.12 and 4.13 for finite Re and Ri_v; even, within the asymptotic framework analyzed here, there exist corrections of $O(Ri_v^{\frac{1}{3}})$ to the threshold $Ri_v/Re^{\frac{3}{2}}$ values in the said figures, owing to the neglect of the smaller $O(Ri_v)$ hydrostatic contribution.

The experiments reported in Mrokowska [2018], Mrokowska [2020a] and Mrokowska [2020b] correspond to a non-linearly stratified ambient where the density varies within an intermediate layer sandwiched between homogeneous upper and lower layers. The effects of the stratification on particle orientation, and the resulting coupling to the settling velocity via the orientation-dependent resistance coefficient, lead to extrema (both maxima and minima) in the settling velocity profile; five different phases have been identified in the settling behavior of thin disks. A detailed theoretical investigation to establish the variation of the settlng velocity profile for small Re andRi_v requires an integration of the coupled translational and orientational equations of motion, and this will be reported separately. It is worth noting one interesting feature in these experiments, however. The particles used in the experiments have a density that is greater than that of the lower denser layer of the non-linearly stratified ambient, and the resulting absence of a neutral buoyancy level renders these experiments closer to the ideal steady state scenario of a constant U, thereby pointing to the possible relevance of the intermediate orientation equilibria identified in figures 4.12 and 4.13. Interestingly, in Mrokowska [2020a], the author observes thick disks to behave differently from thin ones. On entering the transition layer, these disks appear to rotate from an initial broadside-on configuration, attained in the upper layer, towards an intermediate inclined orientation, before rotating back onto a broadside-on orientation in the lower homogeneous layer. The persistence of the inclined orientation in the transition layer appears consistent with the prediction of equilibrium orientations in figure 4.13. The ratio $Ri_v/Re^{\frac{3}{2}}$ equals $\frac{\gamma L^{\frac{3}{2}} \mu^{\frac{1}{2}} g}{U^{\frac{5}{2}} \rho_0^{\frac{3}{2}}}$ in terms of the underlying physical parameters. Further, using the scale $F/(\mu L X_A)$ for U, one obtains the ratio as $(\frac{3X_A}{4\pi})^{\frac{5}{2}} \frac{\gamma\mu^3}{(\rho_0 g)^{\frac{3}{2}}(\Delta\rho)^{\frac{5}{2}} L b^{\frac{5}{2}}}$. Both the thick and thin disks used in the experiments of Mrokowska [2020a] correspond to $\kappa \ll 1$, implying that $X_A(\kappa) \approx X_A(0)$ in the expression for $Ri_v/Re^{\frac{3}{2}}$ above. It is therefore the thickness b that varies significantly in going from the thin to the thick disk in the experiments, and the $b^{-\frac{5}{2}}$ scaling of the above ratio implies that the thick disk will correspond to a significantly lower value of $Ri_v/Re^{\frac{3}{2}}$. Thus, it is possible for the thin disk to correspond to an $Ri_v/Re^{\frac{3}{2}}$ above the upper threshold, with the thick disk falling in between the two thresholds above; In this sense, our predictions again appear broadly consistent with the observations in Mrokowska [2020a].

4.6 Conclusions

To summarize, in this study, we present the first rigorous theoretical description of the orientation dynamics of spheroidal particles in a stably stratified ambient. The stratification-induced hydrodynamic torque, acting on a spheroidal particle, has been calculated for the first time. For large Pe in particular, the torque is shown to rotate both prolate and oblate spheroids towards an edgewise orientation regardless of aspect ratio. The theoretical predictions with regard to the transitions between broadside-on and edgewise settling, and with regard to the existence of intermediate inclined equilibrium orientations, appear broadly consistent with very recent experiments. Unfortunately, and as already mentioned in section 4.5, a detailed quantitative comparison appears out of reach at the moment; the particles used in all of the experiments, referred to in section 4.5, correspond to Ri_v and Re values of order unity and higher. The quantitative disconnect between experiment and theory is also evident from the threshold Froude number condition identified by Mercier et al. [2020] for the so-called perfect disk which, translated to our notation, corresponds to a threshold Ri_v/Re^3; as opposed to the ratio $Ri_v/Re^{\frac{3}{2}}$ identified in section 4.5. We therefore hope that future experiments will use smaller particles, in an attempt to access the regime of small Re and Ri_v, and thereby validate the detailed predictions given here. It needs to be emphasized that the many of the smaller zooplankton, for typical values of the stratifcation pertaining to the oceanic pycnocline, correspond to the small $Re-Ri_v$ regime, and thus the theoretical framework given here is certainly relevant to natural settings (the oceanic realm in particular).

Chapter 5

Conclusions and Future Work

In this thesis, we have carried out detailed analyses of a pair of problems involving the slow motion of particles in a density stratified fluid. The first problem analyzes the fluid motion due to the vertical translation of a sphere, and the second problem analyzes the rotation of a spheroid, both sedimenting in a viscous linearly density-stratified fluid. As part of the first problem, we demonstrated, using a combination of analytical and numerical tools, the existence of a reverse buoyant jet behind a translating particle; further, the velocity field obtained was used to evaluate, numerically, the drift volume in the Stokes stratification regime. Importantly, the drift volume was shown to be a convergent quantity in presence of a weak stratification. The analysis of the second problem involving the spheroid enabled a first explanation of the onset of a longside-on sedimenting regime observed in recent experiments. In the present chapter, we discuss a number of key areas that can be considered as part of future work.

5.1 Future work: Fluid motion due to settling sphere and relevance to oceanic mixing

In order to calculate the drift volume in a density stratified fluid, we have only considered the limit of $\alpha_\infty = 0$ (Stokes-stratification regime), and even here, our focus was on the convection dominant limit ($\beta_| infty << 1$). Although we have also considered the diffusion-dominant limit when characterizing the flow field around the translating sphere, the answer for the drift volume, of $O(Ri_v Pe)^{-1/2}$, was based only on scaling estimates, without detailed calculations. We expect that explicit verificaiton of this scaling, and the calculation of the associated numerical prefactor may be obtained in a manner similar to the large-Pe calculation described in Chapter 3. Note, however, that the dynamical significance of the drift volume in the

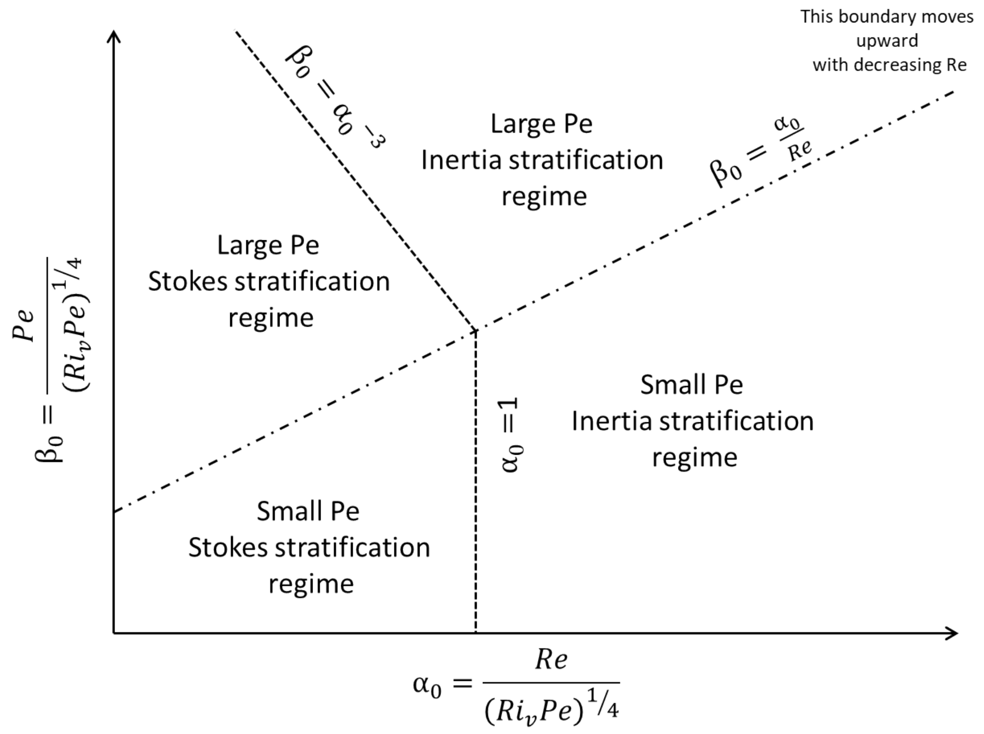

Fig. 5.1 Organization of different stratification regimes based on two parameters α_0 and β_0. This thesis is concerned with the small and large *Pe* Stokes stratification regimes.

small-*Pe* limit, especially with regard to implications for large-scale ocean mixing, is limited on account of diffusion being the dominant influence in the mixing process. In this regard, and more importantly, it is worth considering, in future the effect of finite inertia on the flow field around the translating sphere, and the corresponding drift volume. Indeed, most marine swimmers, including the average-sized zooplankton that contribute to biogenic mixing, pertain to the inertia stratification regime (α_0, $\alpha_\infty \geq 1$, depending on *Pe*). The various dynamical regimes in a density stratified fluid depending on Ri_v, *Re* and *Pe* are depicted in figure 5.1. As can be readily seen from this figure, both the flow field and the drift volume need to be characterized in the large-*Pe* and small-*Pe* inertia stratification regimes through detailed analyses along with the calculation of the drift volume in these cases. These detailed calculations would help validate the proposed drift volume scaling of $(ReRi_v)^{-1/2}$ for the large-*Pe* inertia-stratification regime as detailed in section 3.2.

As discussed in Chapter 3 of the thesis, it is also important to calculate the available potential energy of the density stratified fluid due to steady settling of a sphere in the convection-dominant limit using the results obtained in the thesis. This will help us calculating the mixing efficiency of the density stratified fluid and this calculation will be taken up in future work.

Another calculation of interest that is worth looking into is that of the fluid velocity variance, and the associated tracer diffusivity, associated with a unbounded homogeneous suspension of sedimenting particles in a stratified fluid. The calculation of the above quantities has attracted much attention for a homogeneous suspension on account of the divergence (with system size) predicted for the fluid velocity variance by Caflisch and Luke [1985], this divergence being reflective of the long-ranged hydrodynamic interactions at low Reynolds numbers. Our calculation of the fluid velocity field show a transition from the slow $O(1/r)$ Stokesian decay, to a much more rapid one, beyond a length scale of $O(Ri_v^{-1/3})$ for large Pe. This transition induced by stratification should lead to both a finite velocity variance (of $O(U^2 Ri_v^{-1/3})$) and a finite tracer diffusivity (of $O(UaRi_v^{-2/3})$) in the convection dominant limit, in the Stokes stratification regime. This calculation can be considered in future work

5.2 Future work: Anisotropic particles in stratified fluids

With regard to the work carried out on anisotropic particles moving through density stratified fluids, it is worth mentioning that the focus in the present thesis has been on the large-Pe scenario, in an attempt to explain the transition between broadside-on and edgewise settling observed in experiments all of which correspond to a salt-stratified ambient, and for the millemeter-sized particles used, therefore pertain to large Pe. However, there are several interesting issues that emerge even in the small Pe regime:

1. Scaling arguments given in 4.4.1, and the analysis in Appendix B.1, highlight the possibility of an analogous broadside-on-edgewise transition in the range $Ri_v^{3/5} < Pe \ll 1$. One expects the parametric combination $(Ri_v^{1/4} Pe^{5/4})/Re$ to determine the transition threshold in the range $Ri_v^{3/5} \ll Pe \ll Ri_v^{1/3}$, with the ratio $Ri_v/Re^{3/2}$ controlling this transition for $Pe \gg Ri_v^{1/3}$. The emergence of an $O(Ri_v^{1/3})$ torque for $Pe \gg Ri_v^{1/3}$ suggests that the large-Pe analysis might be applicable to a wider range of Pe that initially apparent. The suggested wider range of validity of the large-Pe analysis for the torque mirrors the drag scenario where the analysis of Zvirin and Chadwick [1975] was found to be valid for a larger interval of Pe than originally anticipated, as shown by Mehaddi et al. [2018].

2. The opposing senses of rotation of oblate spheroids, with $\kappa < 0.41$ in the small- Pe ($Pe \ll Ri_v^{3/5}$) and large-Pe regimes point to a non-trivial dependence of the stratification-induced angular velocity on Pe, one that can be examined in detail through a numerical investigation over the entire range of Pe.

3. It would be of interest to study a fore-aft asymmetric particles (such as a right circular cone, a spherical cap geometry or an asymmetric dumbbell composed of two differently sized spheres) which will allow translational-rotational coupling to be studied in its full generality accounting for both the inner and outer-region contributions to the torque and drag as opposed to the symmetry-induced cancellation that occurs for symmetric shapes.

Some of these aspects can be considered in future work.

Finally, it is also of interest to move beyond orientation dynamics, towards a more detailed illustration of actual particle trajectories which requires an integration of the quasi-steady equations of motion for both translational and rotational degrees of freedom. This would enable a more comprehensive comparsion with the experiments of Mrokowska [2020a] and Mrokowska [2020b]. We expect some of the non-trivial signatures to be revealed in an analysis that might only incorporate an anisotropic Stokes drag for the positional dynamics, a valid leading order approximation for $Re, Ri_v \ll 1$.

Appendix A

A.1 Resistance functions and inertial torque

The expressions for $F_I^p(\xi_0)$ and $F_I^o(\xi_0)$ defined in (4.23) and (4.24) are given in terms of the eccentricity of the spheroid ($e = 1/\xi_0$) as

$$\begin{aligned}
F_I^p(\xi_0) = {} & \frac{-\pi e^2\left(420e + 2240e^3 + 4249e^5 - 2152e^7\right)}{315((e^2+1)\tanh^{-1}e - e)^2((1-3e^2)\tanh^{-1}e - e)} \\
+ {} & \frac{\pi e^2\left(420 + 3360e^2 + 1890e^4 - 1470e^6\right)\tanh^{-1}e}{315((e^2+1)\tanh^{-1}e - e)^2((1-3e^2)\tanh^{-1}e - e)} \\
- {} & \frac{\pi e^2\left(1260e - 1995e^3 + 2730e^5 - 1995e^7\right)(\tanh^{-1}e)^2}{315((e^2+1)\tanh^{-1}e - e)^2((1-3e^2)\tanh^{-1}e - e)},
\end{aligned} \tag{A.1}$$

and

$$\begin{aligned}
F_I^o(\xi_0) = {} & \frac{\pi e^3\sqrt{1-e^2}\left(-420 + 3500e^2 - 9989e^4 + 4757e^6\right)}{315\sqrt{1-e^2}(-e\sqrt{1-e^2} + (1+2e^2)\sin^{-1}e)(e\sqrt{1-e^2} + (2e^2-1)\sin^{-1}e)^2} \\
+ {} & \frac{210\pi e^2\left(2 - 24e^2 + 69e^4 - 67e^6 + 20e^8\right)\sin^{-1}e}{315\sqrt{1-e^2}(-e\sqrt{1-e^2} + (1+2e^2)\sin^{-1}e)(e\sqrt{1-e^2} + (2e^2-1)\sin^{-1}e)^2} \\
+ {} & \frac{105\pi e^3\left(12 - 17e^2 + 24e^4\right)(\sin^{-1}e)^2}{315(-e\sqrt{1-e^2} + (1+2e^2)\sin^{-1}e)(e\sqrt{1-e^2} + (2e^2-1)\sin^{-1}e)^2}.
\end{aligned} \tag{A.2}$$

The resistance functions X_A, Y_A and Y_C are expressed in terms of the spheroid eccentricity as:

$$X_A = \frac{16\pi e^3}{\left(2e-(1+e^2)\log\left(\frac{1+e}{1-e}\right)\right)}, \tag{A.3}$$

$$Y_A = -\frac{32\pi e^3}{\left(2e+(3e^2-1)\log\left(\frac{1+e}{1-e}\right)\right)}, \tag{A.4}$$

$$Y_C = \frac{32\pi e^3(e^2-2)}{3\left(-2e+(1+e^2)\log\left(\frac{1+e}{1-e}\right)\right)}, \tag{A.5}$$

for a prolate spheroid and as:

$$X_A = -\frac{8\pi e^3}{\left[e\sqrt{1-e^2}+(2e^2-1)\cot^{-1}\left(\frac{\sqrt{1-e^2}}{e}\right)\right]}, \tag{A.6}$$

$$Y_A = \frac{16\pi e^3}{\left[e\sqrt{1-e^2}-(1+2e^2)\cot^{-1}\left(\frac{\sqrt{1-e^2}}{e}\right)\right]}, \tag{A.7}$$

$$Y_C = \frac{16\pi e^3(e^2-2)}{3\left[e\sqrt{1-e^2}-(1-2e^2)\cot^{-1}\left(\frac{\sqrt{1-e^2}}{e}\right)\right]}, \tag{A.8}$$

for an oblate spheroid.

Appendix B

B.1 Additional convective contributions to the spheroid angular velocity for $Pe \ll 1$

In section 4.4.1, an $O(Ri_v)$ contribution to the spheroid angular velocity, given by (4.28), arose from the density perturbation driven by the no-flux condition on the spheroid surface (whose solution is obtained in detail by Varanasi et al. [2021] as mentioned in section 4.4.1). This contribution denotes the effect of buoyancy forces acting in a volume of $O(L^3)$ around the spheroid, and may be termed the inner-region contribution. Herein, we show that there exist additional buoyancy-induced contributions to the spheroid angular velocity arising from a perturbation of the ambient stratification, on much larger length scales, due to weak convection effects. Convection effects become important on length scales of order the stratification screening length of $L(Ri_vPe)^{-1/4}$ for $Ri_vPe \ll 1$ (Ardekani and Stocker [2010] and section 4.4.1), and the resulting outer-region contribution may be isolated from the full integral for the hydrodynamic component of the stratification torque in (4.22), by first subtracting the aforementioned inner-region contribution. Thus, we begin from the following difference integral:

$$Ri_v \frac{1}{Y_c} \int (\rho'^{(1)} - \rho'^{(10)}) \hat{g}_j U_{ji}^{(2)} dV, \tag{B.1}$$

where the density disturbance, whose governing equation is given by 4.27, is now denoted as $\rho'^{(10)}$ (as in section 4.4.1); the test velocity field tensor $\boldsymbol{U}^{(2)}$ is given in (4.43). Now, recall from section 4.4.1 that the difference $\rho'^{(1)} - \rho'^{(10)}$ grows as $O(Pe\, r)$, leading to the dominant contribution to the difference integral in (B.1) arising from scales large compared to $O(L)$, even in the limit $Ri_vPe \ll 1$. Therefore, neglecting the volume of the spheroid, and applying the convolution theorem, one obtains:

$$Ri_v\frac{1}{Y_c}\int(\rho'^{(1)}-\rho'^{(10)})\hat{g}_jU_{ji}^{(2)}dV=Ri_v\frac{1}{Y_c}\int[\hat{\rho}'^{(1)}(\mathbf{k})-\hat{\rho}'^{(10)}(\mathbf{k})]\hat{g}_j\hat{U}_{ji}^{(2)}(-\mathbf{k})d\mathbf{k}. \tag{B.2}$$

The Fourier transformed density field, $\hat{\rho}'^{(1)}(\mathbf{k})$, is obtained by solving (4.31-4.33), being given by

$$\hat{\rho}'^{(1)}=\frac{-\tilde{F}Pe[1-(\hat{g}_m\hat{k}_m)^2]+i8\pi^3k^2k_jD_j^s}{\left[iPe8\pi^3k^2k_j\hat{U}_j-PeRi_v(1-(\hat{g}_n\hat{k}_n)^2)-16\pi^4k^4\right]}. \tag{B.3}$$

The Fourier transformed density, $\hat{\rho}'^{(10)}(\mathbf{k})$, in (B.2) corresponds to the approximate form of $\rho'^{(10)}$ at large distances ($k \ll 1$), and may be obtained from Fourier transforming the solution of the diffusion equation with a concentration-dipole forcing at the origin (see discussion after (4.33) in section 4.4.2); thus, $\hat{\rho}'^{(10)}(\mathbf{k})$ is given by:

$$\hat{\rho}'^{(10)}=-\frac{i2\pi k_jD_j^s}{4\pi^2k^2}, \tag{B.4}$$

where the dipole strength, $\boldsymbol{D}^s$, is an order unity function of the spheroid aspect ratio for $Pe \ll 1$; it may be shown that $\boldsymbol{D}^s=D_{1s}\hat{\boldsymbol{g}}.(\boldsymbol{I}-\boldsymbol{pp})+D_{2s}(\hat{\boldsymbol{g}}.\boldsymbol{p})\boldsymbol{p}$, where $D_{1s}=8\pi\left(\xi_0^2-1\right)/3\xi_0^2(-\xi_0^2+(\xi_0^2-1)\xi_0 coth^{-1}\xi_0+2)$ and $D_{2s}=4\pi(\xi_0^2-1)/3\xi_0^3(-\xi_0^2coth^{-1}\xi_0+\xi_0+coth^{-1}\xi_0)$ for prolate spheroids; the corresponding expressions for oblate spheroids may be obtained using the transformation presented in section 4.3.

Since the dominant contributions to (B.2) come from scales of $O[L(Ri_vPe)^{-1/4}]$, we define a rescaled Fourier wavevector pertaining to the outer region as $\mathbf{k}_o=(Ri_vPe)^{-1/4}\mathbf{k}$. On doing so, one finds from (B.3) and (B.4):

$$\begin{aligned}&\hat{\rho}'^{(1)}(\mathbf{k}_o)-\hat{\rho}'^{(10)}(\mathbf{k}_o)=\\&\frac{\tilde{F}[1-(\hat{g}_m\hat{k}_{om})^2]-Ri_v^{\frac{3}{4}}Pe^{-\frac{1}{4}}i8\pi^3{k_o}^2k_{oj}D_j^s}{Ri_v\left[-iPe^{\frac{3}{4}}Ri_v^{-\frac{1}{4}}8\pi^3k_o^2k_{oj}\hat{U}_j+(1-(\hat{g}_n\hat{k}_{on})^2)+16\pi^4k_o^4\right]}+\frac{i2\pi k_{oj}D_j^s}{(Ri_vPe)^{1/4}4\pi^2k_o^2}.\end{aligned} \tag{B.5}$$

The relative magnitudes of the first vis-a-vis the remaining terms in the denominator of $\hat{\rho}'^{(1)}(\mathbf{k}_o)$ depends on the ratio $Pe/Ri_v^{\frac{1}{3}}$, as mentioned in section 4.4.1. In the limit $Pe \ll Ri_v^{\frac{1}{3}}$, the density difference in (B.5) reduces to

$$\hat{\rho}'^{(1)}(\mathbf{k}_o) - \hat{\rho}'^{(10)}(\mathbf{k}_o) \approx \frac{\tilde{F}[1-(\hat{g}_m\hat{k}_{om})^2]}{Ri_v\left[(1-(\hat{g}_n\hat{k}_{on})^2)+16\pi^4k_o^4\right]}, \tag{B.6}$$

at leading order. The test velocity field tensor in (4.43) is again $O(1/k) \sim O[Ri_vPe)^{-1/4}/k_o]$. Using this along with the $O(Ri_vPe)^{\frac{3}{4}}$ volume in Fourier space that contributes to the integral in (B.2) (that is, $d\mathbf{k} = (Ri_vPe)^{\frac{3}{4}}d\mathbf{k}_o$), would appear to lead to an $O(Ri_vPe)^{\frac{1}{2}}$ outer-region contribution to the angular velocity for $Ri_v, Pe \ll 1$. This contribution is, however, identically zero on account of the integrand being an odd function of $\boldsymbol{k}$. The absence of such a contribution arises from the fore-aft symmetry, at leading order, of the density and velocity disturbance fields in the outer region (see Ardekani and Stocker [2010],Varanasi and Subramanian [2021]); the symmetry of the density disturbance field may be seen from its Fourier transform in (B.6) which is an even function of $\mathbf{k}_o$.

Recall that in section 4.4.1, we had mentioned that the $O(Ri_v)$ inner-region contribution remained valid even for finite Ri_v provided $Ri_vPe \ll 1$, this because this torque contribution arose from $O(\gamma L^3 g/\mu)$ baroclinic flow induced due to the deformed iso-pycnals around a stationary spheroid, rather than the $O(U)$ disturbance velocity field associated with translation; the resulting dimensional angular velocity was independent of U. Interestingly, the small-*Pe* screening length above is also independent of U; it equals $(\mu.D/Lg\gamma)^{\frac{1}{4}}$ in terms of the actual physical parameters. The U-independence suggests that screening length for the onset of buoyancy-induced screening is independent of the source of the disturbance flow; it may indeed by verified, using an $O(\gamma L^3 g/\mu)$ scale for the velocity field and going through the arguments of section 4.4.1, that one obtains the same screening length. However, the more rapid $O(1/r^2)$ decay of the dipolar baroclinic flow implies that the $O(1/r)$ Stokeslet field dominates the distorts the pycnals at leading order, and it is this contribution that is accounted for in (B.6).

In light of the symmety-induced cancellation at leading order, one needs to consider the correction to (B.6) to obtain the leading order contribution from the outer region. In the limit $Pe \ll Ri_v^{\frac{1}{3}}$, on expanding (B.5), one readily finds:

$$\begin{aligned}\hat{\rho}'^{(1)}(\mathbf{k}_o) - \hat{\rho}'^{(10)}(\mathbf{k}_o) \approx{}& \frac{[\tilde{F}(1-(\hat{g}_m\hat{k}_{om})^2)]}{Ri_v\left[(1-(\hat{g}_n\hat{k}_{on})^2)+16\pi^4k_o^4\right]}\\ &+\frac{i2\pi k_{oj}D^s_j\left[(1-(\hat{g}_m\hat{k}_{om})^2)\right]}{(Ri_vPe)^{\frac{1}{4}}\left[(1-(\hat{g}_n\hat{k}_{on})^2)+16\pi^4k_o^4\right]4\pi^2k_o^2}+\frac{Pe^{\frac{3}{4}}i\tilde{F}(1-(\hat{g}_m\hat{k}_{om})^2)8\pi^3{k_o}^2k_{oj}\hat{U}_j}{Ri_v^{\frac{5}{4}}\left[(1-(\hat{g}_n\hat{k}_{on})^2)+16\pi^4k_o^4\right]^2},\end{aligned} \tag{B.7}$$

where we have only included correction terms that are odd in $\boldsymbol{k}$ which will lead to a nonzero angular velocity in (B.2). On combining the scalings arising from the test velocity ($(Ri_v Pe)^{-\frac{1}{4}}$), the Fourier space volume ($(Ri_v Pe)^{\frac{3}{4}}$) and the Ri_v prefactor in (B.2), one finds the first correction term (proportional to $\boldsymbol{D}^s$) in (B.7) to lead to an angular velocity of $O(Ri_v^{\frac{5}{4}} Pe^{\frac{1}{4}})$, while the second correction term gives a contribution of $O(Ri_v^{\frac{1}{4}} Pe^{\frac{5}{4}})$. The first correction is, however, always smaller than the O(Ri_v) inner-region contribution for $Ri_v, Pe \ll 1$. Therefore, we only consider the second correction for the explicit calculation below. Substituting (B.7) into the integral in (B.2), one finally obtains the following integral expression:

$$\Omega_i^{(1)d^{outer}} = \frac{Ri_v^{\frac{1}{4}} Pe^{\frac{5}{4}}}{Y_c} \int \frac{i\tilde{F}(1-(\hat{g}_m\hat{k}_{om})^2)8\pi^3 {k_o}^2 k_{oj}\hat{U}_j}{\left[(1-(\hat{g}_n\hat{k}_{on})^2)+16\pi^4 k_o^4\right]^2} \hat{g}_l \hat{U}_{li}^{(2)}(-\mathbf{k}_o)d\mathbf{k}_o, \tag{B.8}$$

for the outer-region contribution to the hydrodynamic component of the stratification-induced angular velocity, where:

$$U_{ij}^{(2)}(\boldsymbol{k}_o) = -\frac{\mathrm{i}}{2\pi k_o}\{B_1[(\varepsilon_{mjr}p_r)p_n + (\varepsilon_{njr}p_r)p_m] + B_3\varepsilon_{mnj}\}\hat{k}_{on}(\delta_{im} - \hat{k}_{oi}\hat{k}_{om}), \tag{B.9}$$

with B_1 and B_3 being given by (4.40) and (4.41), respectively for prolate spheroids. The aspect-ratio- dependent functions B_1 and B_3 for oblate spheroids can again be obtained as mentioned above .

To reiterate, the contribution given by (B.8) exists in addition to the $O(Ri_v)$ contribution evaluated in section 4.4.1, and given by (4.28). A comparison for $Ri_v \ll 1$ readily shows that the (B.8) is dominant when $Pe \gg Ri_v^{\frac{3}{5}}$. Using (B.9) in (B.8), one obtains

$$\begin{aligned}
&\Omega_i^{(1)d^{outer}} = \\
&Ri_v^{\frac{1}{4}} Pe^{\frac{5}{4}} \frac{4\pi^2\tilde{F}}{Y_c}\Bigg[B_1 \int \frac{(1-(\hat{g}_m\hat{k}_{om})^2){k_o}^2\hat{k}_{oj}\hat{U}_j}{\left[(1-(\hat{g}_n\hat{k}_{on})^2)+16\pi^4 k_o^4\right]^2}\varepsilon_{irj}p_r\{\hat{g}_j(\hat{k}_{ol}p_l)+\hat{k}_{oj}(\hat{g}_l p_l)-2(\hat{k}_{ol}p_l)(\hat{k}_{oq}\hat{g}_q)\hat{k}_j\}]d\mathbf{k}_o \\
&\qquad + B_3 \int \frac{(1-(\hat{g}_m\hat{k}_{om})^2){k_o}^2\hat{k}_{oj}\hat{U}_j}{\left[(1-(\hat{g}_n\hat{k}_{on})^2)+16\pi^4 k_o^4\right]^2}\varepsilon_{ijr}\hat{g}_j\hat{k}_{or}d\mathbf{k}_o\Bigg].
\end{aligned} \tag{B.10}$$

The evaluation of the integral in (B.10) is best done in a $\hat{\boldsymbol{g}}$-aligned spherical coordinate system. After expressing $\hat{\boldsymbol{U}}$ in terms of $\hat{\boldsymbol{g}}$, $\boldsymbol{p}$ and $An(\kappa)$ as in (4.48), the unit wave vector

$\hat{\boldsymbol{k}}_o$ and $\boldsymbol{p}$ may be written in the form $-\cos\theta'\hat{\boldsymbol{g}} + \sin\theta'\cos\phi'\mathbf{1}_{g^{\perp 1}} + \sin\theta'\sin\phi'\mathbf{1}_{g^{\perp 2}}$ and $-\cos\psi\hat{\boldsymbol{g}} + \sin\psi\mathbf{1}_{g^{\perp 1}}$, respectively, in a $\hat{\boldsymbol{g}}$-aligned coordinate system similar to the $\hat{\boldsymbol{U}}$-aligned coordinate system used in section 4.4.2; θ' and ϕ' here being the polar and azimuthal angles, with the polar axis being along $-\hat{\boldsymbol{g}}$. Substituting these in (B.10) and using the rescaled wavevector $2\pi\boldsymbol{k}_o$ leads to the following form:

$$\Omega_2^{(1)d^{outer}} = Ri_v^{\frac{1}{4}} Pe^{\frac{5}{4}} \frac{\tilde{F}}{8\pi^3 Y_c} \left[\int_0^\infty dk_o \int_0^\pi d\theta' \int_0^{2\pi} d\phi' [(\cos\psi\cos\theta' + \sin\psi\sin\theta'\cos\psi)\cos\psi(1-An) + \cos\theta' An](B_1 f_1 + B_3\sin\theta'\cos\phi') \frac{k_o^4 \sin^3\theta'}{(k_o^4 + \sin^2\theta')^2} \right], \tag{B.11}$$

$$\Omega_2^{(1)d^{outer}} = Ri_v^{\frac{1}{4}} Pe^{\frac{5}{4}} \frac{\tilde{F}}{8\pi^3 Y_c} \frac{\pi^{\frac{5}{2}}\Gamma(\frac{9}{4})\sin 2\psi}{231\sqrt{2}\Gamma(\frac{3}{4})} \left[-12AnB_1 - 6(1-An)B_1 + 11(1-An)B_3 + (1-An)B_1\cos 2\psi)\right]. \tag{B.12}$$

An explicit calculation shows that the angular velocity given by (B.12) always acts to orient the spheroid edgewise, and as mentioned above, is greater than the inner-region contribution for $Pe > Ri_v^{\frac{3}{5}}$. A comparison with the inertial torque obtained in section 4.3 (given by (4.23) and (4.24) for prolate and oblate spheroids) suggests that the broadside-on-edgewise transition may now be characterized on the $Ri_v^{\frac{1}{4}} Pe^{\frac{5}{4}}/Re - \kappa$ plane in the range $Ri_v^{\frac{3}{5}} \ll Pe \ll Ri_v^{\frac{1}{3}}$. Note that the dependence on ψ in (B.12) is more complicated than that the $\sin 2\psi$-dependence characterizing the regular contributions derived in sections 4.3 and 4.4.1. However, the deviation from the $\sin 2\psi$-dependence turns out to be very small in magnitude, and as a result, the upper and lower thresholds, separating the broadside-on and edgewise orientations in the aforesaid parameter-plane, are nearly coincident.

The above analysis for the outer-region contribution is restricted to the limit $Pe \ll Ri_v^{\frac{1}{3}}$. In the opposite limit, $Pe \gg Ri_v^{\frac{1}{3}}$, the first term in the denominator in (B.5), that denotes the effects of the ambient convection, is dominant over the second one that denotes the buoyancy forces. The first term in the numerator continues to be dominant, and therefore, at leading order, one now obtains $\hat{\rho}'^{(1)}(\mathbf{k}_o) \approx \frac{\tilde{F}[1-(\hat{g}_m\hat{k}_{om})^2]}{[-i(Ri_v Pe)^{\frac{3}{4}} 8\pi^3 k_o^2 k_{oj}\hat{U}_j + Ri_v 16\pi^4 k_o^4]}$. The two terms in the denominator, denoting the convection and diffusion of the density disturbance, are comparable when $k_o \sim O(Ri_v^{-\frac{1}{4}} Pe^{\frac{3}{4}})$ which, in physical space, corresponds to the familiar (dimensional) convective screening length of $O(LPe^{-1})$. However, combining this with the test velocity field leads to an integrand that is $O(1/k^4)$ for small k, in turn leading to the Fourier integral in (B.2) being divergent for $k \to 0$. This suggests that the dominant contribution in the said limit comes from length scales much larger than $O(Pe^{-1})$. A closer examination shows that, for $Pe \gg Ri_v^{\frac{1}{3}}$, the dominant contribution to the integral in (B.2) arises for $k \sim O(Ri_v^{\frac{1}{3}})$, corresponding to the large-Pe stratification screening length of $O(Ri_v^{-\frac{1}{3}})$, and that is indeed much larger than the aforementioned convective screening length; the viscous forces are now asymptotically small compared to the convection and buoyancy terms, so the balance reduces to that considered in section 4.4.2 for large Pe. Thus, the implication is that the angular velocity integral in (B.2) reduces to the same one as that obtained in section 4.4.2 when $Pe \gg Ri_v^{\frac{1}{3}}$, and the outer-region contribution is now $O(Ri_v^{\frac{2}{3}})$.

To summarize, for Pe small compared to unity, the hydrodynamic component of the stratification-induced angular velocity always includes an inner-region contribution of $O(Ri_v)$ that has been derived in section 4.4.1, with an additional outer-region contribution that is $O(Ri_v^{\frac{1}{4}} Pe^{\frac{5}{4}})$ for $Pe \ll Ri_v^{\frac{1}{3}}$, being given by (B.12) above, and that is $O(Ri_v^{\frac{2}{3}})$ for $Pe \gg Ri_v^{\frac{1}{3}}$, the corresponding expression being the same as that obtained in section 4.4.2. The only difference between the angular velocity contributions in the regimes $Ri_v^{\frac{1}{3}} \ll Pe \ll 1$ and $Pe \gg 1$ is that, although sub-dominant, there is still an $O(Ri_v)$ inner-region contribution in the former case owing to the dominance of diffusion on length scales of $O(L)$; in contrast, diffusion is only expected to be important in a boundary layer with a thickness of $O(Pe^{-\frac{1}{3}})$ for $Pe \gg 1$, and there can be no analog of the small-Pe $O(Ri_v)$ contribution.

Finally, we note that the leading $O(Ri_v Pe)^{\frac{1}{2}}$ contribution, obtained by using the analog of (B.6) for a fore-aft asymmetric particle, may not be zero. The inner region contribution continues to be $O(Ri_v)$, and hence, such a particle may experience a broadside-on to edgewise transition at a smaller Pe; that is when $(Ri_v Pe)^{\frac{1}{2}} > Ri_v$ or $Pe > O(Ri_v)$, in contrast to the fore-aft symmetric spheroidal geometry examined above.

Bibliography

Akiyama, S., Waki, Y., Okino, S., and Hanazaki, H. (2019). Unstable jets generated by a sphere descending in a very strongly stratified fluid. *Journal of Fluid Mechanics*, 867:26–44.

Alldredge, A. L., Cowles, T. J., MacIntyre, S., Rines, J. E., Donaghay, P. L., Greenlaw, C. F., Holliday, D., Dekshenieks, M. M., Sullivan, J. M., and Zaneveld, J. R. V. (2002). Occurrence and mechanisms of formation of a dramatic thin layer of marine snow in a shallow pacific fjord. *Marine Ecology Progress Series*, 233:1–12.

Anand, P., Ray, S. S., and Subramanian, G. (2020). Orientation dynamics of sedimenting anisotropic particles in turbulence. *Phys. Rev. Lett.*, 125:034501.

Anis Alias, A. and Page, M. (2017). Low-reynolds-number diffusion-driven flow around a horizontal cylinder. *Journal of Fluid Mechanics*, 825:1035–1055.

Ardekani, A. M. and Stocker, R. (2010). Stratlets: Low Reynolds Number Point-Force Solutions in a Stratified Fluid. *Physical Review Letters*, 105(8):084502.

Auguste, F., J, M., and D, F. (2013). Falling styles of disks. *Journal of Fluid Mechanics*, 719:388–405.

Batchelor, G. K. (1967). *An Introduction to Fluid Dynamics*. Cambridge Mathematical Library. Cambridge University Press.

Benjamin, T. B. (1986). Note on added mass and drift. *Journal of Fluid Mechanics*, 169:251–256.

Caflisch, R. E. and Luke, J. H. (1985). Variance in the sedimentation speed of a suspension. *The Physics of fluids*, 28(3):759–760.

Camassa, R., Falcon, C., Lin, J., McLaughlin, R. M., and Parker, R. (2009). Prolonged residence times for particles settling through stratified miscible fluids in the stokes regime. *Physics of Fluids*, 21(3):031702.

Candelier, F., Mehaddi, R., and Vauquelin, O. (2014). The history force on a small particle in a linearly stratified fluid. *Journal of Fluid Mechanics*, 749:184–200.

Chadwick, R. and Zvirin, Y. (1974). Slow viscous flow of an incompressible stratified fluid past a sphere. *Journal of Fluid Mechanics*, 66(2):377–383.

Childress, S. (1964). The slow motion of a sphere in a rotating, viscous fluid. *Journal of Fluid Mechanics*, 20(2):305–314.

Chisholm, N. G. and Khair, A. S. (2017). Drift volume in viscous flows. *Physical Review Fluids*, 2:064101.

Chisholm, N. G. and Khair, A. S. (2018). Partial drift volume due to a self-propelled swimmer. *Physical Review Fluids*, 3(1):014501.

Clavano, W. E., Boss, E., and Karp-Boss, M. (2007). Inherent optical properties of non-spherical marine-like particles — from theory to observation. In Gibson, R. N., Atkinson, R. J. A., and Gordon, J. D. M., editors, *Oceanography and Marine Biology: an annual review*, pages 1–38. Taylor Francis.

Clercx, H. J., Van Heijst, G. F., et al. (2018). *Mixing and dispersion in flows dominated by rotation and buoyancy*. Springer.

Cox, R. G. (1965). The steady motion of a particle of arbitrary shape at small reynolds numbers. *Journal of Fluid Mechanics*, 23(4):625–643.

Craik, A. D. (2005). George gabriel stokes on water wave theory. *Annual review of fluid mechanics*, 37:23.

Dabade, V., Marath, N., and Subramanian, G. (2015a). Effects of inertia and viscoelasticity on sedimenting anisotropic particles. *Journal of Fluid Mechanics*, 778:133–188.

Dabade, V., Marath, N., and Subramanian, G. (2016). The effect of inertia on the orientation dynamics of anisotropic particles in simple shear flow. *Journal of Fluid Mechanics*, 791:631–703.

Dabade, V., Marath, N. K., and Subramanian, G. (2015b). Effects of inertia and viscoelasticity on sedimenting anisotropic particles. *Journal of Fluid Mechanics*, 778:133–188.

Dabiri, J. O. (2006). Note on the induced lagrangian drift and added-mass of a vortex. *Journal of Fluid Mechanics*, 547:105–113.

Dandekar, R., Shaik, V. A., and Ardekani, A. M. (2020). Motion of an arbitrarily shaped particle in a density stratified fluid. *Journal of Fluid Mechanics*, 890:A16.

Daniel, W. B., Ecke, R. E., Subramanian, G., and Koch, D. L. (2009). Clusters of sedimenting high-reynolds-number particles. *Journal of Fluid Mechanics*, 625:371–385.

Darwin, C. (1953). Note on hydrodynamics. *Mathematical Proceedings of the Cambridge Philosophical Society*, 49(2):342–354.

Doostmohammadi, A. and Ardekani, A. M. (2013). Interaction between a pair of particles settling in a stratified fluid. *Phys. Rev. E*, 88:023029.

Doostmohammadi, A. and Ardekani, A. M. (2014). Reorientation of elongated particles at density interfaces. *Phys. Rev. E*, 90:033013.

Doostmohammadi, A., Dabiri, S., and Ardekani, A. M. (2014). A numerical study of the dynamics of a particle settling at moderate reynolds numbers in a linearly stratiied fluid. *Journal of Fluid Mechanics*, 750:5–32.

Doostmohammadi, A., Stocker, R., and Ardekani, A. M. (2012). Low-reynolds-number swimming at pycnoclines. *Proceedings of the National Academy of Sciences*, 109(10):3856–3861.

Dutkiewicz, A., Müller, R. D., Cannon, J., Vaughan, S., and Zahirovic, S. (2019). Sequestration and subduction of deep-sea carbonate in the global ocean since the early cretaceous. *Geology*, 47(1):91–94.

Eames, I. (2003). The concept of drift and its application to multiphase and multibody problems. *Philosophical Transactions of the Royal Society of London. Series A: Mathematical, Physical and Engineering Sciences*, 361(1813):2951–2965.

Eames, I., Belcher, S., and Hunt, J. (1994). Drift, partial drift and darwin's proposition. *Journal of Fluid Mechanics*, 275:201–223.

Eames, I. and Flor, J.-B. (1998). Fluid transport by dipolar vortices. *Dynamics of atmospheres and oceans*, 28(2):93–105.

Eames, I. and Gilbertson, M. (2005). Mixing and drift in gas-fluidised beds. *Powder technology*, 154(2-3):185–193.

Eames, I., Gobby, D., and Dalziel, S. B. (2003). Fluid displacement by stokes flow past a spherical droplet. *Journal of Fluid Mechanics*, 485:67–85.

Eames, I. and Hunt, J. C. R. (1997). Inviscid flow around bodies moving in weak density gradients without buoyancy effects. *Journal of Fluid Mechanics*, 353:331–355.

Eames, I. and McIntyre, M. E. (1999). On the connection between stokes drift and darwin drift. In *Mathematical Proceedings of the Cambridge Philosophical Society*, volume 126, pages 171–174. Cambridge University Press.

Fouxon, I. and Leshansky, A. (2014). Convective stability of turbulent boussinesq flow in the dissipative range and flow around small particles. *Physical Review E*, 90:053002.

Guillaume, M. and Magnaudet, J. (2002). Path instability of a rising bubble. *Physical Review Letters*, 88(1):014502.

Gustavsson, K., Sheikh, M., Lopez, D., Naso, A., Pumir, A., and Mehlig, B. (2019). Effect of fluid inertia on the orientation of a small prolate spheroid settling in turbulence. *New Journal of Physics*, 21(8):083008.

Hanazaki, H. (1988). A numerical study of three-dimensional stratified flow past a sphere. *Journal of Fluid Mechanics*, 192:393–419.

Hanazaki, H., Kashimoto, K., and Okamura, T. (2009a). Jets generated by a sphere moving vertically in a stratified fluid. *Journal of Fluid Mechanics*, 638:173–197.

Hanazaki, H., Konishi, K., and Okamura, T. (2009b). Schmidt-number effects on the flow past a sphere moving vertically in a stratified diffusive fluid. *Physics of Fluids*, 21(2):026602.

Hanazaki, H., Nakamura, S., and Yoshikawa, H. (2015). Numerical simulation of jets generated by a sphere moving vertically in a stratified fluid. *Journal of Fluid Mechanics*, 765:424–451.

Janowitz, G. S. (1968). On wakes in stratified fluids. *Journal of Fluid Mechanics*, 33(3):417–432.

Jiang, F., Zhao, L., Andersson, H., Gustavsson, K., Pumir, A., and Mehlig, B. (2020). Inertial torque on a small spheroid in a stationary uniform flow. *Phys. Rev. Fluids*.

Joseph, D., Liu, Y., Poletto, M., and Feng, J. (1994). Aggregation and dispersion of spheres falling in viscoelastic liquids. *Journal of Non-Newtonian Fluid Mechanics*, 54:45–86.

Katija, K. and Dabiri, J. O. (2009). A viscosity-enhanced mechanism for biogenic ocean mixing. *Nature*, 460(7255):624–626.

Khayat, R. E. and Cox, R. (1989). Inertia effects on the motion of long slender bodies. *Journal of Fluid Mechanics*, 209:435.

Kim, S. and Karrila, S. (1991). *Microhydrodynamics*. Dover.

Kiorboe, T. (2011). How zooplankton feed: mechanisms, traits and trade-offs. *Biological Reviews*, 86:311–339.

Lab, K. (2018). *Phytoplankton Identification guide 2018*. Blurb.

Lagerstrom, P. (2013). *Matched Asymptotic Expansions: Ideas and Techniques*. Applied Mathematical Sciences. Springer New York.

Leal, L. (1992). *Laminar flow and convective transport processes*. Butterworth-Heinemann.

Leal, L. G. (2007). *Advanced Transport Phenomena: Fluid Mechanics and Convective Transport Processes*. Cambridge Series in Chemical Engineering. Cambridge University Press.

Leshansky, A. M. and Pismen, L. M. (2010). Do small swimmers mix the ocean? *Phys. Rev. E*, 82:025301.

Lighthill, M. J. (1956). Drift. *Journal of Fluid Mechanics*, 1(1):31–53.

List, E. J. (1971). Laminar momentum jets in a stratified fluid. *Journal of Fluid Mechanics*, 45(3):561–574.

Lorenz, E. N. (1955). Available potential energy and the maintenance of the general circulation. *Tellus*, 7(2):157–167.

MacIntyre, S., Alldredge, A. L., and Gotschalk, C. C. (1995). Accumulation of marines now at density discontinuities in the water column. *Limnology and Oceanography*, 40(3):449–468.

Magnaudet, J. and Mercier, M. J. (2020). Particles, Drops, and Bubbles Moving Across Sharp Interfaces and Stratified Layers. *Annual Review of Fluid Mechanics*, 52(1):null.

Marath, N. and Subramanian, G. (2017). The effect of inertia on the time period of rotation on an anisotropic particle in simple shear flow. *Journal of Fluid Mechanics*, 830:830.

Martin, A., Boyd, P., Buesseler, K., Cetinic, I., Claustre, H., Giering, S., Henson, S., Irigoien, X., Kriest, I., Memery, L., Robinson, C., Saba, G., Sanders, R., Siegel, D., Villa-Alfageme, M., and Guidi, L. (2020). The oceans' twilight zone must be studied now, before it is too late. *Nature*, 580(7801):26–28.

Matthew, C., L, P., C, H., and Galloway, T. S. (2011). Microplastics as contaminants in the marine environment: A review. *Marine Pollution Bulletin*, 62:2588–2597.

Maxwell, J. C. (1869). On the Displacement in a Case of Fluid Motion. *Proceedings of the London Mathematical Society*, s1-3(1):82–87.

Mehaddi, R., Candelier, F., and Mehlig, B. (2018). Inertial drag on a sphere settling in a stratified fluid. *Journal of Fluid Mechanics*, 855:1074–1087.

Mercier, M. J., Wang, S., Péméja, J., Ern, P., and Ardekani, A. M. (2020). Settling disks in a linearly stratified fluid. *Journal of Fluid Mechanics*, 885:A2.

Mrokowska, M. M. (2018). Stratification-induced reorientation of disk settling through ambient density transition. *Scientific Reports*, 8:412.

Mrokowska, M. M. (2020a). Dynamics of thin disk settling in two-layered fluid with density transition. *Acta Geophys*, 68:1145–1160.

Mrokowska, M. M. (2020b). Influence of pycnocline on settling behaviour of non-spherical particle and wake evolution. *Scientific Reports*, 10:20595.

Munk, W. and Wunsch, C. (1998). Abyssal recipes ii: Energetics of tidal and wind mixing. *Deep Sea Research Part I: Oceanographic Research Papers*, 45(12):1977–2010.

Munk, W. H. (1966). Abyssal recipes. *Deep Sea Research and Oceanographic Abstracts*, 13(4):707 – 730.

Ochoa, J. L. and Van Woert, M. (1977). Flow visualization of boundary layer separation in a stratified fluid. *Unpublished report, Scripps Insititution of Oceanography*, 28.

Okino, S., Akiyama, S., and Hanazaki, H. (2017). Velocity distribution around a sphere descending in a linearly stratified fluid. *Journal of Fluid Mechanics*, 826:759–780.

Okino, S., Akiyama, S., Takagi, K., and Hanazaki, H. (2021). Density distribution in the flow past a sphere descending in a salt-stratified fluid. *Journal of Fluid Mechanics*, 927.

Patricia, E., Frederic R, D. F., D, F., and J, M. (2012). Wake-induced oscillatory paths of bodies freely rising or falling in fluids. *Annual Review of Fluid Mechanics*, 44:97–121.

Phillips, O. (1970). On flows induced by diffusion in a stably stratified fluid. *Deep-Sea Research*, 17:435–443.

Prairie, J., Ziervogel, K., Camassa, R., Mclaughlin, R., White, B., Dewald, C., and Arnosti, C. (2015). Delayed settling of marine snow: Effects of density gradient and particle properties, and implications for carbon cycling. *Marine Chemistry*, 175:28–38.

Prasad, A., Kondev, J., and Stone, H. A. (2007). Drift in supported membranes. *Physics of Fluids*, 19(11):113103.

Proudman, I. and Pearson, J. R. A. (1957). Expansions at small reynolds numbers for the flow past a sphere and a circular cylinder. *Journal of Fluid Mechanics*, 2(3):237–262.

Pushkin, D. O., Shum, H., and Yeomans, J. M. (2013). Fluid transport by individual microswimmers. *Journal of Fluid Mechanics*, 726:5–25.

Rankine, W. J. M. (1864). X. on plane water-lines in two dimensions. *Philosophical Transactions of the Royal Society of London*, 154:369–391.

Saffman, P. G. (1965). The lift on a small sphere in a slow shear flow. *Journal of Fluid Mechanics*, 22(2):385–400.

Shaik, V. A. and Ardekani, A. M. (2020a). Drag, deformation, and drift volume associated with a drop rising in a density stratified fluid. *Phys. Rev. Fluids*, 5:013604.

Shaik, V. A. and Ardekani, A. M. (2020b). Far-field flow and drift due to particles and organisms in density-stratified fluids. *Phys. Rev. E*, 102:063106.

Srdić-Mitrović, A., Mohamed, N., and Fernando, H. (1999). Gravitational settling of particles through density interfaces. *Journal of Fluid Mechanics*, 381:175–198.

Stokes, G. G. (1847). On the theory of oscillatory waves. *Transactions of the Cambridge philosophical society*, pages 441–455.

Subramanian, G. (2010). Viscosity-enhanced bio-mixing of the oceans. *Current Science*, 98:1103.

Subramanian, G. and Koch, D. (2005). Inertial effects on fiber motion in simple shear flow. *Journal of Fluid Mechanics*, 535:383.

Subramanian, G. and Koch, D. L. (2008). Evolution of clusters of sedimenting low-reynolds-number particles with oseen interactions. *Journal of Fluid Mechanics*, 603:63–100.

Summerhayes, C. P. and Thorpe, S. A. (1996). *Oceanography: an illustrated guide*. CRC Press.

Turner, A. and Holmes, L. (2011). Occurrence, distribution and characteristics of beached plastic production pellets on the island of malta (central mediterranean). *Marine Pollution Bulletin*, 62:377–381.

Turner, J. (1979). *Buoyancy Effects in Fluids*. Cambridge Monographs on Mechanics. Cambridge University Press.

Turner, J. (2015). Zooplankton fecal pellets, marine snow, phytodetritus and the ocean's biological pump. *Progress in Oceanography*, 130:205–248.

Vallis, G. K. (2011). *Climate and the Oceans*. Princeton University Press.

Vallis, G. K. (2017). *Atmospheric and oceanic fluid dynamics*. Cambridge University Press.

Van Dyke, M. (1975). *Perturbation Methods in Fluid Mechanics*. Parabolic Press.

Varanasi, A. and Subramanian, G. (2021). Motion of a sphere in a viscous stratified fluid. *Journal of Fluid Mechanics*, page submitted.

Varanasi, A. K., Marath, N. K., and Subramanian, G. (2021). The rotation of a sedimenting anisotropic particle in a stratified fluid. *Journal of Fluid Mechanics*, page accepted.

Vladimirov, V. and Li'in, K. (1991). Slow motions of a solid in a continuously stratified fluid. *J. Appl. Mech. Tech. Phys.*, 32:194–200.

Wagner, G. L., Young, W. R., and Lauga, E. (2014). Mixing by microorganisms in stratified fluids. *Journal of Marine Research*, 72(2):47–72.

Wikipedia contributors (2022). Atlantic meridional overturning circulation — Wikipedia, the free encyclopedia. [Online; accessed 13-August-2022].

Winters, K. B., Lombard, P. N., Riley, J. J., and D'Asaro, E. A. (1995). Available potential energy and mixing in density-stratified fluids. *Journal of Fluid Mechanics*, 289:115–128.

Wunsch, C. (1970). On oceanic boundary mixing. *Deep-Sea Research*, 17:293–301.

Yick, K. Y., Torres, C. R., Peacock, T., and Stocker, R. (2009). Enhanced drag of a sphere settling in a stratified fluid at small reynolds numbers. *Journal of Fluid Mechanics*, 632:49–68.

Yih, C.-S. (1985). New derivations of darwin's theorem. *Journal of Fluid Mechanics*, 152:163–172.

Yih, C.-S. (1995). Kinetic-energy mass, momentum mass, and drift mass in steady irrotational subsonic flows. *Journal of Fluid Mechanics*, 297:29–36.

Yih, C.-S. (1997). Evolution of darwinian drift. *Journal of Fluid Mechanics*, 347:1–11.

Zhang, J., Mercier, M. J., and Magnaudet, J. (2019). Core mechanisms of drag enhancement on bodies settling in a stratified fluid. *Journal of Fluid Mechanics*, 875:622–656.

Zvirin, Y. and Chadwick, R. S. (1975). Settling of an axially symmetric body in a viscous stratified fluid. *International Journal of Multiphase Flow*, 1:743–752.